12-1-2013

Membrane-Protein Dynamics: New Perspectives in FcepsilonRI Signaling through Single Particle Tracking

Patrick Cutler

Follow this and additional works at: https://digitalrepository.unm.edu/biom_etds

Patrick J. Cutler

Candidate

Biomedical Sciences

Department

This dissertation is approved, and it is acceptable in quality and form for publication:

Approved by the Dissertation Committee:

Dr. Diane Lidke

, Chairperson

Dr. Keith Lidke

Dr. Bridget Wilson

Dr. David Haaland

Membrane-Protein Dynamics: New Perspectives in
FcepsilonRI Signaling through Single Particle Tracking

by

Patrick J. Cutler

B.S. Chemistry/Math, East Carolina University, 2006
M.S. Chemistry, East Carolina University, 2008

DISSERTATION

Submitted in Partial Fulfillment of the
Requirements for the Degree of

Doctor of Philosophy
Biomedical Sciences

The University of New Mexico
Albuquerque, New Mexico

August 2013

ACKNOWLEDGMENTS

I would like to thank all of my committee members (Diane, Keith, Dave, Bridget, Bill) for their continued support and invaluable input without which this work would not be possible. My advisor and committee chair, Dr. Diane Lidke, provided me with the environment in which I was able to grow as a scientist while keeping me on task. My co-advisor, Dr. Keith Lidke, has amazed me time and again with his ability to deconstruct complex problems into their simplest components. I would like to thank both Diane and Keith for being great mentors and friends. Dr. David Haaland was instrumental in my move to UNM and has become a great friend and life mentor. Dr. Bridget Wilson is a great scientist who has been an important driving force in my research. Dr. Bill Shuttleworth provided great outside inputs about direction and the big picture.

I have had the pleasure of working with many awesome people throughout my graduate work at UNM. I would like to acknowledge all current and former members of the OWL (Oliver Wilson Lidke) lab and Keith Lidke's biophysics lab. A great working environment created a great foundation which to perform research. Nick Andrews provided a concrete experimental base from which I could easily expand. Shalini Low-Nam is one of the most dedicated and energetic people that I have ever met, and provided me with an example of a work ethic to aspire towards. I would like to thank Samantha Schwartz for great discussion and friendship. Sam is always available to be distracted for a long discussion about science or non-science related topics. Sam and Chris Valley were always available to help with feasibility studies. There are more members of the OWL lab than I can mention here, but I would also like to thank Anna Holmes, Rachel Grattan, Hannah Johnson, and Richard Pepermans (aka uncle Ricky) for their continued friendship and scientific collaboration. Dr. Fang Huang taught me many things including the value of positive thinking. Dr. Michael Malik's attention to detail was essential for the development of the hyperspectral microscope. Peter Relich is a great colleague with whom it has been a pleasure collaborating on multiple projects.

The friendships that I have made while in New Mexico have made the experience here all that much more valuable and my time here more enjoyable. This includes many of the people mentioned above. Additionally, I would like to thank Kendra, Dave, Zac, Annie, Brian, Susan, Steve, Kristen, Lauren, and many others for their friendship and good memories.

Finally, I would like to thank my family. My mother (Jan), brother (Robert), and sister (Erica) have always supported me in all of my endeavors and continue to be a source of inspiration. My family has expanded during my time in New Mexico with my wife (Rachel) and her family (Otis, Theresa, Toby, Olivia, and Becky), and I thank them for all of their support throughout my dissertation work. Mostly, I need to thank Rachel, my wife, who has lovingly supported me and my scientific goals.

Membrane-Protein Dynamics: New Perspectives in FcεRI Signaling through Single Particle Tracking

by

Patrick J. Cutler

B.S. Chemistry/Math, East Carolina University 2006

M.S. Chemistry, East Carolina University 2008

Ph.D., Biomedical Sciences, 2013

ABSTRACT

Under physiological conditions IgE binds to its high affinity receptor, FcεRI. The aggregation of IgE-FcεRI by crosslinker initiates intracellular signaling resulting in the release of histamines and other cellular mediators that are the basis for allergic disease. In the field of IgE-FcεRI, receptor immobilization was thought to trigger signaling.   Recent single particle tracking (SPT) experiments presented evidence supporting the hypothesis that small mobile aggregates are signaling competent. SPT is an important method for investigating spatio-temporal relationships at the subcellular level. New SPT tools are necessary to adequately investigate this hypothesis. The studies presented here both develop and apply tools for investigating IgE-FcεRI. A Bayesian based approach for the estimation of diffusion coefficients for SPT is presented. The diffusion estimator accounts for several experimental realities including finite camera exposure time, trajectory intermittency, and variable localization uncertainty. Derivation of the method and applications to both real and simulated data are presented. This method provides the capacity to accurately estimate a diffusion coefficient with a credible interval for small sets of data. In order to better interrogate the aggregation of IgE-FcεRI a high speed hyperspectral line-scanning microscope was developed to perform multi-color SPT (mcSPT) experiments at ~30 fps with up to 8 spectrally distinct colors of quantum dots (QDs). A full description the microscope and software necessary for mcSPT are included in this work. Additionally, several applications of the hyperspectral microscope are presented to highlight its capabilities. The dynamics of IgE-FcεRI aggregates are interrogated using the hyperspectral microscope by perform mc SPT with 5- colors of QD probes. Surprisingly, many transient aggregates of QD-IgE are observed.

Corroborating this observation is the observation that transient interactions of a QD crosslinker analog (DNP-QD) are also observed. Multi-color single molecule imaging of 4-colors of DNP-QD with 3-colors of Alexa Fluor IgE are used to characterize the valency of DNP-QD. Finally, signaling competency of a crosslinked aggregate is observed in SPT experiments with DNP-QD and Syk-GFP. This set of experiments provides significant evidence supporting the previous hypothesis and extends it to include the signaling competency of transient interactions.

TABLE OF CONTENTS

CHAPTER 1: INTRODUCTION

1.1 Importance of Dynamic Protein Interactions

The fundamentals of cellular processes are driven by protein-protein interactions. These interactions can either be transient or sustained both of which are vital for regulating protein function [1,2]. Protein interactions are modulated by protein expression, localization, and binding energy [3]. Classical methods for studying protein-protein interactions involve static (i.e. biochemisty, electron microscopy, etc.) or ensemble (i.e. FRET, Microscopy, etc.) techniques, but there is mounting evidence that the properties influencing protein-protein interactions are dynamic. One means of altering binding energies is through protein modifications (i.e. phosphorylation, ion association, etc.). Protein phosphorylation and dephosphorylation is a dynamic process [4] important for regulating protein interactions and consequently cellular signaling [5].

An example of cellular function intertwined with protein-protein interactions is the transduction of signals from extracellular stimuli to intracellular response, and two of the most well-studied receptor families are the receptor tyrosine kinases (RTKs) [6] and multi-chain immune recognition receptors (MIRRs) [7]. Signal initiation for both of these systems is based on receptor dimerization or aggregation. The binding of ligand induces dimerization/aggregation of RTKs by a diverse set of mechanisms (**Figure 1.1A**) while

2
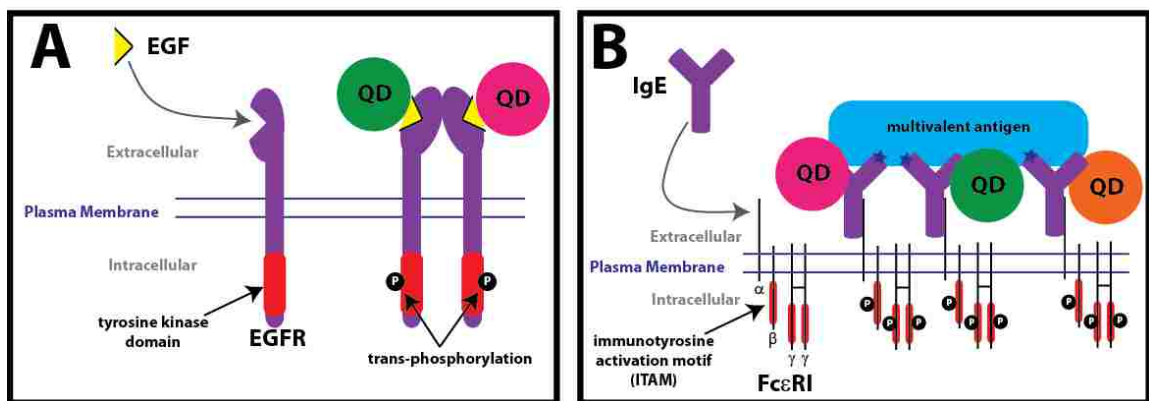
MIRRs are physically crosslinked by a multivalent antigen (**Figure 1.1B**). In either case, dimerization/aggregation leads to phosphorylation of the cytoplasmic tails of receptors, which alters the binding energy to intracellular signaling molecules. Receptor interactions with intracellular signaling molecules initiates signal propagation eventually resulting in a cellular response. More detail on the signal initiation for specific members of the RTK and MIRR families is included in **Figure** . Even though these are two of the most well studied families of receptors, many questions still remain about how dimerization/aggregation leads to phosphorylation of the cytoplasmic tails of the proteins, and how receptor dynamics contribute to signal transduction.

1.2 Protein Localization

Since protein localization is essential for protein interactions and signal transduction, it is important here to have a more in depth discussion of protein localization. The radius of a typical protein is ~2.5-5 nm [8] and the radius of a typical mammalian cell is on the order of 5-10 μm. Cellular compartmentalization is important for protein localization [3] and places restrictions on feasible interactions. For example, proteins restricted to membranes (i.e. transmembrane or tethered proteins) are limited to interacting with proteins that are also constrained to or in close proximity to the same membrane. The local environment (anything in direct contact with the protein) of individual proteins is increasingly complex due to the free energy of interaction with other proteins, lipids, and other molecules in the cellular environment [3]. For proteins restricted to membranes, these concepts contribute into the hypothesis of compartmentalization within the membrane due to lipid rafts [9,10], actin corrals [11], and protein islands [12]. These local environments are dynamic and can be altered by cellular scale events (i.e. endocytosis, actin rearrangement, cell motility, cell division, etc.). This leads to stochasticity in the local environment of individual proteins of the same type. The stochastic attributes of individual proteins are lost in ensemble measurements emphasizing the importance to investigate proteins on the single molecule level.

Traditionally, sub-cellular protein localization is investigated using biochemical methods, electron microscopy (EM), or optical microscopy. Each technique has

advantages and disadvantages. Biochemistry is limited by low time resolution and almost no spatial resolution other than that afforded by cellular fractionation. EM does provide nanometer resolution and is an important technique for investigating submicron-scale structures and local protein environments, but is limited to fixed samples. Optical microscopy has the ability to visualize live or fixed samples, but is limited in resolution by the diffraction limit of light (Abbe reference) which is ~200-300 nm for visible light. Recent technical advances have allowed experimentalists to interrogate cellular systems below the diffraction limit of light with optical microscopy. A summary of representative techniques is included in **Table 1.1**. In the majority of these, the spatio-temporal scale required for directly monitoring protein-protein interactions is not achieved.

1.3 Membrane-Protein Dynamics

Not only are protein-protein interactions dynamic, but individual proteins themselves are dynamic. The most commonly cited theory behind the mobility of membrane bound proteins due to thermodynamics is based on work by Saffman and Delbrück in the 1970's [13]. The Saffman-Delbrück model predicts a weak dependence of mobility on the radius of the transmembrane domain of a protein. More recently several works have put forth theoretical frameworks to account for disagreements between the Saffman-Delbrük model and experimental results. Naji et al. propose that local deformations in the membrane due to height mismatch between the transmembrane domains and the lipid bilayer is a key contributor to receptor mobility [14] and can cause a dependence of mobility on $1/a$ (where a is protein radius). This theory supports experiments in which transmembrane protein mobility was determined in bilayers with variable thickness [15]. The $1/a$ dependence on mobility is consistent with experimental and simulation work by Knight et al. [16]. In this, the mobility of engineered proteins with variable numbers (1 to 3) of pleckstrin homology (pH) domains was observed to be proportional to the number of pH domains. Note that pH domains bind to phosphatidylinositol-(3,4,5)-trisphosphate (PIP_3) lipids. Mobility changes in this work were attributed to additive contributions of friction.

4

The Saffman-Delbrück model and its modifications only consider a single protein in an infinite plane of membrane. As illustrated above, there is a lack of consensus in the field about this simplified system. In reality, the plasma membrane of a live cell is a complex mixture of lipids, proteins, and other molecules.

One of the initial theories on the complexities of the cellular membrane was the fluid mosaic model [17]. The fluid mosaic model proposed that the cellular membrane was composed of a sea of rapidly diffusing lipids and proteins. This model has been refined by the concept of micro- or nano-domain compartmentalization within the plasma membrane [18]. Compartmentalization within the membrane is based on three key organizational hypotheses: lipid rafts [10], protein islands [12], and actin corrals [11]. Additionally, transient or stable binding of proteins to relatively static intra- and extra-cellular structures (insert references) and viscous resistance due to membrane crowding [19–21] have been hypothesized to contribute to the observed mobility of proteins restricted to the plasma membrane. It is important to note that there is conceptual overlap between several of these hypotheses.

Due to the complexities of the plasma membrane, several types of motion are observed for membrane constituents: immobile, confined, anomalous, Brownian, and directed motion [22]. It is very likely that multiple hypotheses discussed above contribute to the modes of motion observed for proteins restricted to the plasma membrane. Depending on the type of motion, the observed mobility of proteins may be dependent on the length and time scale of observations. For example, to observe confinement with a characteristic distance Δx, the observation time (Δt) is proportional to $\Delta x^2/4D$ where D is the diffusion coefficient [23]. This exemplifies the necessity for techniques with high temporal resolution to investigate protein mobility.

Table 1.1 Summary of representative techniques for measuring protein localization and/or dynamics.

Method	Spatial Resolution (nm)	Temporal Resolution (s)	Single Molecule
Biochemistry	NA	10	No
Electron Microscopy	1	NA	Yes
Optical Microscopy			
Confocal	200-300	1	No
Stimulated Emission Depletion (STED)	40	10	No
Fluorescence Correlation Spectroscopy (FCS)	200-300	5	No
STED-FCS[24]	40	5	No
Localization Microscopy (LM)	10	NA	Yes
Single Particle Tracking (SPT)[22]	10-50	1e-3	Yes
Fluorescence Recovery after Photobleaching (FRAP)	1000	10	No
Image Correlation Spectroscopy (ICS) [25]	20-200	0.1	No
FRET	1-10	0.1	No
Single molecule FRET (smFRET)	1-10	1	yes
Structured Illumination Microscopy (SIM)	100	10	No

1.4 Single Particle Tracking

Due to the interplay between proteins and their local environment, it is feasible to obtain information about the local protein environment from protein mobility. Accurate localization of individual membrane associated proteins in live cells requires a spatial resolution on the scale of individual proteins and temporal resolution able to capture protein dynamics. The representative list of techniques in **Table 1.1** highlights that single particle tracking (SPT) provides a platform for investigating the dynamics of individual proteins in live cells. In SPT, there are trade-offs between signal to noise, observation time (i.e. trajectory length) and temporal resolution; therefore, 30 fps is considered to be adequate to capture dynamic processes of individual proteins at the single molecule level.

SPT and localization microscopy (LM) are related techniques in optical microscopy, which use the localization of individually labeled molecules to resolve the location of a molecule below the diffraction limit (**Figure 1.2A**). In LM, individual molecule localizations are acquired over time and used to build up a super resolution image. The time of acquisition typically requires that the sample be fixed. In contrast, SPT is performed on live cells where an observable particle (i.e. fluorescent particle) is localized over several sequential time frames. The individual localizations are then built into a trajectory. Information about the mobility of the protein is determined from the trajectory.

The appropriate treatment of SPT data is vital for proper biological interpretation. The mean squared displacement (MSD) analysis is the most common method used to interpret mobility from SPT data [23]. Several non-ideal experimental conditions including trajectory intermittency (due to fluorophore blinking, movement perpendicular to the focal plane, etc.) and variable localization precision result in deviation of the MSD from the theoretical framework underlying the MSD [26,27]. It is important to emphasize here that many probes used for SPT experiments are susceptible to blinking and photo bleaching; therefore, SPT data is often composed of

Single Particle Single Color | Two Particle Single Color | Two Particle Two Color

100 nm (A) | 100 nm (B) | 100 nm (C)
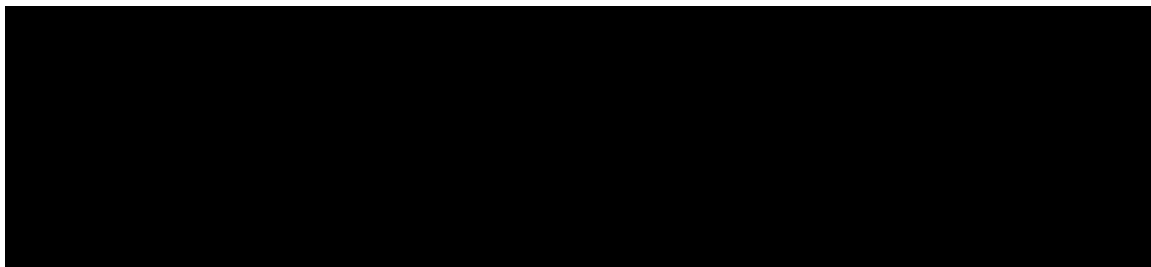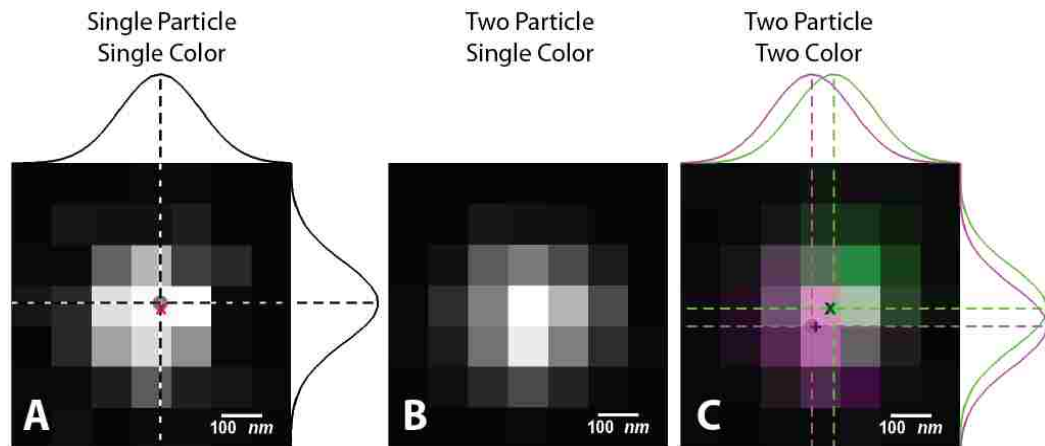
many short trajectories [28]. If mobility information is desired about those individual trajectories then the MSD is not appropriate, since there are not enough data points, and erroneous diffusion coefficients are often obtained. The instantaneous diffusion coefficient is another example of a desired mobility readout for which the MSD is not appropriate [26]. **Chapter 2** addresses these issues by presenting two mobility estimators which account for trajectory intermittency and variable localization precision. The methods presented in **Chapter 2** are compared with the MSD using both simulated and real data. The newly presented methods provide mobility estimators suited for quantifying the mobility of short intermittent trajectories with variable localization precision. These methods contribute to the appropriate analysis of SPT data in subsequent chapters.

The localization precision of methods based on the localization of individually labeled molecules (i.e. LM and SPT) is limited by the density of single particles in the field of view (FOV). Under the ideal case of randomly distributed molecules, increasing the density of particles in the FOV will result in an increase in the probability of having overlapping diffraction limited spots. The apparently heterogeneous distribution of

molecules observed in many biological systems further increases the probability of observing overlapping diffraction limited spots. For example, if two proteins labeled with identical probes approach each other within 100 nm, then the precision with which the two probes can be localized is affected by the overlap of the two diffraction limited spots (**Figure 1.2B**). This limits the direct observation of protein-protein interactions. A few recent studies [29,30] have interpreted dimerization from the overlap of two diffraction limited spots. A key issue in these studies is differentiating between co-localization and true dimerization. It is important to note here that even though, SPT is a powerful technique allowing the experimentalist to observe stochastic events of individual proteins, caution should be taken in analyzing SPT data in order to prevent over interpretation. In contrast to using single color SPT to directly observe protein-protein interactions, two-color SPT provides a technique that uses two probe populations to label the protein(s) of interest (**Figure 1.2C**). This helps to retain localization precision (~10 nm) in each channel for highly overlapping diffraction limited spots.

1.4.1 Epidermal Growth Factor Receptor

Since receptor interactions are the basis for signal initiation in RTKs [31] and MIRRs [32,33] (**Figure 1.1**), understanding the spatiotemporal organization of the receptors is important for appropriate positive and negative signal regulation. Recent work has used one- and two-color SPT to correlate the spatiotemporal organization of RTKs and MIRRs with signal initiation.

EGFR is one of the best-studied members of the RTK family. Binding of EGF to EGFR is thought to induce/stabilize a conformational change in the EGFR's extracellular domain [34]. This model is supported by two-color SPT experiments investigating dimerization [35]. Sustained and repetitive interactions were observed between two colors of QD-EGF bound to EGFR (**Figure 1.1A**). In this study, observed dimerization events were used to quantify interactions using a Hidden Markov Model (HMM). Due to the observation of repetitive interactions, a three state HMM was required to explain the data. The three states were interpreted as dimer, co-confined, and free states.

Additional experiments in this study suggest that the cortical cytoskeleton (actin corrals) has a greater influence on receptor co-confinement than cholesterol (lipid rafts). While two-color labeling allowed for identification of dimer events, the low labeling density required for SPT means that capturing protein interactions is a fairly rare event. The capacity to observe receptors with more than two colors in a similar investigation would allow the experimentalist to more readily observe interactions. Furthermore, an increase in spectrally distinct probes will allow for investigation of higher-order aggregates.

1.4.2 IgE-FcεRI

Several members of the MIRR family including the B-cell receptor [36], T-cell receptor [37], and the high affinity receptor for IgE (FcεRI) [38–40] have been investigated using SPT. FcεRI is of particular interest here and will therefore be discussed in more detail. Two recent SPT investigations of FcεRI [39,40] have revealed important insights into FcεRI signaling. In both of these studies, QD labeled IgE (QD-IgE; **Figure 1.1B**) was used to track QD-IgE-FcεRI complexes on live cells.

In the first investigation [39], prolonged overlap of diffraction limited spots was observed using single color SPT; therefore, two-color SPT was used to investigate this phenomenon in finer detail. Two-color SPT provided the spatial resolution (~10 nm for each color) necessary to determine that receptors were co-confined and not actually interacting. Simultaneous single color SPT of QD-IgE with GFP-actin provided the first direct evidence of receptor corralling by actin. Combining these results with additional experiments provided evidence to suggest that actin corralling contributes to co-localization of IgE and changes in receptor mobility upon crosslinking. This work also provided general insights into receptor confinement.

The second investigation [40] tested the long-standing hypothesis that IgE-FcεRI immobilization is a prerequisite for signaling. This hypothesis is mainly supported by ensemble experiments using fluorescence recovery after photobleaching (FRAP) [41–43], fluorescence correlation spectroscopy (FCS) [43], and anisotropy [44–47]. SPT of QD-IgE-FcεRI in the presence of crosslinker with multivalent antigen of different doses and valencies

was used to probe the relationship between receptor dynamics and signaling. In contrast to the standard perception in the field, QD-IgE-FcεRI mobility increased for low dose/valency crosslinkers, while sufficient signaling (i.e. secretion of cellular mediators) was maintained.

In an additional experiment, a hyperspectral microscope (HSM) revealed that small aggregates are mobile under crosslinking conditions sufficient for signaling. The HSM used in this experiment is a custom built point-scanning system with the capacity to acquire 512 spectral channels (500-800 nm) for each spatial pixel within the image [48], and provided the ability to image 5-colors of QD-IgE-FcεRI simultaneously [49]. An illustration of a hyperspectral image is included in **Figure 1.3**. Small aggregates were identified by visual identification of consistent spectral features over time. Due to the point scanning nature of this instrument, its frame rate is proportional to the number of pixels acquired. This provided a frame rate of 0.25 frames per second (fps) for the experiments presented in this work; therefore, reliable mobility information could not be extracted from the data. The observation of small mobile aggregates in this experiment was interpreted from the tedious procedure of manual identification and the qualitative observation of mobility.

The two SPT studies on FcεRI discussed here redefine the relationship between the dynamics of crosslinked IgE-FcεRI and signaling. The concluding hypothesis from these studies was that the immobilization of IgE-FcεRI is more related to endocytosis than signal propagation. Automated multi-color SPT (mcSPT) at 30 fps would help to further interrogate this hypothesis.

1.5 Hyperspectral Microscopy

The limitation of the currently available technology was the impetus to develop an HSM and corresponding software capable of performing mcSPT at 30 fps. The description and several applications of a hyperspectral line-scanning microscope (UNM HSM) and corresponding software for mcSPT of up to 8 colors of commercially available QDs is described in **Chapter 3**. This is the first work to report mcSPT of 8 colors of QDs. Algorithms for the automated localization and subsequent building of trajectories in

hyperspectral images are a significant contribution of this work and a notable advantage over previous work [40]. **Chapter 3** includes several applications of mcSPT with QD-EGF and QD-IgE on live cells many of which are expansions of the work discussed above. One application is high density SPT, which provides the capacity to obtain spatial diffusion maps and instantaneous diffusion coefficients from a single acquisition. One of the methods developed in **Chapter 2** was applied here to compute the spatial diffusion maps and instantaneous diffusion coefficients. This highlights the necessity for the development of appropriate analysis techniques to extract useful information from raw experimental data. While the experiments presented in **Chapter 3** are mere demonstrations of the instruments capabilities they provide feasibility for performing full studies.

1.6 Dynamics of FcεRI-IgE Aggregates

The UNM HSM provides the opportunity to study FcεRI-IgE with unprecedented detail to investigate the relationships between aggregate size, dynamics, and signaling. **Chapter 4** presents a study of aggregation dynamics for QD-IgE-FcεRI and directly examines its relationships to signaling. In this study, mcSPT with 5 colors of QD-IgE is used to directly observe dynamic interactions of aggregates under several crosslinking and signaling conditions. Since the recruitment of signaling complexes to the cytoplasmic tail of FcεRI is dependent on phosphorylation of immunotyrosine activation motifs (ITAMs) by src family kinases[50], inhibition of src family kinases with PP2[51] is used to compare aggregation stability independent of signaling. Multi-color single molecule imaging of 3-color of fluorescent IgE and 4-colors of DNP-QD provides information about distributions of aggregates in relation to crosslinker. Additionally, 2-color SPT in total internal reflection fluorescence (TIRF) microscopy images with DNP-QD and GFP-Syk provides a direct readout of signaling while observing receptor aggregate mobility.
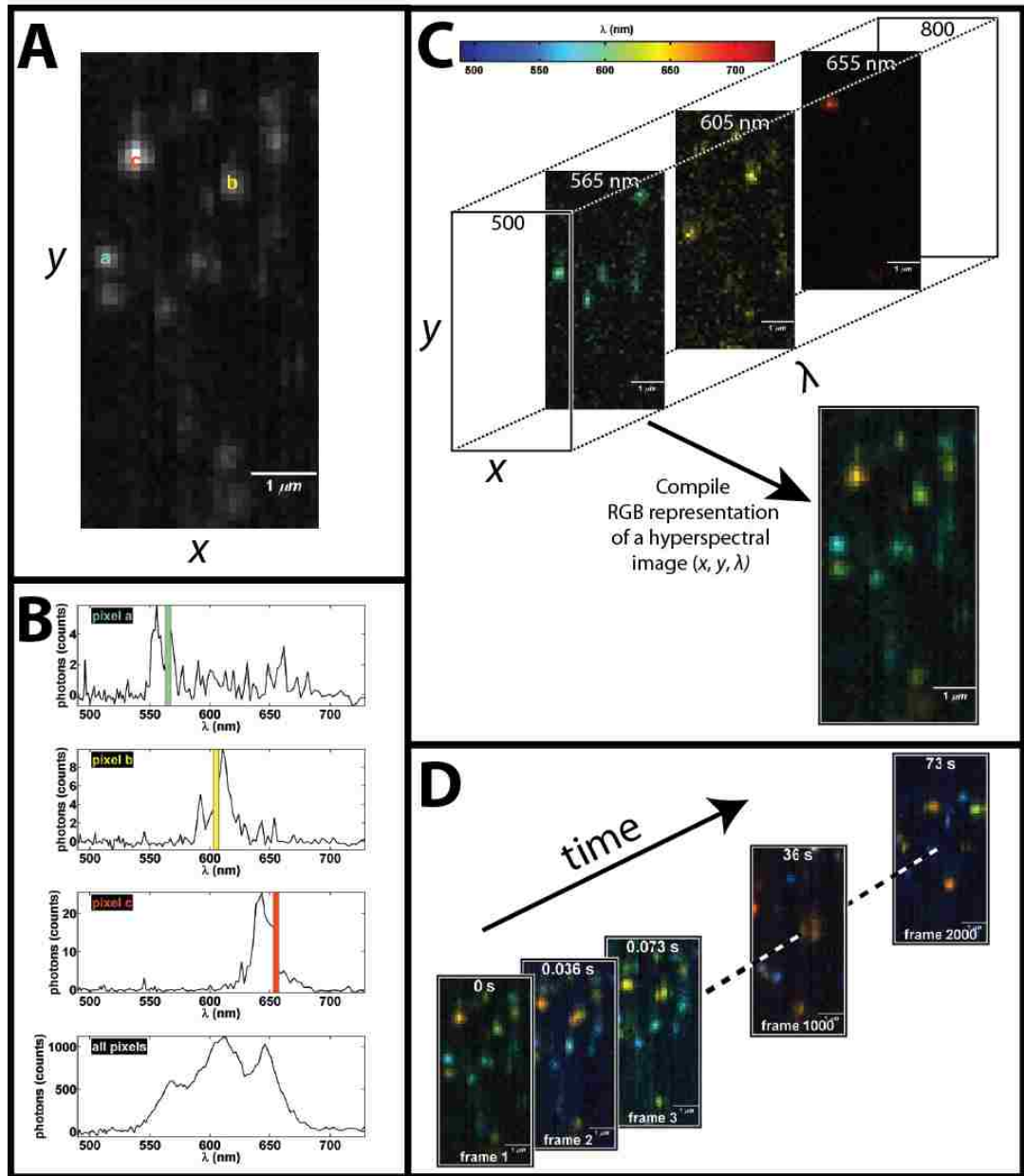
1.7 References

(1)   Jones, S.; Thornton, J. M. *Proc. Natl. Acad. Sci. U. S. A.* **1996**, *93*, 13–20.

(2)   Nooren, I. M. .; Thornton, J. M. *J. Mol. Biol.* **2003**, *325*, 991–1018.

(3)   Nooren, I. M. A.; Thornton, J. M. *EMBO J.* **2003**, *22*, 3486–92.

(4)   Mayer, B. J. *FEBS Lett.* **2012**, *586*, 2575–9.

(5)   Cohen, P. *Nat. Cell Biol.* **2002**, *4*, E127–30.

(6)   Lemmon, M. a; Schlessinger, J. *Cell* **2010**, *141*, 1117–34.

(7)   Sigalov, A. B. *Trends Immunol* **2004**, *25*, 583–9 ST – Multichain immune recognition receptor.

(8)   Erickson, H. P. *Biol. Proced. Online* **2009**, *11*, 32–51.

(9)   Lingwood, D.; Simons, K. *Science (80-.).* **2010**, *327*, 46–50 ST – Lipid Rafts As a Membrane–Organizing P.

(10)   Pike, L. J. *J. Lipid Res.* **2006**, *47*, 1597–8.

(11)   Kusumi, A.; Nakada, C.; Ritchie, K.; Murase, K.; Suzuki, K.; Murakoshi, H.; Kasai, R. S.; Kondo, J.; Fujiwara, T. *Annu. Rev. Biophys. Biomol. Struct.* **2005**, *34*, 351–378 ST – PARADIGM SHIFT OF THE PLASMA MEMBRAN.

(12)   Lillemeier, B. F.; Pfeiffer, J. R.; Surviladze, Z.; Wilson, B. S.; Davis, M. M. *Proc. Natl. Acad. Sci.* **2006**, *103*, 18992–18997 ST – Plasma membrane–associated prote.

(13)   Saffman, P. G.; Delbrück, M. *Proc. Natl. Acad. Sci.* **1975**, *72*, 3111–3113.

(14)   Naji, A.; Levine, A. J.; Pincus, P. A. *Biophys. J.* **2007**, *93*, L49–51.

(15)   Gambin, Y.; Lopez-Esparza, R.; Reffay, M.; Sierecki, E.; Gov, N. S.; Genest, M.; Hodges, R. S.; Urbach, W. *Proc. Natl. Acad. Sci. U. S. A.* **2006**, *103*, 2098–102.

(16)   Knight, J. D.; Lerner, M. G.; Marcano-Velázquez, J. G.; Pastor, R. W.; Falke, J. J. *Biophys. J.* **2010**, *99*, 2879–87.

(17)   Singer, S. J.; Nicolson, G. L. *Science (80-.).* **1972**, *175*, 720–731 ST – The Fluid Mosaic Model of the Struct.

(18)   Cambi, A.; Lidke, D. S. *ACS Chem. Biol.* **2012**, *7*, 139–49.

(19)   Bussell, S. J.; Koch, D. L.; Hammer, D. A. *Biophys. J.* **1995**, *68*, 1836–1849.

(20)   Saxton, M. J. *Biophys. J.* **1993**, *64*, 1766–1780.

(21)   Kucik, D. F.; Elson, E. L.; Sheetz, M. P. C.-P. *Biophys J* 1999, *76*, 314–22.

(22)   Saxton, M. J.; Jacobson, K. *Annu. Rev. Biophys. Biomol. Struct.* 1997, *26*, 373–399.

(23)   Qian, H.; Sheetz, M. P.; Elson, E. L. C.-P. *Biophys. J.* 1991, *60*, 910–21.

(24)   Eggeling, C.; Ringemann, C.; Medda, R.; Schwarzmann, G.; Sandhoff, K.; Polyakova, S.; Belov, V. N.; Hein, B.; von Middendorff, C.; Schönle, A.; Hell, S. W. *Nature* 2009, *457*, 1159–62.

(25)   Digman, M. A.; Gratton, E. 2013, 645–668.

(26)   Michalet, X. *Phys Rev E Stat Nonlin Soft Matter Phys* 2010, *82*, 041914 ST − Mean square displacement analysis of.

(27)   Michalet, X.; Berglund, A. J. *Phys. Rev. E. Stat. Nonlin. Soft Matter Phys.* 2012, *85*, 061916.

(28)   Manley, S.; Gillette, J. M.; Patterson, G. H.; Shroff, H.; Hess, H. F.; Betzig, E.; Lippincott-schwartz, J. *Nat. Methods* 2008, *5*, 2007–2009.

(29)   Chung, I.; Akita, R.; Vandlen, R.; Toomre, D.; Schlessinger, J.; Mellman, I. *Nature* 2010, *464*, 783–7.

(30)   Kasai, R. S.; Suzuki, K. G. N.; Prossnitz, E. R.; Koyama-Honda, I.; Nakada, C.; Fujiwara, T. K.; Kusumi, A. *J. Cell Biol.* 2011, *192*, 463–80.

(31)   Kholodenko, B. N. *Nat. Rev. Mol. Cell Biol.* 2006, *7*, 165–76.

(32)   Sigalov, A. *Semin. Immunol.* 2005, *17*, 51–64.

(33)   Treanor, B.; Batista, F. D. *Curr. Opin. Immunol.* 2010, *22*, 299–307.

(34)   Dawson, J. P.; Berger, M. B.; Lin, C.-C.; Schlessinger, J.; Lemmon, M. A.; Kathryn, M.; Dawson, J. P.; Berger, M. B.; Lin, C.-C.; Schlessinger, J.; Lemmon, M. A.; Ferguson, K. M. *Mol. Cell. Biol.* 2005, *25*, 7734–42.

(35)   Low-Nam, S. T.; Lidke, K. A.; Cutler, P. J.; Roover, R. C.; van Bergen en Henegouwen, P. M. P.; Wilson, B. S.; Lidke, D. S. *Nat. Struct. Mol. Biol.* 2011, *advance on*.

(36)   Treanor, B.; Depoil, D.; Gonzalez-Granja, A.; Barral, P.; Weber, M.; Dushek, O.; Bruckbauer, A.; Batista, F. D. *Immunity* 2010, *32*, 187–99.

(37)   Douglass, A. D.; Vale, R. D. C.-P. *Cell* 2005, *121*, 937–50.

(38)   Feder, T. J.; Brust-Mascher, I.; Slattery, J. P.; Baird, B.; Webb, W. W. *Biophys. J.* 1996, *70*, 2767–73.

(39)   Andrews, N. L.; Lidke, K. a; Pfeiffer, J. R.; Burns, A. R.; Wilson, B. S.; Oliver, J. M.; Lidke, D. S. *Nat. Cell Biol.* 2008, *10*, 955–963.

(40)   Andrews, N. L.; Pfeiffer, J. R.; Martinez, a M.; Haaland, D. M.; Davis, R. W.; Kawakami, T.; Oliver, J. M.; Wilson, B. S.; Lidke, D. S. *Immunity* 2009, *31*, 469–479.

(41)   Mao, S. Y.; Varin-Blank, N.; Edidin, M.; Metzger, H.; Cells, T.; Ma, S. *J Immunol* 1991, *146*, 958–66.

(42)   Menon, A. K.; Holowka, D.; Webb, W. W.; Baird, B. C.-P. A. *J Cell Biol* 1986, *102*, 541–50.

(43)   Pyenta, P. S.; Schwille, P.; Webb, W. W.; Holowka, D.; Baird, B. A. *J. Phys. Chem. A* 2003, *107*, 8310–8318 ST – Lateral Diffusion of Membrane Lipi.

(44)   Myers, J. N.; Holowka, D.; Baird, B. A. *Biochemistry* 1992, *31*, 567–75 ST – Rotational motion of monomeric and di.

(45)   Rahman, N. A.; Pecht, I.; Roess, D. A.; Barisas, B. G. *Biophys J* 1992, *61*, 334–46 ST – Rotational dynamics of type I Fc epsi.

(46)   Tamir, I.; Schweitzer-Stenner, R.; Pecht, I. *Biochemistry* 1996, *35*, 6872–83.

(47)   Zidovetzki, R.; Bartholdi, M.; Arndt-Jovin, D. J.; Jovin, T. M. *Biochemistry* 1986, *25*, 4397–401 ST – Rotational dynamics of the Fc recep.

(48)   Sinclair, M. B.; Haaland, D. M.; Timlin, J. a; Jones, H. D. T. *Appl. Opt.* 2006, *45*, 6283–91.

(49)   Haaland, D. M.; Jones, H. D. T.; Van Benthem, M. H.; Sinclair, M. B.; Melgaard, D. K.; Stork, C. L.; Pedroso, M. C.; Liu, P.; Brasier, A. R.; Andrews, N. L.; Lidke, D. S. *Appl. Spectrosc.* 2009, *63*, 271–279.

(50)   Kitaura, J.; Eto, K.; Kinoshita, T.; Kawakami, Y.; Leitges, M.; Lowell, C. a; Kawakami, T. *J. Immunol.* 2005, *174*, 4495–4504 ST – Regulation of Highly Cytokinergic .

(51)   MacGlashan, D.; Miura, K.; Lavens-Phillips, S. *Biochem Pharmacol* 2000, *60*, 1717–27 ST – Pharmacology of IgE–mediated desensi.

CHAPTER 2: ESTIMATION OF DIFFUSION COEFFICIENTS IN INTERMITTENT SINGLE PARTICLE TRACKING DATA WITH VARIABLE LOCALIZATION PRECISION

Chapter 2

Estimation of Diffusion Coefficients in Intermittent Single Particle Tracking Data with Variable Localization Precision

Authors: Patrick J. Cutler, Peter K. Relich, and Keith A. Lidke

2.1   Abstract

Single particle tracking (SPT) is a powerful tool for investigating the mobility of proteins in the cellular environment. After trajectories are generated from imaging data, it has long been typical to fit to the Mean Squared displacement (MSD) versus time to a diffusion model to extract a diffusion coefficient (D). However, MSD analysis is ill-suited to straight-forwardly handle variable localization precisions and trajectory intermittency that often occurs in practice when tracking blinking fluo-

rophores such as quantum dots. Here we describe a method to directly estimate D from an observed trajectory maximizing the use of the acquired data while accommodating missing data, variable localization precision and finite exposure time of the detector. We show that under the assumption of free Brownian motion the likelihood expression $P(\overrightarrow{\sigma}|D)$ can be solved with a recursion relation. We use the likelihood to calculate a Bayesian posterior and define credible intervals for D. We compare this estimator to MSD fitting and to a simplified likelihood estimator that doesn't include frame-to-frame covariance effects, but for which the Cramér Rao Bound is easily described. The estimators are compared with simulated data, experimental data generated with known trajectories, and live cell single particle tracking data. The Bayesian estimator is shown to be superior in all cases.

2.2   Introduction

The spatial and temporal resolution afforded by single particle tracking (SPT) methods utilizing colloidal gold [5, 7], fluorescent molecules [22, 26], and quantum dots (QDs) [4] provide significant biological insights [9]. The ability to probe the dynamics and heterogeneity of the cellular environment at the single molecule level is a key advantage of SPT over other ensemble techniques. For example, SPT of QD labeled IgE (QD-IgE) bound to its high affinity receptor (FcεRI) on the surface of mast cells has provided important insights into the receptor dynamics in the initiation of the allergic response [1, 2].

The field of SPT lacks a consensus in the proper treatment of experimental data, and many commonly used methods do not account for experimental realities. **Figure 2.1** demonstrates several non-ideal features of experimental SPT data (e.g. finite camera exposure time, trajectory intermittency and variable localization uncertainties). The movement of probes during a single camera exposure leads to motion blur
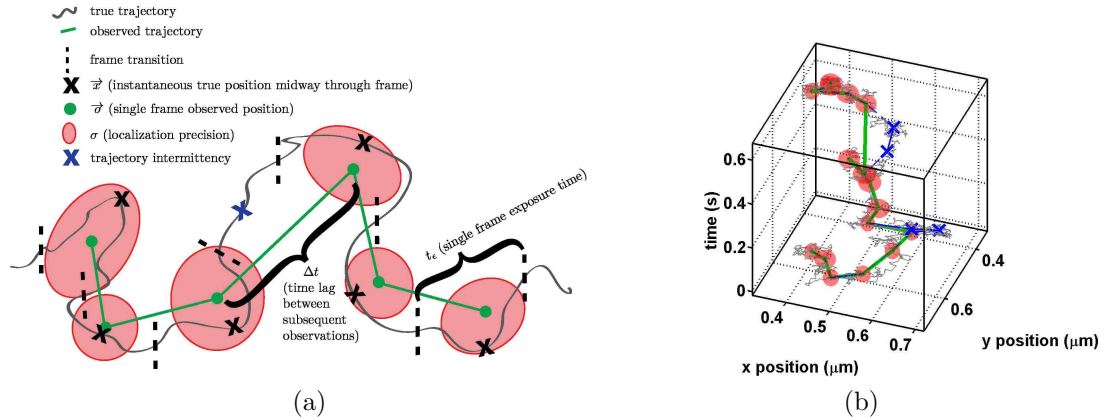
Figure 2.1: **Features in experimental SPT data. (2.1a)** is a conceptual rendition highlighting several issues observed in experimental SPT data. **(2.1b)** is a simulated trajectory with a similar depiction as in **(2.1a)**. The actual trajectory (black line) with 100 steps per camera exposure is used to simulate Gaussian blobs which are subsequently localized and built in a trajectory (dashed blue line). Trajectory intermittency (20%) is included in the simulation by random omission of observations (blue x). The observed trajectory is represented by the green line, and the estimated localization precision for each localization is represented by the red ellipsoids.

in experimental SPT data. Due to motion blur, the observed position for a probe during a single camera exposure (**figure 2.1a** green dot) is an average of all positions of the probe (**figure 2.1a** gray line) during the exposure [12]. This leads to an increase in the overall localization uncertainty due to a convolution of the static localization uncertainty with the dynamic localization uncertainty. The observation of the average position leads to correlated information in sequential observations. See references [20, 15, 12] for a thorough treatment of this topic. Trajectory intermittency (**figure 2.1a** blue x) is commonly observed in experimental SPT data due to out of focus motion and fluorophore blinking [8, 6]. Causes for variable localization uncertainties (**figure 2.1a** red ellipses) include non-uniform sample illumination, camera pixelation, and blinking on time scales shorter than the camera exposure time.

Based on the principles of thermodynamics, the diffusion coefficient (D) is the simplest model for quantifying mobility in an isotropic medium. Typically, D is

estimated by fitting a line to the MSD (D_{MSD}; **figure 2.2a**) to quantify mobility in SPT data [18]. A recent work [12] addressed inconsistencies in the literature for the number of points used to compute D_{MSD}. In this work, it was demonstrated that the number of points needed to optimally fit the MSD is related to the reduced square localization error

$$\text{RLE}^2 = \frac{\sigma^2}{D\Delta t} + 2R \tag{2.1}$$

where σ^2 is the variance due to localization uncertainty, Δt is the time lag between consecutive observations, and R is the motion blur coefficient. The motion blur coefficient is discussed in more detail in the Theory section (Eq. 2.8). Another recent work [3] described a maximum likelihood estimator for D. A comparison of this maximum likelihood estimator and the fitting of the optimal number of points in the MSD revealed that the accuracy of the two algorithms to estimate D is related to RLE^2 and the number of observations (N) [13]. Taking these findings into account D_{MSD} in this work refers to fitting a line to the MSD with the number of points set by the empirical formula defined by Michalet [13]

$$\text{MSD}_{\text{fitpoints}} = E(2 + 2.3(\text{RLE}^2)^{0.52}). \tag{2.2}$$

While Michalet and Berglund [13] provide a significant advance by taking into account track length, localization uncertainty, and finite integration time for calculating D and its expected variance, both methods expect contiguous trajectories and a single representative value for the localization uncertainty. As highlighted above, these conditions are not met under many typical experimental conditions.

More recent work by the Landes group has expanded the MLE developed by Berglund to account for intermittent trajectories [23]. The Landes group utilizes the uniqueness of the diagonal components of the covariance matrix to allow for heterogeneities in the variance due to observed diffusion with different time spacings.

21
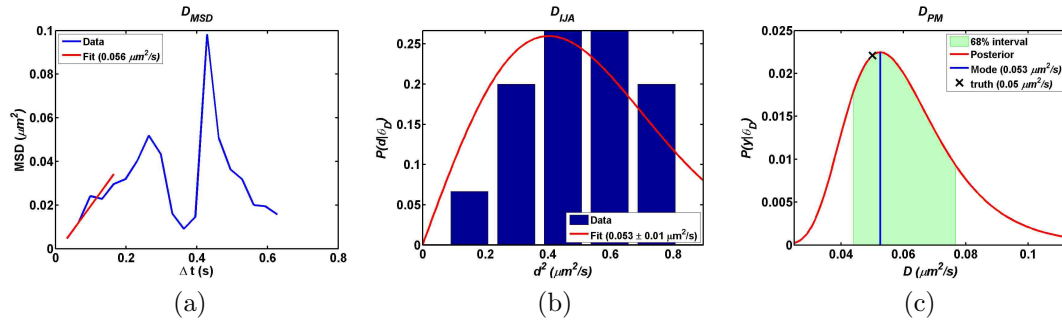
Figure 2.2: **Estimating D for a Simulated Trajectory.** D is estimated for the trajectory shown in **figure 2.1b**. **(2.2a)** A fit (red line) of the first 5 points of the MSD (blue line) are used to estimate D. **(2.2b)** A unit normalized histogram of individual squared jumps divided by Δt (blue) compared with the distribution of displacements given the D_{est}. The uncertainty in D_{IJA} (noted in the legend) is provided by the CRB. **(2.2c)** Shows the posterior distribution (red line), the mode (blue line), and the 68% confidence interval (green shading) for D_{PM}. The true underlying D (black x;0.05 $\mu m^2/s$) is indicated in **2.2c**.

The applicability of this method is limited to short trajectories due to computational expense.

Michalet[12] and Berglund[3] separately highlight the benefit of estimating the localization uncertainty independent of D. Estimating the position of individual particles using a maximum likelihood based method provides a straight forward platform for the independent estimate of the localization uncertainty by computing the Cramér Rao Bound (CRB) [19, 24].

Due to the complexity of biological systems, several types of motion are observed (i.e. Brownian, corraled, anomalous, or directed motion)[7]. Characterizing different modes of motion in SPT data is of great interest to biologists and an active area of research [14]. The shape of the mean squared displacement (MSD) curve can be used to characterize the mode of motion. Characterization of motion based on the MSD can be problematic due to limited information (i.e. trajectory length) and correlated

information from trajectory sampling; therefore, it is often advantageous to use the simplest model to characterize mobility in SPT data.

The main contribution of this work is the derivation and application of a Bayesian based method (D_{PM}) for estimating D in SPT data. D_{PM} is a posteriori based method that separates the variance in trajectories due to localization uncertainty and diffusion. Additionally, a simplified maximum likelihood estimator (D_{IJA}) that treats each observed displacement independently is described and used for comparison. Both methods (D_{PM} and D_{IJA}) take into account finite camera exposure time, trajectory intermittency, and variable localization accuracies. Both methods also provide a statistical basis for estimating the accuracy of the of the estimated D. This work compares D_{MSD}, D_{IJA}, and D_{PM} on both simulated and real data. The utility of the approaches presented here is that accurate quantitative information about the mobility of a single receptor or population of receptors can be performed with limited amounts of data. The instantaneous D (D_{instant}) is one example of an application in which it is important to estimate D with limited amounts of data; therefore, estimating D_{instant} for QDs on glass with simulated stage movements based on Brownian motion and QD-IgE-FcϵRI on live mast cells is used in the comparison.

2.3   Theory

The probability of a set of observations ($\overrightarrow{o}$) in a trajectory given D depends on the probability of $\overrightarrow{o}$ given the true position ($\overrightarrow{x}$) and the probability of $\overrightarrow{x}$ given D which is written in general terms as

$$P(\overrightarrow{o}|D) = P(\overrightarrow{o}|\overrightarrow{x})P(\overrightarrow{x}|D). \tag{2.3}$$

or more specifically

$$P(\overrightarrow{o}|D) = \int dx_1 dx_2 \ldots dx_N P(o_N|x_N) \prod_{i=1}^{N-1} P(o_i|x_i)P(x_{i+1}|x_i). \qquad (2.4)$$

Here we define N as the number of points under observation, o as a particular observation, x as the correlated true position, and i as an index for a particular observation/point. Note that many of the variables used in this section are depicted in **figure 2.1a**. For the subsequent calculations, we assume a normal distribution for the linking probabilities:

$$\begin{aligned} P(o_i|x_i) &= \frac{1}{\sqrt{2\pi\sigma_{\epsilon_i}^2}} \cdot e^{-(o_i-x_i)^2/2\sigma_{\epsilon_i}^2} \\ P(x_{i+1}|x_i) &= \frac{1}{\sqrt{2\pi\sigma_{D_i}^2}} \cdot e^{-(x_{i+1}-x_i)^2/2\sigma_{D_i}^2}, \end{aligned} \qquad (2.5)$$

where the variance due to the exposure time is

$$\sigma_{\epsilon_i}^2 = -4Dt_\epsilon R + \sigma_{o_i}^2 \qquad (2.6)$$

and the variance due to diffusion is

$$\sigma_{D_i}^2 = 2D\Delta t_i. \qquad (2.7)$$

Δt_i is the time lag $(t_{i+1} - t_i)$, t_ϵ is the camera exposure time, R is the motion blur coefficient, and σ_{o_i} is the localization uncertainties for o_i. Note that the term Δt_i accounts for observational intermittency. The terms $\sigma_{o_i}^2$ and $\sigma_{o_{i+1}}^2$ are estimated using the CRB for each localization [24] and account for variable localization uncertainties for individual observations. The motion blur coefficient [3] is

$$R = \int_0^{t_\epsilon} S(t)[1 - S(t)]dt \qquad (2.8)$$

24

where

$$S(t) = \int\limits_0^t s(t')dt' \tag{2.9}$$

describes the sample illumination/camera exposure. For the typical case of full frame illumination/camera exposure, $s(t)$ is $1/t\epsilon$, and R is $1/6$. Trajectory intermittency, finite camera exposure, and variable localization precision are accounted for here. Fortunately, the integral product in Eq. 2.4 can be solved analytically via recursion relation when the constituent probabilities are represented as normal distributions (**Appendix A.1**).

An example of the posterior computed in Eq. A.15 is shown in **figure 2.2c**. D is estimated using the mode of the posterior, and the confidence interval for the posterior is used to estimate the precision of the estimated D. The derivation in this section is performed for a single dimension and a single trajectory. Posteriors are easily combined for multiple dimensions to obtain a posterior describing 2- or 3-dimensional diffusion. Similarly, posterior's from several trajectories are combined to form an ensemble posterior. The method derived here is referred to as D_{PM} throughout the this manuscript.

By ignoring the covariance, jumps can be analyzed independently to estimate D. This method is referred to as D_{IJA} and is a simplified diffusion estimator that takes into account finite camera exposure time, trajectory intermittency, and variable localization uncertainty. For more details, see **Appendix A.2** for a derivation of this method.

2.4 Results and Discussion

2.4.1 Distribution of estimated diffusion coefficients

Figure 2.2 compares D estimated by fitting the simulated trajectory shown in **figure 2.1b** in which the RLE^2 is 0.63. D_{MSD}, D_{IJA}, and D_{PM} estimate D (D_{est}) to be 0.0555, 0.0534, and 0.0526 $\mu m^2/s$ respectively where D_{true} is 0.05 $\mu m^2/s$. Note the noise in the MSD shown in **figure 2.2a** due to only having 18 observations in the trajectory. D_{IJA} and D_{PM} provide more accurate estimates of D than D_{MSD} for this individual example. D_{PM} is also slightly better than D_{IJA} **figure 2.2b** and **2.2c** highlight that D_{IJA} and D_{PM} provide estimates for the precision of the estimated D, and the D_{true} lies within the estimated precision of D_{est} for D_{IJA} and D_{PM}.

Table 2.1: **Summary of results for 1200 simulated trajectories with variable amounts of reduced localization error.** Note that the shading highlights relatively positive (light) and negative (dark) values for each figure of merit.

Diffusion Estimator	RLE[2]	σ[6]	D_{true}	$\bar{D}_{est}$[1]				$\|\epsilon\|^2$[2]				$\sigma_{D_{est}}$[3]				Percent within CRB[4]				Percent within CI[5]			
			N	10	30	100	1000	10	30	100	1000	10	30	100	1000	10	30	100	1000	10	30	100	1000
D_{MSD}	7.00	87	0.023	0.023	0.022	0.023	0.023	0.9	0.5	0.3	0.1	0.03	0.01	0.01	0.00	66	66	67	68	55	47	43	38
	2.00	87	0.091	0.088	0.090	0.092	0.091	0.6	0.4	0.2	0.1	0.08	0.04	0.02	0.01	53	56	56	57	57	51	47	45
	1.00	87	0.228	0.234	0.229	0.228	0.228	0.6	0.3	0.2	0.1	0.17	0.09	0.05	0.01	45	47	50	51	57	49	46	47
	0.60	17	0.023	0.023	0.023	0.023	0.023	0.5	0.3	0.2	0.0	0.02	0.01	0.00	0.00	43	47	42	47	53	50	41	41
	0.40	17	0.091	0.089	0.092	0.092	0.091	0.5	0.3	0.2	0.0	0.06	0.03	0.02	0.01	38	40	40	42	49	43	41	41
	0.36	17	0.228	0.234	0.229	0.228	0.228	0.5	0.3	0.2	0.0	0.15	0.09	0.05	0.01	37	41	41	42	47	45	43	42
D_{IJA}	7.00	87	0.023	0.028	0.024	0.023	0.023	0.9	0.5	0.3	0.1	0.03	0.02	0.01	0.00	69	63	65	65	56	42	39	37
	2.00	87	0.091	0.092	0.091	0.091	0.091	0.5	0.3	0.2	0.0	0.06	0.03	0.02	0.01	67	65	66	67	56	57	55	55
	1.00	87	0.228	0.227	0.227	0.227	0.228	0.4	0.2	0.1	0.0	0.11	0.06	0.03	0.01	69	66	68	67	63	63	65	62
	0.60	17	0.023	0.023	0.023	0.023	0.023	0.3	0.2	0.1	0.0	0.01	0.01	0.00	0.00	66	68	64	67	62	66	63	59
	0.40	17	0.091	0.089	0.091	0.091	0.091	0.3	0.2	0.1	0.0	0.03	0.02	0.01	0.00	63	66	66	67	65	63	65	65
	0.36	17	0.228	0.230	0.228	0.227	0.228	0.3	0.2	0.1	0.0	0.08	0.05	0.02	0.01	66	65	67	64	62	64	65	64
D_{PM}	7.00	87	0.023	0.023	0.023	0.023	0.023	0.5	0.3	0.1	0.0	0.02	0.01	0.00	0.00	85	87	91	92	65	66	65	59
	2.00	87	0.091	0.086	0.090	0.091	0.091	0.4	0.2	0.1	0.0	0.05	0.03	0.01	0.00	73	76	79	79	68	67	67	67
	1.00	87	0.228	0.220	0.225	0.226	0.228	0.3	0.2	0.1	0.0	0.10	0.06	0.03	0.01	71	69	73	70	70	66	68	65
	0.60	17	0.023	0.022	0.023	0.023	0.023	0.3	0.2	0.1	0.0	0.01	0.00	0.00	0.00	66	68	65	65	66	67	63	55
	0.40	17	0.091	0.085	0.090	0.091	0.091	0.3	0.2	0.1	0.0	0.03	0.02	0.01	0.00	63	68	68	67	68	66	67	66
	0.36	17	0.228	0.219	0.224	0.227	0.228	0.3	0.2	0.1	0.0	0.07	0.04	0.02	0.01	67	66	68	68	68	67	68	66

[1] mean in D_{est} in $\mu m^2/s$

[2] mean of the normalized absolute error $|D_{est} - D_{true}|/D_{true}$

[3] standard deviation in D_{est} in $\mu m^2/s$

[4] Percent of D_{est} within the CRB as estimated by D_{IJA}(i.e. $(D_{est} - D_{true})^2 < $ **CRB**)

[5] Percent of D_{est} within the 68% credible interval as estimated by D_{PM} (i.e. $D_{est} - CI_L < D_{true}$ and $D_{est} + CI_U > D_{true}$, where CI_L and CI_U are the lower and upper widths of the credible interval respectively)

[6] localization precision in nm

For an initial comparison, trajectories were simulated with variable D and σ to provide a range of RLE^2 values. These simulations include finite camera exposure time and variable localization precision, but trajectory intermittency is omitted from this comparison for simplicity. Details on simulation parameters are included in **Section 2.6.1**. D is estimated (D_{est}) for 1200 independently simulated trajectories using D_{MSD}, D_{IJA}, and D_{PM}. Different track lengths (N) were also used to test the effects of variable amounts of data. A quantitative comparison of the estimators is included in **table 2.1**.

The mean D (μ_D) for all estimators is relatively close to D_{true}. This is quantified by the mean of the normalized absolute error ($|\epsilon|$). The correlation between ($|\epsilon|$) and RLE^2 further emphasizes the conclusion by Michalet[13] about the importance of the RLE^2 in interpreting D from SPT data. The standard deviation in D_{est} ($\sigma_{D_{est}}$) is correlated with D_{true} for all methods.

The percent of D_{est} within the CRB for D_{IJA} is as expected (i.e. approximately 68% for a single standard deviation). Similarly, the percent of D_{PM} within the 68% credible interval is around 68%. For comparison, the percent within the CRB and the 68% credible interval are computed for all estimators.

In general, this comparison demonstrates that D_{IJA} and D_{MSD} are comparable under most conditions, but D_{PM} outperforms both D_{IJA} and D_{MSD}. All figures of merit presented in **table 2.1** highlight that D_{PM} provides a more accurate estimate in situations with limited data and high RLE^2 (i.e. high localization precision and low D). This result is not surprising since D_{PM} is the most rigorous treatment of D included in this study.

In order to test all aspects of the SPT process (i.e. localizing, tracking, and estimating D), additional comparisons are perform on SPT data which was simulated, localized, and tracked (see the **Section 2.6.2** for more details). These simulations test
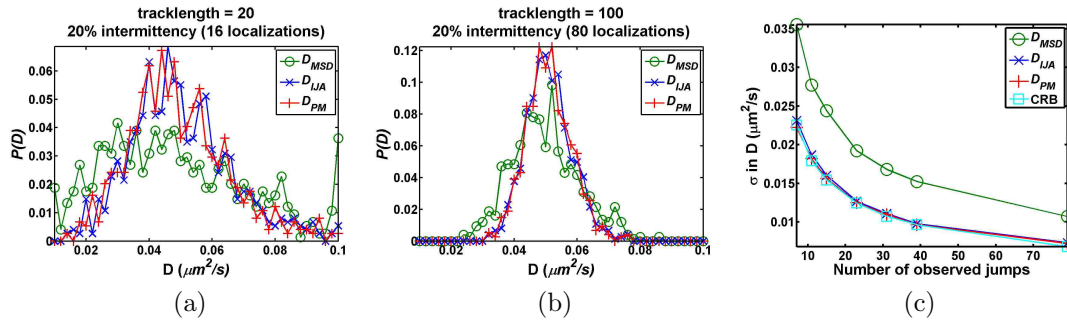
Figure 2.3: **Distribution of** D. Diffusion coefficients estimated for approximately 1200 independent simulations with 20% intermittency. The distribution of D for trajectories with tracklengths of 20 **(2.3a)** and 100 **(2.3b)**. A comparison of the CRB with the variance in D using each method is included in **2.3c**. The true D for these simulations is 0.05 $\mu m^2/s$.

D_{IJA} and D_{PM} on data with real static and dynamic localization uncertainty. There are two key difference to highlight between the simulations presented here and those presented above: (1) the localization uncertainty is estimated using the CRB of the localizations; and (2) trajectory intermittency is included in these simulations. The distribution of D's estimated for 1200 independent trajectories are compared using D_{MSD}, D_{IJA}, and D_{PM} in **figure 2.3**. The distributions of D for simulated SPT with N of 20 and 100 both with 20% intermittency are shown in **figure 2.3a** and **2.3b** respectively. Qualitatively, D_{IJA} and D_{PM} provide tighter distributions for D than D_{MSD}. This is quantified in **figure 2.3c** where the standard deviation in the distribution of estimated D's are compared with the square root of the CRB as estimated by D_{IJA} (see **Appendix A.2** for derivation). Note that the standard deviation of the distribution of D's estimated using D_{MSD} is significantly larger than the standard deviation in the distributions of D estimated using D_{IJA} and D_{PM}. Additionally, the distribution of D's estimated using D_{IJA} and D_{PM} correspond well with the distribution predicted by the CRB. These results agree with those presented in **table 2.1**.

2.4.2 Estimating instantaneous diffusion

Interpreting D_{instant} from SPT data requires the accurate estimation of D with limited observations. This provides an application in which to compare D_{MSD}, D_{IJA}, and D_{PM}.

In order to demonstrate D_{MSD}, D_{IJA}, and D_{PM} on microscope data with a known true underlying D, stage movements are used to simulate Brownian motion with QDs non-specifically adsorbed on glass at 100 Hz with a 10 Hz acquisition rate[21](see **section 2.6.3** for more details). Individual trajectories from 5 independent simulations are pooled together to estimate D_{instant} (**figure 2.4**). A comparison of fit values for the 8 segments with different D values are included in **table 2.2**. Five fit points are used to calculate D_{MSD} (optimal number of fit points for the highest RLE^2). Time windows near transitions (i.e. 20, 40, 60, 80, 100, 120, 140 $\pm$ 3 s) are not included in the statistical analysis. The slightly longer camera exposure time than 0.1 s (i.e. 0.1017 s) resulted in a slight offset between when the stage finished its movements and when the camera acquisition ended. This artifact is observed by the dip in D_{est} at the end of the acquisition; therefore, the last 3 s were also excluded from the statistical analysis. Even though, the statistics presented in **table 2.2** are not rigorous due to the limited number of time windows included in each segment; the overall trends are in agreement with the observations in the previous section. According to the figures of Merit in **table 2.2**, D_{IJA} and D_{PM} out perform D_{MSD} for most segments.
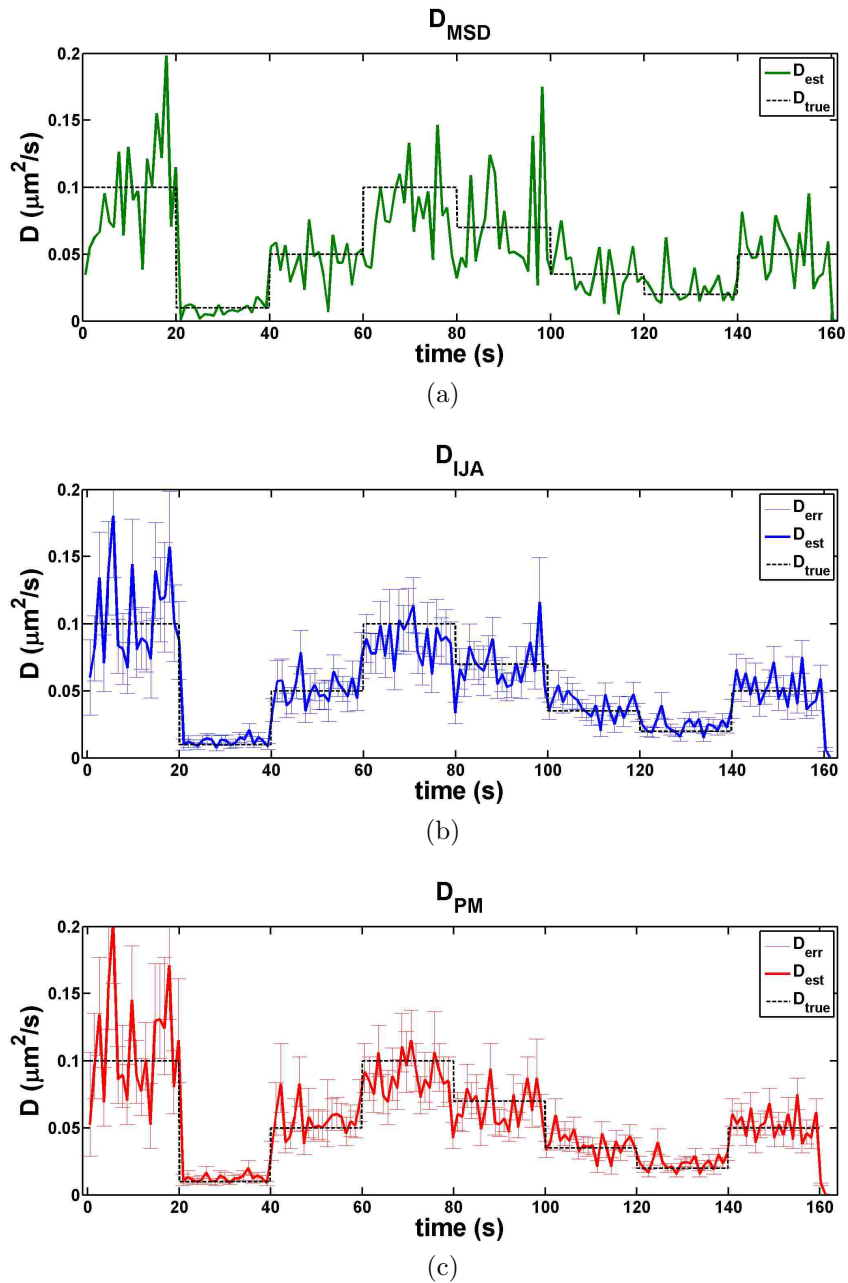
Figure 2.4: **Simulated Brownian Motion.** Brownian motion is simulated by subexposure stage movements (100 Hz discrete stage movement observed by 10 Hz camera exposures) of QDs non-specifically adsorbed onto a glass coverslip. The true underlying D is shown in black overlaid with D_{instant} estimated with each estimator is shown in **(2.4a)**, **(2.4b)**, and **(2.4c)**. D_{instant} is estimated on a independent time windows spanning 10 frames (1 s). Error bars included in **(2.4b)** and **(2.4c)** are estimated using the CRB and 68% confidence interval respectively.

www.manaraa.com

Table 2.2: **Summary of results for experiments with simulated stage movements.** Note that the shading highlights relatively positive (light) and negative (dark) values for each figure of merit.

Diffusion Estimator	Segment	Number of time windows	$\bar{N}$[7]	RLE[28]	$\bar{\sigma}$[9]	D_{true}	$\bar{D}_{est}$[10]	$|\epsilon|$[11]	$\sigma_{D_{est}}$[12]	Percent within CRB[13]	Percent within CI[14]
D_{MSD}	1	17	16	0.37	18	0.100	0.089	0.30	0.03	0.47	0.35
	2	13	26	0.77	21	0.010	0.007	0.35	0.00	0.54	0.38
	3	14	26	0.41	19	0.050	0.045	0.27	0.02	0.57	0.57
	4	14	30	0.37	19	0.100	0.092	0.21	0.03	0.43	0.43
	5	13	34	0.39	20	0.070	0.072	0.38	0.03	0.23	0.15
	6	14	36	0.44	18	0.035	0.032	0.35	0.01	0.36	0.29
	7	14	39	0.53	19	0.020	0.025	0.43	0.01	0.29	0.21
	8	13	40	0.42	20	0.050	0.053	0.35	0.02	0.15	0.15
D_{IJA}	1	17	16	0.37	18	0.100	0.103	0.30	0.03	0.53	0.47
	2	13	26	0.77	21	0.010	0.013	0.33	0.00	0.54	0.46
	3	14	26	0.41	19	0.050	0.051	0.16	0.01	0.71	0.71
	4	14	30	0.37	19	0.100	0.089	0.14	0.02	0.64	0.64
	5	13	34	0.39	20	0.070	0.067	0.13	0.01	0.54	0.54
	6	14	36	0.44	18	0.035	0.037	0.20	0.01	0.57	0.57
	7	14	39	0.53	19	0.020	0.024	0.28	0.01	0.5	0.43
	8	13	40	0.42	20	0.050	0.052	0.21	0.01	0.38	0.38
D_{PM}	1	17	16	0.37	18	0.100	0.106	0.32	0.04	0.53	0.41
	2	13	26	0.77	21	0.010	0.013	0.29	0.00	0.69	0.54
	3	14	26	0.41	19	0.050	0.054	0.17	0.01	0.71	0.71
	4	14	30	0.37	19	0.100	0.091	0.15	0.01	0.71	0.64
	5	13	34	0.39	20	0.070	0.065	0.18	0.01	0.38	0.38
	6	14	36	0.44	18	0.035	0.037	0.18	0.01	0.71	0.64
	7	14	39	0.53	19	0.020	0.024	0.25	0.01	0.57	0.36
	8	13	40	0.42	20	0.050	0.052	0.20	0.01	0.54	0.38

---

[7] average number of observations per time window

[8] approximated using D_{true} and $\bar{\sigma}$

[9] mean localization precision in nm

[10] mean in D_{est} in $\mu m^2/s$

[11] mean of the normalized absolute error $|D_{est} - D_{true}|/D_{true}$

[12] standard deviation in D_{est} in $\mu m^2/s$

[13] percent of D_{est} within the CRB as estimated by D_{IJA} (i.e. $(D_{est} - D_{true})^2 < \mathbf{CRB}$)

[14] percent of D_{est} within the 68% credible interval as estimated by D_{PM} (i.e. $D_{est} - CI_L < D_{true}$ and $D_{est} + CI_U > D_{true}$, where CI_L and CI_U are the lower and upper widths of the credible interval respectively)
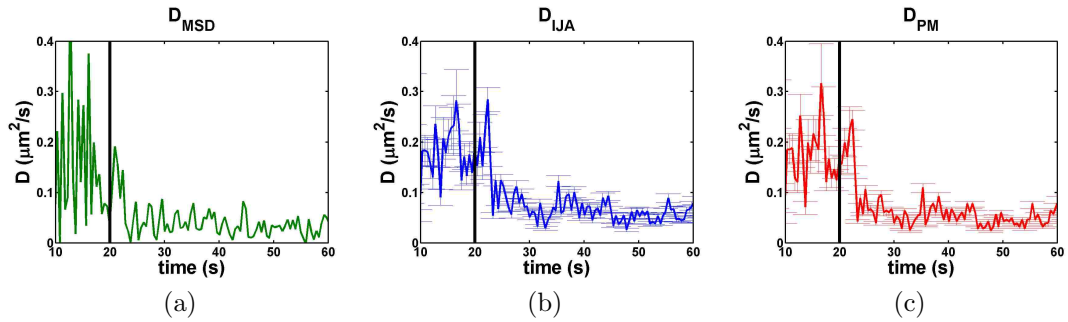
Figure 2.5: **SPT of QD-IgE-FcϵRI on Live RBL Cells During Crosslinking.** Changes in D_{instant} are compared for D_{MSD}, D_{IJA}, D_{PM} in **2.5a**, **2.5b**, and **2.5c** respectively. Crosslinker (DNP$_3$) was added 20 s into the acquisition as indicated by the vertical black line.

Changes in mobility of IgE-FcϵRI upon crosslinking has been the focus of several studies [1, 2, 10, 11, 16, 17, 25, 27]. In two of these studies, D_{instant} of QD-IgE [1, 2] was used to observe the change in mobility of QD-IgE-FcϵRI in RBL cells. D_{MSD} was used to estimate D_{instant}. Due to the distribution of D_{est} highlighted in **figure 2.3** several experiments were needed to be averaged together to obtain sufficient signal to noise to observe changes in D. Cellular heterogeneity provides additional impetus to be able to estimate D_{instant} from a single acquisition. Here we compare the estimation of D_{instant} for a single acquisition using D_{MSD}, D_{IJA}, and D_{PM} in **figure 2.5**. Qualitatively D_{PM} and D_{IJA} provide a tighter distribution of D's. This demonstrates the application of these methods on SPT on live cells and the transition of QD-IgE-FcϵRI from mobile to immobile is much clearer using the D_{PM} and D_{IJA} methods.

2.5 Conclusion

We have derived and tested a statistically rigorous method for computing D using Bayesian statistics (D_{PM}) which accounts for finite camera exposure, variable localization uncertainty, and trajectory intermittency. The results presented in **table 2.1** and **figure 2.3** support that D_{MSD}, D_{IJA}, and D_{PM} converge with large N. In the application to real SPT data, D_{IJA} and D_{PM} provide a significant advantage when limited data is available. Additionally, simulated data (**table 2.1**) demonstrates that D_{PM} provides the best estimate for D in situations with high RLE^2.

D_{IJA} and the MLE approaches by Berglund [3] and Shuang [23] do not take advantage of extended temporal information available in single particle trajectories. On the contrary, the sampling of several different time lags in MSD analysis contains information about trajectory mobility. This is especially important in situations with high RLE^2. One issue with D_{MSD} is correlation between time lags due to trajectory sampling which is further complicated by trajectory intermittency and limited observations in short trajectories. D_{PM} avoids these issues by relating all observed localizations to each other during the estimation of D using the recursion relation (**Appendix A.1**).

The comparison presented here agrees with previous work[12] in that the ability to estimate D is correlated with the RLE^2 (**table 2.1**). The theory behind the original implementation of D_{MSD} relies heavily on the several idealistic assumptions [18]. More recently adaptations of D_{MSD} have been made to account for finite camera integration time[12] and maximum likelihood estimators which account for finite camera integration time[15, 3] and trajectory intermittency[23]. Implementations are often only discussed in ideal scenarios. Here we have developed and demonstrated a diffusion estimator on both theoretical (simulated trajectories) and practical applications (i.e. simulated gaussian blobs, simulated stage movements with QDs, and a live cell

application). Both D_{IJA} and D_{PM} outperform the traditional D_{MSD} in theoretical and practical applications. Our results demonstrate that D_{PM} provides the best estimate of D from the techniques that are compared in this manuscript applications with high RLE^2 and limited numbers of observations.

2.6   Materials and Methods

2.6.1   Simulated trajectories

This section describes the simulated data summarized in **table 2.1**. Combinations of 3 different D's and 2 different σ's were used to produce 6 data sets with variable amounts of RLE^2. 1200 trajectories with 1000 observations each were simulated with parameters representative of SPT data acquired at 20 fps with 107 nm pixel size. The mean position of 100 simulated Brownian steps was used to simulate finite camera exposure time. Uniformly distributed random values between 0 and either 107 nm or 21 nm were used to simulate variable localization uncertainty (σ). Mean positions were perturbed in each dimension by a normally distributed random number with the standard deviation of the localization uncertainty to determine the observed positions ($\overrightarrow{o}$). For the analysis of different track lengths (N), the first N observations in a trajectory were used. Using Eq. 2.2 10, 6, 5, 5, 4, and 4 points were used in to fit the MSD of simulated data with an RLE^2 of 7, 2, 1, 0.6, 0.4, and 0.36 respectively.

2.6.2   Simulated SPT data

Diffraction limited spots were simulated using 2D Gaussians corrupted with Poisson. 1200 trajectories with 100 time steps were simulated. Simulation parameters

include D = 0.1 $\mu m/s$, τ_ϵ = 0.05 s, pixel size = 107 nm/pixel, PSF = 1.3 pixels. Each simulation contained a single simulated trajectory to avoid tracking errors. To simulate finite camera exposure time 10 Brownian steps were performed during each simulated exposure. Variable localization uncertainty was added by simulating Gaussian blobs with varying intensity. Intensities were determined by normal random distributions with mean values of 100 and 200 counts and standard deviations of 20 and 30 counts respectively. Localization was performed and the localization uncertainty was estimated using a maximum likelihood method with a finite pixel model for a 2D Gaussian[24]. Trajectories were built from individual localizations using a likelihood base cost matrix approach (manuscript in preparation). After tracking, random trajectory intermittency was added to the SPT data by randomly omitting 20% of localizations.

2.6.3   Simulated Brownian Motion with Stage Movement

QDs were non-specifically adsorbed onto glass by incubating 400 ul of 50 pM QDs (Invitrogen; 3 colors 605, 625, and 655) in an 8 well chamber (LabTek). Stage movement controlled by analog signal to a piezo stage (MCL nanodrive stage) through a National Instruments data acquisition card were used to simulate Brownian motion at a rate of 100 Hz. Data acquisition rate 10 fps (0.1017 s exposure time). Initialization of stage movements and data acquisition were synchronized by the camera (Andor) initialization. A 1.45 NA TIRF objective (U-APO 150x NA 1.45, Olympus America Inc) and camera pixel size of 16 μm gives a 107 nm pixel size. A quadView image splitter was used to simultaneously collect data in two channels. Trajectories from 5 independent simulations were pooled together to compute D_{instant} using independent time segments of 10 frames (1 s).

36

2.6.4 SPT of QD-IgE on Live RBL cells

QD-IgE preparation and cell labeling was performed as described previously[1]. Briefly, RBL-2H3 cells were primed with 200 pM of 3-colors (605, 625, and 655) of QD-IgE for 15 minutes at 37 °C followed by a 15 minute incubation with 1.86 ug/ml of dark IgE at 37 °C. Microscope setup was identical to that described in section 2.6.3. Camera acquisition rate was approximately 30 fps (τ_ϵ 0.0303 s). All live cell data was collected at approximately 37 °C. Approximately, 20 s into the acquisition 100 μL of crosslinker (30 nM DNP3) was added to the well containing 200 μL of imaging buffer (i.e. hanks buffered saline solution). Data was tracked, and D_{instant} was computed for independent time segments of 15 frames (0.5 s).

References

[1] Nicholas L Andrews, Keith a Lidke, Janet R Pfeiffer, Alan R Burns, Bridget S Wilson, Janet M Oliver, and Diane S Lidke. Actin restricts FceRI diffusion and facilitates antigen-induced receptor immobilization. *Nature cell biology*, 10(8):955–963, August 2008.

[2] Nicholas L Andrews, Janet R Pfeiffer, a Marina Martinez, David M Haaland, Ryan W Davis, Toshiaki Kawakami, Janet M Oliver, Bridget S Wilson, and Diane S Lidke. Small, Mobile FceRI Receptor Aggregates Are Signaling Competent. *Immunity*, 31(3):469–479, September 2009.

[3] A J Berglund. Statistics of camera-based single-particle tracking. *Phys Rev E Stat Nonlin Soft Matter Phys*, 82:011917, 2010.

[4] Maxime Dahan, Sabine Lévi, Camilla Luccardini, Philippe Rostaing, Béatrice Riveau, and Antoine Triller. Diffusion dynamics of glycine receptors revealed by single-quantum dot tracking. *Science (New York, N.Y.)*, 302(5644):442–5, October 2003.

[5] H Geerts, M De Brabander, R Nuydens, S Geuens, M Moeremans, J De Mey, and P Hollenbeck. Nanovid tracking: a new automatic method for the study of mobility in living cells based on colloidal gold and video microscopy. *Biophysical journal*, 52(5):775–82, December 1987.

[6] Taekjip Ha and Philip Tinnefeld. Photophysics of fluorescent probes for single-molecule biophysics and super-resolution imaging. *Annual review of physical chemistry*, 63:595–617, January 2012.

[7] A Kusumi, Y Sako, and M Yamamoto. Confined lateral diffusion of membrane receptors as studied by single particle tracking (nanovid microscopy). Effects of calcium-induced differentiation in cultured epithelial cells. *Biophysical journal*, 65(5):2021–40, November 1993.

[8] Steven F Lee and Mark a Osborne. Brightening, blinking, bluing and bleaching in the life of a quantum dot: friend or foe? *Chemphyschem : a European journal of chemical physics and physical chemistry*, 10(13):2174–91, September 2009.

[9] Diane S Lidke and Bridget S Wilson. Caught in the act: quantifying protein behaviour in living cells. *Trends in Cell Biology*, 19:566–574 ST – Caught in the act: quantifying prote, 2009.

[10] S Y Mao, N Varin-Blank, M Edidin, Henry Metzger, Transfected Cells, and Su-yau Ma. Immobilization and internalization of mutated IgE receptors in transfected cells. *J Immunol*, 146(3):958–66, 1991.

[11] A K Menon, D Holowka, W W Webb, and Barbara C2 PMC2114094 A Baird. Cross-linking of receptor-bound IgE to aggregates larger than dimers leads to rapid immobilization. *J Cell Biol*, 102:541–50, 1986.

[12] Xavier Michalet. Mean square displacement analysis of single-particle trajectories with localization error: Brownian motion in an isotropic medium. *Phys Rev E Stat Nonlin Soft Matter Phys*, 82(4):041914, October 2010.

[13] Xavier Michalet and Andrew J Berglund. Optimal diffusion coefficient estimation in single-particle tracking. *Physical review. E, Statistical, nonlinear, and soft matter physics*, 85(6 Pt 1):061916, June 2012.

[14] Nilah Monnier, Syuan-Ming Guo, Masashi Mori, Jun He, Péter Lénárt, and Mark Bathe. Bayesian approach to MSD-based analysis of particle motion in live cells. *Biophysical journal*, 103(3):616–26, August 2012.

[15] D Montiel, H Cang, and H Yang. Quantitative characterization of changes in dynamical behavior for single-particle tracking studies. *Journal of Physical Chemistry B*, 110:19763–70, 2006.

[16] Israel Pecht, Enrique Ortega, and Thomas M. Jovin. Rotational dynamics of the Fc epsilon receptor on mast cells monitored by specific monoclonal antibodies and IgE. *Biochemisty*, 30(14):3450–3458, 1991.

[17] Paul S. Pyenta, Petra Schwille, Watt W. Webb, David Holowka, and Barbara A Baird. Lateral Diffusion of Membrane Lipid-Anchored Probes before and after Aggregation of Cell Surface IgE-Receptors. *The Journal of Physical Chemistry A*, 107(40):8310–8318 ST – Lateral Diffusion of Membrane Lipi, October 2003.

[18] H Qian, M P Sheetz, and E L Elson. Single particle tracking. Analysis of diffusion and flow in two-dimensional systems. *Biophysical journal*, 60(4):910–21, October 1991.

[19] Sripad Ram, E Sally Ward, and Raimund J Ober. Beyond Rayleigh's criterion: a resolution measure with application to single-molecule microscopy. *Proceedings of the National Academy of Sciences of the United States of America*, 103(12):4457–62, March 2006.

[20] Thierry Savin and Patrick S Doyle. Static and dynamic errors in particle tracking microrheology. *Biophysical journal*, 88(1):623–38, January 2005.

[21] Michael J Saxton. Wanted: a positive control for anomalous subdiffusion. *Biophysical journal*, 103(12):2411–22, December 2012.

[22] Th. Schmidt, G. J. Schutz, W. Baumgartner, H.J. Gruber, and H. Schindler. Imaging single molecule diffusion. *Proceedings of the National Academy of Sciences of the United States of America*, 93:2926, May 1996.

[23] Bo Shuang, Chad P Byers, Lydia Kisley, Lin-Yung Wang, Julia Zhao, Hiroyuki Morimura, Stephan Link, and Christy F Landes. Improved analysis for determining diffusion coefficients from short, single-molecule trajectories with photoblinking. *Langmuir : the ACS journal of surfaces and colloids*, 29(1):228–34, January 2013.

[24] Carlas S Smith, Nikolai Joseph, Bernd Rieger, and Keith a Lidke. Fast, single-molecule localization that achieves theoretically minimum uncertainty. *Nature methods*, 7(5):373–5, May 2010.

[25] I Tamir, R Schweitzer-Stenner, and I Pecht. Immobilization of the type I receptor for IgE initiates signal transduction in mast cells. *Biochemistry*, 35:6872–83, 1996.

[26] X.-H. Xu and Edward S. Yeung. Direct Measurement of Single-Molecule Diffusion and Photodecomposition in Free Solution. *Science*, 275:1106–1109, February 1997.

[27] R Zidovetzki, M Bartholdi, Donna J. Arndt-Jovin, and Thomas M. Jovin. Rotational dynamics of the Fc receptor for immunoglobulin E on histamine-releasing

rat basophilic leukemia cells. *Biochemistry*, 25(15):4397–401 ST – Rotational dynamics of the Fc recep, July 1986.

CHAPTER 3: MULTI-COLOR QUANTUM DOT TRACKING USING A HIGH-SPEED HYPERSPECTRAL LINE-SCANNING MICROSCOPE

Title

Multi-color Quantum Dot Tracking using a High-Speed Hyperspectral Line-Scanning Microscope

Authors

Patrick J. Cutler[2‡], Michael D. Malik[1‡], Sheng Liu[1], Jason M. Byars[1], Diane S. Lidke[2], Keith A. Lidke[1]*

[‡]These two authors contributed equally to this work and are co-first authors.
[*]Corresponding Author (E-mail: klidke@unm.edu)

Affiliations

[1]Department of Physics & Astronomy, University of New Mexico, Albuquerque, NM, USA

[2]Department of Pathology and Cancer Research and Treatment Center, University of New Mexico, Albuquerque, NM, USA

3.1 Abstract

Many cellular signaling processes are initiated by dimerization or oligomerization of membrane proteins. However, since the spatial scale of these interactions is below the diffraction limit of the light microscope, the dynamics of these interactions have been difficult to study on living cells. We have developed a novel high-speed hyperspectral microscope (HSM) to perform single particle tracking of up to 8 spectrally distinct species of quantum dots (QDs) at 27 frames per second. The distinct emission spectra of the QDs allows localization with ~ 10 nm precision even when the probes are clustered at spatial scales below the diffraction limit. The capabilities of the HSM are demonstrated here by application of multi-color single particle tracking to observe membrane protein behavior, including: 1) dynamic formation and dissociation of Epidermal Growth Factor Receptor dimers; 2) resolving antigen induced aggregation of the high affinity IgE

receptor, FcεR1; 3) four color QD tracking while simultaneously visualizing GFP-actin; and 4) high-density tracking for fast diffusion mapping.

3.2 Introduction

Cellular signal transduction is regulated through the interactions and output of membrane receptors. However, the study of molecular-level protein-protein interactions in living cells continues to be a challenging goal in cell biology. While the nanometer-scale distribution of receptors can be observed using electron microscopy (EM), this technique is limited to fixed samples [1–6]. Super-resolution microscopy techniques [6–9] can also reveal nanometer-scale protein distributions, yet these measurements are inherently slow, making the observation of dynamic events difficult. Therefore, new live cell microscopy techniques are needed in order to determine the role of receptor dynamics in the regulation of cell signaling.

One method for studying the dynamics of membrane components is single particle tracking (SPT) [10], in which a fluorescent or light scattering probe is attached to the component of interest and its position is recorded over time. The probe can be localized with precision much better than the diffraction limit (typically tens of nanometers) by fitting the spatial distribution of light intensity recorded to the point spread function (PSF) of the microscope [11]. Connecting particle coordinates across frames generates particle trajectories that can be analyzed to deduce properties of the probe target or the membrane. Although SPT has been used extensively for characterizing membrane environments [12], it has seen limited use for the study of protein interactions since the localization precision of the probe is greatly reduced when the particle spacing approaches that found in protein dimers or oligomers [13]. Simultaneous tracking of two spectrally distinct probes can be easily achieved using filter-based separation of the emission. Two-color SPT allows the spatially overlapping particles to be separated by emission spectrum, and in the case of isolated, two-color pairs, the localization precision is restored. This concept has been used for the study of interacting membrane proteins in several systems [14–18] . Despite its advantages, two-color SPT has several limitations: 1) successful tracking requires each color of probe be present at a density of less than

about 1 μm^{-2}; 2) same-color dimers are as likely as two-color dimers; and 3) higher order oligomers cannot be easily resolved.

Here we describe a high-speed hyperspectral microscope (HSM) that is capable of resolving and tracking eight or more spectrally distinct fluorescent probes. A hyperspectral imaging system collects a region of the spectrum divided into many contiguous channels for each spatial element of the image. Our microscope design is based around the concept of a spectrally-resolved, line-scanning confocal microscope [19], illustrated in **Figure 3.1**. A laser focused to a line provides high excitation intensity in a region in and around the focal plane of the objective. The line geometry and the use of a confocal slit on the emission path rejects much of the out-of-focus light that is emitted from either fluorophores or sample auto-fluorescence, thereby providing optical sectioning [20]. To create a two-dimensional (2D) hyperspectral image, the line is scanned across the sample plane in discrete steps (along the *x*-axis) and the camera captures a frame at each step. Each single camera capture consists of 64 pixels of 1D spatial information and 128 spectral channels. Therefore, a 2D hyperspectral image consists of a 3D (x,y,λ) data cube collected in these steps. The rate at which complete hyperspectral images can be captured is limited by the readout rate of the electron multiplying charge coupled device (EMCCD) camera and is 27 frames per second (fps) when scans are configured for 32 steps per image (each image is 32×64×128). In this configuration the camera is collecting approximately 900 images per second where each camera image corresponds to a single position of the excitation line. In the application of multi-color SPT (mcSPT), each hyperspectral image is analyzed to find the positions of the fluorescent probes and these positions are used to construct particle trajectories.

We describe the design and performance of our instrument and the analysis process required for mcSPT. We then demonstrate the capabilities of the instrument through several proof-of-principle experiments by applying mcSPT to biological systems of interest in our laboratory. Specifically, we show that: 1) The increased labeling density afforded by mcSPT makes detection of rare and transient receptor interactions more efficient, as demonstrated in observations of Epidermal Growth Factor Receptor (EGFR) dimerization [14]; 2) The multiplexing capability of the HSM can be used for determination of antigen-induced FcεRI aggregate size based on spectral signature and

therefore could be used for cluster size correlation with diffusion coefficient [17,21,22]; 3) mcSPT can be used while simultaneously visualizing other membrane associated structures, which we demonstrate by performing mcSPT while imaging GFP-actin; and 4) High density tracking facilitated by mcSPT can be exploited for fast diffusion mapping of the cell membrane. Because of the advantages in speed, sensitivity and spectral imaging afforded by our HSM, it is likely that the instrument will find use in a wide variety of biological imaging studies and we briefly discuss a few of these other potential applications.
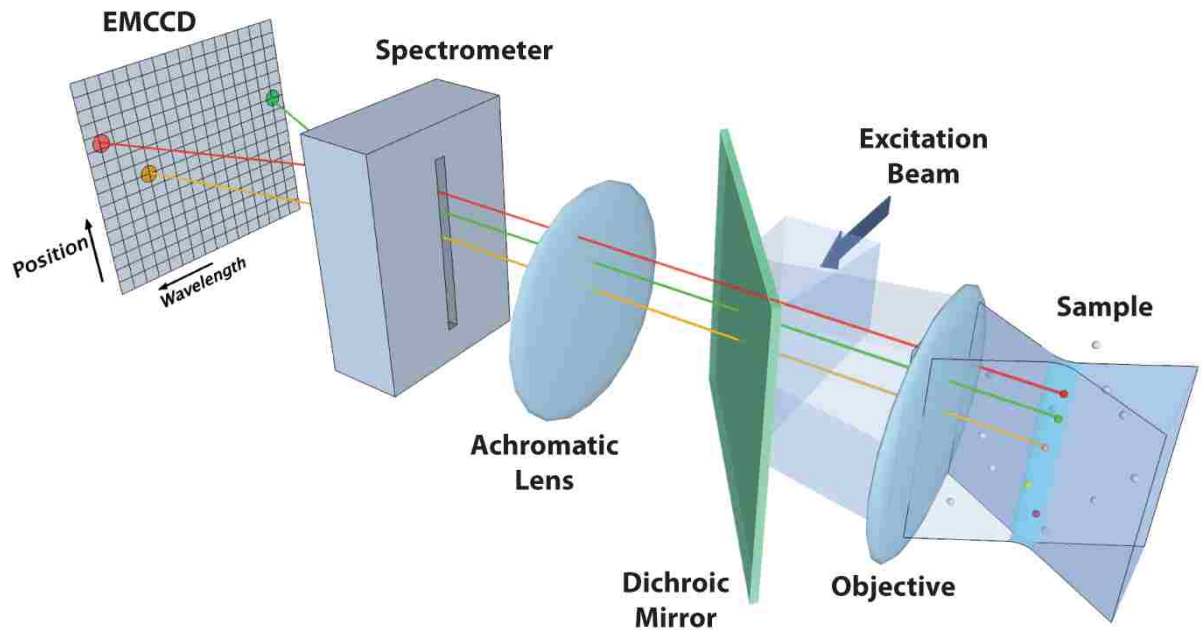

Figure 3.1 Conceptual diagram of microscope.

The excitation beam (optics not shown) is reflected by a dichroic mirror and forms a laser line focused at the sample plane by the objective, concentrating the excitation light to a small volume of diffraction limited width. Here, the white spheres in the sample represent fluorophores that remain mostly in the ground state while the colored spheres denote those which are excited. The emitted light passes through the dichroic mirror and into a spectrometer, which distributes the light onto an EMCCD camera such that each exposure captures information of wavelength and position along the line. The entrance slit on the spectrometer also serves to reject out-of-focus light, providing a semi-confocal ability for imaging at any depth in the sample. A scanning mirror (not shown) advances the line position by one back-projected pixel length on the sample and another exposure is acquired. One hyperspectral "frame" is a reconstructed series of these steps (performed in post processing) to form an image containing x, y, and λ. A time series of these hyperspectral

frames is acquired at 27 fps, providing spatial, spectral, and temporal resolution that enables localized single molecule tracking of multiple emitters within a given diffraction limited volume. For a more detailed description, see **Figure 3.2 and Text B.3.1.**

3.3 Results

3.3.1 Microscope design and performance

The HSM described here can operate at a frame rate of up to 27 fps for an imaging area of 28 μm^2 while each spatial pixel collects 128 spectral channels. Our system is designed to span the spectral range from 500 to 750 nm. The system is built around a standard inverted microscope base (Olympus IX71) in order to facilitate live cell imaging. A single 488 nm wavelength laser (which is used to simultaneously excite all spectral species of QDs) is modified with a laser line generating lens (Edmund Optics) and other optics to provide a uniform (vertical) and diffraction limited (horizontal) line at the microscope focal plane. The laser line is scanned across the sample using a galvanometer controlled scanning mirror (Cambridge Research). Emission light is de-scanned and passes through a prism spectrometer and is imaged with a high-speed EMCCD camera (Andor iXon 860). The microscope design layout is provided in **Figure 3.2** and a more detailed description of the instrument is given in **Text B.3.1**. Synchronization of the camera and scanning mirror is achieved by using the camera as the master clock. Specific digital sequences are pre-programmed in a data acquisition card (NI PCIe-6343) and the camera fire signal is used to trigger the next output state. **Figure B.1.1** shows the overall instrument control schematic, and **Figure B.1.2** provides a few example plots that illustrate the signal timing. When collecting a time series of hyperspectral images (four-dimensional data sets (x,y,λ,t)), the camera is set to collect a single kinetic series, and therefore absolute timing is preserved. Data is saved asynchronously as one file for each hyperspectral image.

The localization precision of single fluorophores is proportional to the square root of the number of photons captured [11] and therefore, for throughput efficiency, a prism spectrometer is used as the dispersing element. Prism spectrometers have a higher transmission efficiency over a wide spectral range as compared with diffraction gratings

[23], so they are more suitable for this application. The spectrometer is an aplanatic design [24], with a dispersion element that consists of a spherical wedge prism and a spherical concave mirror. The design was optimized using optical design software (Optics Software for Layout and Optimization, Lambda Research Corporation) to minimize distortion. Custom optical components were fabricated (Rainbow Optics, Eugene, Oregon USA) to the specifications of the optimized design. The details of the design (**Figure B.1.3** and **Text B.3.2**) and the spectrometer distortion and dispersion (**Figure B.1.4**) of the design are included in the supporting information. Spectral calibration was performed using a spectral calibration lamp (MIDL® Wavelength Calibration Lamp) and the 543 nm and 633 nm lines from HeNe lasers. There is no observable curvature in the spectral lines with respect to the spatial axis (**Figure B.1.5**).
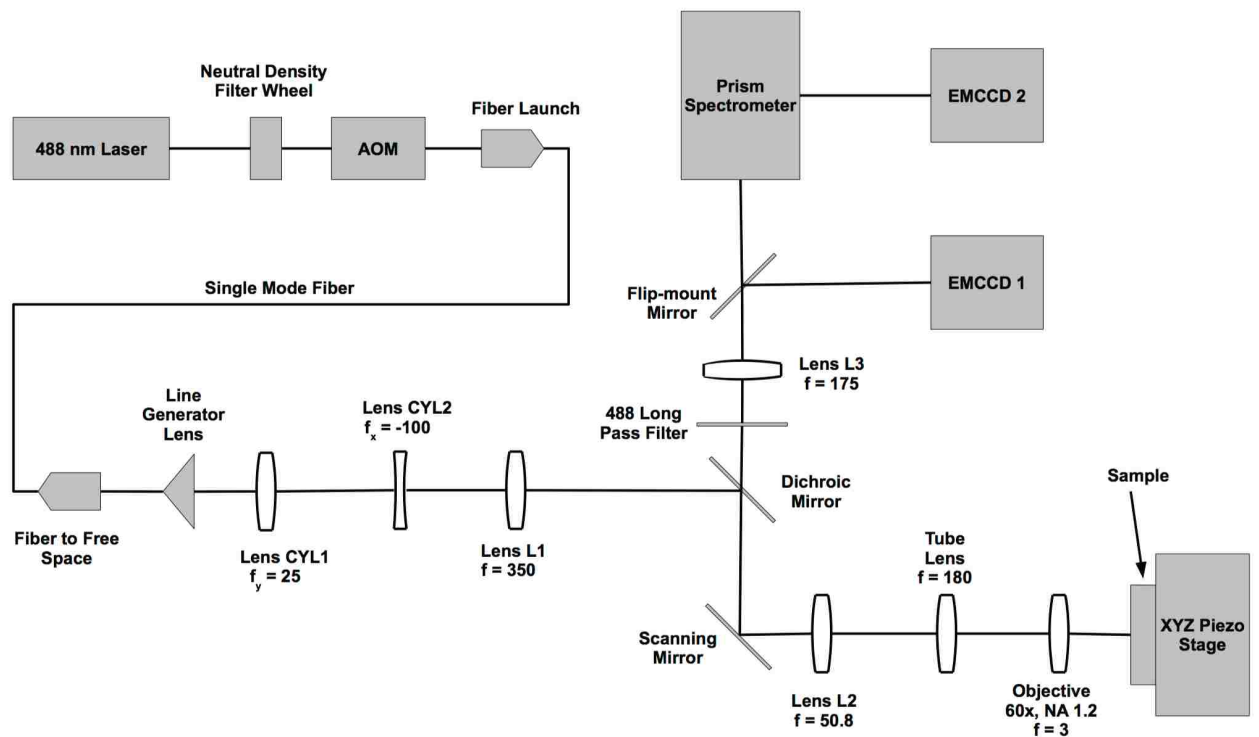

Figure 3.2 Optical layout.

This schematic layout of the laser line scanning hyperspectral microscope displays the key components of the system. Focal lengths are shown in units of mm. A detailed description and parts reference is provided in **Text B.3.1**.

The measured 4D (x,y,z,λ) microscope point spread function (PSF) shows good agreement with that expected for a diffraction limited system (**Figure B.1.6**, **B.1.7**, and **Text B.3.3**). Localization of multi-fluorophore beads (TetraSpeck, Invitrogen) broken into spectral bins of 504-534, 562-611, and 641-712 nm show less than 15 nm of chromatic induced shift anywhere in the image (**Figure B.1.8**).

Custom graphical user interfaces (GUIs) were developed using MATLAB (Natick, Massachusetts USA) for data acquisition and live viewing of hyperspectral images (**Figure B.1.9**). The data acquisition GUI allows for efficient adjustment and optimization of acquisition parameters for experiments. The live viewing GUI provides the experimentalist instantaneous feedback on sample quality and the ability to find a field of view and focus on the sample.

3.3.2 QD localization and trajectory connection

Single particle tracking is carried out by the localization of single molecules and the subsequent building of trajectories from those localizations [25]. The light emitted from a point source (such as a fluorescently tagged protein) is distributed on the detector according to the PSF of the microscope. The 2D (x,y) spatial PSF is well modeled by a 2D Gaussian distribution [26] and the emission spectra profiles of QDs are also well modeled by a Gaussian shape (**Figure 3.3A**). The position of QDs are found by performing a maximum likelihood estimate of spatial position, intensity and spectral peak position using a 3D (x,y,λ) Gaussian PSF model and a Poisson noise model (**Figure B.1.10**, **Text B.3.4**, and **Table B.4.1**). Localizations are performed using an iterative update method [27] that includes the possibility of fitting multiple point emitters within a diffraction limited area [28]. As with previous work [27,28], the analysis is implemented on graphics processing units in a parallel fashion in order to take advantage of the high computational performance of modern graphical processing units (GPUs) (**Figure B.1.11** and **Text B.3.5**).

To characterize the imaging capability of the HSM, QDs are non-specifically adsorbed onto a glass coverslip and imaged at the fastest scan rate for this geometry. For the field of view collected in these images (64 vertical spatial pixels and 32 line steps; 28 μm^2), the pixel dwell time was 1.14 ms and the frame rate was 27 fps. The spectral

characteristics of individual QDs for 8 colors (commercially available from Invitrogen) are investigated in **Figure B.1.12** and **Table B.4.2**. The procedure for localizing QDs using hyperspectral data is demonstrated with all 8 colors of QDs in a single acquisition (**Figures 3.3B-E**). See materials and methods for more details. The simultaneous localization of two highly spatially and spectrally overlapping QDs (QD585 and QD605) is highlighted in **Figures 3.3C**. Additionally, a total of four highly spatially overlapping QDs are localized simultaneously. This is highlighted by the colored boxes in **Figure 3.3B** and the corresponding fits in **Figures 3.3C**, **3.3D** and **3.3E**. The fit precision for each parameter is estimated from the Cramér-Rao Bound (CRB) however, it is important to note that QD blinking during line scanning can contribute to higher than expected error in QD localization in the line-scanning dimension of the data (**Figure B.1.13**). Trajectories are constructed from found QD (x,y,λ) positions (**Video B.2.1**, **Text B.3.6**, and **Figure B.1.14**; manuscript in preparation Relich P, Cutler PJ, Huang F, Lidke KA) [29]. The use of spectral information to build trajectories helps to improve the overall accuracy of the trajectory building process (**Figure B.1.14**).
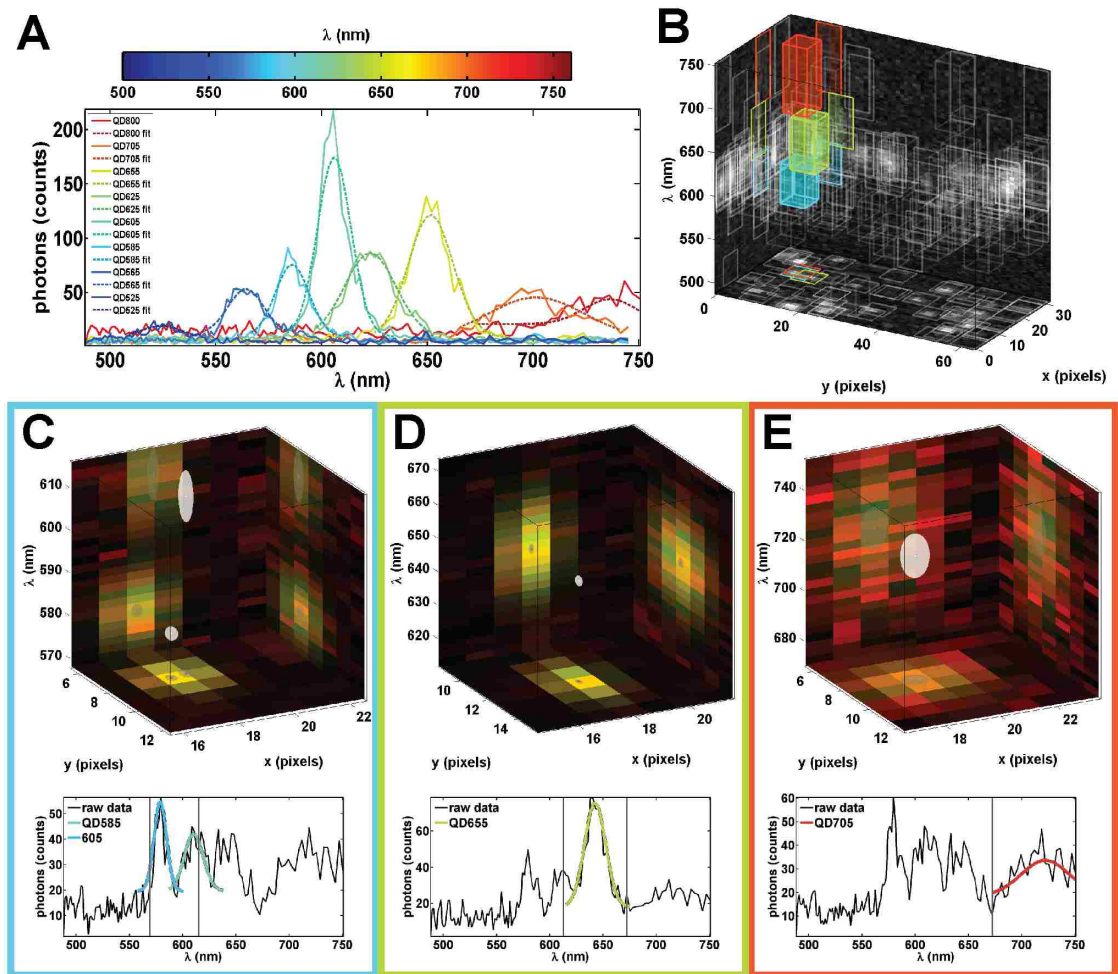
Figure 3.3 SPT of individual QDs non-specifically adhered to a glass surface.

(A) Progressing from blue to red are sum projections of raw data (solid) and Gaussian fits (dashed) for single 525, 565, 585, 605, 625, 655, 705 and 800 nm QDs. (B) 3D representation of a single hyperspectral time frame with 3D boxes representing sub-volumes identified for further particle localization. Sum projections of the data onto each plane are used to represent the raw data (gray scale). Likewise, 2D projections of each 3D box onto each plane are used to highlight the sub-volumes. Fitting results for the colored sub-volumes (color corresponds to the spectral center of the box) in (B) are shown in (C), (D), and (E). In the top figures in (C), (D), and (E) red and green are sum projections of the raw data and fit respectively. Note that the color outlining (C), (D), and (E) correlate with the respective sub-volumes highlighted in (B) with the same color. The localized particles are represented by white ellipsoids in which the radius in each dimension shows 3 standard deviations in the estimated error in the fit using the Cramér Rao Bound and their projection onto each axis is represented by a gray ellipse. The bottom figures in (C), (D), and (E) show raw spectral features (black) and Gaussian fits (color corresponds to fit spectral emission peak). The vertical gray lines represent the spectral cutoffs for independently fit sub-volumes. See **Video B.2.1**.

3.3.3 mcSPT of membrane proteins

3.3.3.1 Observation of rare, transient events.

Protein-protein interactions can be difficult or impossible to observe with single color SPT since the spacing of proteins at distances less than the diffraction limit make it difficult to discern the difference between merely close proximity and real interactions. Two-color tracking restores the ability to calculate separation and deduce dimerization state. Previously, we used two-color SPT to visualize and quantify EGFR homodimerization under various physiological conditions [14]. These studies required low labeling density such that capturing a sufficient number of dimerization events between two labeled receptors required a large amount of data. Multi-color SPT improves upon two-color SPT by increasing the overall labeling density and thereby increases the potential observation rate of rare events while reducing the probability of same color interactions. Using our HSM, we imaged 8 colors of QD-labeled Epidermal Growth Factor (QD-EGF) bound to EGFR expressed on live A431 cells. **Video B.2.2** shows the analysis results of a data set collected at 27 fps. Highlighted trajectories in **Figure 3.4A** and **3.4B** show several interacting pairs of QD-EGF-EGFR complexes. Consistent with our previous work [14], we observed long-lived (**Figure 3.4C**) and transient (**Figure 3.4D-F**) receptor dimerization events, marked by periods of sustained correlated motion. Note that even in a single time series, multiple interactions are readily identified, demonstrating that the higher labeling density allows for more efficient detection of dimers than with two-color imaging [14].
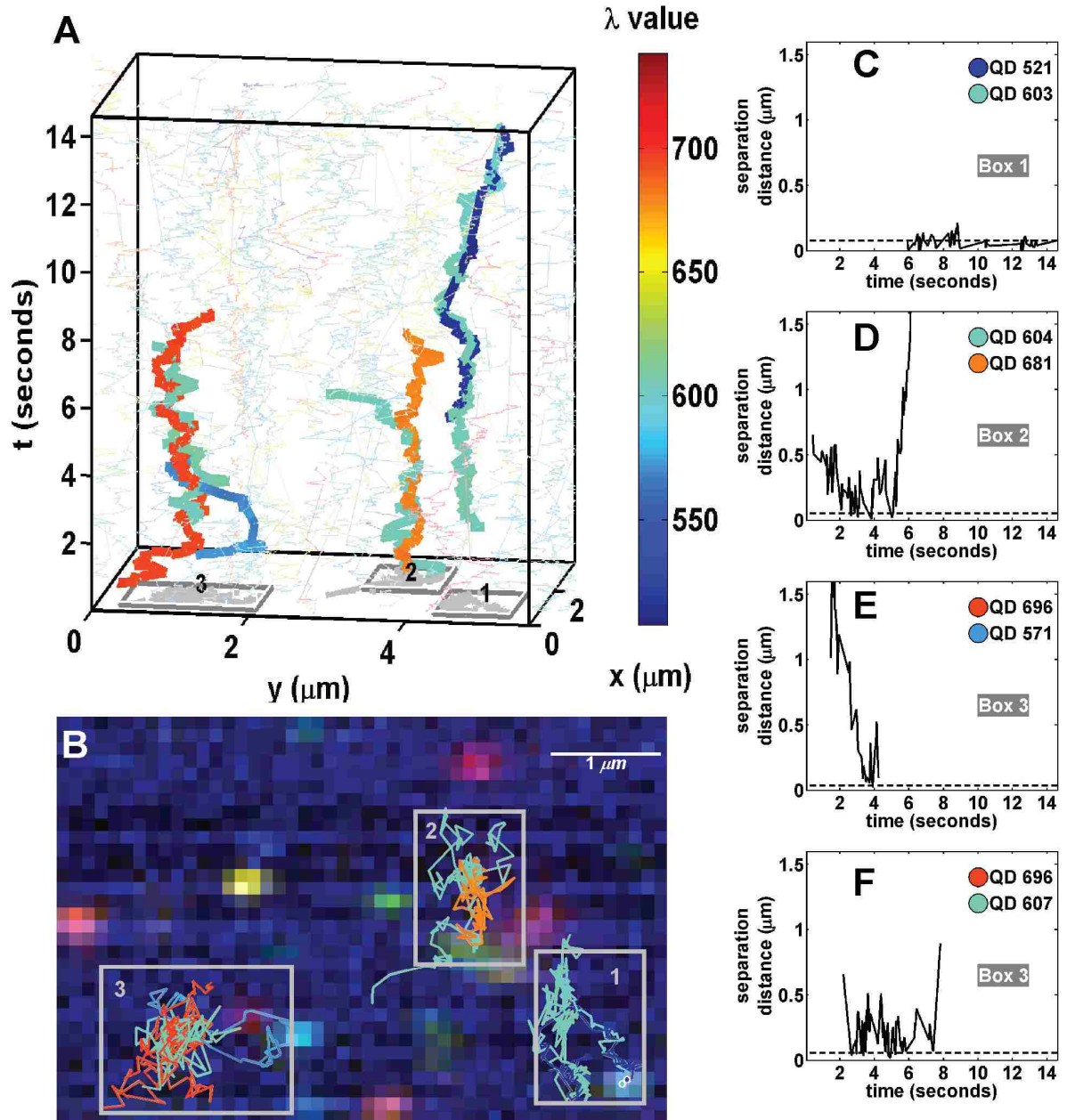
Figure 3.4 SPT of 8-colors (525, 565, 585, 605, 625, 655, 705, 800 nm) of QD-EGF on live A431 cells.
(A) 3D (*x,y,t*) representation of trajectories. Trajectories are represented by colored lines. Selected interacting trajectories are highlighted by thicker lines. Interactions are grouped by boxes in the xy-plane (identified numerically). (B) Red-green-blue (RGB) representation of raw data for the last time frame with overlaid trajectories and boxes corresponding to (A). Pairwise interaction distances for the selected pairs of QDs are shown in (C), (D), (E), and (F). Note the text identifying how the pairwise interaction distances correspond to the boxes in which the QDs are observed in (A) and (B). See **Video B.2.2**.

3.3.3.2 Oligomer dynamics.

Previous studies of FcεRI have shown that receptor mobility is a function of antigen dose and valency, and consequently aggregate size [21]. However, in these experiments, the size of aggregates could not be directly determined since a mixture of dark and QD-labeled IgE (QD-IgE) was used to maintain SPT density. Using the HSM to perform mcSPT of QD-IgE-FcεRI on live cells captures not only the dynamics of IgE-FcεRI complexes, but also reveals the number of proteins in the aggregate based on spectral signature. **Figure 3.5** and **Video B.2.3** show the results of mcSPT of QD-IgE-FcεRI approximately 7 minutes after the addition of a crosslinking agent (DNP_3). Several long-lived complexes are observed that demonstrate correlated motion. **Figure 3.5A** highlights the observation of a trimer and dimer. Spectral separation is further beneficial for accurate quantification of diffusion of QD-IgE-FcεRI oligomeric complexes due to their high degree of spatial and spectral overlap (**Figures 3.5B** and **3.5C**). Note that the localization of the QDs in these complexes would not be possible using single color SPT represented by the gray scale projection in **Figures 3.5B** and **3.5C**. The red ellipse in **Figure 3.5C** (upper left subfigure) is a QD655-IgE-FcεRI that comes in close proximity but does not interact with the observed dimer. The spectral features of the QD655-IgE-FcεRI are observed in the raw spectrum (**Figure 3.5C**; lower left subfigure; solid black line). In a two color SPT experiment, the proximity of a third QD to an observed dimer would disrupt one of the trajectories in the dimer. The diffusion coefficients of the individual trimer and dimer seen in this example are 0.013 and 0.024 μm^2/s, respectively. These results demonstrate the ability of mcSPT to investigate the dynamics and composition of protein complexes.
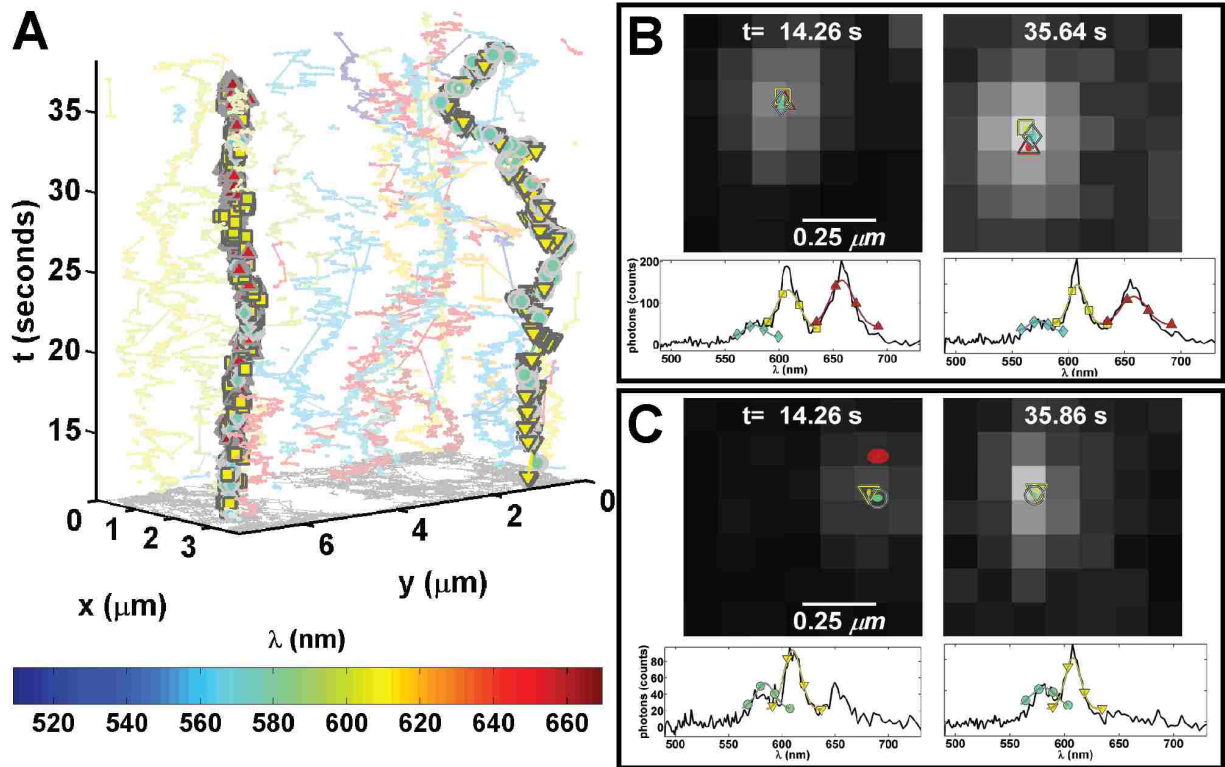
Figure 3.5 SPT of 5-colors (565, 585, 605, 625, 655) of QD-IgE on live RBL cells.

All subfigures are derived from a single acquisition (27 fps) ~7 minutes after crosslinking with DNP$_3$. (A) 3D (x, y, t) depiction of trajectories. The color scheme for the trajectories is dependent on the estimated emission peak of each QD as noted by the color bar. A trimer (565 QD cyan diamond; 605 QD yellow square; 655 QD red up triangle) and dimer (585 QD cyan circle; 605 QD yellow down triangle) are highlighted by their respective symbols. (B) and (C) show localizations for specified time frames. Coloration and symbols correspond to (A). Ellipses in the upper subfigures represent 3 times the localization accuracies over a gray scale projection of the raw data. Red ellipse in the upper left subfigure of (C) is a localized 655 QD that doesn't interact with the dimer. Raw spectra (solid black lines) and Gaussian fit (colored lines with symbols) for individual QDs are shown in the lower subfigures. See **Video B.2.3**.

3.3.3.3 Interactions with membrane components.

The dynamics of membrane proteins may be influenced by membrane-associated structures such as actin [17], clathrin [30] or other microdomains [31] and interaction with such structures could be correlated with oligomerization state. Our HSM allows the simultaneous observations of several colors of QDs at the same time as other fluorescent probes that can be excited efficiently with 488 nm light, such as GFP. Here we

demonstrate mcSPT using 4 colors of QD-IgE-FcεRI (605, 625, 655, and 705 nm) while simultaneously imaging GFP-actin. Imaging was performed on rat basophilic leukemia (RBL-2H3) cells transiently transfected with GFP-actin. **Figure 3.6** (**Video B.2.4**) provides observations that highlight several advantages of this technique. Comparison of the actin structure in the top and bottom images demonstrates how dynamic the actin structure is over the time course of this acquisition. Actin corralling of QD-IgE-FcεRI is also observed (red triangle and red circle in the bottom image). These results are consistent with previous reports of actin corralling first observed by tracking QD655-IgE-FcεRI with respect to GFP-actin [17]. However, these previous studies were limited to tracking in total internal reflection fluorescence (TIRF) at the adherent surface since wide field imaging of actin structures at the apical surface was insufficient and point scanning confocal was too slow for tracking. Using the HSM, we can perform fast confocal imaging while simultaneously tracking single quantum dots. Moreover, the increased number of spectrally distinct QDs allow for tracking of many receptors simultaneously such that their interactions within the actin domains can be observed. The mobility of the dimer complex (0.004 μm^2/s; purple blue diamond and red square, top and bottom) is less than that of highlighted monomers (0.044 μm^2/s). A transition of the mobility of a monomer from relatively immobile (red triangle, top) to relatively mobile (red triangle, bottom) is observed. Crossing trajectories are appropriately connected due to the spectral information (red triangle and yellow star).
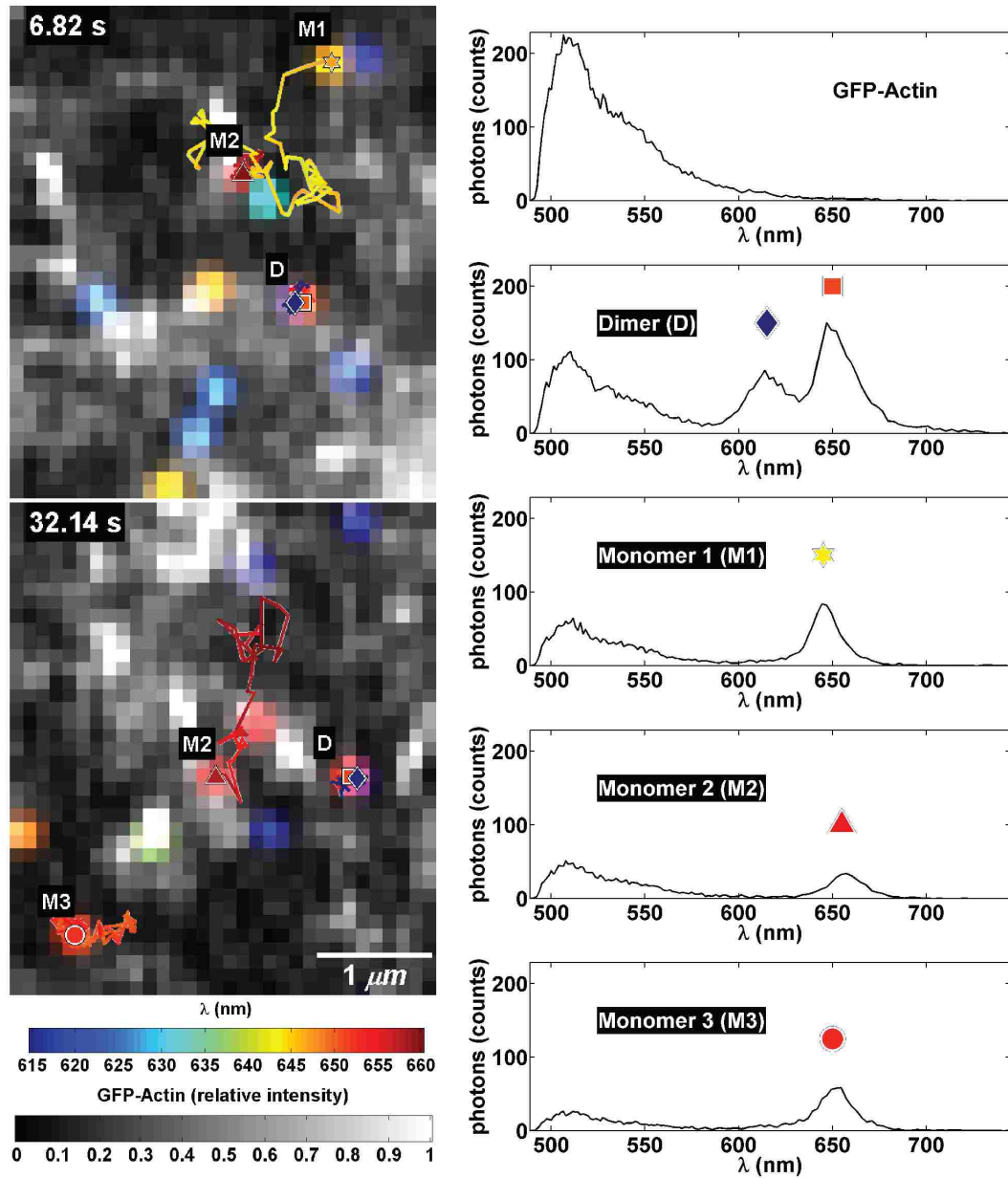
Figure 3.6 SPT of 4-colors (605, 625, 655, and 705) of QD-IgE-FcεRI on live RBL cells transiently transfected with GFP-actin acquired at 27 fps.

(*left*) Two representative frames are shown. The GFP-actin presented in normalized gray scale is the spatially deconvolved portion of the spectrum between 500-570 nm. It is overlaid with Gaussian blobs reconstructed for localized QDs and trajectories for QD-IgE-FcεRI spanning the previous 3.7 s (100 frames; coloration of blobs and trajectories according to emission peak; see color bar). Colored symbols highlight QD-IgE-FcεRI positions at the specified frame, and representative spectra are shown to the right. Text identifiers (D, M1, M2, and M3) are used to indicate monomers (M#) and dimer (D) trajectories. See **Video B.2.4**.

3.3.4 Fast membrane diffusion mapping

Labeling with multiple colors enables SPT at densities of several particles per square micron. By binning squared displacement both temporally and spatially, high-density mcSPT can be used to probe local receptor mobility [32]. The uncertainty in the diffusion coefficient scales as approximately $D*(A*\rho*n)^{-1/2}$ where D is the diffusion coefficient, A is area, ρ is particle density and n is the number of time frames (**Text B.3.7**); therefore, higher density allows better spatial and/or temporal resolution in the diffusion map. In a similar manner, high density mcSPT also allows global changes in protein diffusion to be observed quickly. To demonstrate this, a high density mcSPT experiment was devised in which the relative labeling density for 8 colors of QD-IgE-FcεRI was refined to provide similar high density labeling for each color of QD. The labeling density achieved here is ~2.4 particles per μm^2 which to the authors' knowledge is higher density than any previously reported SPT method. Crosslinker (DNP-BSA) was added ~20 seconds into the acquisition and a corresponding change in the estimated instantaneous diffusion coefficient is observed (**Figure 3.7A**). Due to the increased labeling density, this instantaneous change in mobility observed from a single acquisition of a single cell correlates well with that observed in a previous study that required the combined analysis of multiple (~10) SPT experiments of single color of QD-IgE [17,21]. Similarly, squared displacements can be binned both temporally and spatially to build diffusion maps in relation to QD-IgE-FcεRI. In **Figures 3.7B** and **3.7C**, squared displacements are binned in 280 frame temporal bins (~10 seconds) and 1 pixel by 1 pixel spatial bins (0.116 μm by 0.116 μm). Changes in diffusion maps subsequent to the addition of crosslinker are apparent upon comparison of **Figures 3.7B** and **3.7C** (**Video B.2.5**).
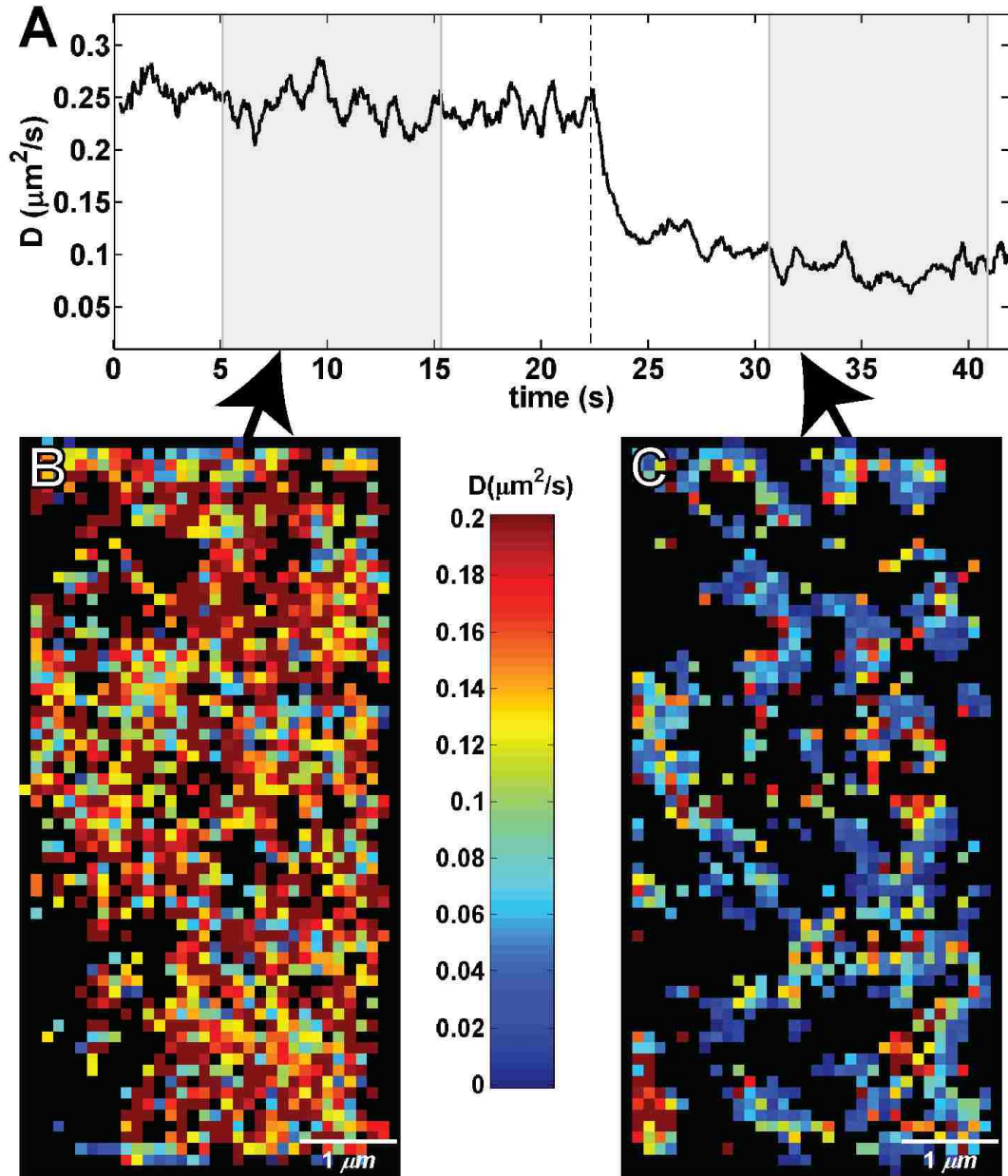
Figure 3.7 High density single particle tracking (QD 525, 565, 585, 605, 625, 655, 705, and 800).

(A) Shows the instantaneous diffusion for a mcSPT experiment with an acquisition rate of 27 fps of QD-IgE. 1 μg/ml of DNP-BSA was added ~20 seconds into the acquisition (vertical dashed line). (B) and (D) show spatial maps of diffusion coefficients (estimated diffusion coefficient for each spatial bin is defined by the color scheme indicated in the color bar; red faster, blue slower, black insufficient sampling) for the same experiment shown in (A) estimated using all squared displacements observed between ~5-15 seconds (B) and ~30-40 seconds (C). A maximum likelihood estimator is used to estimate the diffusion coefficient (**Chapter 2**). See **Video B.2.5**.

3.3.5 Other imaging modalities

Our fast, line scanning HSM has the potential to be used for many other imaging modalities that are not explicitly demonstrated. Some of these modalities are variants of combinations of the demonstrated approaches. mcSPT could be performed to image several types of proteins labeled with various permutations of QD colors. (e.g. two colors on one membrane receptor and two on another). mcSPT could also be performed simultaneously with more than one additional marker, such as both GFP and yellow fluorescent protein (YFP), which could be separated from each other using multivariate curve resolution (MCR) [22].

Since the instrument is a line scanning system with optical sectioning capability, the microscope can be used to obtain hyperspectral *z*-slices of a sample. Using the fast scanning ability and a piezoelectric stage, our HSM can make three dimensional observations of samples with hyperspectral information, providing 5D data sets with spatial (*x*,*y*,*z*), spectral (λ), and temporal (*t*) dimensions. A demonstration of live cell, 5D imaging of three cellular markers is shown in the (**Figure B.1.15** and **Video B.2.6**).

Given the ability of the instrument to image single molecules with high temporal and spectral resolution, the HSM could be used with a variety of probes that report on local environment via spectra [33–36], for single-molecule, multi-color Foerster resonance energy transfer (FRET) studies [37–39] or for studying the fluorophores themselves, particularly QDs [40–42].

Finally, the instrument could also be used for more typical hyperspectral imaging tasks, such as imaging samples labeled with many spectrally overlapping fluorophores [43], and imaging spectral shifts of native fluorescence in organisms [22].

3.4 Discussion

Here we have detailed the development of a novel hyperspectral microscope that provides an unprecedented combination of speed, sensitivity and a spectral detection. Our

www.manaraa.com

HSM design provides acquisition rates of 27 fps over a 28 μm^2 field of view with 128 spectral channels. These features allow the determination of stoichiometry and dynamics of small oligomers, which cannot be measured using any other currently available techniques. We have demonstrated these capabilities of our HSM by multi-color single QD tracking and diffusion mapping of membrane protein dynamics. While EM or super-resolution techniques do provide a nanometer-scale image of protein distributions and clustering, they cannot provide information on protein diffusion or clustering dynamics. One variant of super-resolution that captures dynamics uses SPT of sequentially photo-activated fluorescent proteins [32], but it still requires long acquisition times to build up a diffusion map and cannot track a single protein or aggregate for more than a few seconds and cannot be used to identify interactions.

The maximum speed is limited by the EMCCD readout rate and is achieved by imaging only 64 of 128 pixels in the vertical shift direction. In this configuration, the maximum frame rate scales directly with the image area. A higher frame rate or larger field of view could be achieved by rotating the camera such that spectral binning in the vertical shift direction would increase frame rate. This would most benefit fast, 3D imaging of conventional fluorophores. We estimate that the imaging area could be increased by a factor of two while maintaining similar signal to noise levels with a state-of-the-art scientific complementary metal oxide (sCMOS) camera [44,45]. However, pixel-to-pixel noise and gain variation of sCMOS cameras may complicate particle localization and MCR analysis [46].

Several other spectral imaging methods could be envisioned for performing mcSPT. In principle, a widefield microscope could be used with a series of dichroic and emission filters to setup an arbitrarily large number of spectral channels. This approach has been used for two color [14] and four color imaging [47]. However, for image registration better than 20 nm, which is required for studying protein-protein interactions, careful mapping between all channels must be periodically performed using multispectral reference beads. In contrast, our spectrometer system provides less than 15 nm shift in spatial localization due to chromatic aberration from 500 nm to 750 nm (**Figure B.1.8**). Another recently described approach for wide field, fluorescence spectral imaging uses an image mapping spectrometer [48]. This apparatus would seem not to suffer from

channel registration problems and although has only been demonstrated at ~ 7 fps, would in principle be capable of video rate imaging. Of course, these wide field approaches do not provide a mechanism for rejecting out of focus light and could therefore suffer as compared to a line-scanning system when imaging in an environment with high cellular auto-fluorescence or other background.

Spectral imaging capabilities can be found on many commercial point scanning microscopes as well as custom built point-scanning hyperspectral systems [23,43,49]. However the finite lifetime of fluorophores limits photon yield even at arbitrarily high laser power and leads to a practical limit for SPT in point scanning systems. For a region of interest that is 128×128 spatial pixels, with a desired localization precision of ~10 nm, the maximum point scanning frame rate is ~2 fps and the maximum line scanning frame rate is ~250 fps (**Text B.3.8**). In terms of achieving a maximum area scanned for a given specific frame rate of 30 fps (33 ms per frame) and with the same 10 nm localization precision, these limits are ~ 512 um^2/33 ms for organic fluorophores (τ = 2 ns) and as low as 51 um^2/33 ms for QDs (τ = 20 ns) for a point scanning system. The latter value is fairly close to the area covered by this instrument when acquiring at 30 fps, and does not include consideration of spectral data acquisition. In addition, any non-linear photobleaching, photo-destruction or long-lived dark states would further reduce these values in practice. In comparison, a line-scanning system has the advantage of parallel observations along the spatial dimension and therefore gives an additional factor equal to the number of pixels that are simultaneously observed.

QDs have a broad excitation spectrum, narrow emission spectrum and high photo-stability. All of these properties are taken advantage of for mcSPT using our HSM. However, QDs do have practical limiting properties [40] such as fluorescence intermittency, the potential for non-fluorescent QDs [50] and a difficultly in producing monovalent probes [51]. For example, the presence of non-fluorescent QDs leads to the possibility of underestimating the oligomer size of complexes in mcSPT experiments. Consideration must also be taken when using biotin-protein:streptavidin-QD conjugation schemes since unlabeled protein could also lead to underestimation of oligomer size. Consequently, the oligomers identified in **Figures 3.5** and **3.6** should be considered as minimal dimers and trimers. Contribution from non-biotynilated protein can be

minimized by purification on streptavidin resin prior to conjugation with the QDs. The dark fraction of QDs for each spectral species can be measured and used in a statistical analysis of the properties under study as a function of oligomer size. mcSPT could also be performed with other probes that may have overlapping spectra, such as non-blinking QDs [52,53], 'Cornell dots' [54] or other systems that use combinations of organic fluorophores and could have the benefit of reduced or non-existent fluorescence intermittency.

In summary, we have developed a high-speed hyperspectral microscope and the required analysis software to perform simultaneous SPT of up to 8 spectrally distinct QDs at video rate. We have provided a description of the instrument, software, and several proof-of-principle applications of the HSM. The applications presented in this manuscript (mcSPT, mcSPT with GFP background, high density mcSPT, and 3D scanning) highlight how the HSM can provide unique insight into dynamic cellular events.

3.5 Materials and methods

3.5.1 Reagents

Purification [55] of mouse monoclonal anti-DNP IgE and preparation [17] of functionally monovalent QD-IgE was previously reported. Streptavidin conjugated quantum dots were purchased from Invitrogen either individually (525-Q10141MP, 565-Q10131MP, 585-Q10111MP, 605-Q10101MP, 625-A10196, 655-Q10121MP, 705-Q10161MP, 800- Q10171MP) or in the Qdot® Streptavidin Sampler Kit (Q10151MP). Biotin-X, SSE used for monovalent biotinlylation of IgE for linkage to streptavidin QDs was purchased from Invitrogen (B6352). Biotin was purchased from Invitrogen (B1595). CellMask™ orange plasma membrane stain was purchased from Invitrogen (C10045). Multivalent DNP-BSA was purchased from Invitrogen (A23018). DNP_3 (manuscript in preparation Mahajan A, Barua D, Cutler P, Lidke DS, et al.), which is a small trimer of peptides that presents three DNP moieties for crosslinking DNP-specific IgE, was synthesized by AnaSpec (Fremont, CA). Plasmid used for transfection of GFP-actin into

RBL-2H3 cells was purchased from Clontech (pAcGFP1-Actin 632453). Biotinylated EGF at a 1:1 ratio was purchased from Invitrogen (E-3477). The EGFR inhibitor PD153035 was purchased from Calbiochem (234491).

3.5.2 Imaging of QDs non-specifically adhered to glass

The quantum dots (Invitrogen Corporation Qdot® 525, 565, 585, 605, 625, 655, 705, and 800) were each diluted to 50 pM in 1x phosphate buffered saline (PBS) and then mixed together in equal volumes. 300 ul of this mixture was then added to each well in an 8-well chamber. 10 ul of 2 M NaCl (aqueous) was then added to each well and then incubated at 4º C for up to 8 hours to allow the quantum dots to attach to the glass. The solution was then replaced by 1x PBS. 250 frames of data (providing x, y, and λ information) were acquired at 27 frames/sec over an area of 28 μm^2 (the intended scan rate for our typical live cell imaging) with an excitation laser line intensity of ~1000 W/cm^2.

3.5.3 Image acquisition for SPT experiments on live cells

Samples were maintained at 34-36 °C using an objective heater (Bioptechs, Butler, PA, USA) for imaging. For an acquisition rate of 27 fps, a region of interest (ROI) of 3.7 μm in x and 7.4 μm in y is acquired. This ROI consists of 32 steps (x dimension; ~0.116 μm steps) of the line across the sample by the scanning mirror and 64 pixels (y dimension; ~0.116 μm pixel size) along the line.

3.5.4 Single particle tracking (preprocessing, localizations, and trajectory building)

Immediately prior to the acquisition of each HSM image, 1000 frames of dark images were acquired for background correction. The mean dark image was subtracted from each frame of the HSM image. The spectrometer was aligned so that several columns of spectral pixels are dark due to a long pass filter.. The mean value of a dark column of pixels was subtracted from the SPT image to correct a baseline offset. The HSM image

was then multiplied by a calibrated gain factor [56] to convert arbitrary pixel counts to photons.

The steps in SPT in an HSM image are similar to steps used in traditional SPT algorithms: image segmentation, single particle localization, and trajectory building. Uniform and maximum filtering procedures outlined in previous work by Huang et. al. [28] for two dimensions are expanded to three dimensions (x,y,λ) and used to identify centers for sub-volumes in which to localize single molecules. The empirically determined sub-volume size used for single molecule localization in this work was 25 spectral pixels by 7 spatial pixels by 7 spatial pixels. A 3D Gaussian PSF/spectral model and Poisson noise model (**Figure B.1.10** and **Text B.3.4**) were used to model the spatial and spectral features of individual QDs. The variance in the parameters estimated by the localization algorithm converges to the CRB (**Figure B.1.10B**). Multiple 3D Gaussians were used to fit multiple spatially and spectrally overlapping QDs (**Figure B.1.11** and **Text B.3.5**). An artifact of using a line-scanning instrument is that blinking during the scanning of a single QD causes errors in QD localization in the scan direction (**Figure B.1.13**). Typically, each sub-volume was fit using 1-4 emitter models. Accurate fits were then selected using an empirically derived filtering scheme (**Text B.3.4**). Trajectories are built from filtered localizations using a cost matrix approach to form a linear assignment problem [29] (**Text B.3.6**).

3.5.5 Quantification of trajectory mobility

Diffusion coefficients (*D*) for groups of trajectories (**Figures 3.5** and **3.6**) were determined by fitting a line to the first 3 points of the ensemble mean squared displacement. A maximum likelihood estimator based on independent jump analysis (**Chapter 2**) is used to estimate the instantaneous *D* and diffusion mapping (**Figure 3.7**). For the instantaneous *D*, individual jumps were grouped temporally using a sliding window of 14 frames (~ 0.5 s) according the temporal midpoint of the observations. For diffusion mapping, individual jumps were binned spatially according to camera pixel sampling (~116 nm in each dimension) and temporally according to the midpoint of the temporal jump using a sliding window of 280 frames (~10 s).

3.5.6 Cell culture

A431 human epithelial carcinoma cells were cultured and passaged in Dulbeccos' modified eagle medium (DMEM, Sigma-Aldrich), with 10% fetal bovine serum (FBS, Invitrogen), penicillin, and streptomycin [14]. RBL-2H3 cells were cultured and passaged using MEM (Gibco® 11095-080) supplemented with penicillin-streptomycin, L-glutamine, and 10% FBS [21,30]. For all experiments using GFP-actin, RBL-2H3 cells were transiently transfected by electroporation with an Amaxa Nucleofactor II using program T-020. Transiently transfected cells were used within 24-48 h of transfection. For all image acquisitions, cells were plated in Lab-Tek 8-well chambers (Thermo Scientific, 177402) approximately 24-48 hours prior to the experiment at ~2×10^4 cells per well.

3.5.7 Cell treatment for SPT of QD-EGF

Procedures for labeling A431 cells with QD-EGF were adapted from previous work [14]. Cells were serum starved in the presence of 1 μM PD153035 for several hours prior to imaging. PD153035 (1 μM) was included in imaging buffer throughout the remainder of the experiment to prevent receptor endocytosis. Tyrodes solution with 0.1% BSA and 20 mM glucose was used as an imaging buffer. Media was exchanged with 200 μl of imaging buffer prior to imaging. Immediately prior to data acquisition, 100 μl of 12 pM (concentration for each individual color) of QD-EGF (final concentration of 4 pM) equilibrated at 37 °C was added to the well to be imaged and data was acquired within 10 minutes.

3.5.8 Cell treatment for SPT of QD-IgE

Procedures for labeling RBL-2H3 cells with QD-IgE for SPT were adapted from previous work [17]. For mcSPT experiments, cells were incubated in 200 μl of Hanks' balanced salt solution (HBSS) with 1 nM of each color of QD-IgE simultaneously for 15 min at 37 °C. For the experiment, cells were incubated in 200 μl of HBSS with optimized concentrations of each color of QD-IgE (2 nM of 605, 625, and 655; 4 nM of 565 and

585; 10 nM of 525, 705, and 800) for 15 min at 37 °C. Final volume of HBSS in each well was 200 µl. All SPT experiments were performed within 1 hour of labeling. For the mcSPT experiment (**Figure 5**), 100 µl of crosslinker (DNP$_3$; final concentration of 1 nM) equilibrated at 37 °C was added to the well ~7 minutes prior to the collection of the acquisition. For the high density mcSPT experiment (**Figure 7**), 100 µl of crosslinker (DNP-BSA; final concentration of 1 µg/ml) equilibrated at 37 °C was added ~20 seconds into the image acquisition.

3.5.8 3D-scanning of live cells

RBL-2H3 cells were incubated in 200 µl of 5 nM QD-IgE (655) in HBSS for 30 minutes at 37 °C followed by 2 washes with HBSS. The cells were incubated with 200 µl of 5 µg/ml CellMask orange for 3 min at 37 °C followed by 3 washes with HBSS. Imaging was performed immediately after labeling. Crosslinker (DNP-BSA; final concentration 10 µg/ml) was added ~60 seconds into the image acquisition. In order to assure rapid mixing of crosslinker and to prevent focal drift, 100 µl of crosslinker stock at 3x final concentration in HBSS preheated to 37 °C was added (contains 200 µl HBSS).

Z-stacks covering an ROI of 14.8 µm in *x*, 14.8 µm in *y*, and 7.0 µm in *z* were acquired at a rate of 7.72 seconds per *z*-stack. Each *z*-slice for this ROI consists of 128 steps (*x* dimension; ~0.116 µm steps) of the line across the sample by the scanning mirror and 128 pixels (*y* dimension; ~0.116 µm pixel size) along the line to make each *z*-slice, and each *z*-stack for this ROI contains 29 *z*-slices with a step size of 0.25 µm. In order to conserve CPU memory for storage and post-processing, the data was binned into 32 spectral bins instead of 128. It is important to note that altering the number of spectral bins does not significantly alter the acquisition time with the current camera configuration. A total of 50 *z*-stacks were acquired giving a total acquisition time of ~6.5 min. *Z*-stacks were processed using 3D deconvolution. The experimentally measured PSF was used with the built-in Matlab deconvolution algorithm *deconvlucy*. An isosurface rendering was then used to represent the data.

3.6 Keywords

single particle tracking, hyperspectral microscopy, quantum dots, EGFR, FcεRI, IgE, line-scanning, spectrometer, spectroscopy

3.7 Acknowledgements

3.8 References

1. Wilson BS, Pfeiffer JR, Oliver JM (2000) Observing FceRI Signaling from the Inside of the Mast Cell Membrane. J Cell Biol 149: 1131–1142 ST – Observing FceRI Signaling from the. Available: http://jcb.rupress.org/cgi/content/abstract/149/5/1131.

2. Wilson BS, Pfeiffer JR, Surviladze Z, Gaudet EA, Oliver JM (2001) High resolution mapping of mast cell membranes reveals primary and secondary domains of FceRI and LAT. The Journal of Cell Biology 154: 645–658. Available: http://jcb.rupress.org/content/154/3/645.abstract.

3. Stump RF, Pfeiffer JR, Schneebeck MC, Seagrave JC, Oliver JM (1989) Mapping gold-labeled receptors on cell surfaces by backscattered electron imaging and digital image analysis: studies of the IgE receptor on mast cells. The American journal of anatomy 185: 128–141. Available: http://www.ncbi.nlm.nih.gov/pubmed/2773808. Accessed 14 March 2012.

4. Seagrave J, Pfeiffer JR, Wofsy C, Oliver JM (1991) Relationship of IgE receptor topography to secretion in RBL-2H3 mast cells. Journal of cellular physiology 148: 139–151. Available: http://www.ncbi.nlm.nih.gov/pubmed/1830592. Accessed 6 March 2012.

5. Veatch SL, Chiang EN, Sengupta P, Holowka DA, Baird BA (2012) Quantitative Nano-Scale Analysis of IgE-FcεRI Clustering and Coupling to Early Signaling Proteins. The journal of physical chemistry B. Available: http://dx.doi.org/10.1021/jp300197p. Accessed 22 March 2012.

6. Veatch SL, Machta BB, Shelby SA, Chiang EN, Holowka DA, et al. (2012) Correlation functions quantify super-resolution images and estimate apparent clustering due to over-counting. PloS one 7: e31457. Available: http://dx.plos.org/10.1371/journal.pone.0031457. Accessed 9 March 2012.

7. Hell SW (2007) Far-field optical nanoscopy. Science (New York, NY) 316: 1153–1158. Available: http://www.ncbi.nlm.nih.gov/pubmed/17525330. Accessed 1 November 2012.

8. Schermelleh L, Heintzmann R, Leonhardt H (2010) A guide to super-resolution fluorescence microscopy. The Journal of cell biology 190: 165–175. Available: http://jcb.rupress.org/content/190/2/165.full. Accessed 3 October 2012.

9. Lidke DS, Lidke KA (2012) Advances in high-resolution imaging--techniques for three-dimensional imaging of cellular structures. Journal of cell science 125: 2571–2580. Available: http://jcs.biologists.org/content/125/11/2571.long. Accessed 6 November 2012.

10. Saxton MJ, Jacobson K (1997) SINGLE-PARTICLE TRACKING:Applications to Membrane Dynamics. Annual Review of Biophysics and Biomolecular Structure 26: 373–399. Available: http://arjournals.annualreviews.org/doi/abs/10.1146/annurev.biophys.26.1.373.

11. Ober RJ, Ram S, Ward ES (2004) Localization accuracy in single-molecule microscopy. Biophysical journal 86: 1185–1200. Available: http://www.pubmedcentral.nih.gov/articlerender.fcgi?artid=1303911&tool=pmcentrez&rendertype=abstract.

12. Alcor D, Gouzer G, Triller A (2009) Single-particle tracking methods for the study of membrane receptors dynamics. Eur J Neurosci 30: 987–97 ST – Single–particle tracking methods for . Available: http://www.ncbi.nlm.nih.gov/pubmed/19735284. Accessed 19 July 2011.

13. Ram S, Ward ES, Ober RJ (2006) Beyond Rayleigh's criterion: a resolution measure with application to single-molecule microscopy. Proceedings of the National Academy of Sciences of the United States of America 103: 4457–4462. Available: http://www.pnas.org/content/103/12/4457. Accessed 7 November 2012.

14. Low-Nam ST, Lidke KA, Cutler PJ, Roovers RC, Van Bergen en Henegouwen PMP, et al. (2011) ErbB1 dimerization is promoted by domain co-confinement and stabilized by ligand binding. Nat Struct Mol Biol 18: 1244–1249. Available: http://dx.doi.org/10.1038/nsmb.2135.

15. Hern JA, Baig AH, Mashanov GI, Birdsall B, Corrie JET, et al. (2010) Formation and dissociation of M1 muscarinic receptor dimers seen by total internal reflection fluorescence imaging of single molecules. Proceedings of the National Academy of Sciences of the United States of America 107: 2693–2698. Available: http://www.pubmedcentral.nih.gov/articlerender.fcgi?artid=2823895&tool=pmcentrez&rendertype=abstract. Accessed 12 November 2012.

16. You C, Wilmes S, Beutel O, Löchte S, Podoplelowa Y, et al. (2010) Self-controlled monofunctionalization of quantum dots for multiplexed protein tracking in live cells. Angewandte Chemie (International ed in English) 49: 4108–4112. Available: http://www.ncbi.nlm.nih.gov/pubmed/20432494. Accessed 31 August 2012.

17. Andrews NL, Lidke K a, Pfeiffer JR, Burns AR, Wilson BS, et al. (2008) Actin restricts FceRI diffusion and facilitates antigen-induced receptor immobilization. Nature cell biology 10: 955–963. Available: http://dx.doi.org/10.1038/ncb1755. Accessed 17 August 2011.

18. Lidke DS, Lidke KA, Rieger B, Jovin TM, Arndt-Jovin DJ (2005) Reaching out for signals: filopodia sense EGF and respond by directed retrograde transport of activated receptors. The Journal of cell biology 170: 619–626. Available: http://jcb.rupress.org.libproxy.unm.edu/content/170/4/619.long. Accessed 6 March 2013.

19. Sinclair MB, Timlin JA, Haaland DM, Werner-washburne M (2004) Design, construction, characterization, and application of a hyperspectral microarray scanner. Applied Optics 43: 2079–2088.

20. Pawley JB (2006) Handbook of Biological Confocal Microscopy (Third Edition). 3rd ed. Pawley JB, editor Springer.

21. Andrews NL, Pfeiffer JR, Martinez a M, Haaland DM, Davis RW, et al. (2009) Small, Mobile FceRI Receptor Aggregates Are Signaling Competent. Immunity 31: 469–479.

Available:
http://www.pubmedcentral.nih.gov/articlerender.fcgi?artid=2828771&tool=pmcentrez&re
ndertype=abstract. Accessed 17 August 2011.

22.   Haaland DM, Jones HDT, Van Benthem MH, Sinclair MB, Melgaard DK, et al. (2009)
        Hyperspectral Confocal Fluorescence Imaging : Exploring Alternative Multivariate Curve
        Resolution Approaches. Applied Spectroscopy 63: 271–279. Available:
        http://openurl.ingenta.com/content/xref?genre=article&issn=0003-
        7028&volume=63&issue=3&spage=271.

23.   Lerner JM (2006) Imaging spectrometer fundamentals for researchers in the biosciences--
        a tutorial. Cytometry Part A : the journal of the International Society for Analytical
        Cytology 69: 712–734. Available: http://www.ncbi.nlm.nih.gov/pubmed/16615140.
        Accessed 6 February 2012.

24.   Warren DW (1997) Compact prism spectrographs based on aplanatic principles. Optical
        Engineering 36: 1174 – 1182. Available:
        http://link.aip.org/link/OPEGAR/v36/i4/p1174/s1&Agg=doi.

25.   Cheezum MK, Walker WF, Guilford WH (2001) Quantitative comparison of algorithms
        for tracking single fluorescent particles. Biophysical journal 81: 2378–2388. Available:
        http://www.cell.com/biophysj/fulltext/S0006-3495(01)75884-5. Accessed 12 July 2011.

26.   Zhang B, Zerubia J, Olivo-Marin J-C (2007) Gaussian approximations of fluorescence
        microscope point-spread function models. Applied Optics 46: 1819. Available:
        http://www.opticsinfobase.org/abstract.cfm?uri=ao-46-10-1819. Accessed 10 August
        2012.

27.   Smith CS, Joseph N, Rieger B, Lidke K a (2010) Fast, single-molecule localization that
        achieves theoretically minimum uncertainty. Nature methods 7: 373–375. Available:
        http://www.pubmedcentral.nih.gov/articlerender.fcgi?artid=2862147&tool=pmcentrez&re
        ndertype=abstract.

28.   Huang F, Schwartz SL, Byars JM, Lidke KA (2011) Simultaneous multiple-emitter fitting
        for single molecule super-resolution imaging. Biomed Opt Express 2: 1377–1393.

29. Jaqaman K, Loerke D, Mettlen M, Kuwata H, Grinstein S, et al. (2008) Robust single-particle tracking in live-cell time-lapse sequences. Nat Meth 5: 695–702. Available: http://dx.doi.org/10.1038/nmeth.1237.

30. Wilson BS, Pfeiffer JR, Oliver JM (2000) Observing FceRI Signaling from the Inside of the Mast Cell Membrane. J Cell Biol 149: 1131–1142 ST – Observing FceRI Signaling from the. Available: http://jcb.rupress.org/cgi/content/abstract/149/5/1131.

31. Kusumi A, Nakada C, Ritchie K, Murase K, Suzuki K, et al. (2005) PARADIGM SHIFT OF THE PLASMA MEMBRANE CONCEPT FROM THE TWO-DIMENSIONAL CONTINUUM FLUID TO THE PARTITIONED FLUID: High-Speed Single-Molecule Tracking of Membrane Molecules. Annual Review of Biophysics and Biomolecular Structure 34: 351–378. Available: http://arjournals.annualreviews.org/doi/abs/10.1146/annurev.biophys.34.040204.144637. Accessed 16 June 2011.

32. Manley S, Gillette JM, Patterson GH, Shroff H, Hess HF, et al. (2008) High-density mapping of single-molecule trajectories with photoactivated localization microscopy. Nature Methods 5: 2007–2009. doi:10.1038/NMETH.1176.

33. Balkay L, Márián T, Emri M, Krasznai Z, Trón L (1997) Flow cytometric determination of intracellular free potassium concentration. Cytometry 28: 42–49. Available: http://www.ncbi.nlm.nih.gov/pubmed/9136754. Accessed 28 March 2013.

34. Chacon E, Reece JM, Nieminen AL, Zahrebelski G, Herman B, et al. (1994) Distribution of electrical potential, pH, free Ca2+, and volume inside cultured adult rabbit cardiac myocytes during chemical hypoxia: a multiparameter digitized confocal microscopic study. Biophysical journal 66: 942–952. Available: http://dx.doi.org/10.1016/S0006-3495(94)80904-X. Accessed 28 March 2013.

35. Williams DA, Fogarty KE, Tsien RY, Fay FS (1985) Calcium gradients in single smooth muscle cells revealed by the digital imaging microscope using Fura-2. Nature 318: 558–561. Available: http://dx.doi.org/10.1038/318558a0. Accessed 28 March 2013.

36. Parasassi T, De Stasio G, Ravagnan G, Rusch RM, Gratton E (1991) Quantitation of lipid phases in phospholipid vesicles by the generalized polarization of Laurdan fluorescence.

Biophysical journal 60: 179–189. Available:
http://www.pubmedcentral.nih.gov/articlerender.fcgi?artid=1260049&tool=pmcentrez&re
ndertype=abstract. Accessed 28 March 2013.

37.   Shcherbakova DM, Hink MA, Joosen L, Gadella TWJ, Verkhusha V V (2012) An orange
       fluorescent protein with a large Stokes shift for single-excitation multicolor FCCS and
       FRET imaging. Journal of the American Chemical Society 134: 7913–7923. Available:
       http://pubs.acs.org.libproxy.unm.edu/doi/full/10.1021/ja3018972. Accessed 28 March
       2013.

38.   Lee J, Lee S, Ragunathan K, Joo C, Ha T, et al. (2010) Single-molecule four-color FRET.
       Angewandte Chemie (International ed in English) 49: 9922–9925. Available:
       http://www.ncbi.nlm.nih.gov/pubmed/21104966. Accessed 14 March 2013.

39.   Milles S, Koehler C, Gambin Y, Deniz AA, Lemke EA (2012) Intramolecular three-colour
       single pair FRET of intrinsically disordered proteins with increased dynamic range.
       Molecular bioSystems 8: 2531–2534. Available:
       http://pubs.rsc.org/en/content/articlehtml/2012/mb/c2mb25135c. Accessed 28 March
       2013.

40.   Lee SF, Osborne M a (2009) Brightening, blinking, bluing and bleaching in the life of a
       quantum dot: friend or foe? Chemphyschem : a European journal of chemical physics and
       physical chemistry 10: 2174–2191. Available:
       http://www.ncbi.nlm.nih.gov/pubmed/19691081. Accessed 21 July 2012.

41.   Jones M, Nedeljkovic J, Ellingson RJ, Nozik AJ, Rumbles G (2003) Photoenhancement of
       Luminescence in Colloidal CdSe Quantum Dot Solutions. The Journal of Physical
       Chemistry B 107: 11346–11352. Available:
       http://pubs.acs.org/doi/abs/10.1021/jp035598m.

42.   Hoyer P, Staudt T, Engelhardt J, Hell SW (2011) Quantum dot blueing and blinking
       enables fluorescence nanoscopy. Nano letters 11: 245–250. Available:
       http://www.ncbi.nlm.nih.gov/pubmed/21128678. Accessed 24 March 2013.

43.   Sinclair MB, Haaland DM, Timlin J a, Jones HDT (2006) Hyperspectral confocal microscope. Applied optics 45: 6283–6291. Available: http://www.ncbi.nlm.nih.gov/pubmed/16892134.

44.   Huang Z-L, Zhu H, Long F, Ma H, Qin L, et al. (2011) Localization-based super-resolution microscopy with an sCMOS camera. Optics Express 19: 19156. Available: http://www.opticsinfobase.org/abstract.cfm?uri=oe-19-20-19156. Accessed 25 September 2012.

45.   Long F, Zeng S, Huang Z-L (2012) Localization-based super-resolution microscopy with an sCMOS camera Part II: Experimental methodology for comparing sCMOS with EMCCD cameras. Optics Express 20: 17741. Available: http://www.opticsinfobase.org/abstract.cfm?uri=oe-20-16-17741. Accessed 21 July 2012.

46.   Jones HDT, Haaland DM, Sinclair MB, Melgaard DK, Collins AM, et al. (2012) Preprocessing strategies to improve MCR analyses of hyperspectral images. Chemometrics and Intelligent Laboratory Systems null: 1–10. Available: http://linkinghub.elsevier.com/retrieve/pii/S0169743912000226. Accessed 21 August 2012.

47.   Arnspang EC, Brewer JR, Lagerholm BC (n.d.) Multi-color Single Particle Tracking with Quantum Dots. PloS one.

48.   Elliott AD, Gao L, Ustione A, Bedard N, Kester R, et al. (2012) Real-time hyperspectral fluorescence imaging of pancreatic β-cell dynamics with the image mapping spectrometer (IMS). Journal of cell science Advanced O. Available: http://jcs.biologists.org/cgi/content/abstract/jcs.108258v1. Accessed 21 August 2012.

49.   Esposito A, Bader AN, Schlachter SC, Heuvel DJ Van Den, Schierle GSK, et al. (2011) Design and application of a confocal microscope for spectrally resolved anisotropy imaging. Optics Express 19: 1020–1027. doi:10.1002/cphc.201000833.16.

50.   Yao J, Larson DR, Vishwasrao HD, Zipfel WR, Webb WW (2005) Blinking and nonradiant dark fraction of water-soluble quantum dots in aqueous solution. Proceedings of the National Academy of Sciences of the United States of America 102: 14284–14289. Available: http://www.pnas.org/content/102/40/14284.full. Accessed 4 August 2012.

51. Mittal R, Bruchez MP (2011) Biotin-4-fluorescein based fluorescence quenching assay for determination of biotin binding capacity of streptavidin conjugated quantum dots. Bioconjugate chemistry 22: 362–368. Available: http://www.pubmedcentral.nih.gov/articlerender.fcgi?artid=3059817&tool=pmcentrez&rendertype=abstract.

52. Chen Y, Vela J, Htoon H, Casson JL, Werder DJ, et al. (2008) "Giant" multishell CdSe nanocrystal quantum dots with suppressed blinking. J Am Chem Soc 130: 5026–5027. Available: http://www.ncbi.nlm.nih.gov/pubmed/18355011.

53. Marchuk K, Guo Y, Sun W, Vela J, Fang N (2012) High-precision tracking with non-blinking quantum dots resolves nanoscale vertical displacement. Journal of the American Chemical Society 134: 6108–6111. Available: http://www.ncbi.nlm.nih.gov/pubmed/22458433. Accessed 21 August 2012.

54. Ow H, Larson DR, Srivastava M, Baird BA, Webb WW, et al. (2005) Bright and stable core-shell fluorescent silica nanoparticles. Nano letters 5: 113–117. Available: http://dx.doi.org/10.1021/nl0482478. Accessed 13 August 2012.

55. Liu FT, Bohn JW, Ferry EL, Yamamoto H, Molinaro C a, et al. (1980) Monoclonal dinitrophenyl-specific murine IgE antibody: preparation, isolation, and characterization. Journal of immunology (Baltimore, Md : 1950) 124: 2728–2737. Available: http://www.ncbi.nlm.nih.gov/pubmed/7373045.

56. Van Vliet LJ, Sudar D, Young IT (1998) Digital fluorescence imaging using cooled charge-coupled device array cameras. In: Celis JE, editor. Cell Biology. A laboratory handbook. Academic Press, Vol. III. pp. 109–120.

CHAPTER 4: SIGNALING COMPETENCY OF MOBILE AND TRANSIENT FcεRI-IGE AGGREGATES ON MAST CELLS

Signaling Competency of Mobile and Transient FcεRI-IgE Aggregates on Mast Cells

Authors

Patrick J. Cutler[*], Hannah Johnson[*], Samantha Schwartz[*], Rachel Grattan[*], Bridget Wilson[*], Keith Lidke[^], Diane Lidke[*#]

[*]Department of Pathology, University of New Mexico

[^]Department of Physics and Astronomy, University of New Mexico

[#]Corresponding Author: dlidke@salud.unm.edu

4.1 Abstract

Aggregation of the IgE-FcεRI on mast cells is an initial step in the allergic response; therefore, a fundamental understanding of the aggregation of IgE-FcεRI is important for advancing our understanding of allergies. This work investigates the dynamics IgE-FcεRI aggregation. Multi-color single particle tracking of 5-colors of QD-IgE and DNP-QD on live cells reveal transient aggregates of IgE-FcεRI for which the stability is quantified by hidden Markov model analysis. Multi-color single molecule imaging and electron microscopy confirms these observations in fixed samples. Additionally, 2-color single particle tracking of DNP-QD and GFP-Syk are used to directly show the signaling competency of mobile crosslinked aggregates of IgE-FcεRI. These findings lead to the hypothesis that mobile transient aggregates of IgE-FcεRI are signaling competent.

4.2 Introduction

The high affinity receptor for IgE, FcεRI, is a key player in the allergic response and a member of the multi-chain immune recognition receptor (MIRR) family [1]. FcεRI has four subunits (**Figure 4.1A**), and due to its high affinity, IgE essentially acts as an additional subunit of the receptor upon binding. FcεRI is the focus of this study, but it is important to discuss FcεRI in the context of the MIRR family, because there are many unifying characteristics among this family of receptors. Two other key members of the MIRR family are the T-cell and B-cell receptors. Signal initialization through receptor aggregation via crosslinking due to multivalent extra cellular ligand is a key characteristic of MIRRs. Dimerization is the minimal stimulus necessary for signal initiation [2–4], although not all dimerizing reagents are signaling competent.

In general, receptor crosslinking leads to phosphorylation of immunoreceptor tyrosine-based activation motifs (ITAMs) by the recruitment of protein tyrosine kinases[5] (i.e. membrane

tethered Lyn/ Fyn for FcεRI [6]). Syk family kinases (ZAP-70 for TCR; Syk for BCR and FcεRI [7]) then bind to phosphorylated ITAMs through the tandem SRC homology 2 (SH2) domains and are subsequently phosphorylated. Activated Syk phosphorylates substrates, including LAT, PI3K, and PLCγ, to propagate downstream signaling. For FcεRI this leads to degranulation for the release of histamines and the de novo synthesis of other cellular mediators implicated in the allergic response.

Many MIRRs participate in the formation of immunological synapses as established in B cells[8], T cells[9], and Mast cells[10]. The study of the immunological synapse has provided significant insights into the spatio-temporal relationship of MIRRs with signaling. For example, the TCR signals at the periphery of the immunological synapse in the pSMAC[11] where it is mobile[12]. As the TCR coalesces into the cSMAC[13] it immobilizes, signaling is quenched, and it is endocytosed[11]. Recent work on immunological synapses in mast cells[14] demonstrated that monovalent ligand in a lipid bilayer can be used to form an immunological synapse, which induces cellular degranulation. This suggests that a simple increase in the local density of FcεRI without the formation of true aggregates is sufficient to elicit an immune response.

Early observations that crosslinked IgE-FcεRI is rapidly immobilized led to the hypothesis that immobilization is the trigger for signal initiation [15–19]. However, recent work[20] provided evidence supporting the hypothesis that small mobile aggregates of IgE-FcεRI are signaling competent. This work used single particle tracking (SPT) of a quantum dot (QD) labeled IgE (QD-IgE; **Figure 4.1B**) and a QD analog of multivalent antigen (DNP-QD; **Figure 4.1C**). In experiments with activating doses of crosslinker, there were minimal changes in the mobility of QD-IgE-FcεRI. Additionally, activating doses of DNP-QD remained mobile. To observe interactions of QD-IgE-FcεRI, multi-color SPT (mcSPT) of 5-colors of QD-IgE on a hyperspectral microscope was performed. This demonstrated that aggregates of at least 3 QD-IgE-FcεRI remained mobile under signaling competent conditions. It is important to note here that quantifying the mobility of these aggregates was limited by the acquisition rate of the existing hyperspectral microscope (0.25 frames per second (fps)).
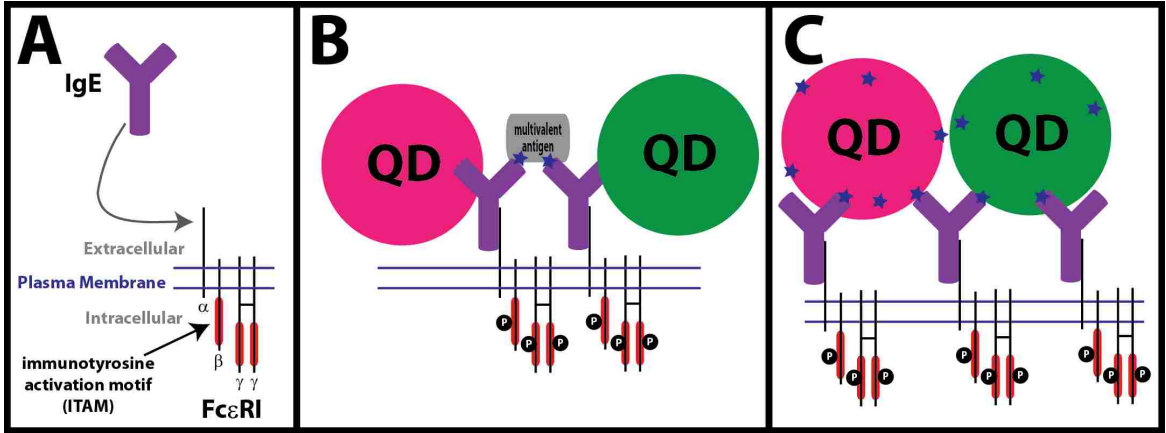
Figure 4.1 QD-IgE-FcεRI and DNP-QD probes. (A) Representation of the 4 subunits of FcεRI and ITAMS on the beta and gamma subunits. IgE binds to the alpha subunit. (B) QD-IgE is used to track FcεRI in the absence or presence of crosslinker. (C) DNP-QD is used to directly track multivalent antigen.

In this manuscript, we further investigate the spatio-temporal relationship of IgE-FcεRI aggregates with signaling by using a high-speed hyperspectral microscope [21] and total internal reflection fluorescence (TIRF) microscopy. The high-speed hyperspectral microscope provides the capacity of performing mcSPT of up to 8 spectrally distinct colors of QDs simultaneously at an acquisition rate of 30 fps. These experiments provide sufficient temporal resolution to quantify the stability of interactions through the determination of interaction off rates using a hidden Markov model (HMM). This technique was originally used to characterize EGFR dimerization in 2-color SPT data[22], but is easily adapted in this work for analyzing pair-wise interactions in mcSPT data. Additionally, hyperspectral multi-color single molecule imaging (mcSMI) of 3-colors of Alexa Fluor-labeled IgE (AF-IgE) and TIRF microscopy with GFP labeled Syk (GFP-Syk) are used to further characterize cellular interactions and signaling competency of DNP-QD. Our findings confirm the previous hypothesis by Andrews et al.[20] by directly demonstrating that mobile aggregates are signaling competent. Furthermore, we extend the mechanistic model of FcεRI signaling by quantifying transient receptor interactions that can also initiate signaling.

4.3 Results

4.3.1 Purification of QD-IgE

Due to the potential presence of dark IgE or multiple QD-IgE-FcεRI with similar emission spectra, the aggregate size detected in mcSPT experiments with QD-IgE is the minimal size of the aggregate. The presence of dark IgE in the experimental setup used here originates from two sources: (1) non-biotinylated IgE (i.e. streptavidin QDs cannot bind to IgE which are not biotinylated); or (2) QD-IgE in which the QD is non-fluorescent. The presence of non-biotinylated IgE is a result of the Poisson process by which IgE is biotinylated via NHS-ester linkage to lysine residues on IgE. Given a mean biotin:IgE ratio of 0.6, approximately 55% of all IgE will be non-biotinylated (**Supplemental Figure C.1.1**). In order to eliminate this source of dark IgE, biotinylated IgE was purified from non-biotinylated IgE (referred to as QD-IgE$_p$; see Materials and Methods for more details). The mean observed biotin:IgE ratio before purification (0.6) and after purification (1.2) corresponds well with expected values (0.6 and 1.3 respectively; **Supplemental Figure C.1.1**). QD-IgE formulated with biotinylated IgE that is not purified from non-biotinylated IgE is referred to as QD-IgE$_{np}$. Further evidence of the purification is demonstrated by the larger shift in mobility upon crosslinking for QD-IgE$_{np}$ (**Supplementary Figure C.1.2**).

The experimental conditions for QD-IgE$_{np}$ in the work presented here are comparable to that of the hyperspectral experiments performed in previous work by Andrews et al. in which degranulation was observed. In summary, while degranulation was stimulated under these conditions (RBL-2H3 cells primed with 2 nM of QD-IgE$_{np}$ for 15 minutes at room temperature), it was approximately 50% less than under standard conditions (cells primed over night with saturating concentrations of dark IgE)[20]. Here Ca^{+2} imaging of cells primed with QD-IgE$_p$ is used to measure the cellular activation due to crosslinking with QD-IgE$_p$. This experiment showed a subdued response with 100 % of cells responding to crosslinker (0.1 μg/ml DNP-BSA) with saturating dark IgE and 30% responded with 2 nM QD-IgE$_p$ for 15 minutes at 37 °C. This was significantly above the background of 0 to 3% Ca^{+2} flux for negative controls. The subdued yet significant Ca^{+2} flux observed for QD-IgE$_p$ agrees with the degranulation results from of QD-IgE$_{np}$ and demonstrates signaling competency for cells primed with QD-IgE$_p$. Further experimentation is necessary to fully characterize the signaling characteristics of QD-IgE$_p$ with variable concentrations of crosslinker (DNP-F3 and DNP-BSA).

4.3.2 Stable and transient IgE-FcεRI interactions

Multi-color SPT was used to investigate the dynamics of anti-DNP-IgE-FcεRI with multivalent antigen (**Figure 4.1B**). Five distinct colors of QD-IgE (565, 585, 605, 625, 655) were simultaneously tracked on RBL-2H3 cells to probe the dynamics of IgE-FcεRI under resting and crosslinking conditions. The discrete spectral features of QDs provides a platform to determine aggregate sizes of QD-IgE-FcεRI from unique spectral signatures of individual QDs[20]. Moreover, automated methods for mcSPT have been implemented to allow for high through put data analysis[21].

Stable and transient interactions of QD-IgE-FcεRI are observed upon crosslinking either with DNP-BSA or DNP-F3, but aggregates larger than dimers were rarely observed. HMM analysis was used to quantify the stability of crosslinked aggregates. This analysis provides off rates as a measure of aggregate stability (i.e. higher off rate is interpreted as less stable aggregates; **Figure 4.2A** and **Supplementary Table C.2.1**). The HMM analysis was initially performed across a range of possible interaction distances and the optimal interaction distance (according to the data) was determined by the quality of the fit. Data sets commonly converged to a 50 nm interaction distance, which agrees with expectations; therefore, a 50 nm interaction distance was used for all HMM analyses presented here.

Viterbi analysis of HMM results provides state distributions for interactions. Interaction lifetimes (**Figure 4.2B**) and diffusion coefficient by state (**Supplementary Figure C.1.4** and **Supplementary Table C.2.1**) were then able to be determined. An example of a transient interaction of QD-IgE$_p$-FcεRI is presented in **Figure 4.2C,** and its relative state distribution is included in **Figure 4.2D**. Additional examples of transient interactions for the conditions presented in **Figure 4.2A** are included in **Supplementary Figure C.1.5** and **Supplementary Figure C.1.6**.

The baseline (resting treatment; i.e. no crosslinker) off rate was approximately within the error of the fit for all conditions (i.e. QD-IgE$_{np}$, QD-IgE$_p$, and QD-IgE$_p$+PP2; **Figure 4.2A**). There was not a significant change in the off rate for QD-IgE$_p$ over a wide range of concentrations of DNP-F3 (i.e. 0.1 to 100 nM for DNP-F3; **Supplementary Figure C.1.3**). Similarly, no significant change in the off rate is observed for QD-IgE$_{np}$ with several concentrations of DNP-F3 (i.e. 1 nM and 5 nM DNP-F3; **Supplementary Figure C.1.3**). These comparisons provide several independent data sets with consistent results supporting the validity of the HMM analysis.

A trend of decreasing off rates was observed for QD-IgE$_p$ with increasing concentrations of DNP-BSA (i.e. 0.01, 0.1, and 1 µg/ml DNP-BSA; **Supplementary Figure C.1.3**). Further experimentation is necessary to determine the statistical significance and meaning of this trend. For simplification, off rates reported in **Figure 4.2A** and **Supplementary Table C.2.1** for DNP-F3 and DNP-BSA are from the HMM analysis of data sets with all concentrations pooled together.
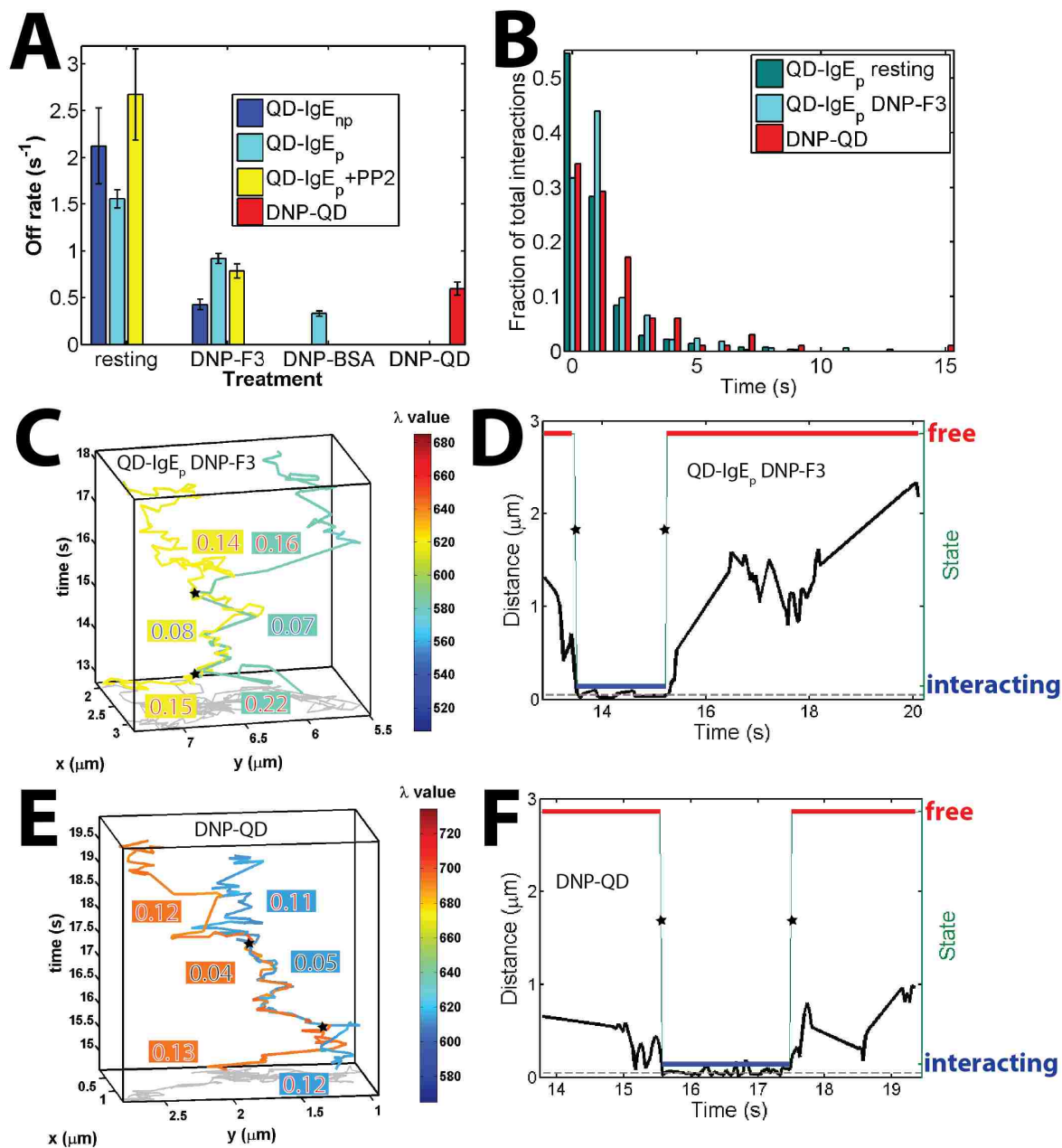
Figure 4.2 Transient interactions of QD-IgE and DNP-QD. (A) Interaction off rates estimated by HMM analysis for QD-IgE$_p$, QD-IgE$_{np}$, or DNP-QD under several treatment conditions. Off rates additional information is included in **Supplementary Table C.2.1**. (B) Distribution of interaction times determined from Viterbi analysis. (C) An example of a transient interaction observed for QD-IgE$_p$ and corresponding (D) Viterbi state distribution. (E) An example of a transient interaction observed for DNP-QD and (F) corresponding Viterbi state distribution. The color scheme for trajectories in (C) and (E) represent the estimated emission peak for the individually localized QDs. The background and foreground colors for the diffusion coefficients in (C) and (E) correspond to the trajectory color and state respectively. The 68% credible interval for values of D in (C) and (E) are included in **Supplementary Table C.2.2**. Stars in C-F highlight transitions between free and interacting states.

The off rate for resting QD-IgE$_{np}$, QD-IgE$_p$, and QD-IgE$_p$+PP2 is significantly higher than that under any of the crosslinked conditions (i.e. DNP-F3 or DNP-BSA; **Figure 4.2A; Table C.2.1**). This observation implies that interactions of QD-IgE-FcεRI are less stable without crosslinker, which is to be expected. We do note the unexpected observation of a few long-lived interactions in the resting case. Since such interactions were not observed in previous work[20,22,23], it appears that this may not be a biologically significant interaction, but an artifact of the QDs themselves. Nevertheless, there were clear differences in interactions between resting and crosslinked conditions. This was further highlighted by the shift in the distribution of interaction lifetimes for QD-IgE$_p$ resting (**Figure 4.2B** blue/green) and QD-IgE$_p$ DNP-F3 (**Figure 4.2B** light blue; i.e. longer lifetimes are observed after DNP-F3 treatment).

A higher off rate was observed for QD-IgE$_p$ when crosslinked with DNP-F3 than with DNP-BSA (**Figure 4.2A** light blue). DNP-BSA is an ill-defined multivalent crosslinker with Poisson distributed amounts of DNP attached randomly to the surface of BSA. This result suggests that the higher valency of DNP-BSA stabilizes receptor aggregation in comparison with DNP-F3.

Similarly, a higher off rate is observed for QD-IgE$_p$ (**Figure 4.2A** light blue) in comparison to QD-IgE$_{np}$ (**Figure 4.2A** dark blue). This observation suggests some stabilization of interactions for the QD-IgE$_{np}$. This observation combined with the observed change in mobility upon crosslinking with DNP-F3 (QD-IgE$_{np}$-FcεRI 0.18 to 0.11 vs QD-IgE$_p$-FcεRI 0.16 to 0.14 μm^2/s; **Supplementary Figure C.1.2** and **Supplementary Table C.2.1**) suggests that dark IgE is stabilizing the aggregates for QD-IgE$_{np}$-FcεRI. As indicated by the 'Number of acquisitions', 'Candidate pairs', and 'Observed interactions' columns in **Supplementary Table C.2.1** more data is necessary to draw firm conclusions from HMM analysis of QD-IgE$_{np}$.

A consistent decrease in D is observed for free (D$_{free}$) and interacting (D$_{interacting}$) trajectory segments for all treatment conditions with QD-IgE$_p$ (**Supplementary Figure C.1.4** and **Supplementary Table C.2.1**). The consistency in the change (approximate factor of 2; shift in cumulative probability analysis (CPA) plots in **Supplementary Figure C.1.4**) for many independent conditions suggests significance. Changes in D for interacting and free segments in specific examples (**Figure 4.2C**, **Supplementary Figure C.1.5E**) further support the significance of the shift. Note that the 68% credible interval is included in **Supplementary Table C.2.2**.

83

No significant difference in the off rate was observed when crosslinking was performed either in the presence or absence of the Src-family kinase inhibitor, PP2 (**Figure 4.2A** yellow and light blue respectively). This observation agrees with previous work in which degranulation was inhibited but no difference in the mobility of QD-IgE was observed upon treatment with PP2[20] and suggests that there is not an intracellular feedback mechanism required for stabilizing aggregation of IgE-FcεRI.

4.3.3 Stable and transient aggregates of IgE-FcεRI

Multi-color SPT of DNP-QD (i.e. QD analog of DNP-BSA; **Figure 4.1C**) was used to investigate aggregate formation and signaling independent of QD-IgE. Cells were treated with 5-colors of DNP-QD (585, 605, 625, 655, 705) at 20 pM for a final concentration of 100 pM. This corresponds to a dose for which DNP-QD remains mobile and induced degranulation[20]. Importantly, experiments were concluded within approximately 10 minutes after the addition of DNP-QD to minimize the observation of endocytosed DNP-QD.

Similar to mcSPT of QD-IgE experiments, mcSPT of DNP-QD revealed both stable and transient interactions. An example of a transient interaction is included in **Figure 4.2E** and **4.2F**. Similar off rates observed for DNP-QD (**Figure 4.2A** red) and QD-IgE$_p$ (DNP-F3 and DNP-BSA treatments; **Figure 4.2** light blue) suggests a common underlying mechanism (i.e. transient association and dissociation of IgE from DNP crosslinker; **Figure 4.2A**; **Supplementary Table C.2.1**).

The shift in the distribution of interaction lifetimes between resting QD-IgE$_p$ (**Figure 4.2B** blue/green) and DNP-QD (**Figure 4.2B** red) demonstrates a significant difference in observed lifetimes of DNP-QD interactions and control (i.e. SPT data in which biologically significant interactions are not expected).

Note that the difference between D$_{free}$ and D$_{interacting}$ for DNP-QD is similar to that of QD-IgE$_p$ (i.e. approximate 2 fold change; **Supplementary Table C.2.1**). The example shown in **Figure 4.2 E** highlights this change (credible intervals included in **Supplementary Table C.2.2**).

4.3.4 Multi-color single molecule imaging of AF-IgE

In order to better characterize the aggregate size induced by DNP-QD, mcSMI of 3-colors of AF-IgE (Alexa Fluor 488, 514, and 532) and 4-colors of DNP-QD (625, 655, 705, and 800) was performed on fixed cells (**Figure 4.3**). This experiment provides localizations of AF-IgE-FcεRI with respect to DNP-QD. This allows for the characterization of DNP-QD binding to IgE-FcεRI. Due to the high degree of spectral overlap observed in the data (**Figure 4.3A**), hyperspectral microscopy and sufficient signal to noise is essential for the spectral separation of all components. The peak observed in the spectra for all AF-IgE spectra in **Figure 4.3A** at approximately 585 nm is a Raman peak from water[24]. This is observed due to the relatively high laser power necessary to obtain signal to noise levels sufficient to spectrally separate the 3-colors of highly spectrally overlapping AF-IgE. Spectrally separated color maps for each component are shown in **Figure 4.3B**, **C**, **D**, and **E**. A merge of all 4 pseudo channels is presented in **Figure 4.3F**. Once data is spectrally separated, standard single molecule localization techniques are used to localize individual molecules with precision on the scale of 10s of nm (**Figure 4.3G**). More details about the procedure used to spectrally separate the data are included in the Materials and Methods section. To the author's knowledge, this experiment is the first demonstration of simultaneous single molecule imaging of multiple-colors of fluorescent dyes and multiple-colors of QDs. This provides a platform to simultaneously probe the distribution of several fluorescently labeled moieties at the nm scale not only in the IgE-FcεRI system but in many other systems as well. The true utility of the experiment is demonstrated in **Figure 4.3G** where a 625 and 705 DNP-QDs are shown to be clustered with at least 1 and 3 IgE respectively as indicated by the enumerations. More results from mcSMI experiments are discussed in the next section.
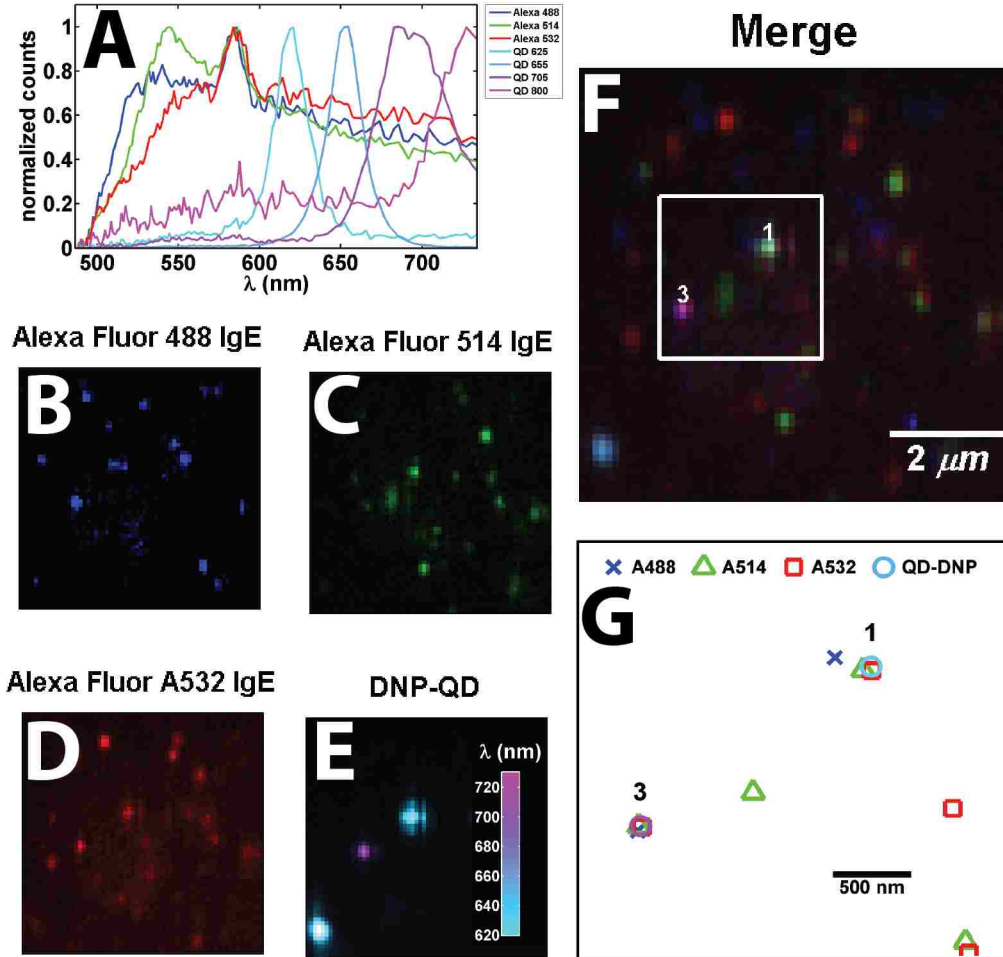
Figure 4.3 Characterization of QD-DNP valancy with mcSMI (multi-color single molecule imaging). (A) Fluorescence emission spectra of single molecules of 3-colors AF-IgE and 4-colors of DNP-QD. (B), (C), (D), and (E) show spectrally separated channels for the indicated fluorescent molecules and a merge of all channels is shown in (F). A zoom of the inset in (F) with single molecule localizations represented by symbols indicated at the top of the figure is included in (G). The numbers in (F) and (G) highlight where the indicated numbers of AF-IgE are estimated to be within 50 nm of a DNP-QD. Note that the separation distance between the triangle and square in the upper right is greater than 50 nm; therefore, it is identified as a monomer instead of a dimer. The color scheme retained throughout this figure is blue, green, and red represent Alexa Fluor 488, 514, and 532 respectively and the colorbar inset in (E) describes the color scheme for DNP-QD. The contrast in the AF-488 pseudo channel in (B) has been altered to highlight blue on a black background.

4.3.5 Distribution of IgE-FcεRI upon crosslinking

A simplistic cluster size analysis was performed on mcSPT, EM, and multi-color single molecule imaging (mcSMI) to corroborate results from HMM analysis and investigate the distribution of IgE-FcεRI upon crosslinking. Intra-method (mcSPT, EM, and mcSMI) discrepancies in the absolute percentages reported for the cluster size distributions (**Figure 4.4** and **Supplementary Figure C.1.7**) are attributed to multiple aspects of each individual type of experiment. The observation of QD-IgE in EM images requires manual identification, which is susceptible to subjectivity. Non-fluorescent QDs and QD blinking [25,26] are limiting factors in the observation of QDs for mcSPT (QD-IgE or DNP-QD) and mcSMI (DNP-QD) experiments. Sufficient signal to noise is necessary for the observation of AF-IgE. It is important to note here that many important relationships between the observations provided by these methods can be used to help understand the distributions of IgE-FcεRI and validate the techniques themselves.

In order to investigate the results of the HMM analysis, the observed changes in off rates are directly compared to changes in the cluster size distributions. Changes in cluster size distribution should have an inverse correlation with the off rate from HMM analysis. The relative change (i.e. decrease) in off rates for $QD\text{-}IgE_{np}$ and $QD\text{-}IgE_p$ for the resting and crosslinked conditions (DNP-3 and DNP-BSA; **Figure 4.2A**) agreed with the change (i.e. shift to larger clusters) in the cluster size distribution (**Figure 4.4A** and **Figure 4.4B**). This is most apparent for cluster size 2, but the same general trend is observed for larger cluster sizes. Note that clusters larger than 2 were rarely observed in mcSPT data. The change in the off rate (**Figure 4.2A**; 0.88 s^{-1} $QD\text{-}IgE_p$ light blue and 0.42 s^{-1} $QD\text{-}IgE_{np}$ dark blue) for $QD\text{-}IgE_p$ and $QD\text{-}IgE_{np}$ when crosslinked with DNP-F3 was in good agreement with the shift in the cluster size distribution (**Figure 4.4A**; 0.391% $QD\text{-}IgE_p$ blue squares and 1.286% $QD\text{-}IgE_{np}$ green diagonals). Similarly, the relative off rates (**Figure 4.2A** light blue; DNP-F3 0.88 and DNP-BSA 0.33) and cluster size distributions for DNP-F3 and DNP-BSA (**Figure 4.4B** DNP-F3 0.598% and DNP-BSA 1.234%; green and red respectively) agreed well. The relative similarities of off rates (**Figure 4.2A** 0.42 s^{-1} $QD\text{-}IgE_{np}$ DNP-F3 dark blue and 0.33 s^{-1} $QD\text{-}IOgE_{np}$ DNP-BSA light blue) for $QD\text{-}IgE_{np}$ crosslinked with DNP-F3 and $QD\text{-}IgE_p$ crosslinked with DNP-BSA agreed well with the relative similarities in the cluster size distributions (**Figure 4.4A** 1.286% $QD\text{-}IgE_{np}$ DNP-F3 green diagonals and **Figure 4.4B** 1.234% $QD\text{-}IgE_p$ DNP-BSA red). The consistency between cluster size analysis and HMM analysis of mcSPT data supports the validity of the HMM analysis.

The inverse relationship between the HMM off rate from mcSPT of QD-IgE$_p$-FcεRI on live cells (**Figure 4A** 0.88 DNP-F3 and 0.33 DNP-BSA) and the percent of IgE-FcεRI in a cluster size 2 from mcSMI of AF-IgE on fixed cells (**Figure 4C** 7.9% DNP-F3 and 15% DNP-BSA) for DNP-F3 and DNP-BSA provided correlated results from independent methods; thusly, providing additional support for the validity of the HMM analysis.

Cluster analysis for mcSPT and EM results for QD-IgE$_p$-FcεRI with the same total concentration of QD-IgE$_p$ (2nM) was compared. No qualitative change in the distribution of cluster sizes was observed in EM cluster analysis (**Supplementary Figure C.1.7A**) for crosslinking with variable concentrations of DNP-F3 (0.1, 1, and 10 nM). This is consistent with the observation of HMM off rates for the same conditions (**Supplementary Figure C.1.3A**). Due to this observation, the limited amount of EM data, and for simplification, all DNP-F3 data is pooled together in **Supplementary Figure C.1.7B**.

As discussed previously, mcSMI of AF-IgE provides a method to characterize the distribution of IgE-FcεRI upon crosslinking with all crosslinkers used in this work (i.e. DNP-F3, DNP-BSA, and DNP-QD). The distribution of cluster sizes is included in **Figure 4.4C**.

In 8 images acquired with mcSMI, 31 DNP-QD were observed and 13 (42%) of which were observed within 50 nm of at least 1 AF-IgE. The distribution of cluster sizes of AF-IgE observed within 50 nm of a DNP-QD was 7 (23%), 5 (16%), and 1 (3%) for cluster sizes of 1, 2, and 3 respectively. This is a limited amount of data and therefore only minimal conclusions can be drawn about the interaction between DNP-QD and IgE-FcεRI. That withstanding, there were a total of 2 clusters of size 3 observed for all mcSMI experiments with AF-IgE and DNP-QD (**Figure4.4**; cyan), 1 of which is located within 50 nm of a DNP-QD. This is highly unlikely to occur by random chance alone, and therefore implies that DNP-QD is able to form aggregates of at least 3 IgE-FcεRI. These results suggest that a more in-depth study of the distribution of AF-IgE with DNP-QD using mcSMI should provide significant insights into the valency of DNP-QD.

The distribution of IgE-FcεRI under several crosslinking conditions was compared for EM, mcSPT, and mcSMI experiments. The ratio between the percent in cluster size 2 for DNP-F3 treatment (green) and resting (blue) is strikingly similar for EM QD-IgEp (**Supplementary Figure C.1.7** 16% / 13% = 1.23) and mcSMI AF-IgE (**Figure 4.4C** 7.9% / 6.9% = 1.14). The ratio between the percent in cluster size 2 for DNP-BSA (red) and DNP-F3 (green) treatments for mcSMI (16% /

7.9% = 2.03; **Figure 4.4C**) and mcSPT (1.234% / 0.598% = 2.06; **Figure 4.4B**) demonstrate a similar pattern. The interpretation of these observations is limited due to the small sample size for the EM and mcSMI data, but the trends with independent methods lend credence to the mcSMI technique.

It is prudent to reemphasize that mcSMI uses AF-IgE instead of QD-IgE to observe IgE-FcεRI; therefore, a comparison of mcSMI and mcSPT provides direct insights into the QDs impact on the distribution of IgE-FcεRI. Given this, the relatively large disparity of the ratio between cluster size 3 and 2 with DNP-BSA (red) for mcSPT (0.005% / 1.234% = 0.004; **Figure 4.4B**) and mcSMI (15% / 4.8% = 3.1; Figure **4.4C**) supports the hypothesis that the sizes of QDs impose steric constraints on the valency of IgE. Performing the same comparison between cluster size 3 and 2 for DNP-F3 (green) for mcSPT (0.005% / 0.598% = 0.083; **Figure 4.4B**) and mcSMI (0.83% / 7.9% = 0.11; Figure **4.4C**) further corroborates this hypothesis.

The distribution of clusters size 2 for DNP-QD is observed to be in between that of DNP-F3 and DNP-BSA (**Figure 4.4C**; red). This observation agrees well with **Figure 4.1A** in which the off rate for DNP-QD is between the off rate for DNP-F3 and DNP-BSA. This supports the hypothesis that the valency of DNP-QD is between that of DNP-F3 and DNP-BSA.
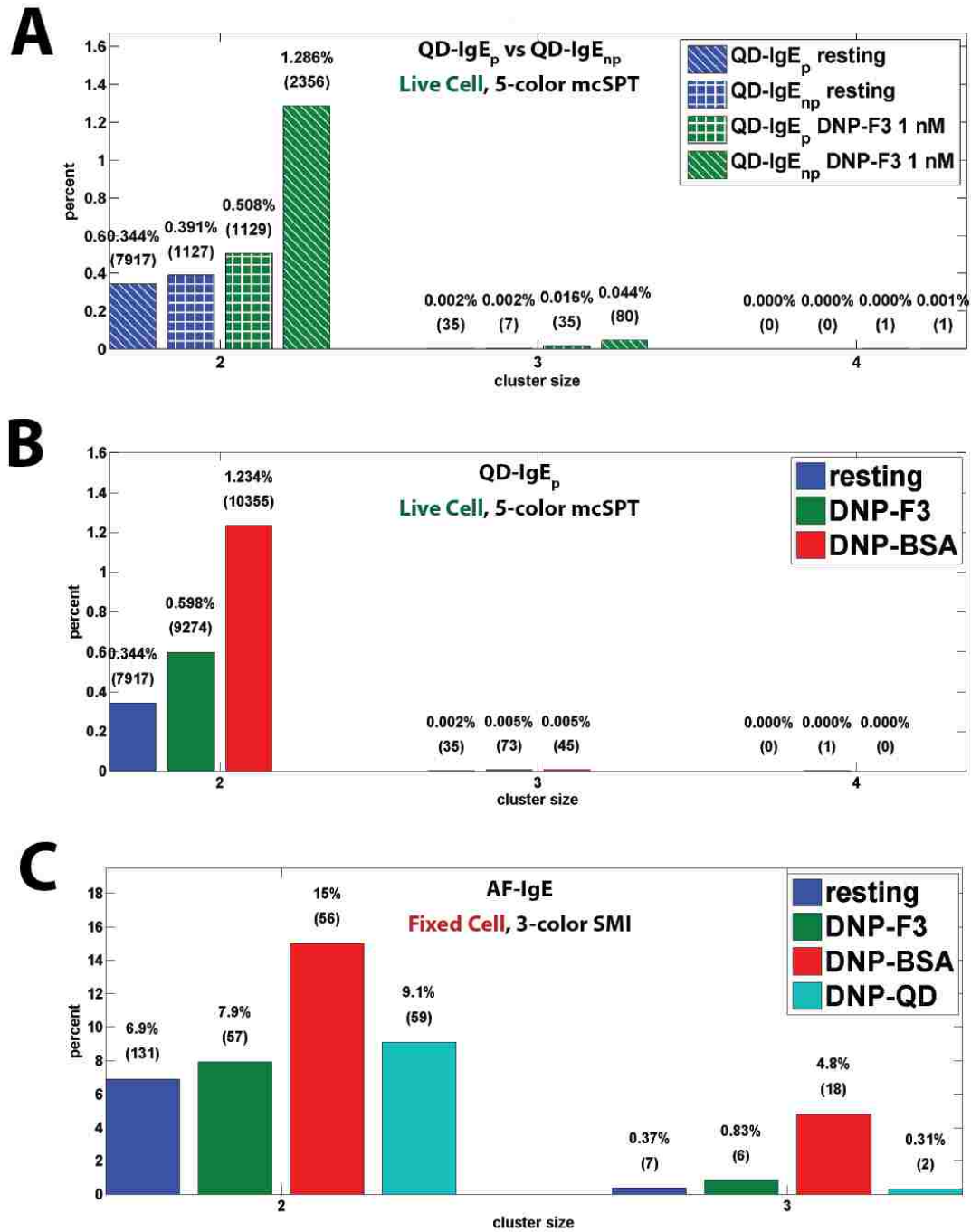
Figure 4.4 Distribution of QD-IgE-FcεRI with crosslinker compared with mcSMI. (A), (B), and (C) show distributions of clusters observed for IgE-FcεRI in mcSPT, AF-IgE and EM experiments respectively.   The DNP-F3 and DNP-BSA conditions contain acquisitions with several different concentrations of crosslinker. The percent and number of observations (parentheses) are shown above each bar.

4.3.6 Direct Observation of the signaling competency of mobile crosslinker
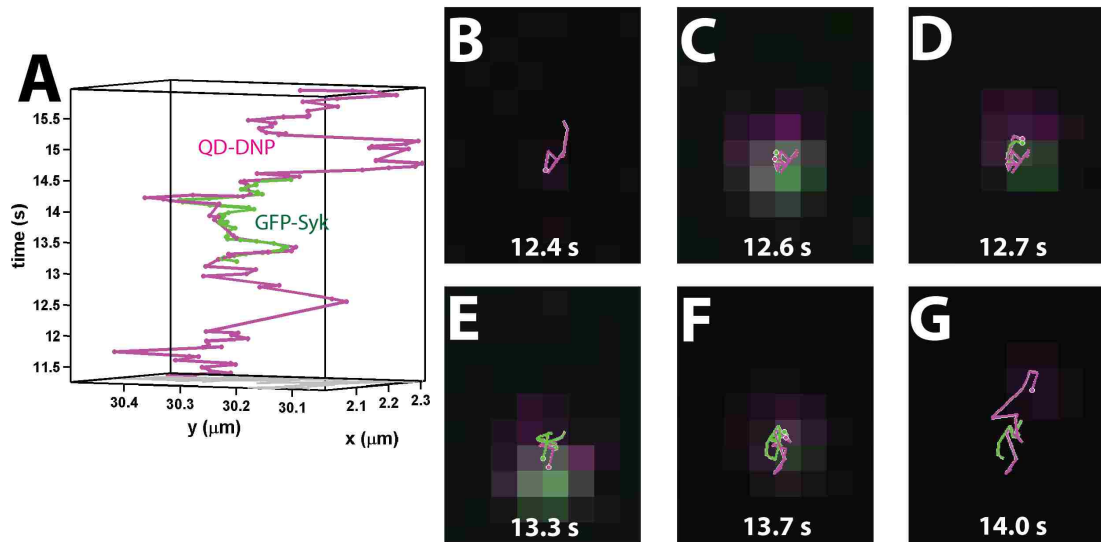
www.manaraa.com

Figure 4.5. Signaling competency of mobile DNP-QD. TIRF microscopy of DNP-QD on RBL-2H3 cells transfected with GFP-Syk. (A) single particle trajectories for DNP-QD and GFP-Syk. (B-G) Select frames and color overlay for DNP-QD and GFP-Syk. For a size reference in (B-F) the pixel size in the image is ~107 nm.

DNP-QD was observed to form transient interactions in **Figure 4.1** and demonstrated the capacity to form aggregates of at least 3 IgE-FcεRI in **Figure 4.3**. The simultaneous observation of DNP-QD and GFP-Syk was then used to directly interrogate signaling competency of aggregates of IgE-FcεRI formed by DNP-QD. In this experiment, TIRF microscopy was used to perform simultaneous SPT on DNP-QD and GFP-Syk. The use of TIRF microscopy here helps to decrease the background of cytoplasmic GFP-Syk and allows for the observation of binding events for GFP-Syk at the membrane. Many binding events of GFP-Syk were observed at the membrane. This included the common observation of repetitive GFP-Syk binding events at the location of an immobile DNP-QD (data not shown). This is indicative of an actively signaling complex of DNP-QD and IgE-FcεRI. Additionally, there were observations of correlated motion between a mobile DNP-QD and GFP-Syk. An example of this is shown in **Figure 4.5**. This is a direct observation of the signaling competency of a mobile DNP-QD bound to IgE-FcεRI providing direct evidence supporting the hypothesis that mobile aggregates are signaling competent.

4.4 Discussion

Multi-color SPT experiments were used to investigate the interactions of IgE-FcεRI under resting and crosslinked conditions. Due to previous observations by Andrews et al.[20], long-lived interactions were expected in mcSPT experiments with QD-IgE. Interestingly, transient interactions were also commonly observed in the current study (**Figure 4.2 C-f**, **Supplementary Figure C.1.5**, and **Supplementary Figure C.1.6**). The time scale (several seconds; **Figure 4.2 B**) of these transient interactions would prevent their observation in previous hyperspectral experiments due to the acquisition rate of approximately 1 frame every 4 seconds. Additionally, very few stable aggregates larger than dimers were observed when tracking QD-IgE$_p$-FcεRI in the presence of crosslinker. The previous hyperspectral experiments by Andrews et al. suggested that stable higher-ordered aggregates should be observed.

There are a few notable differences in the experimental setups used here and in the previous hyperspectral imaging of QD-IgE that might help to explain this difference: (1) previous work was performed at room temperature whereas work presented here is performed at 34-36 °C; (2) the inverted microscope setup and acquisition interface used in the current work allowed for imaging immediately after the addition of crosslinker whereas the upright microscope setup and acquisition interface in the previous work was not optimal for live cell experiments; (3) the presence of dark IgE may stabilize the formation of larger aggregates.

Differences in the mobility (**Supplementary Figure C.1.2**), HMM off rates (**Figure 4.2A**, **Supplementary Table C.2.1**), and cluster size analysis of mcSPT data (**Figure 4.4A**) for QD-IgE$_p$ and QD-IgE$_{np}$ suggest that dark IgE has a stabilizing effect. The affect of dark IgE on mobility and aggregate stability of QD-IgE are directly testable by performing mcSPT experiments with QD-IgE$_p$ supplemented with variable concentrations of dark IgE.

There are two ways in which the presence of dark IgE could stabilize the formation of larger aggregates: (1) the presence of dark IgE may simply increase the cellular density of IgE-FcεRI; (2) steric issues due to the size of the QDs may reduce the capacity of IgE to act as a bivalent receptor and the presence of dark IgE provides bivalent receptors which allow for the formation of larger aggregates. These hypotheses are directly testable by performing mcSPT experiments with QD-IgE$_p$ supplemented with variable concentrations of dark IgE.

The observation of transient aggregates and the correlation between changes in stability from mcSPT experiments and changes in observed distributions of cluster sizes in mcSMI experiments are in agreement with previous experimental and modeling results. Xu et al. used ensemble fluorescence quenching experiments to investigate the binding kinetics of DNP-BSA[27]. Modeling of these experiments revealed a complex binding model for DNP-BSA with an off rate of approximately 0.01 s^{-1}. The discrepancy in the off rate reported by Xu et al. (0.01) and the off rate reported here from HMM analysis of mcSPT (0.33 s^{-1}) is attributed to the difference in the temperature at which the experiments were performed (15 °C and 37 °C respectively). Monine et al. predicted that steric effects are important for limiting the size of IgE-FcεRI aggregates and for the formation of transient receptor aggregates[28]. In that work, a flow cytometry binding assay of a fluorescent trivalent ligand to FcεRI-IgE on RBL-2H3 cells was used as the basis for a mathematical model investigating geometries of a trivalent ligand binding to a bivalent cell-surface receptor. This relates directly to the experiments here that used DNP-F3 for crosslinking since DNP-F3 is a well-defined trivalent ligand with all three DNP simultaneous available for receptor binding (Mahajan et. al., manuscript in preparation).

Several works in the literature allude to the biological significance of transient interactions for membrane bound receptors. Work by Collins et al.[29] observed activation for high valency crosslinker with low antigen affinity IgE suggesting that transient aggregates are signaling competent. The signaling competency of transient aggregates may be the mechanism for signal initiation in experiments in which signaling is observed for mast cells in contact with a mobile lipid bilayer containing monovalent ligand[14]. Similarly, the signaling competency of transient aggregates would provide a basis for signal initiation in the pSMAC of the immunological synapse in T-cells[11].

The valency of DNP-QD is approximated to range between 10 and 20[20], however, as with DNP-BSA, the presentation of available DNP to IgE-FcεRI is ill-defined. The off rate for DNP-QD (0.59 s^{-1}) was between that of DNP-F3 (0.88 s^{-1}) and DNP-BSA (0.33 s^{-1}) suggesting an intermediate valency of DNP-QD between that of DNP-F3 (3) and DNP-BSA (approximately 18).

The HMM analysis of mcSPT experiments also provides general insights into the question of mobility membrane bound receptor mobility. The most commonly cited theory behind the mobility of membrane bound proteins due to thermodynamics is based on work by Saffman and Delbrück in the 1970's [30]. The Saffman-Delbrück model predicts a weak

93

dependence of mobility on the radius of the transmembrane domain of a protein. More recently several works have put forth theoretical frameworks to account for disagreements between the Saffman-Delbrük model and experimental results. Naji et al.[31] propose that local deformations in the membrane due to height mismatch between the transmembrane domains and the lipid bilayer is a key contributor to receptor mobility and can cause a dependence of mobility on $1/a$ (where a is protein radius). This theory supports experiments in which transmembrane protein mobility was determined in bilayers with variable thickness [32]. The $1/a$ dependence on mobility is consistent with experimental and simulation work by Knight et al. [33]. In this work, the mobility of engineered proteins with variable numbers (1 to 3) of pleckstrin homology (pH) domains was observed to be proportional to the number of pH domains. Note that pH domains bind to phosphatidylinositol-(3,4,5)-trisphosphate (PIP_3) lipids. Mobility changes in this work were attributed to additive contributions of friction. The agreement between D_{free} and $D_{interacting}$ for QD-IgEp DNP-F3 with and without PP2 (**Supplementary Table C.2.1**) suggests that changes the mobility are due to receptor aggregation and independent of signal initiation. This provides a support for investigating the relationship between aggregate size and mobility using results from HMM analysis of mcSPT experiments. An approximate factor of 2 difference in the mobility of receptors is observed between free and interacting trajectory segments (**Figure 4.2**, **Supplementary Table C.1.1**, and **Supplementary Figure C.1.4**). This pattern is exemplified by the example shown in **Figure 4.2C**. These observations support the theory of a *$1/a$* dependence of membrane-receptor mobility.

4.5 Conclusions

The use of several methods (i.e. HMM of mcSPT and cluster analysis of mcSPT, EM, and mcSMI) in this work to investigate the same underlying phenomenon (i.e. distribution and mobility of IgE-FcεRI upon crosslinking) provides corroborative and complementary information. The independent observation of stable and transient aggregates with QD-IgE and DNP-QD under signaling competent conditions suggests that these interactions are biologically relevant to signal initiation. The stability of aggregates was quantified using an HMM analysis to determine off rates which provided significant detail into how crosslinker valency relates to off rates. Comparisons between off rates from mcSPT experiments and cluster size analysis performed on mcSPT, EM, and mcSMI data provided further corroborating evidence for transient aggregates.

The characterization of DNP-QD crosslinker using mcSMI revealed that DNP-QD is capable of forming aggregates of at least 3 IgE-FcεRI. This result in combination with the observation of correlated motion of GFP-Syk with DNP-QD provides direct evidence of that small mobile aggregates of FcεRI are signaling competent. The observation of transient aggregates further extends this hypothesis to the signaling competency of small mobile transient aggregates of IgE-FcεRI.

4.6 Materials and methods

4.6.1 Reagents

Purification of anti-DNP IgE was previously reported[34]. Multivalent DNP-BSA was purchased from Invitrogen (A23018). It is noteworthy that the distribution of DNPs on BSA in DNP-BSA is batch dependent and for the specific lot (913924) used in all experiments presented in this work the mean DNP:BSA ratio as determined by the manufacturer is approximately 18. DNP conjugated to a fibritin trimer (DNP-F3) was synthesized by AnaSpec (Fremont,CA).

4.6.2 Preparation of QD labeled probes for SPT

QD-IgE was formulated as previously described[35]. Briefly, IgE was incubated with a four times excess of Biotin-XX,SE (Invitrogen;B6352) for 15 minutes. A PD Spin Trap G-25 (GE) was used to remove any free biotin and quench the reaction. This typically provided a biotin:IgE ratio between 0.5 and 1 as estimated using the FluoReporter® Biotin Quantitation Assay Kit (Invitrogen). At this point the the IgE is either directly linked to streptavidin QDs (Invitrogen) by mixing at a 1:1 ratio to generate QD-IgE. This reagent contains non-biotynilated IgE and is referred to as "non-purified" (QD-IgE$_{np}$). In experiments where removal of non-biotin IgE was required, a purification step was performed. Biotinylated IgE was purified from non-biotinylated IgE using Promega SoftLink™ Avidin Resin. Due to small volumes (approximately 600 ul) and low concentrations of biotinylated IgE, the process was performed in a batch operation. The avidin resin was reconstituted according to manufacturer's specifications. The biotinylated IgE was incubated overnight on a rotor at 4 °C with the avidin resin. The resin was washed thoroughly with PBS to remove any non-biotinylated IgE. The resin was then incubated with 5 mM D-biotin (Invitrogen) for approximately 8 hours. Washing with PBS was used to collect biotinylated IgE. The collected eluent was then dialyzed against PBS for at least 2 hours with 2 or 3 buffer exchanges. The dialyzed product is referred to as purified IgE (IgE$_p$). The biotin to IgE ratio was

then typically determined to be slightly larger than 1 which is as expected for eliminating all non-biotinylated IgE from the originally Poisson distributed of biotin:IgE between 0.5 and 1. From this step, QD-IgE$_p$ was generated in the same manner as QD-IgE$_{np}$. QD-DNP was prepared as previously described[20].

4.6.3 Cell culture

RBL-2H3 cells were cultured and passaged using MEM (Gibco® 11095-080) supplemented with penicillin-streptomycin, L-glutamine, and 10% FBS[20,36]. For all image acquisitions, RBL-2H3 cells were plated at approximate 20,000 cells per well in Lab-Tek 8-well chambers (Thermo Scientific, 177402) 1-3 days prior to imaging.

4.6.4 Single particle tracking

Multi-color SPT experiment were performed on a custom built hyperspectral line scanning microscope and tracking of hyperspectral data was performed as previously described[21]. Data was acquired at a frame rate of approximately 27 fps for all mcSPT experiments. TIRF microscopy was performed on an epi-fluorescence microscope setup with an inverted microscope base (IX71, Olympus America Inc.), 1.45 NA TIRF objective (U-APO 150x NA 1.45, Olympus America Inc.), a 488 nm diode laser (Newport Cyan488, 100mW), and an EMCCD camera (Andor Ixon 897). The emission path was separated on the EMCCD using a custom built channel splitter with a 575 dichroic, 525/30 emission filter for the GFP channel, and a 600/37 band pass for the QD channel. Localizations for 2-color SPT were performed as previously described[37] and trajectories were built using a likelihood based cost matrix approach (manuscript in preparation Relich, Cutler, Huang, Lidke). Data was acquired at a frame rate of approximately 30 fps for all 2-color SPT experiments.

4.6.4.1 QD-IgE

Cellular media was exchanged with imaging buffer (Hanks). Cells were primed with 200 µl of 400 pM of each color (5-colors; 565, 585, 605, 625, 655) of QD-IgE (2nM total QD-IgE) in Hanks for 15 minutes at 37 °C. Unbound QD-IgE was removed using multiple washes with Hanks (4x). Cells were imaged within 1 hour of priming and within 10 minutes after the addition of crosslinker.

4.6.4.2 DNP-QD

Cellular media was exchanged with imaging buffer (Hanks). Cells were primed with 200 µl of either 300 pM or 7 nM of IgE in Hanks for 15 minutes at 37 °C. Unbound IgE was removed

using multiple washes with Hanks (4x). A volume of 100 μL DNP-QD 60 nM of each color (5 colors; 585, 605, 625, 655, 705) of DNP-QD was added to 200 μl of Hanks in a single well. This gives a final concentration of 20 nM per color of DNP-QD and 100 nM total. Each well was imaged within 10 minutes after the addition of DNP-QD.

4.6.4.3 DNP-QD and GFP-Syk

RBL-2H3 cells stably transfected with GFP-Syk were used in place of wt RBL-2H3 cells. Fusion PCR was used to construct the Syk-eGFP plasmid (pcDNA3.1) from a Turbo-GFP plasmid purchased from Origene (Rockville, MD). For SPT, cellular media was exchanged with imaging buffer (Hanks). Cells were primed with either 7 nM or 300 pM of IgE for 15 minutes at 37 °C. Unbound IgE was removed using multiple washes with Hanks (4x). Just prior the acquisitions with DNP-QD 100 μl of 300 pM DNP-QD (655) was added to 200 μl of Hanks in a single well. This gives a final concentration of 100 pM.

4.6.5 Hidden Markov model

The 2-state HMM is a modification of a previously published 3-state HMM analysis[22] of SPT data. Pair-wise comparisons of trajectories for spectrally distinct QDs were used in the 2-state HMM analysis to determine a characteristic off-rate for all interactions. The Viterbi algorithm used the results from the 2-state HMM analysis to provide a state sequence (free or interacting) for pairs of trajectories. A Bayesian based diffusion estimator (manuscript in preparation Cutler, Relich, Lidke) was used to estimate the diffusion coefficient for free and interacting trajectory segments. The median diffusion coefficient is reported.

4.6.6 Electron microscopy of QD-IgE

RBL-2H3 cells were plated on 18 mm coverslips approximately 1-2 days prior to the experiment. Cellular media was exchanged with Hanks. Cells were primed with 2 nM of QD-IgE (705) for 15 minutes at 37 °C. Unbound QD-IgE was removed using multiple washes with Hanks (4x). Cells were incubated with indicated amounts of crosslinker for 5 minutes before fixation with 4% PFA for 15 minutes. Membrane sheets were prepared as previously described[36].

4.6.7 Cluster size estimation

This is described as a cluster size analysis instead of an aggregate size analysis, because in a static image the aggregate size cannot be determined without additional information. In this work an aggregate is defined as two receptors interacting through some physical interface (i.e. crosslinker). Distributions of IgE-FcεRI are interrogated by a simple measure of distance. IgE localized to within 50 nm of one another are considered to be in a cluster[38]. This allows for

the direct comparison of multi-color QD-IgE on live RBL cells with AF-IgE labeling and EM of QD-IgE on fixed RBL cells. For live cell data (multi-color QD-IgE), individual time frames were analyzed independently and identically to fixed cell data.

4.6.8 Hyperspectral single molecule imaging

Cellular media was exchanged with imaging buffer (Hanks). Cells were primed with 200 µl of 100 pM of each color of AF-IgE (3 colors; 488, 514, 532) at 37 °C for 15 minutes. Unbound AF-IgE was removed using multiple washes with Hanks (4x). Cells were then treated with indicated amounts of crosslinker for 5 minutes prior to fixation with 4% PFA for 30 minutes. Fixed samples were either imaged in PBS or oxygen scavenging buffer (Gloxy + 1 mM Trolox) and covered in paraffin oil. For experiments with DNP-QD cells were treated with 5 pM of each color of DNP-QD (4 colors; 625, 655, 705, 800).

Data was acquired on a custom built hyperspectral line-scanning microscope with 488 nm excitation laser[21]. In order to improve the signal to noise, data was acquired with 50 ms exposure time per line position. This provided a frame rate of 0.16 fps (1 frame every 6.4 seconds) for 128 line positions. 20 time frames were acquired for each acquisition.

Spectral unmixing of hyperspectral images was performed using a simple classical least squares method. Spectral data acquired from samples with individual probes (i.e. Alexa Fluor 488, 514, or 532) were used as pure component spectra for each component. For samples containing DNP-QD the data was divided into 2 channels prior to spectral unmixing (i.e. 500 – 600 nm for AF-IgE and 600 – 730 nm for QDs). The QD channel was localized in the same manner as in mcSPT[21]. Concentration maps for each component were obtained by performing constrained[39] non-negative least squares[40] with pure component spectra for each AF-IgE probe and a constant off set term to account for background and offset. Non-negativity constraints were applied to the concentrations of all components except for the offset term. Once concentration profiles were obtained for each component they were summed over time. Single molecules were then localized using standard single molecule localization software[37].

4.7 References

(1)   Sigalov, A. B. *Trends Immunol* **2004**, *25*, 583–9 ST – Multichain immune recognition receptor.

(2) Fewtrell, C.; Metzger, H. *J. Immunol.* **1980**, *125*, 701–710.

(3) Bachmann, M. F.; Ohashi, P. S. *Immunol. Today* **1999**, *5699*, 568–576.

(4) Heldin, C. H. *Cell* **1995**, *80*, 213–23.

(5) Iwashima, M.; Irving, B.; van Oers, N.; Chan, A.; Weiss, A. *Science (80-.).* **1994**, *263*, 1136–1139.

(6) Hernandez-Hansen, V.; Smith, A. J.; Surviladze, Z.; Chigaev, A.; Mazel, T.; Kalesnikoff, J.; Lowell, C. A.; Krystal, G.; Sklar, L. A.; Wilson, B. S.; Oliver, J. M. *J. Immunol.* **2004**, *173*, 100–12.

(7) Sada, K.; Zhang, J.; Siraganian, R. P. *Blood* **2001**, *97*, 1352–1359.

(8) Harwood, N. E.; Batista, F. D. *Annu. Rev. Immunol.* **2010**, *28*, 185–210.

(9) Dustin, M. L. *Immunol. Rev.* **2008**, *221*, 77–89.

(10) Carroll-Portillo, A. *Front. Immunol.* **2012**, *3*, 1–9.

(11) Campi, G.; Varma, R.; Dustin, M. L. *J. Exp. Med.* **2005**, *202*, 1031–6.

(12) Kaizuka, Y.; Douglass, A. D.; Varma, R.; Dustin, M. L.; Vale, R. D. *Proc. Natl. Acad. Sci. U. S. A.* **2007**, *104*, 20296–301.

(13) DeMond, A. L.; Mossman, K. D.; Starr, T.; Dustin, M. L.; Groves, J. T. *Biophys. J.* **2008**, *94*, 3286–92.

(14) Carroll-Portillo, A.; Spendier, K.; Pfeiffer, J.; Griffiths, G.; Li, H.; Lidke, K. a; Oliver, J. M.; Lidke, D. S.; Thomas, J. L.; Wilson, B. S.; Timlin, J. a *J. Immunol.* **2010**, *184*, 1328–1338 ST – Formation of a Mast Cell Synapse: .

(15) Mao, S. Y.; Varin-Blank, N.; Edidin, M.; Metzger, H.; Cells, T.; Ma, S. *J Immunol* **1991**, *146*, 958–66.

(16) Menon, A. K.; Holowka, D.; Webb, W. W.; Baird, B. C.-P. A. *J Cell Biol* **1986**, *102*, 541–50.

(17) Pyenta, P. S.; Schwille, P.; Webb, W. W.; Holowka, D.; Baird, B. A. *J. Phys. Chem. A* **2003**, *107*, 8310–8318 ST – Lateral Diffusion of Membrane Lipi.

(18) Myers, J. N.; Holowka, D.; Baird, B. A. *Biochemistry* **1992**, *31*, 567–75 ST – Rotational motion of monomeric and di.

(19) Pecht, I.; Ortega, E.; Jovin, T. M. *Biochemisty* **1991**, *30*, 3450–3458.

(20) Andrews, N. L.; Pfeiffer, J. R.; Martinez, a M.; Haaland, D. M.; Davis, R. W.; Kawakami, T.; Oliver, J. M.; Wilson, B. S.; Lidke, D. S. *Immunity* **2009**, *31*, 469–479.

(21) Cutler, P. J.; Malik, M. D.; Liu, S.; Byars, J. M.; Lidke, D. S.; Lidke, K. A. *PLoS One* **2013**, *8*, 14.

(22) Low-Nam, S. T.; Lidke, K. A.; Cutler, P. J.; Roover, R. C.; van Bergen en Henegouwen, P. M. P.; Wilson, B. S.; Lidke, D. S. *Nat. Struct. Mol. Biol.* **2011**, *advance on*.

(23) Lidke, D. S.; Lidke, K. A.; Rieger, B.; Jovin, T. M.; Arndt-Jovin, D. J. *J. Cell Biol.* **2005**, *170*, 619–26.

(24) Cowles, T. J.; Moum, J. N.; Desiderio, R. A.; Angel, S. M. *Appl. Opt.* **1989**, *28*, 595–600.

(25) Yao, J.; Larson, D. R.; Vishwasrao, H. D.; Zipfel, W. R.; Webb, W. W. *Proc. Natl. Acad. Sci. U. S. A.* **2005**, *102*, 14284–9.

(26) Lee, S. F.; Osborne, M. a *Chemphyschem* **2009**, *10*, 2174–91.

(27) Xu, K.; Goldstein, B.; Holowka, D.; Baird, B. *J. Immunol.* **1998**, *160*, 3225–35.

(28) Monine, M. I.; Posner, R. G.; Savage, P. B.; Faeder, J. R.; Hlavacek, W. S. *Biophys. J.* **2010**, *98*, 48–56.

(29) Collins, A. M.; Basil, M.; Nguyen, K.; Thelian, D. *Clin Exp Allergy* **1996**, *26*, 964–70.

(30) Saffman, P. G.; Delbrück, M. *Proc. Natl. Acad. Sci.* **1975**, *72*, 3111–3113.

(31) Naji, A.; Levine, A. J.; Pincus, P. A. *Biophys. J.* **2007**, *93*, L49–51.

(32) Gambin, Y.; Lopez-Esparza, R.; Reffay, M.; Sierecki, E.; Gov, N. S.; Genest, M.; Hodges, R. S.; Urbach, W. *Proc. Natl. Acad. Sci. U. S. A.* **2006**, *103*, 2098–102.

(33) Knight, J. D.; Lerner, M. G.; Marcano-Velázquez, J. G.; Pastor, R. W.; Falke, J. J. *Biophys. J.* **2010**, *99*, 2879–87.

(34) Liu, F. T.; Bohn, J. W.; Ferry, E. L.; Yamamoto, H.; Molinaro, C. a; Sherman, L. a; Klinman, N. R.; Katz, D. H. *J. Immunol.* **1980**, *124*, 2728–37.

(35) Andrews, N. L.; Lidke, K. a; Pfeiffer, J. R.; Burns, A. R.; Wilson, B. S.; Oliver, J. M.; Lidke, D. S. *Nat. Cell Biol.* **2008**, *10*, 955–963.

(36) Wilson, B. S.; Pfeiffer, J. R.; Oliver, J. M. *J. Cell Biol.* **2000**, *149*, 1131–1142 ST – Observing FcεRI Signaling from the.

(37) Smith, C. S.; Joseph, N.; Rieger, B.; Lidke, K. a *Nat. Methods* **2010**, *7*, 373–5.

(38)   Zhang, J.; Leiderman, K.; Pfeiffer, J. R.; Wilson, B. S.; Oliver, J. M.; Steinberg, S. L. *Micron* **2006**, *37*, 14–34.

(39)   Van Benthem, M. H.; Keenan, M. R.; Haaland, D. M. *J. Chemom.* **2002**, *16*, 613–622.

(40)   Van Benthem, M. H.; Keenan, M. R. *J. Chemom.* **2004**, *18*, 441–450.

CHAPTER 5: CONCLUSIONS

5.1 Summary

The studies presented in this dissertation develop and apply tools necessary for advancing our understanding of membrane-protein dynamics. More specifically, tools applicable to SPT studies were developed to help better interpret membrane-protein mobility and dynamic interactions of multiple receptors. These tools were then applied to the study of dynamic interactions of IgE-FcεRI to provide a better understanding of the signal initiation process (**Chapter 4**).

SPT is a technique vital to the study of protein dynamics and even though its first applications were presented over 30 years ago[1] it is still a highly technical field yet to reached maturity. To that point, there is a great need for software for both performing SPT on raw data and interpreting biologically relevant information from single particle trajectories. **Chapters 2 and 3** of this dissertation present new tools for experimentation and interpretation of SPT data. Building the foundation for these tools is a major undertaking and an aspect of this project which has not been thoroughly discussed in this dissertation. The core of this undertaking was developing a class structure in Matlab® for performing and analyzing SPT data. A user manual for this SPT class and associated tools is included in **Appendix D**.

The technical ability to observe up to 8 spectrally distinct species of QD labeled probes at 30 fps is another major contribution of this work to investigate dynamics. The development of the UNM HSM presented in **Chapter 3** is vital for mcSPT another major contribution of this work. The UNM HSM provides a platform for the simultaneous investigation of the dynamics of multiple proteins, and as with any instrument there are many technical aspects of both hardware and software that are important for the proper operation and data interpretation. Many technical aspects of the UNM HSM are discussed **Chapter 3**, but many of the specific details for proper data acquisition etc. are omitted. A user manual for the HSM is included in **Appendix E**.

5.2 Current State of the Field

The push between technology and biological research spawns innovation and discovery. **Figure 5.1** demonstrates this relationship for several fields that relate to the work presented in this dissertation. Due to the tight binding of IgE with FcεRI[2], IgE-FcεRI has been used as a model system for the study of membrane bound proteins since the original isolation of IgE in 1966[3]. This is exemplified by the a fluorescence recovery after photobleaching (FRAP) study on the mobility of IgE-FcεRI soon after its discovery in 1976[4]. The following year in 1977 a study using stable oligomers demonstrated that dimers are the minimal signaling subunit for IgE-FcεRI. This was further corroborated by the observation of the association of small clusters with robust degranulation in electron microscopy experiments in 1991.

The general understanding of membrane-protein dynamics has developed significantly since the fluid mosaic model was proposed in 1972[5]. This model presented the cellular membrane as a sea of lipids containing a mixture (mosaic) of protein complexes. Shortly after this in 1975, Saffman and Delbrück proposed a model for Brownian motion in biological membranes[6]. This model is simplistic in relation to the complexity that has been discovered for the cellular membrane. This is highlighted in the first SPT experiment by Barak and Webb in 1982[1]. In this study at least 2 orders of magnitude difference in the mobility of fluorescently labeled protein was observed on the surface of membrane blebs and human fibroblasts. During this same time, there were many studies on the mobility of IgE-FcεRI using FRAP[7,8] and fluorescence/phosphorescence anisotropy [9–12]. One of the key findings at this time was that IgE-FcεRI mobility decreases with receptor crosslinking. This lead to the general acceptance in the field that immobilization preceded signaling.

Even though the MSD was used to quantify mobility in the early work by Barak and Webb, the formalism was not thoroughly described until the seminal paper in 1991 by Qian et al.[13]. This work presented formalisms for the MSD for Brownian and directed motion. With advancements in probe and camera technology, several platforms for SPT began to develop including SPT of colloidal gold particles (1993)[14] and QDs (1998)[15]. Initial SPT experiments with colloidal gold particles provided insights into the complexities of the cellular membrane by implicating actin in the confinement of membrane proteins, offering one possible explanation for the discrepancy between the Saffman-Delbrück model and observations by Barak and Webb.
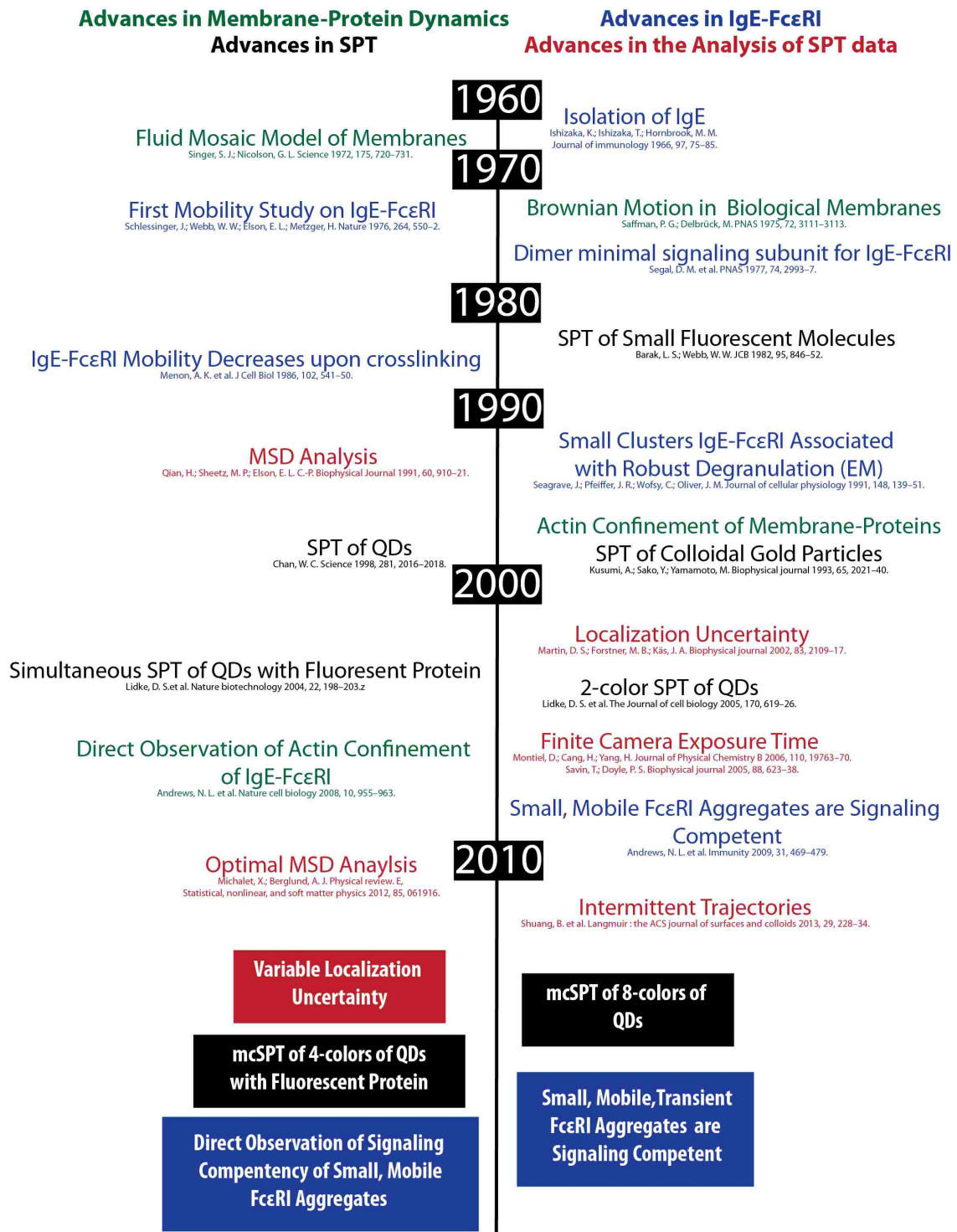
Advances in Membrane-Protein Dynamics
Advances in SPT

Advances in IgE-FcεRI
Advances in the Analysis of SPT data

1960

Isolation of IgE
Ishizaka, K.; Ishizaka, T.; Hornbrook, M. M.
Journal of immunology 1966, 97, 75–85.

Fluid Mosaic Model of Membranes
Singer, S. J.; Nicolson, G. L. Science 1972, 175, 720–731.

1970

First Mobility Study on IgE-FcεRI
Schlessinger, J.; Webb, W. W.; Elson, E. L.; Metzger, H. Nature 1976, 264, 550–2.

Brownian Motion in Biological Membranes
Saffman, P. G.; Delbrück, M. PNAS 1975, 72, 3111–3113.

Dimer minimal signaling subunit for IgE-FcεRI
Segal, D. M. et al. PNAS 1977, 74, 2993–7.

1980

IgE-FcεRI Mobility Decreases upon crosslinking
Menon, A. K. et al. J Cell Biol 1986, 102, 541–50.

SPT of Small Fluorescent Molecules
Barak, L. S.; Webb, W. W. JCB 1982, 95, 846–52.

1990

MSD Analysis
Qian, H.; Sheetz, M. P.; Elson, E. L. C.-P. Biophysical Journal 1991, 60, 910–21.

Small Clusters IgE-FcεRI Associated
with Robust Degranulation (EM)
Seagrave, J.; Pfeiffer, J. R.; Wofsy, C.; Oliver, J. M. Journal of cellular physiology 1991, 148, 139–51.

Actin Confinement of Membrane-Proteins
SPT of Colloidal Gold Particles
Kusumi, A.; Sako, Y.; Yamamoto, M. Biophysical journal 1993, 65, 2021–40.

SPT of QDs
Chan, W. C. Science 1998, 281, 2016–2018.

2000

Localization Uncertainty
Martin, D. S.; Forstner, M. B.; Käs, J. A. Biophysical journal 2002, 83, 2109–17.

Simultaneous SPT of QDs with Fluorescent Protein
Lidke, D. S.et al. Nature biotechnology 2004, 22, 198–203.z

2-color SPT of QDs
Lidke, D. S. et al. The Journal of cell biology 2005, 170, 619–26.

Finite Camera Exposure Time
Montiel, D.; Cang, H.; Yang, H. Journal of Physical Chemistry B 2006, 110, 19763–70.
Savin, T.; Doyle, P. S. Biophysical journal 2005, 88, 623–38.

Direct Observation of Actin Confinement
of IgE-FcεRI
Andrews, N. L. et al. Nature cell biology 2008, 10, 955–963.

Small, Mobile FcεRI Aggregates are Signaling
Competent
Andrews, N. L. et al. Immunity 2009, 31, 469–479.

2010

Optimal MSD Anaylsis
Michalet, X.; Berglund, A. J. Physical review. E,
Statistical, nonlinear, and soft matter physics 2012, 85, 061916.

Intermittent Trajectories
Shuang, B. et al. Langmuir : the ACS journal of surfaces and colloids 2013, 29, 228–34.

> **Variable Localization Uncertainty**

> **mcSPT of 8-colors of QDs**

> **mcSPT of 4-colors of QDs with Fluorescent Protein**

> **Small, Mobile,Transient FcεRI Aggregates are Signaling Competent**

> **Direct Observation of Signaling Compentency of Small, Mobile FcεRI Aggregates**

Figure 5.1 Timeline of significant events. This diagram highlights historical advancements in the fields of Membrane-Protein dynamics (green), IgE-FcεRI (blue), SPT (black), and the analysis of SPT data (red). The list is not exhaustive and only includes studies pertinent for discussion. The colored boxes at the bottom of the time line show the ways in which the work in this dissertation impact each of the fields.

In 2002, Martin et al. found that apparent subdiffusion observed in the MSD was actually due to localization uncertainty. This was followed by independent work by Savin et al. (2005) and Montiel et al. (2006) in which they addressed the issue of correlated information in SPT due to finite camera exposure time. These findings helped to progress the thought in the field towards more experimentally friendly methods for determining D from SPT data. In recent years, several papers have addressed additional limitations present in the determination of D for SPT data. In more recent years, Michalet and Berglund presented a string of 3 papers[16–18] that provide a more thorough discussion of the computation of D from the MSD and using a maximum likelihood estimator. A key impact of this work is the emphasis placed on the reduced squared localization precision which relates the localization uncertainty with the diffusion coefficient. An expansion of the maximum likelihood estimator formulated by Berglund which accounts for trajectory intermittency was presented by Shuang et al. in 2013. There has been a flurry of papers in recent years pertaining to estimates of D in SPT data and the trend is progressing towards more experimental application, which primes the field for the work presented in **Chapter 2**.

Lidke et al. began to expand the application of SPT with QDs by performing SPT of QD-EGF in presence of fluorescent proteins (2004)[19]. Lidke also introduced 2-color SPT of QD-EGF in 2005[20]. Both of these works were direct predecessors to work by Andrews et al. in 2008[21] and 2009[22]. In 2008, Andrews presented SPT data of QD-IgE-FcεRI and GFP-Actin which directly showed actin confinement of IgE-FcεRI. This provides direct support for the interaction of actin with membrane bound proteins and supports the findings presented by Kusumi et al. in 1993[14]. The second work by Andrews et al. in 2009 used SPT tracking to investigate the mobility of IgE-FcεRI under various crosslinking conditions. The results provided strong evidence that small, mobile aggregates of IgE-FcεRI are signaling competent. Expanding on this work to further investigate the relationship between mobility and signal initiation presents many technical challenges and set the stage for the work presented in **Chapter 3** and **Chapter 4**.

5.3 Chapter 2 Summary

5.3.1 Significance

As discussed in the previous section the analysis of SPT data has progressed significantly in the past 10 years. The progression of the field has led to several impactful studies in recent years[16–18,23]. The study presented in **Chapter 2** provides the field with two methods to estimate D when limited amounts of data with variable localization precision are available. Our new methods for estimating D have further helped to advance the field (**Figure 5.1** red). The analysis of SPT data began with very theoretical roots in the use of the MSD (1991)[13] and has built on that theoretical basis to include localization uncertainty (2002)[24], finite camera integration time (2005)[25,26], optimal numbers of fit points for the MSD(2012)[16,17], and finally trajectory intermittency (2013)[23]. These studies have also progressed from algorithm testing to on purely theoretical data to experimental applications. In line with the progression of the field, the work presented in **Chapter 2** contributes advancements not only in the estimation of D, but also presents a framework in which to test data on real microscope images.

5.3.2 Future Directions

D_{PM} is the truly novel method presented in **Chapter 2** which has the most potential to significantly impact the field. The use of Bayesian statistics and building a Posterior are the most novel aspects of this algorithm. The study presented in **Chapter 2** does not take full advantage of D_{pm} and leaves room for advancement. For example, it is feasible to use information in the posterior to identify subpopulations with different diffusion coefficients.

The use of simulated stage movements for testing SPT algorithms in general (i.e. building and analyzing trajectories) is important for the progression of the field. Idealistic computer generated data is never quite the same as data collected from real probes on the microscope. By having real microscope data with known truth provides data sets in which to truly test the performance of SPT algorithms.

5.4 Chapter 3 Summary

5.4.1 Significance

As discussion in **Section 5.2** SPT of QDs has developed over the past 15 years. The ability to excite multiple spectrally distinct species of QDs with a single excitation source and their relatively narrow emission spectra make them good candidates for mcSPT. The 2009 work by Andrews et al. expanded on previous 2-color SPT experiments and recent advances in

hyperspectral microscopy[27] to perform mcSPT tracking with 5-colors of QD-IgE[22]. One limitation of this experiment was that the hyperspectral microscope was not optimally designed for performing SPT experiments of dynamic cellular systems. The system was limited to a frame rate of 0.25 fps (approximately 1 frame every 4 seconds).

Chapter 3 of this dissertation presents a hyperspectral line-scanning (UNM HSM) system that was designed specifically for collecting hyperspectral images at 30 fps. This design goal was achieved and the instrument is able acquire spectral images at a frame rate of 27 fps. Not only are specifications of the instrument discussed, but several applications are also presented. A major undertaking here besides the successful development of the instrument is the development of the data acquisition and analysis software. In the previous work by Andrews et al., time consuming manual analysis of each image was used to identify individual QDs and their trajectories. **Chapter 3** describes software developed to perform automated single particle tracking of multiple colors of QDs simultaneously. Several applications of the instrument and data analysis are presented in Chapter 4 including: characterization of 8-colors of QDs; mcSPT of 8-colors of QD-EGF; mcSPT of 4-colors of QD-IgE with GFP-Actin; high density mcSPT of 8 colors of QD-IgE; and fast z-scans of a live cell labeled with GFP-Actin, cell mask orange, and QD-IgE. The combination of the hyperspectral microscope and analysis software presents a tool suited to interrogate dynamic samples with multiple fluorescent probes.

5.4.2 Future Directions

The UNM HSM is currently being used for multiple investigations. One such investigation is described in **Chapter 4**. There are multiple currently ongoing experiments taking advantage of the mcSPT aspects of the HSM. A few examples include investigations of the dimerization kinetics of mutant EGFR, cytokinergic IgE, and interactions between EP-2 and EP-4. An additional study is on the relationship between endocytosed of IgE with actin and tubulin. For this study, the HSM provides a platform for simultaneous single particle tracking of DNP-QD and the observation of GFP-tubulin and YFP-Actin.

5.5 Chapter 4 Summary

5.5.1 Signifiance

The development of the UNM HSM provided an experimental platform from which to expand on the previous work by Andrews et al.[22]. **Chapter 4** presents studies using both QD-IgE and DNP-QD on the HSM to investigate the dynamics of aggregates of IgE-FcεRI. One impact of this study is the observation of transient aggregates of QD-IgE which is substantiated by the observation of transient interactions of DNP-QD. This study also provides some evidence of limitations of QD probes. Some of our observations support the hypothesis that QDs bound to IgE affect its ability to act as a bivalent receptor. This study presented the need to characterize the valency of DNP-QD. Fortunately, the UNM HSM provided an experimental platform up to the task. Multi-color single molecule imaging (mcSMI) of 3-colors of Alexa Fluor IgE (488, 514, 532) with 4-colors of DNP-QD was performed. This is the first time to the author's knowledge that the multiplexing of 3 fluorophores and 4 colors of QDs in a single molecule imaging application has been achieved. Lastly, mobile DNP-QD and GFP-Syk were observed to have correlated motion in 2-color TIRF microscopy experiments directly demonstrating the signaling competency of small mobile aggregates proposed by the previous work by Andrews et al.[22]. The observation of transient interactions under signaling competent conditions also extends the mechanistic model of FcεRI signaling to include that transient receptor interactions can initiate signaling.

5.5.2 Future Directions

As indicated throughout **Chapter 4**, additional replicate experiments are necessary to improve the statistics of the data and to confirm our initial conclusions. Additionally, ongoing experiments with cytokinergic IgE may provide additional information about how transient interactions relate to signaling initiation. The mcSMI experiments developed here provides a basis for performing similar experiments with other systems as well.

5.6 Concluding Remarks

The aggregation of IgE-FcεRI on the surface of mast cells is a dynamic system of significant interest due to its role in allergic disease. Many studies have interrogated the relationship between the mobility of IgE-FcεRI and signaling[7,8,22,28]. In recent years, the spatio-temporal capabilities of SPT studies have provided significant insights into the signal initiation for IgE-FcεRI[21,22] and the MIRR family[29] in which is a member. This dissertation presents technical advances in SPT which are directly applied to investigate the spatio-temporal dynamics

of membrane-proteins providing insights into signal initiation and receptor dynamics. SPT is one example of how technology is impacting the way that we do science and allowing us to redefine what we understand about the world around us.

5.7 References

(1)   Barak, L. S.; Webb, W. W. *The Journal of cell biology* **1982**, *95*, 846–52.

(2)   Wan, T.; Beavil, R. L.; Fabiane, S. M.; Beavil, A. J.; Sohi, M. K.; Keown, M.; Young, R. J.; Henry, A. J.; Owens, R. J.; Gould, H. J.; Sutton, B. J. *Nat Immunol* **2002**, *3*, 681–6 ST – The crystal structure of IgE Fc reveal.

(3)   Ishizaka, K.; Ishizaka, T.; Hornbrook, M. M. *Journal of immunology (Baltimore, Md. : 1950)* **1966**, *97*, 75–85.

(4)   Schlessinger, J.; Webb, W. W.; Elson, E. L.; Metzger, H. *Nature* **1976**, *264*, 550–2.

(5)   Singer, S. J.; Nicolson, G. L. *Science* **1972**, *175*, 720–731 ST – The Fluid Mosaic Model of the Struct.

(6)   Saffman, P. G.; Delbrück, M. *Proceedings of the National Academy of Sciences* **1975**, *72*, 3111–3113.

(7)   Mao, S. Y.; Varin-Blank, N.; Edidin, M.; Metzger, H.; Cells, T.; Ma, S. *J Immunol* **1991**, *146*, 958–66.

(8)   Menon, A. K.; Holowka, D.; Webb, W. W.; Baird, B. A. C.-P. *J Cell Biol* **1986**, *102*, 534–40 ST – Clustering, mobility, and triggering .

(9)   Myers, J. N.; Holowka, D.; Baird, B. A. *Biochemistry* **1992**, *31*, 567–75 ST – Rotational motion of monomeric and di.

(10)   Rahman, N. A.; Pecht, I.; Roess, D. A.; Barisas, B. G. *Biophys J* **1992**, *61*, 334–46 ST – Rotational dynamics of type I Fc epsi.

(11)   Tamir, I.; Schweitzer-Stenner, R.; Pecht, I. *Biochemistry* **1996**, *35*, 6872–83.

(12)   Zidovetzki, R.; Bartholdi, M.; Arndt-Jovin, D. J.; Jovin, T. M. *Biochemistry* **1986**, *25*, 4397–401 ST – Rotational dynamics of the Fc recep.

(13)   Qian, H.; Sheetz, M. P.; Elson, E. L. C.-P. *Biophysical journal* **1991**, *60*, 910–21.

(14)   Kusumi, A.; Sako, Y.; Yamamoto, M. *Biophysical journal* **1993**, *65*, 2021–40.

(15)   Chan, W. C. *Science* **1998**, *281*, 2016–2018.

(16)   Michalet, X. *Phys Rev E Stat Nonlin Soft Matter Phys* **2010**, *82*, 041914 ST – Mean square displacement analysis of.

(17)   Michalet, X.; Berglund, A. J. *Physical review. E, Statistical, nonlinear, and soft matter physics* **2012**, *85*, 061916.

(18)   Berglund, A. J. *Phys Rev E Stat Nonlin Soft Matter Phys* **2010**, *82*, 011917 ST – Statistics of camera–based single–par.

(19)   Lidke, D. S.; Nagy, P.; Heintzmann, R.; Arndt-Jovin, D. J.; Post, J. N.; Grecco, H. E.; Jares-Erijman, E. a; Jovin, T. M. *Nature biotechnology* **2004**, *22*, 198–203.

(20)   Lidke, D. S.; Lidke, K. A.; Rieger, B.; Jovin, T. M.; Arndt-Jovin, D. J. *The Journal of cell biology* **2005**, *170*, 619–26.

(21)   Andrews, N. L.; Lidke, K. a; Pfeiffer, J. R.; Burns, A. R.; Wilson, B. S.; Oliver, J. M.; Lidke, D. S. *Nature cell biology* **2008**, *10*, 955–963.

(22)   Andrews, N. L.; Pfeiffer, J. R.; Martinez, a M.; Haaland, D. M.; Davis, R. W.; Kawakami, T.; Oliver, J. M.; Wilson, B. S.; Lidke, D. S. *Immunity* **2009**, *31*, 469–479.

(23)   Shuang, B.; Byers, C. P.; Kisley, L.; Wang, L.-Y.; Zhao, J.; Morimura, H.; Link, S.; Landes, C. F. *Langmuir : the ACS journal of surfaces and colloids* **2013**, *29*, 228–34.

(24)   Martin, D. S.; Forstner, M. B.; Käs, J. A. *Biophysical journal* **2002**, *83*, 2109–17.

(25)   Montiel, D.; Cang, H.; Yang, H. *Journal of Physical Chemistry B* **2006**, *110*, 19763–70.

(26)   Savin, T.; Doyle, P. S. *Biophysical journal* **2005**, *88*, 623–38.

(27)   Sinclair, M. B.; Timlin, J. A.; Haaland, D. M.; Werner-washburne, M. *Applied Optics* **2004**, *43*, 2079–2088.

(28)   Menon, A. K.; Holowka, D.; Baird, B. A. C.-P. *J Cell Biol* **1984**, *98*, 577–83.

(29)   Douglass, A. D.; Vale, R. D. C.-P. *Cell* **2005**, *121*, 937–50.

APPENDIX A: SUPPLEMENTARY INFORMATION FOR CHAPTER 2

Appendix A

SUPPLEMENTARY INFORMATION FOR CHAPTER 2

A.1   Posterior mode recursion relation

The integral product in **equation 2.4** can be solved analytically via recursion relation when the constituent probabilities are represented as normal distributions. We do so by analytically integrating the x_1 position first and then we integrate positions x_2 through x_N in sequential order. Since the algebraic form of the integrals from x_2 to x_{N-1} are exactly the same, the solutions of each subsequent integral can be expressed as a recursion of the prior integrand solution. The integral with respect to x_1 is

$$
\int_{-\infty}^{\infty} dx_1 \, \frac{1}{2\pi\sigma_\epsilon \sigma_{D_1}} \cdot e^{-(o_1-x_1)^2/2\sigma_{\epsilon_1}^2} \cdot e^{-(x_2-x_1)^2/2\sigma_{D_1}^2}
$$
$$
= \frac{1}{\sqrt{2\pi(\sigma_{\epsilon_1}^2 + \sigma_{D_1}^2)}} \cdot e^{-(o_1-x_2)^2/2(\sigma_{\epsilon_1}^2+\sigma_{D_1}^2)}. \tag{A.1}
$$

Integrating with respect to x_1 results in an expression that is dependent on x_2. Therefore, the terms relevant to the x_2 integral look like

$$\int_{-\infty}^{\infty} dx_2 \; \frac{1}{\sqrt{2\pi(\sigma_{\epsilon_1}^2 + \sigma_{D_1}^2)}} \cdot \frac{1}{2\pi\sigma_{\epsilon_2}\sigma_{D_2}} \cdot e^{-(o_2-x_2)^2/2(\sigma_{\epsilon_1}^2 + \sigma_{D_1}^2)} \cdot e^{-(o_2-x_2)^2/2\sigma_{\epsilon_2}^2} \cdot$$

$$e^{-(x_3-x_2)^2/2\sigma_{D_2}^2}. \quad (A.2)$$

As each subsequent integral is introduced and evaluated, the complexity of the evaluated integrands increase. Thus it is necessary to introduce the following symbols to simplify A.2:

$$\begin{aligned} \delta_1 &= o_1 \\ \beta_1 &= \sqrt{\sigma_{\epsilon_1}^2 + \sigma_{D_1}^2} \\ H_1 &= \frac{1}{\sqrt{2\pi}}. \end{aligned} \quad (A.3)$$

This puts the integral in A.2 in the form of

$$\int_{-\infty}^{\infty} dx_2 \; H_1 \cdot \frac{1}{2\pi\beta_1\sigma_{\epsilon_2}\sigma_{D_2}} \cdot e^{-(\delta_1-x_2)^2/2\beta_1^2} \cdot e^{-(o_2-x_2)^2/2\sigma_{\epsilon_2}^2} \cdot e^{-(x_3-x_2)^2/2\sigma_{D_2}^2}, \quad (A.4)$$

where

$$\begin{aligned} \alpha_2 &= (\beta_1^2 + \sigma_{\epsilon_2}^2) \\ \rho_2 &= o_2\beta_1^2 + \delta_1\sigma_{\epsilon_2}^2 \\ \gamma_2 &= \sigma_{\epsilon_2}^2\delta_1^2 + \beta_1^2 o_2^2 + \sigma_{D_2}^2(o_2 - \delta_1)^2 \\ \lambda_2 &= \beta_1^2(\sigma_{\epsilon_2}^2 + \sigma_{D_2}^2) + \sigma_{\epsilon_2}^2\sigma_{D_2}^2. \end{aligned} \quad (A.5)$$

The integral in A.4 can be evaluated as

$$H_1 \cdot \frac{1}{\sqrt{2\pi}\sqrt{\lambda_2}} \cdot e^{-\left[(x_3 - \frac{\rho_2}{\alpha_2})^2 - (\frac{\rho_2}{\alpha_2})^2 + \frac{\gamma_2}{\alpha_2}\right]/\frac{2\lambda_2}{\alpha_2}}. \tag{A.6}$$

We can then identify the next set of variables as

$$
\begin{aligned}
\delta_2 &= \frac{\rho_2}{\alpha_2} \\
\beta_2 &= \sqrt{\frac{\lambda_2}{\alpha_2}} \\
H_2 &= \frac{1}{\sqrt{2\pi\alpha_2}} \cdot e^{-(\gamma_2/\alpha_2 - \delta_2^2)/2\beta_2^2}.
\end{aligned} \tag{A.7}
$$

Thus the next integral would be in the following form

$$\int_{-\infty}^{\infty} dx_3 \, H_1 \cdot H_2 \cdot \frac{1}{2\pi\beta_2\sigma_{\epsilon_3}\sigma_{D_3}} \cdot e^{-(\delta_2 - x_3)^2/2\beta_2^2} \cdot e^{-(o_3 - x_3)^2/2\sigma_{\epsilon_3}^2} \cdot e^{-(x_4 - x_3)^2/2\sigma_{D_3}^2}. \tag{A.8}$$

From induction, we see that every integral in 2.4 up to the (N-1)th integral can be expressed in the same form as

$$\int_{-\infty}^{\infty} dx_i \left(\prod_{k=1}^{i-1} H_k\right) \cdot \frac{1}{2\pi\beta_{i-1}\sigma_{\epsilon_i}\sigma_{D_i}} \cdot e^{-(\delta_{i-1} - x_i)^2/2\beta_{i-1}^2} \cdot e^{-(o_i - x_i)^2/2\sigma_{\epsilon_i}^2} \cdot$$
$$e^{-(x_{i+1} - x_i)^2/2\sigma_{D_i}^2}. \tag{A.9}$$

Once again, we apply the following substitutions for the i_{th} integral, where in this case $i \in 2 : N - 1$

$$
\begin{aligned}
\alpha_i &= (\beta_{i-1}^2 + \sigma_{\epsilon_i}^2) \\
\rho_i &= o_i\beta_{i-1}^2 + \delta_{i-1}\sigma_{\epsilon_i}^2 \\
\gamma_i &= \sigma_{\epsilon_i}^2\delta_{i-1}^2 + \beta_{i-1}^2 o_i^2 + \sigma_{D_i}^2(o_i - \delta_{i-1})^2 \\
\lambda_i &= \beta_{i-1}^2(\sigma_{\epsilon_i}^2 + \sigma_{D_i}^2) + \sigma_{\epsilon_i}^2\sigma_{D_i}^2.
\end{aligned} \tag{A.10}
$$

115

With the solution

$$\left(\prod_{k=1}^{i-1} H_k\right) \cdot \frac{1}{\sqrt{2\pi} \cdot \sqrt{\lambda_i}} \cdot e^{-\left[(x_{i+1} - \frac{\rho_i}{\alpha_i})^2 - (\frac{\rho_i}{\alpha_i})^2 + \frac{\gamma_i}{\alpha_i}\right]/\frac{2\lambda_i}{\alpha_i}}, \tag{A.11}$$

where the variables, given their initial $(i = 1)$ values, can be recursively expressed as

$$
\begin{aligned}
\delta_i &= \frac{\rho_i}{\alpha_i} \\
\beta_i &= \sqrt{\frac{\lambda_i}{\alpha_i}} \\
H_i &= \frac{1}{\sqrt{2\pi\alpha_i}} \cdot e^{-\left(\frac{\gamma_i}{\alpha_i} - \delta_i^2\right)^2 / 2\beta_i^2}.
\end{aligned}
\tag{A.12}
$$

With the updated variables, the expression in A.11 can be expressed in the form

$$\left(\prod_{k=1}^{i} H_k\right) \cdot \frac{1}{\beta_i^2} \cdot e^{-(x_{i+1} - \delta_2)^2 / 2\beta_i^2}. \tag{A.13}$$

Taking these recursion relations into consideration, the final Nth integral in 2.4 can be expressed as

$$\int_{-\infty}^{\infty} dx_N \left(\prod_{k=1}^{N-1} H_k\right) \cdot \frac{1}{\sqrt{2\pi}\beta_{N-1}\sigma_{\epsilon_N}} \cdot e^{-(\delta_{N-1} - x_N)^2 / 2\beta_{N-1}^2} \cdot e^{-(o_N - x_N)^2 / 2\sigma_{\epsilon_N}^2}. \tag{A.14}$$

In order to simplify the likelihood expression, the last integral is evaluated and H_1 is expressed explicitly so that the likelihood is in the following form

$$P(y|\theta_D) = \left(\prod_{k=2}^{N-1} H_k\right) \cdot \frac{1}{\sqrt{2\pi(\sigma_{\epsilon_N}^2 + \beta_{N-1}^2)}} \cdot e^{-(o_N - \delta_{N-1})^2 / 2(\sigma_{\epsilon_N}^2 + \beta_{N-1}^2)}. \tag{A.15}$$

The log of which is expressed as

$$
\begin{aligned}
log\left(P(y|\theta_D)\right) = \left(\sum_{k=2}^{N-1} log(H_k)\right) &- \frac{1}{2}log(2\pi(\sigma_{\epsilon_N}^2 + \beta_{N-1}^2)) - \\
&\left\{(o_N - \delta_{N-1})^2 / 2(\sigma_{\epsilon_N}^2 + \beta_{N-1}^2)\right\},
\end{aligned}
\tag{A.16}
$$

116

where

$$log(H_i) = -\frac{1}{2}log(2\pi\alpha_i) - \left(\frac{\gamma_i}{\alpha_i} - \delta_i^2\right)/2\beta_i^2 \quad \forall i \in 2:N-1. \tag{A.17}$$

A.2   Independent Jump Analysis

The method derived in this section is identified as D_{IJA} throughout this manuscript. Under the assumption of Brownian motion, the probability distribution function for 1-dimensional displacements ($\overrightarrow{d}$) given an underlying D is

$$P\left(\overrightarrow{d}|\theta_D\right) = \prod_{i=1}^{N_d} \frac{1}{\sqrt{2\pi\sigma_i^2}} e^{\frac{-d_i^2}{2\sigma_i^2}} \tag{A.18}$$

where N_d is the number of observed displacements, d_i is the observed displacement ($o_i - o_{i+1}$) between observation i (o_i) and observation 2 (o_{i+1}), and σ_i^2 is the variance in the observed displacements. Here,

$$\sigma_i^2 = 2D\Delta t_i - 4Dt_\epsilon R + \sigma_{o_i}^2 + \sigma_{o_{i+1}}^2. \tag{A.19}$$

The log likelihood is

$$\ln\left(L\left(\theta_D|\overrightarrow{d}\right)\right) = \sum_{i=1}^{N_d} -\frac{1}{2}\ln(2\pi) + -\frac{\ln(\sigma_i^2)}{2} + \frac{-d_i^2}{2\sigma_i^2}. \tag{A.20}$$

The Newton-Raphson iterative update method is used to find the maximum log likelihood. According to information theory, the minimum variance for an estimated parameter is related to the maximum likelihood estimate by the fisher information matrix. The fisher information matrix for the problem at hand is

$$I(\theta_D) = \sum_{i=1}^{N_d} \frac{1}{2\sigma_i^4}\left(\frac{\partial\sigma_i^2}{\partial\theta_D}\right)^2, \tag{A.21}$$

117

and the variance in the estimation of θ_D is bounded by

$$\mathrm{CRB} = I(\theta_D)^{-1}. \tag{A.22}$$

The probability distribution in Eq. A.18 is easily extended to n-dimensions

$$P\left(d|\theta_D\right) = \prod_{j=1}^{n} \prod_{i=1}^{N_d} \frac{1}{\sqrt{2\pi\sigma_{i,j}^2}} e^{\frac{-d_{i,j}^2}{2\sigma_{i,j}^2}}, \tag{A.23}$$

and it is trivial to expand the entire derivation to the n-dimensional case. Jumps from multiple trajectories are easily pooled together to estimate an ensemble estimate of D using D_{IJA}.

APPENDIX B: SUPPLEMENTARY INFORMATION FOR CHAPTER 3

B.1 Supplementary Figures
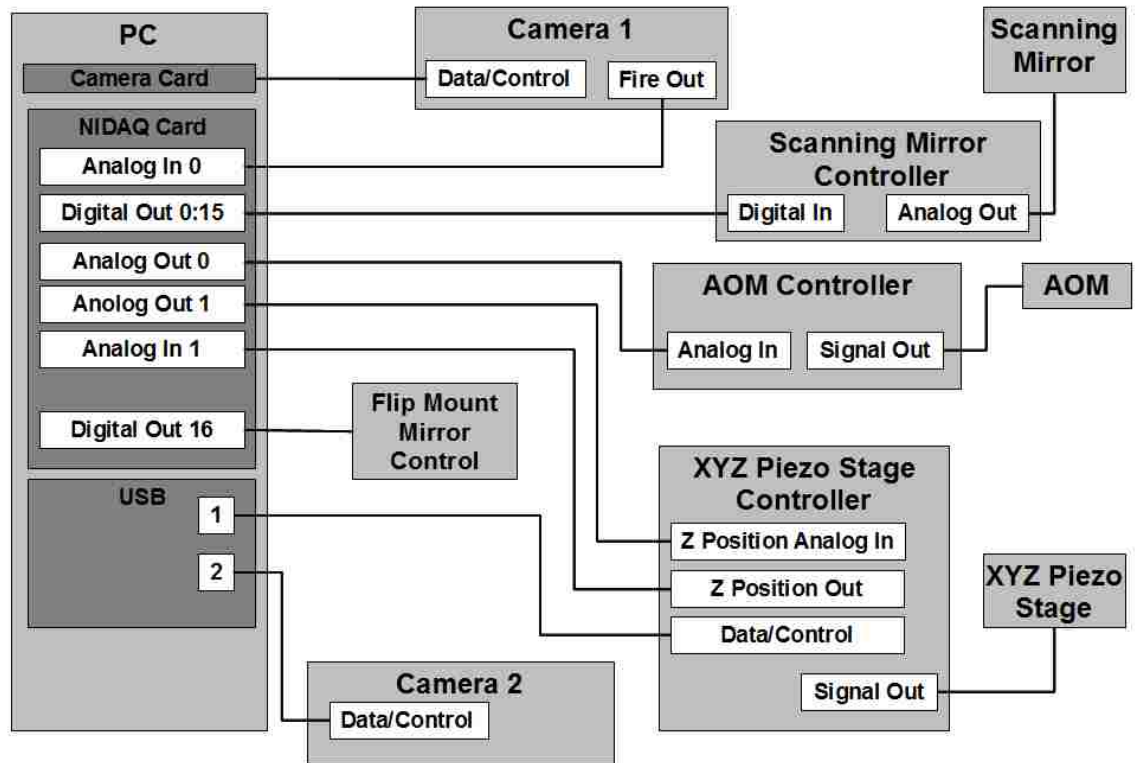
Figure B.1.1 Instrument control schematic.

The fire out signal from the camera is used as the clock to advance the scanning mirror, stepping through a list of digital words provided to the scanning mirror control board. The acousto-optic modulator (AOM) controller accepts analog DC voltage input and controls the RF power output to the AOM's piezoelectric transducer. The flip-mount controller toggles the mirror position with a single 5V pulse. The *XYZ* Piezo-stage controller applies a *z*-position change based on analog DC voltage input and returns position information to an analog voltage input on the data acquisition board. The secondary camera (used for widefield viewing to center a sample or select ROI) uses a single USB connection.
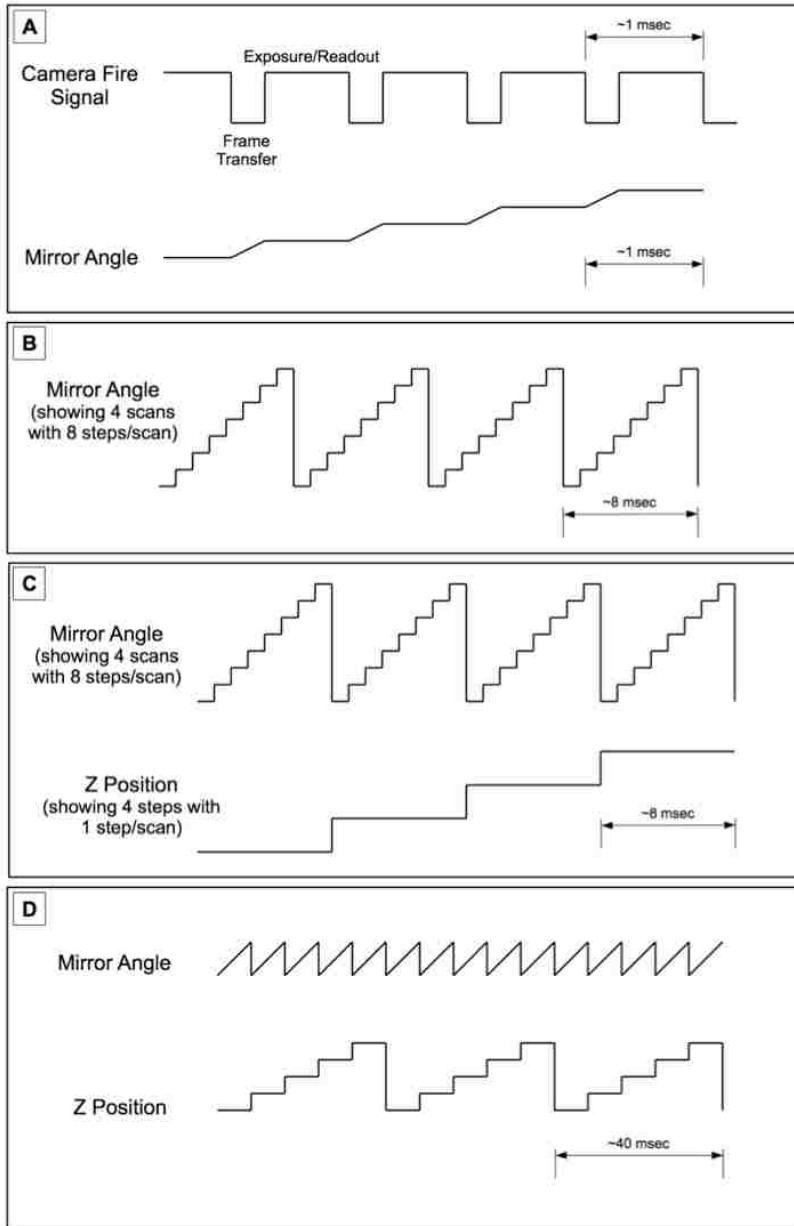
Figure B.1.2 Signal timing.

(A) As the camera finishes an exposure the falling edge trigger is used as a clock to advance the mirror scan angle by one step. A frame transfer mode EMCCD camera is used, so readout occurs during exposure. The mirror step response time actually exceeds the frame transfer interval, but is much less than a single exposure, such that mirror motion is negligible during acquisition. (B) Scans are completed after a set number of steps, where the mirror angle is returned to the starting position. (C) In fast 3D scans, as a single scan is completed the z stage is translated by one step. (D) As the z steps are completed through the depth of the region of interest, the z stage is returned to the starting position to begin another pass.
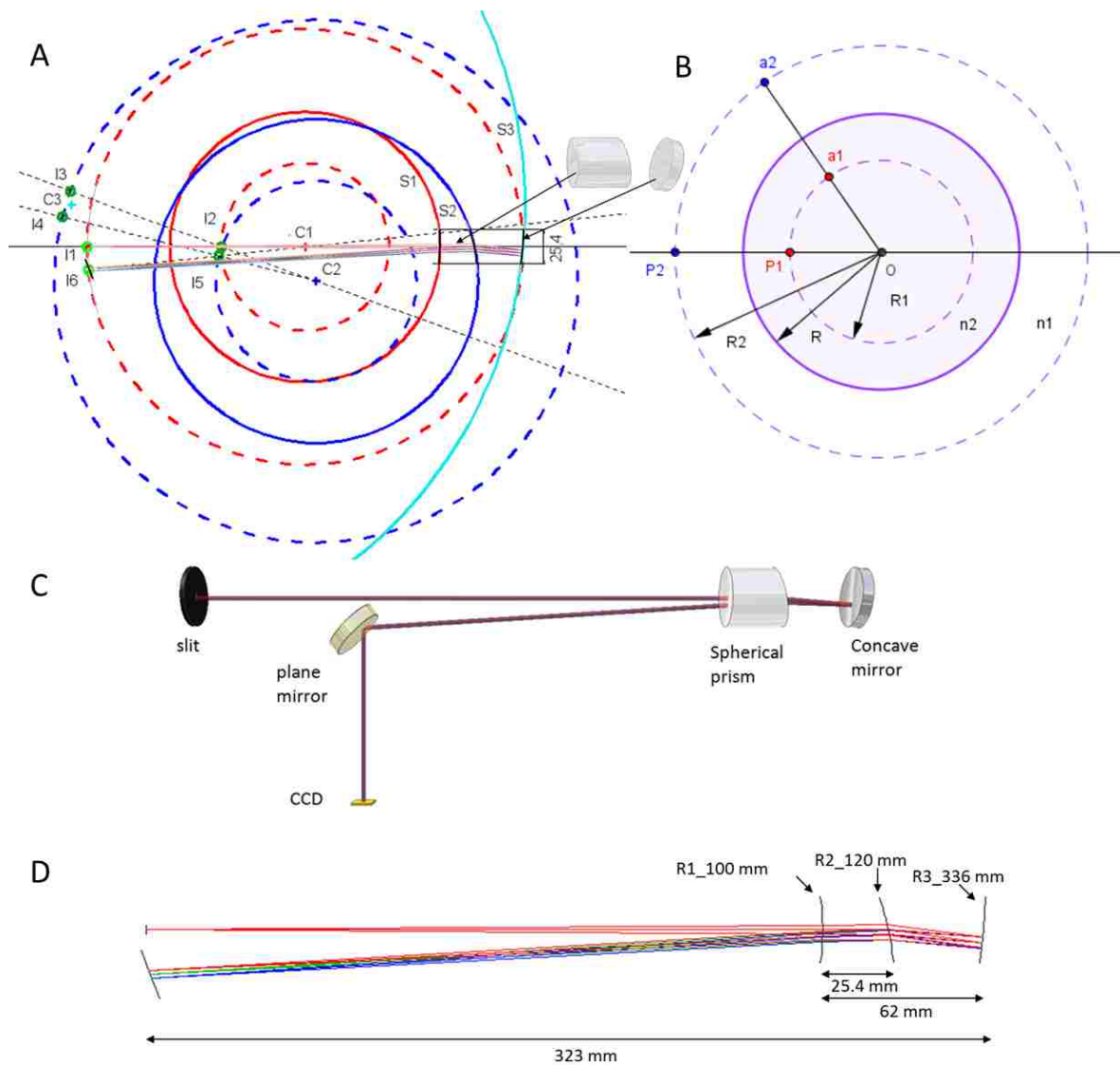
Figure B.1.3 Spectrometer design.

A more detailed discussion of the principles of the spectrometer design is in **Text S2**. (A) Relative positions of each spherical surface of the prism spectrometer. S1 (red solid circle) and S2 (blue solid circle) are refractive surfaces of the spherical prism, S3 (cyan solid circle) is the reflective surface of the concave mirror. The dotted circles are conjugate aplanatic surfaces of S1 and S2. (B) Relationship of conjugate aplanatic surfaces (dotted circles) of the refractive spherical surfaces (solid circles). (C) 3D drawing of the spectrometer. (D) Spectrometer design in OSLO (Optics Software for Layout and Optimization).
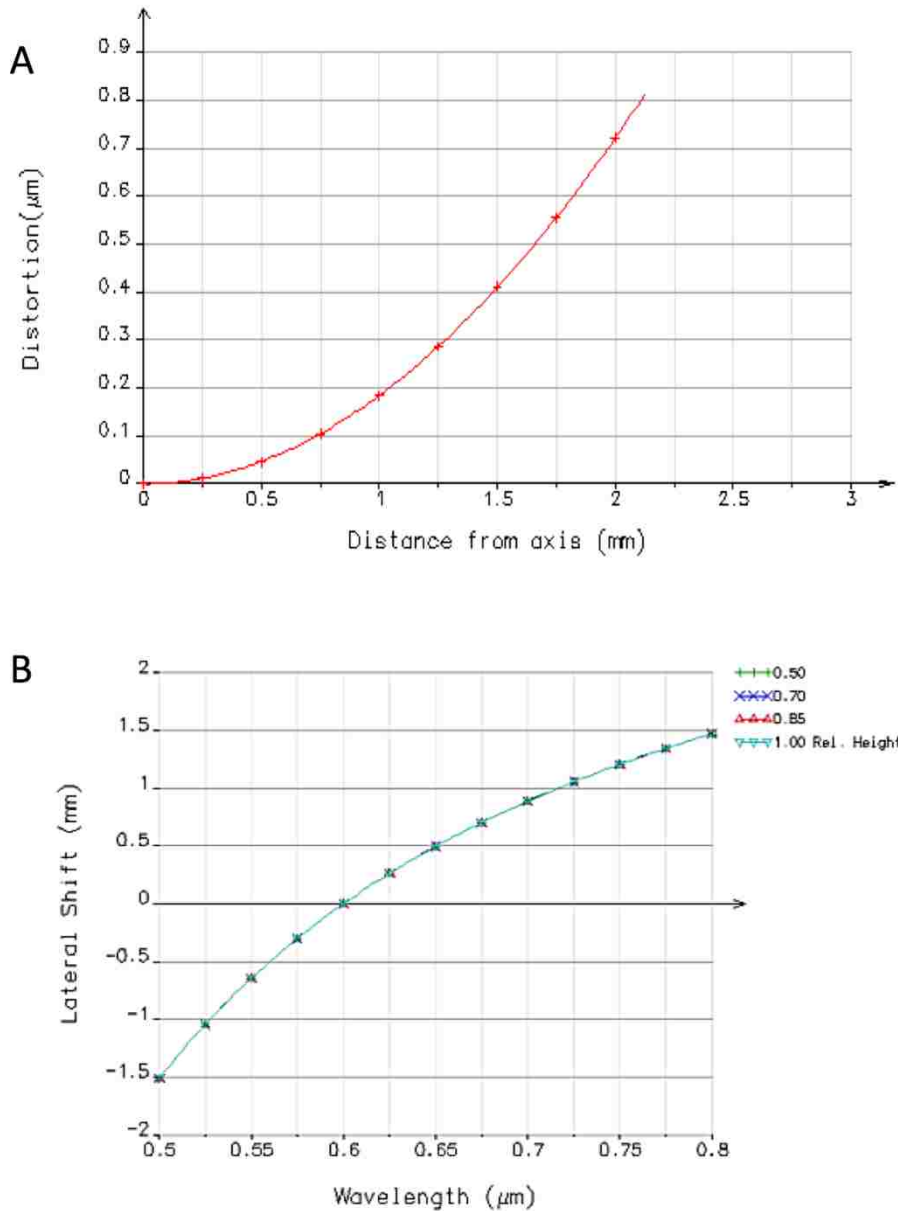
Figure B.1.4 Spectral distortion and dispersion.

The distortion and dispersion curves are generated from OSLO. (A) Distortion shows offset of the true image position from the ideal image position at various off axis points. In the HSM setup, the maximum distance from the axis is 1.5 mm, so the designed maximum distortion is 0.4 μm, which is less than 2% of CCD pixel size (24 μm). (B) Lateral shift shows the dispersion, designed to span a total of 3 mm from 500 nm to 800 nm. It shows dispersions in four relative heights (distance from the optical axis), the four curves are right on top of each other, so the spectral lines are straight, which also indicates a minimal distortion.
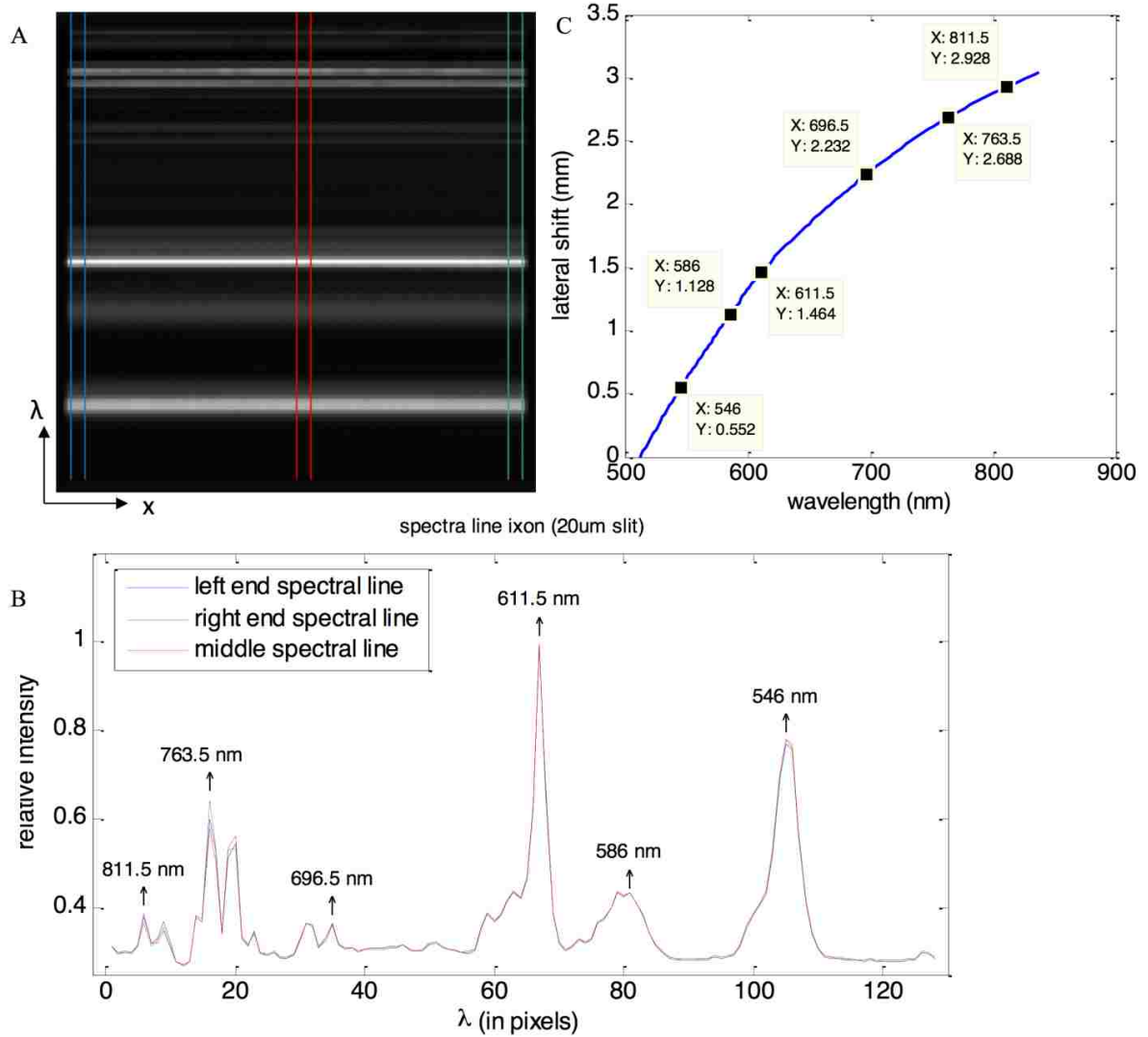
Figure B.1.5 Spectral calibration.

(A) Image of the calibration lamp on the camera (the vertical axis is the spectral dimension). The calibration lamp is a LightForm multi-ion discharge lamp (MIDL), the slit width is 20 μm, and the camera is an Andor iXon 860 EMCCD with an array size of 128×128, pixel size 24 μm. (B) Spectral curve, generated by the sum projection of (A) along the x dimension; the peak wavelengths are identified from the specification sheet of the calibration lamp. The blue, green, and red lines correspond to the regions in (A) with the same color. All three colored lines almost overlap with each other, which demonstrates a very small distortion in the spectral lines. (C) Dispersion curve, generated from the spectral curve (C), by polynomial fit of specific wavelengths.
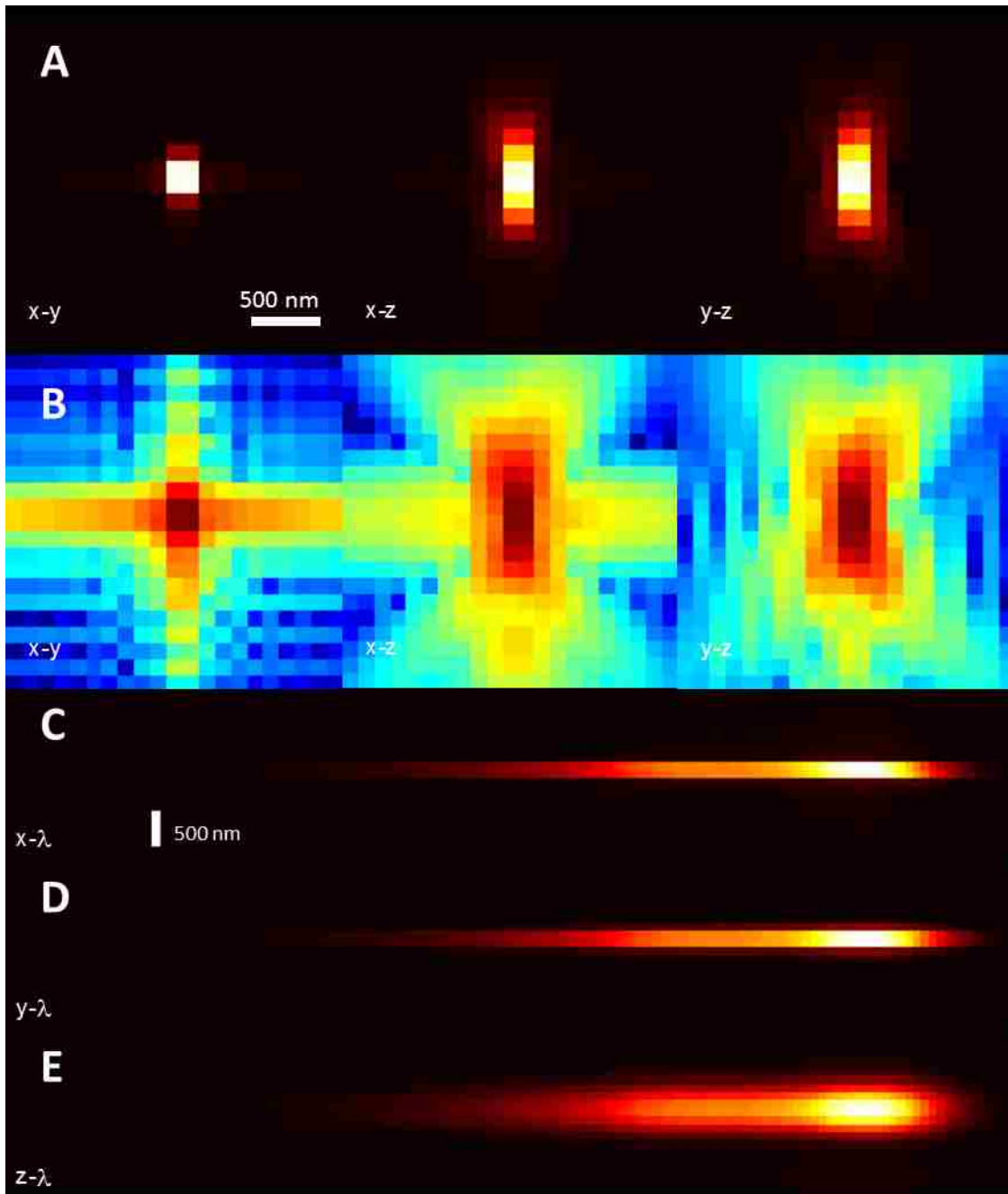
Figure B.1.6 4D PSF theoretical.

The 4D PSF is calculated from the theory as described in **Text S3**. The spectra and wide field point spread function is based on 100 nm yellow bead. The simulation includes aberrations generated from phase retrieving process. A linear stretch (A) and log stretch (B) of intensity for projections on the *x-y*, *x-z*, and *y-z* planes are shown along with the *x*, *y*, and *z* vs. wavelength projections (C, D, and E).
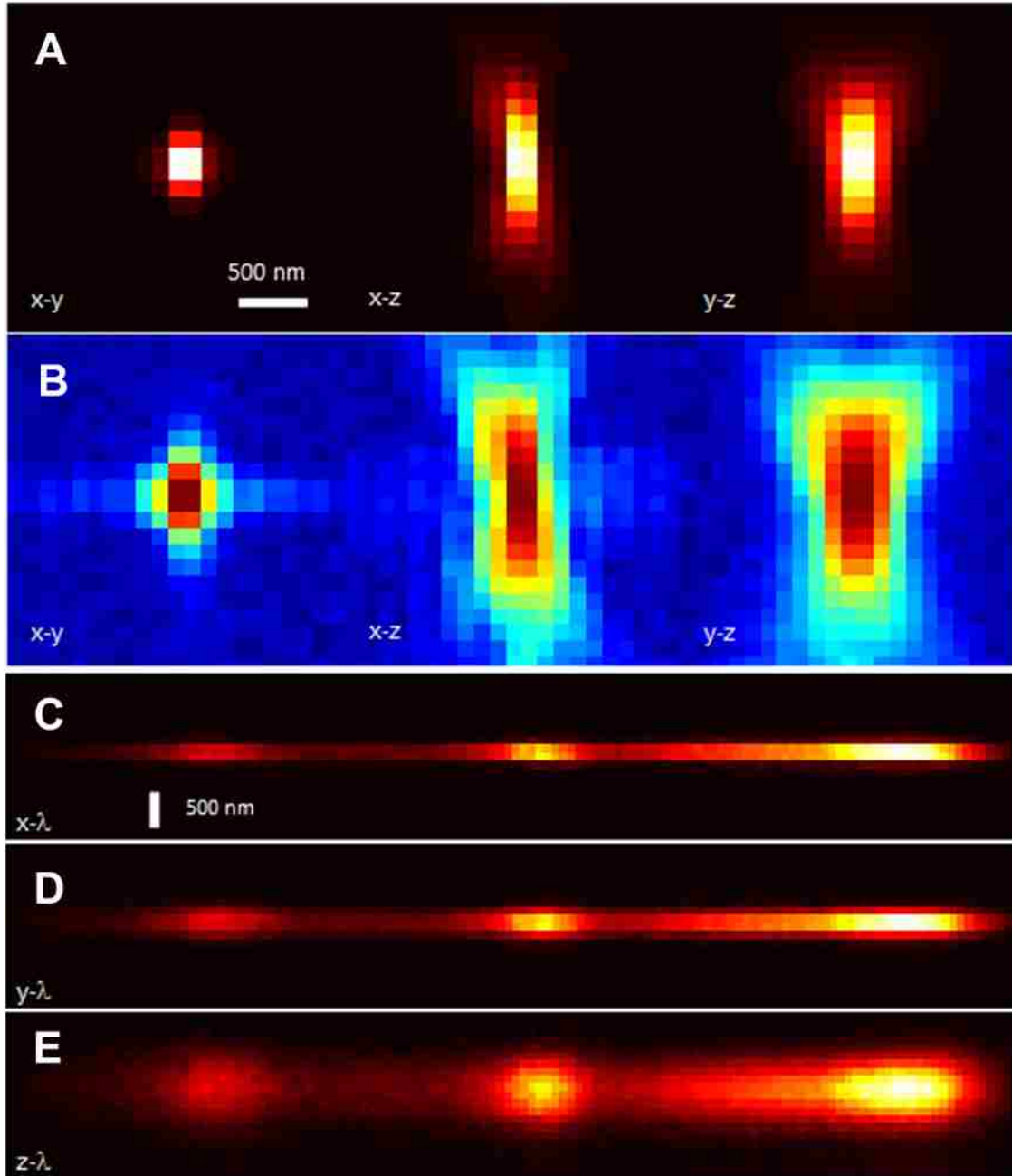
Figure B.1.7 4D PSF experimental.

The sample is a 100 nm TetraSpeck bead imaged at 100 nm steps in z. A linear stretch (A) and log stretch (B) of intensity for projections on the *x-y*, *x-z*, and *y-z* planes are shown along with the *x*, *y*, and *z* vs. wavelength projections (C, D, and E). The figures show three emission peaks of TetraSpeck bead, 505/515 nm (green), 560/580 nm (orange) and 660/680 nm (dark red). Data were acquired at room temperature, using a 60x water objective, *NA*=1.2.
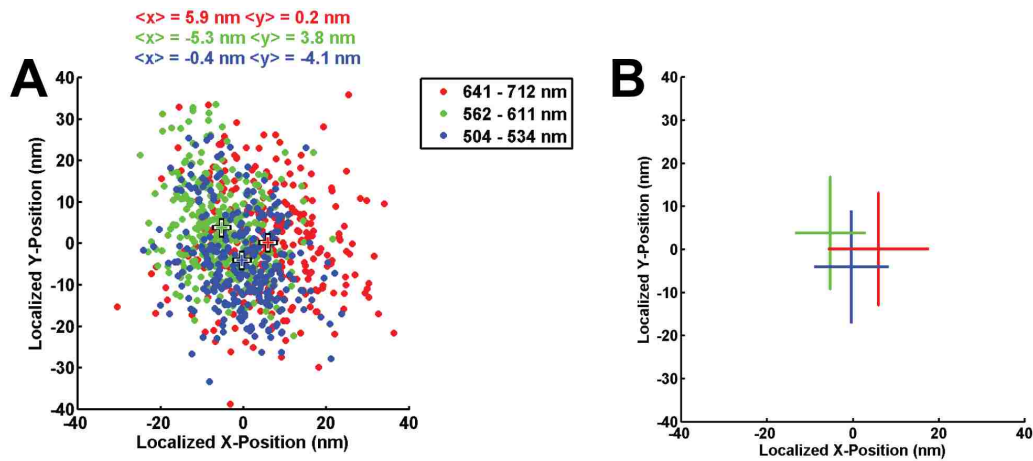
Figure B.1.8 Color dependence of localizations.

Scatter plot of 300 localizations of a single 100 nm TetraSpeck bead on glass using three different wavelength ranges. The purpose here is to quantify any chromatic dependence on particle localization. Emitters were 100 nm Tetraspeck beads diluted 2000:1 in 1x PBS and allowed to stick to a glass cover slip. The sample was then scanned 300 times and localizations were obtained for each scan using emitted light from each of three different wavelength ranges. The mean of the localized *x*-positions varied by ~10 nm and the mean of the localized *y*-positions varied by ~ 8 nm. (A) Scatter plot of localizations with the mean identified by '+' and listed at the top of the figure. (B) Error bars indicating one standard deviation.
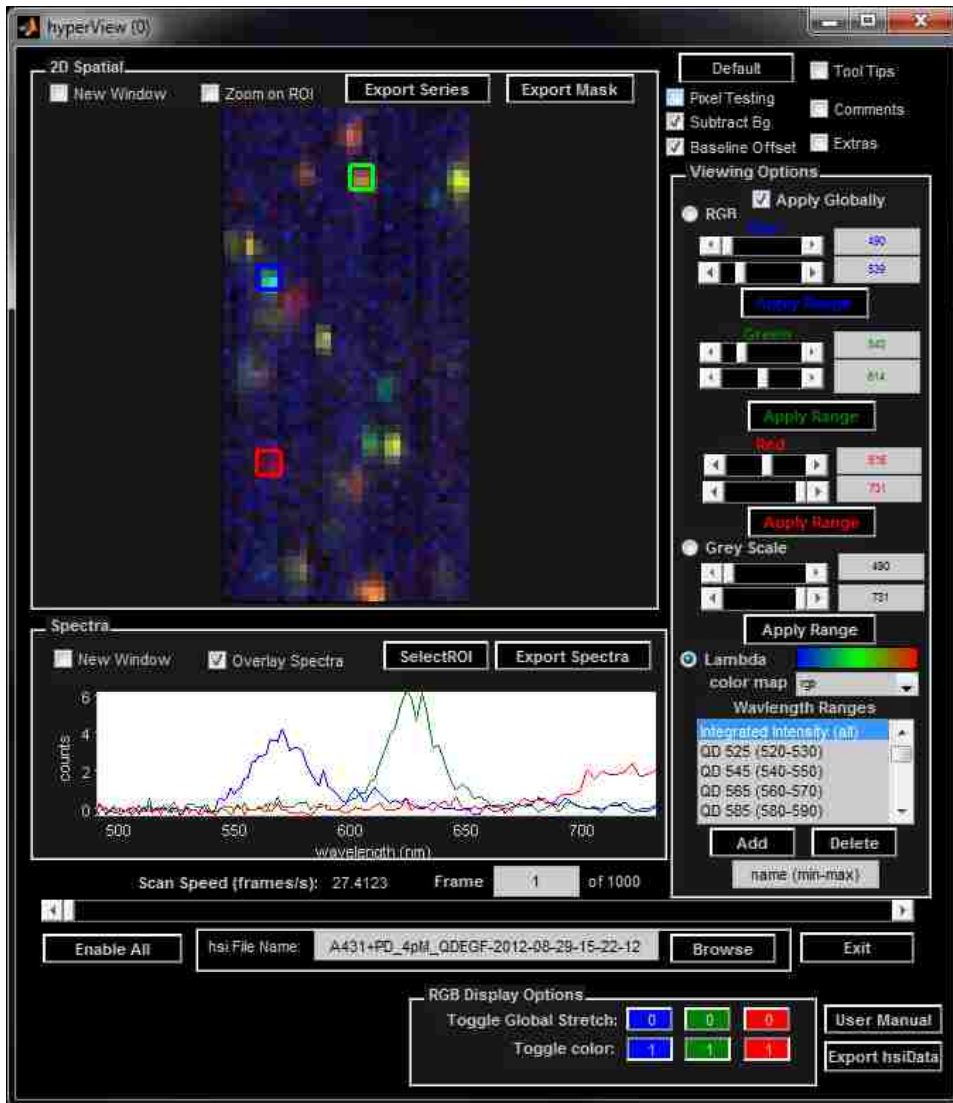
Figure B.1.9 Hyperspectral viewing GUI.

Hyperspectral viewing GUI provides real-time feedback for instrument control (focusing, ROI determination, etc.) and experimental observations (sample quality, QD labeling density, etc.). The GUI can also be used for preliminary investigations of data in post processing. For example, the blue, green, and red boxes in the RGB image (top left of GUI) highlight single 565, 625, and 800 nm QDs respectively. Spectra for pixels within those boxes are shown in the axes below the RGB image. The GUI provides flexibility in the coloration scheme for the RGB image. For the default RGB representation, each spectral channel is assigned an RGB color progressing from blue to green to red. RGB values for each spatial pixel are determined by relative contributions from of RGB values from each spectral channel.
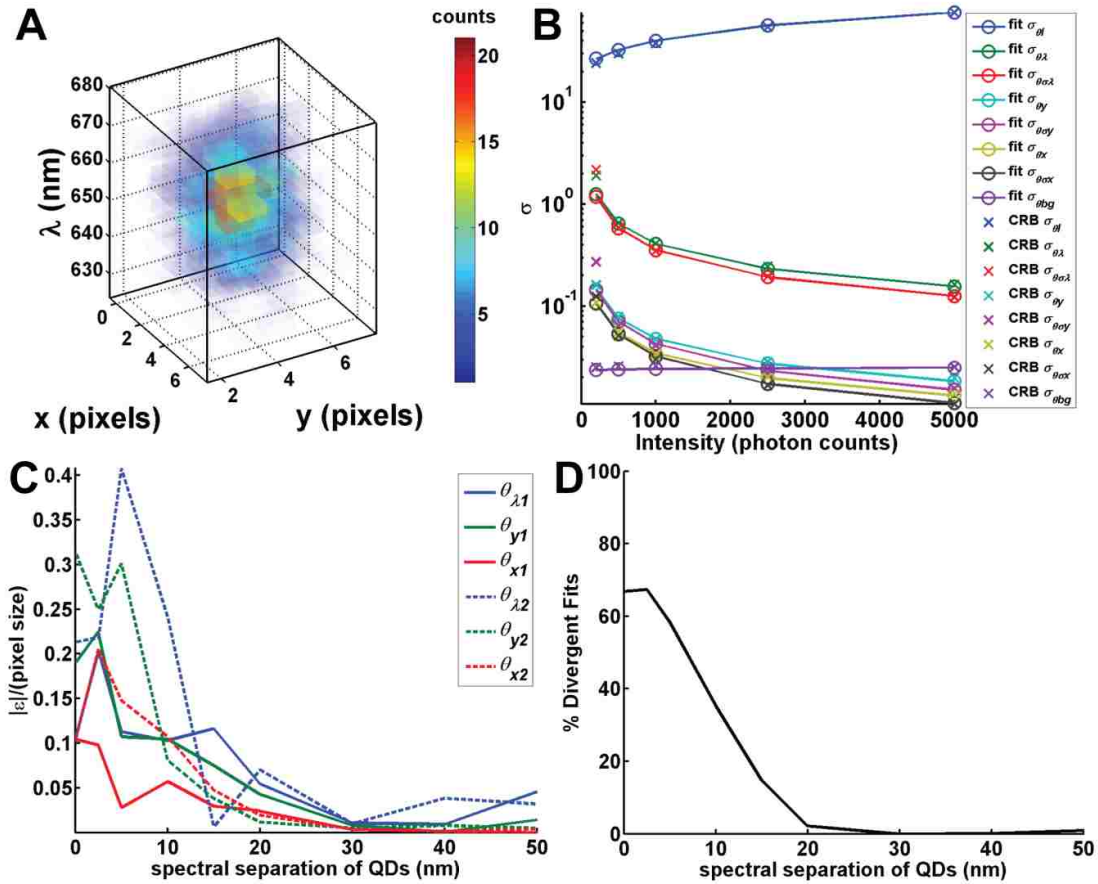
Figure B.1.10 3D Gaussian model.

(A) 3D pixelated Gaussian model for a single QD with Poisson noise. (B) The standard deviation in parameter estimates from 500 fits of simulated data with Poisson noise (open circles) agree well with the theoretical standard deviation (square root of the Cramér Rao Bound; *x*). No blinking was included in this simulation. (C) and (D) show results for fitting. Simulations of 2 QDs with a fixed spatial separation (0.5 pixels or ~60 nm) and variable spectral separation (0 to 50 nm) are fit with a 2 QD model. (C) The relative accuracies (absolute error (ε) normalized by the pixel size) for positional parameters for QD 1 (solid lines; θ_{x1}, θ_{y1}, $\theta_{\lambda1}$) and QD 2 (dashed lines; θ_{x2}, θ_{y2}, $\theta_{\lambda2}$). (D) The percent of divergent fits (yielded unreasonable parameter estimates).
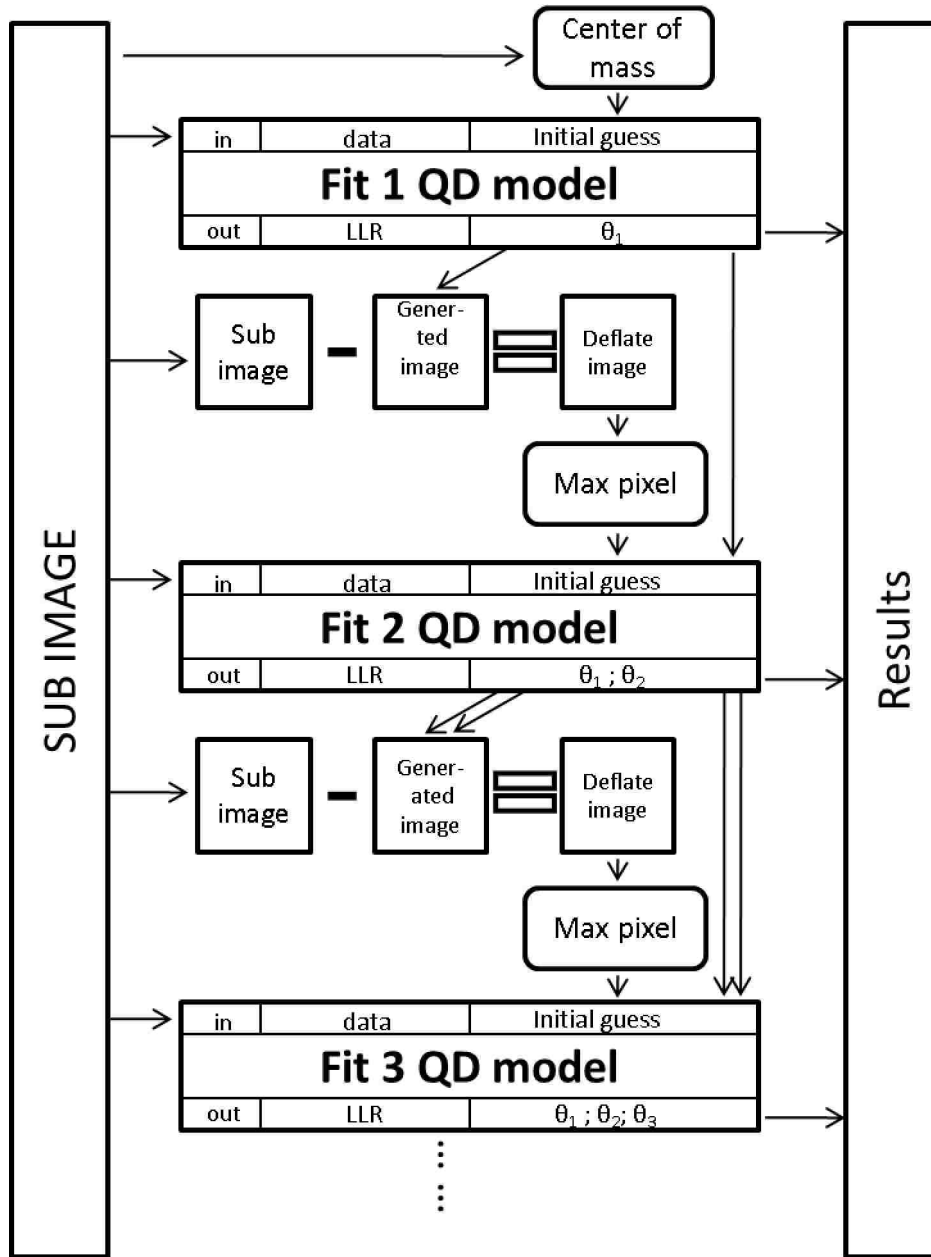
Figure B.1.11 Multi-QD fitting routine.

QD fitting is performed sequentially for 1 to *N* QDs. Figure adapted from Huang et al. More details about the fitting steps are included in **Text S5**.
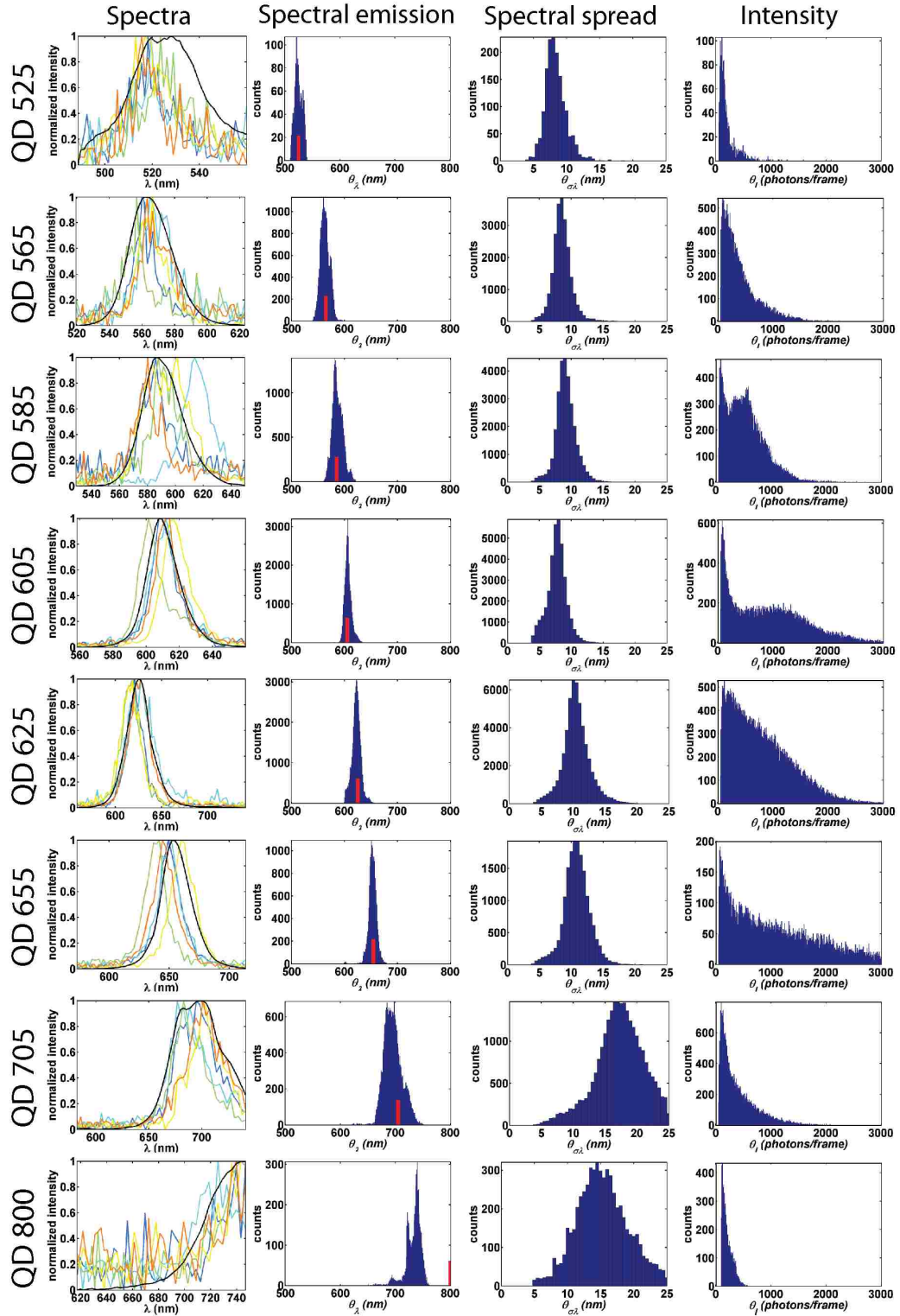
Figure B.1.12 QD characterization (525-800).

The rows contain figures related to the indicated QD species. Column 1 shows spectral features of individual QDs (colored lines; 5 randomly selected spectra) and the ensemble of all individual

www.manaraa.com

QDs (black line; total number of spectra used to compute each ensemble is included in **Table S2**). Column 2 contains histograms of fit spectral emission peaks (θ_λ) identified by 3D Gaussian fitting (x,y,λ) for individual QDs. Red ticks indicate the expected emission peak for each QD specie. Note that the expected emission peak for QD800 is significantly different from the histogram. This is attributed to the spectral range of the camera (i.e. only the tail of the spectrum is observed on the camera). Column 3 contains histograms of the fit standard deviation in the spectral dimension ($\theta_{\sigma\lambda}$) identified by 3D Gaussian fitting for individual QDs. Column 4 contains histograms of fit photons per frame ($\theta_{\sigma\lambda}$) for individual QDs. **Table S1** includes further description of the model parameters. Statistics are included in **Table S2**.
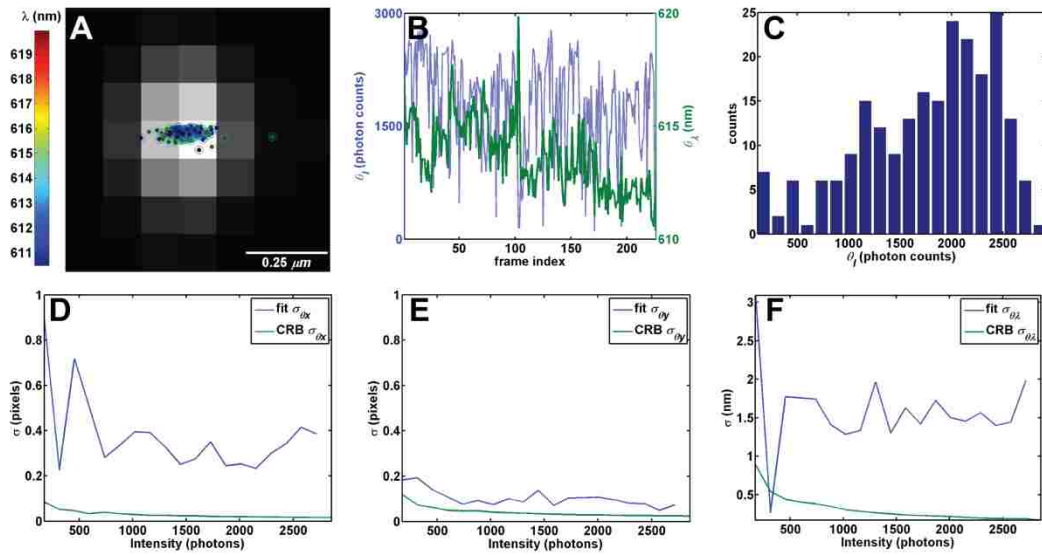
Figure B.1.13 QD localization and blinking.

(A) Localizations for a single QD605 overlaid on the sum projection of raw data. Coloration of localizations corresponds to the localized emission peak (color bar). The estimated intensity (left axis; blue) and spectral emission peak (right axis; green) are shown over time (~3.8 fps) in (B). Note the blue shifting of the QD is observed in (A) and (B). Localizations were binned by intensity in (C) and the standard deviation of the localization parameters were compared to the square root of the CRB in (D), (E), and (F). The standard deviation in the line dimension (E) corresponds well to the theoretical lower bound. The standard deviation in the scanning dimension (D) and the spectral dimension (F) do not correspond well with theory. This is attributed to QD blinking during the line scan and QD blue shifting respectively.
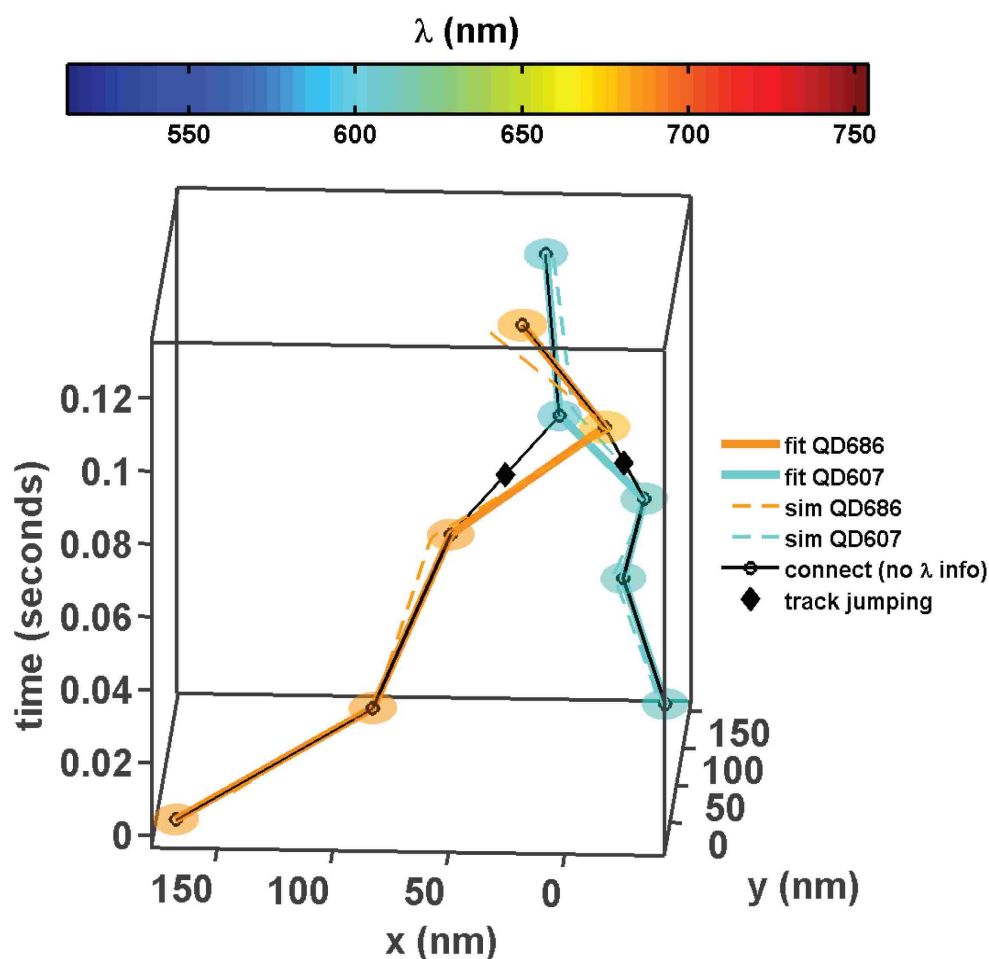
Figure B.1.14 Spectral information improves trajectory connections.
Hyperspectral image data (100 frames) with diffusing QDs were simulated (QD simulation
parameters attained from the characterization of QDs in **Figure S12** and **Table S2**) and localized
(**Text S4**, **Figure S10**, **Text S5**, and **Figure S11**). Trajectories were subsequently built either
utilizing (solid colored lines) or ignoring spectral information (solid black lines). Localizations
are shown in ellipsoids (size of the ellipsoid corresponds to 3x the estimated localization
accuracy), and solid colored lines correspond to the connected trajectories. Dashed colored lines
represent the 'true' simulated trajectories. The black line with circles identifies trajectories built
from connecting localizations without spectral information. Black diamonds represent positions
were tracks jump from one true underlying track to another.
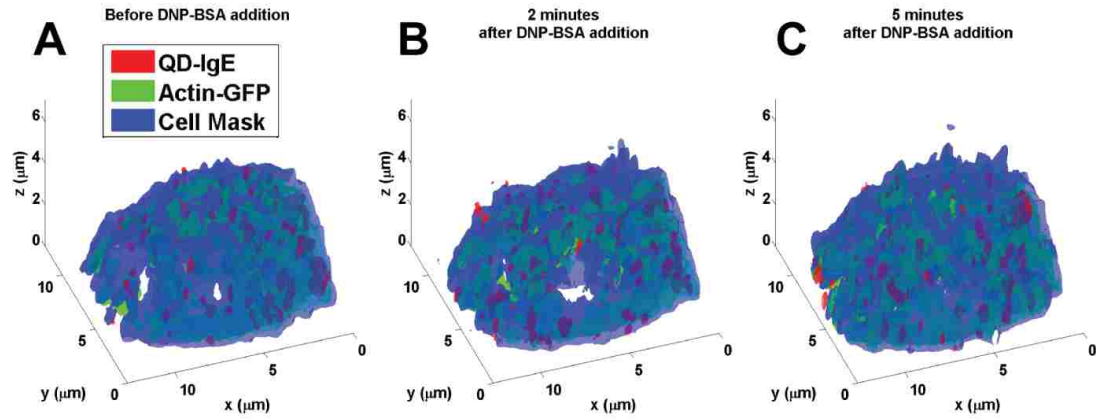
Figure S15. 3D scanning of live cells.

Change in cell morphology upon activation of IgE-FcεRI by crosslinking with multivalent antigen (DNP-BSA). (A), (B), and (C) show 3D isosurface representations of deconvolved z stacks for a single cell acquired at 1 hyperspectral image stack every 7.72 seconds at several time points before and after activation as indicated. Cells are labeled with Cell Mask orange (blue), Actin-GFP (green), and QD-IgE-FcεRI (red). See **Video S6**.

B.2 Supplementary Video Legends

Video B.2.1 SPT on glass.
SPT of 8-colors of QDs non-specifically adsorbed on glass. (top) RGB representation of the raw data with overlaid trajectories (coloration of trajectories are according to color bar in **Figure 3**). The white box is approximately representative of the spatial region for the highlighted sub-volumes in **Figure 3B-E**. (bottom) Spectrum for the ROI in the white box. This movie accompanies **Figure 3B-E**.

Video B.2.2 Transient interactions.
Transient (boxes 2 and 3) and stable (box 1) interactions are observed for SPT of 8-colors of QD-EGF on a live A431 cell. This movie is a temporal animation of **Figure 4**.

Video B.2.3 Oligomer dynamics.
Oligomers are observed after crosslinking QD-IgE-FcεRI with DNP_3 on a live RBL-2H3 cell. This movie highlights a dimer (top; circle and down triangle) and a trimer (bottom; diamond, square and up triangle). Representative spectra for the highlighted ROIs are shown to the right. This movie accompanies **Figure 5**.

Video B.2.4 Observation of GFP-actin and QD-IgE-FcεRI.
Simultaneous observation of GFP-actin (gray scale) and SPT of 4-colors of QD-IgE-FcεRI on a live RBL-2H3 cell. This movie accompanies **Figure 6**.

Video B.2.5 Membrane diffusion mapping.
High density mcSPT of QD-IgE-FcεRI on a live RBL-2H3 cell. (upper left) RGB representation of localized particles and trajectories (color bar below indicates emission peak for localizations and trajectories). Trajectory positions observed in the previous 10 frames (~0.36 s) are shown. (upper right) Diffusion map relative to QD-IgE-FcεRI (color bar below indicates estimated diffusion coefficients). (bottom) Instantaneous diffusion coefficient corresponding to **Figure 7a** with a moving window indicating the temporal window used to determine the diffusion map. Upon the addition of DNP-BSA, the window changes from red to green (text indicator in the upper right of the movie also changes color) marking the addition of DNP-BSA. This movie accompanies **Figure 7**.

Video B.2.6 3D scanning of live cells.

Isosurface representation for 3D scanning of a live RBL-2H3 cell. DNP-BSA was added ~60 s into the acquisition as indicated by the text at the top of the movie. Cells are labeled with Cell Mask orange (blue), Actin-GFP (green), and QD-IgE-FcεRI (red). This movie accompanies **Figure S15**.

B.3 Supplementary Text

Text B.3.1 Details about general instrument design.

Unless otherwise specified, the spatial dimensions will be defined such that the z-axis is along beam line, the y-axis will be perpendicular to the optics table surface, and the x-axis will be parallel to the optics table surface. Beam steering mirrors, optics mounts, and micro-positioners are omitted to simplify the diagram. The numbers in brackets {} are references to parts listed below.

Excitation Path:

Starting with the 488 nm laser (**Figure 2** upper left, {1}) the beam is 40 mW which turns out to be much more than needed for most experiments with this system, so neutral density filters ({2}, {3}) are used for coarse adjustment of the initial laser power. The beam is steered (using mirrors {4}, {5}) through an acousto-optic modulator (AOM, {6}) and the first order diffracted beam is coupled into the fiber {7}, {8}. The amount of laser light in the coupled beam depends on the radio frequency (RF) power in the AOM, which can be smoothly and quickly controlled, providing a good mechanism for modulation and tuning the power of the laser light as desired. The AOM power is controlled by providing a voltage to the signal processor unit. This voltage signal is provided by an analog output from a data acquisition and control PC card {9} that is controlled via software. The fiber is single-mode, polarization preserving and is used as a means to control intensity as well as for acting as a good spatial filter since light emitted from the fiber is collimated (via objective {10}) into a good approximation of a Gaussian beam TEM 00 mode with an $1/e^2$ diameter of ~0.8 mm. The polarization is maintained such that the light which is

focused to create the laser line has the *E* field oriented along the length of the line at the focal plane so that the line has the minimum possible width.

The free space Gaussian beam is steered into a laser line generator lens {11} that has a 15 degree fan angle in the *y*-dimension and distributes the light evenly over the angle. This light is then collimated with a cylindrical lens (CYL1, {12}). Lens CYL2 {13} is a concave cylindrical lens oriented along the *x*-axis, which serves to expand the beam along the *x*-axis such that the beam will ultimately fill the back aperture of the objective lens, which reduces the excitation focal volume along the *z*-axis. Lenses L1 {14} and L2 {17} are used as a telescope to reduce the size of the line before entering the microscope base {18}, such that the line will be ~15 um in length on the sample (which is also the approximate length of one column of 128 CCD pixels back-projected on the sample). L1 focuses the light onto the scanning mirror {16} after being reflected off of the dichroic mirror {15}, which is fixed at a 45-degree angle to the beam.

Emission Path:

The light emitted from a fluorophore excited by the laser line will be distributed over all angles and the light which is accepted by the aperture of the objective lens {**Error! Reference source not found.**} will then be collimated and will propagate to the tube lens. The tube lens will focus the light to an image plane which is also the focal plane of lens L2, so it will then be collimated and de-scanned by the mirror, which causes the emission light to match the axis of excitation light for all scan angles, allowing fixed positions of the remaining optical elements.

The emitted light then passes through the dichroic mirror and a 488 nm long pass filter {22}, which has the purpose of further reducing any amount of excitation light that may have passed through the dichroic filter. Lens L3 {23} then focuses this light onto the entrance slit {24} of the spectrometer, which also serves as a line-scanning confocal slit that blocks much of the light from sources that are out of focus.

The custom-made prism spectrometer {27} is described fully in **Text S2**, and focuses the light onto the CCD pixel array (**Figure 2** and **Figure S3**). This provides a 128×128 array of data from the CCD {28} that consists of *y*-position (along the laser line and slit) and wavelength along the other dimension. As the line is scanned across the sample another 128×128 (*y*, *λ*) array is taken for each line position (one angle step in the *x*-dimension). The full field of view (*x*, *y*) is then reconstructed into a data set of (*x*, *y*, and *λ*) for one scan or "hyperspectral image".

Other (some not shown in diagram): 3D scanning is enabled by the *x*, *y*, *z* piezo stage {19}. Widefield excitation (used for finding regions of interest within a sample) is performed using a white light source {20} and filter cube set {21}. The

electromechanical flip-mount mirror {25}, changes the emission path into the widefield CCD {26} and is controlled through the DAQ GUI.

Parts Reference List

1. Laser: Newport Spectra Physics 488 Cyan, Model PC14011
2. ND Filters: Newport FRQ-ND03, FRQ-ND07, FRQ-ND10, FRQ-ND15, and FRQ-ND20
3. ND Filter Wheels: Newport FWM1X12
4. Mirrors: Newport 10D20ER.1
5. Mirror Mounts: Newport U100-A with precision actuators AJS100-0.5
6. AOM: IntraAction Corp. Model AOM-402AF1 with signal processor from IntraAction Corp. model ME-402
7. Fiber: Newport F-PM480-C-2FC
8. Fiber Coupler: Newport F-91-C1 with objective lens M-40X
9. DAQ Card: National Instruments PCIe-6343 X Series Data Acquisition Card (P/N 781047-01) with BNC-2110 shielded connector block (P/N 777643-01) and SHC68-68-EPM 5m cable (P/N 192061-05).
10. Fiber to Collimated Free Space Beam: Newport L-40X (f = 4.6 mm, NA = 0.66), Thorlabs HPT1 X,Y Translator (holds FC connector), Thorlabs SM1Z Z-Axis Translator (holds the objective)
11. Laser line generator lens: Edmund Optics 46632 (15-degree fan angle)
12. CYL1: Edmund Optics 48353 (f = 25 mm, d = 12.5 mm, MgF2 Coated)
13. CYL2: Thorlabs LK1743R-A (f = -100 mm, d = 25.4 mm, BK7)
14. Lens L1: Newport KPX114AR.14 (f = 350 mm, d = 25.4 mm)
15. Dichroic: Semrock LPD01-488RU-25x36x2.0
16. Scanning Mirror: Cambridge Technology 6210H
17. Lens L2: Newport PAC040AR.14 (f = 50.5 mm, d = 25.4 mm)
18. Microscope Base: Olympus IX71
19. X,Y,Z Piezo Stage: Mad City Labs Nano-LPS200
20. Widefield Lamp: X-cite 120Q
21. Widefield Filter Cube Set: Chroma Z473-10x (excitation), Semrock LPD01-488RS-25x36x2.0 (dichroic), Semrock LP02-488RU-25 (emission).
22. Long Pass Filter: Semrock LP02-488RU-25
23. Lens L3: Newport PAC061AR.14 (f = 175 mm, d = 25.4 mm)
24. Spectrometer Entrance Slit: Thorlabs S100R (100 +/- 4 μm wide, 3mm tall)
25. Flip-Mount Mirror: Thorlabs MFF001
26. EMCCD1: Andor Luca R
27. Prism Spectrometer: Custom Design, Rainbow Optics

Text B.3.2 Principles of spectrometer design.

Aplanatic image formation of spectrometer

In **Figure S3A**, S_1 and S_2 are the front and rear spherical surfaces of the spherical prism. S_3 is the surface of the concave mirror. I_1 is the object point at the entrance slit. I_6 is the image point at the spectral plane. I_2-I_5 are intermediate image points. I_1-I_6 are on the concentric spherical surfaces of S_1 and S_2. Since the concentric surfaces are an aplanatic pair of image and object conjugates, the spectrometer is aplanatic. Those concentric surfaces satisfy the relationship $n_1^2 R_1 = n_2^2 R_2 = n_1 n_2 R$ in **Figure S3B**.

The detailed image formation of the spectrometer is:

(1) The front surface of prism S_1 forms a virtual image of object I_1 at the position of its aplanatic conjugates I_2. C_1 is the center of surface S_1.

(2) Notice that I_2 also lies on the aplanatic conjugate surface of the rear prisms spherical surface S_2, which forms the virtual image of I_2 at position I_3. C_2 is the center of surface S_2.

(3) Mirror S_3 forms a virtual image of I_3 at position I_4 by reflection. Since I_3 and I_4 are near the center of S_3, the magnification is 1:1.

(4) Notice that I_4 is still at the aplanatic conjugate surface of S_2, which relays I_4 to I_5.

(5) Although I_5 doesn't lie on the inner aplanatic conjugate of S_1, it is near the intersection and S_1 can still form the real image I_6 at the outer aplanatic conjugate of S_1. Therefore, this last refraction is still near aplanatic.

Calculation of spectrometer design

First, given an approximate size of the spectrometer 300 mm, we choose R_1=100 mm, and R_2=120 mm (**Figure S3D**), the glass type of prism is F2, which has a refractive index n_c=1.615 (the refractive index at 656.3 nm). All the calculations follow the aplanatic rule.

$$I_1 C_1 = nR_1 = 1.615 \times 100 = 161.5 \text{ mm}$$

$$I_2 C_1 = \frac{R_1}{n} = \frac{100}{1.615} = 62 \text{ mm}$$

$$I_5C_2 = \frac{R_2}{n} = \frac{120}{1.615} = 74.3 \text{ mm} *$$

*It's 74.56 mm in the final design, so there is a little offset from the perfect image

$$I_3C_2 = nR_2 = 1.615 \times 120 = 193.8 \text{ mm}$$

R_3 is decided by making I_3 near C_3. Since I_4 should also be on the outer dotted blue circle, C_3 should be near the midpoint of I_3 and I_4. $R_3 = I_3C_2 + R_2 + L$, where L is an arbitrary distance. For a starting value, we choose $L = 25$ mm which gives $R_3 = 338.3$ mm ($R_3 = 336$ mm in the final design).

These numbers are chosen to be the starting point of the prism spectrometer design in OSLO. The radius and angle of the surfaces S_2, S_3, and the distance between the three surfaces are adjusted to minimize aberrations (mainly astigmatism, coma, and distortion). The table below shows the dimensions of the optimized spectrometer design in OSLO.

Dimensions of each surface in OSLO design

Surface	Radius	Thickness	Glass	Notes
object	0.00	261.50	Air	
1	-100.00	25.40	F2	Tilt 0.00 deg
2	-120.00	36.69	Air	Position then tilt (Y-tilt, clockwise) -12.200 deg
3	-336.00	-36.69	Reflect	Position then tilt (Y-tilt, clockwise) 5.458 deg
4	-120.00	-25.4	F2	Same as S_2
5	-100.00	-259.94	Air	Same as S_1
image	0.00	0.00	Air	Position then tilt (Y-tilt, clockwise) -20.879 deg, global coordinate: Y is -17.14, Z is -259.94, origin is at S_1

Units are mm.

Text B.3.3 Theoretical point spread function of HSM

In the HSM, the excitation path is the same as a line scanning confocal microscope. On the sample plane, assuming that a single fluorophore is at point $(0,0,z)$, the excitation laser line is along the y-axis at position x. The excitation field at the fluorophore is

$$U_{\text{ex}}(0 - x, z).$$

We use U for magnitude point spread function, and PSF for intensity point spread function. U_{ex} is a line spread function, assuming the intensity along y-axis is uniform. In the emission path, after light passes through the slit, the emission field at slit will be dispersed along x-axis by spectrometer at the image plane. The field at image plane is generated by shifting the slit field along x-axis (spectral dimension) and multiplying each shifted field by the spectral function at the corresponding wavelength. We define the spectral function as $SP(x_\lambda)$, which depends on the spectrum of the sample. The field at position (x_λ, y) on image plane is

$$\int_l U_{\text{em}}(x - \xi, y, z)L(\xi)SP(x_\lambda + \xi)d\xi.$$

$U_{\text{em}}(x, y, z)$ is the wide field emission point spread function, and $L(x)$ is the slit shape function along x axis, which is a rectangular function with the width equal to the slit width l. The above expression is the convolution of $U_{\text{em}}(x, y, z)$ with $L(x)SP(x_\lambda)$. Combining the excitation and emission fields gives the magnitude point spread function of the HSM

$$U_{\text{HSM}}(x, y, z, x_\lambda) = U_{\text{ex}}(-x, z) \int_l U_{\text{em}}(x - \xi, y, z)L(\xi)SP(x_\lambda + \xi)d\xi.$$

$U_{\text{ex}}(-x, z)$ is the wide field excitation line spread function. U_{HSM} is a 4D point spread function, with spatial dimension x, y, z, and spectral dimension x_λ. The intensity point spread function is

$$PSF_{\text{HSM}} = |U_{\text{HSM}}|^2.$$

Text B.3.4 3D Gaussian fitting.

The 3D Gaussian model used to estimate the microscope PSF and spectral features of individual QDs is

$$PSF(x, y, \lambda) = \frac{1}{(2\pi)^{3/2}\theta_{\sigma_x}\theta_{\sigma_y}\theta_{\sigma_\lambda}} e^{-\frac{(x-\theta_x)^2}{2\theta_{\sigma_x}^2} - \frac{(y-\theta_y)^2}{2\theta_{\sigma_y}^2} - \frac{(\lambda-\theta_\lambda)^2}{2\theta_{\sigma_\lambda}^2}}.$$

Definitions of all variables are included in **Table S1**. Due to the optical setup of the HSM, the intensity for a single QD is distributed over several spatial and spectral pixels. The contribution of a single QD to the detected counts in pixel k of an HSM image is modeled by

$$\mu_k(x, y, \lambda) = \theta_I \int_{A_k} PSF(u, v, w) du dv dw,$$

where A_k is the area for a single pixel. Integration of the equation above gives

$$\mu_k(x, y, \lambda) = \theta_I \Delta E_x(x, y, \lambda) \Delta E_y(x, y, \lambda) \Delta E_\lambda(x, y, \lambda),$$

where the contribution of the Gaussian in the spectral dimension is

$$\Delta E_\lambda(x, y, \lambda) = \frac{1}{2} \left[\text{erf}\left(\frac{\lambda - \theta_\lambda + \lambda_{width}/2}{\sqrt{2}\theta_{\sigma_\lambda}} \right) - \text{erf}\left(\frac{\lambda - \theta_\lambda - \lambda_{width}/2}{\sqrt{2}\theta_{\sigma_\lambda}} \right) \right].$$

The terms $\Delta E_x(x, y, \lambda)$ and $\Delta E_y(x, y, \lambda)$ are equivalently defined relative to x and y respectively. The 3D Gaussian model for a single QD is depicted in **Figure S10A**. The model is easily expanded to N spatially and spectrally overlapping QDs with background

$$\mu_{k_{All}}(x, y, \lambda) = \sum_i^N \mu_{k_i}(x, y, \lambda) + \theta_{bg}.$$

Model parameters for individual QDs are fit to experimental data by maximizing the likelihood function:

$$L(\theta|D) = \prod_k \frac{\mu_{k_{All}}(x,y,\lambda)^{d_k} e^{-\mu_{k_{All}}(x,y,\lambda)}}{d_k!}.$$

Parameter optimization is performed using the Newton-Raphson method which is an extension of previous work [1]. The variance in parameter estimates approaches the theoretical limit set by the Cramér Rao Bound for simulated data (**Figure S10B**). The accuracy for localizing two highly overlapping emitters simultaneously is demonstrated in **Figure S10C** and **S10D**. Relatively accurate localizations (spatial and spectral) for both QDs is achieved with a high degree of spatial overlap and spectral separation distances down to 20 nm.

Similar to previous work, the 3D Gaussian fitting algorithm is implemented in Compute Unified Device Architecture (CUDA) for Graphics Processing Units (GPUs). The algorithmic implementation for fitting single and multi-QD models for an individual sub image is an adaptation of previous work (**Figure S11**).

QD blinking while the excitation line is scanning over a single QD causes errors in localization in the scan dimension of the line (**Figure S13**). The assumption that the mobility of individual receptors is dimension independent means that this artifact has a minimal impact on physical interpretation of the data. This artifact causes difficulties for the 3D Gaussian model in x (scan dimension) and complicates several facets of SPT in HSM images:

    (1) The log likelihood ratio test cannot be used to select the appropriate model;
    (2) The CRB does not accurately approximate the variance in parameter estimates in x (scan dimension).

Thusly, an empirically determined algorithm is used to identify 'appropriate' fits (see below).

Steps for Filtering QD Localizations

1. Eliminate fits with unreasonable fit parameters
2. Eliminate multi-emitter fits in which localizations are too close to one another.
   o An error scaling term (a) defined by the user is used to identify closeness of position parameter values. The error scaling term is defined independently for spatial and spectral dimensions.
   o Fits in which position parameters for QD$_i$ (θ_{λ_i}, θ_{y_i} or, θ_{x_i}) and for QD$_j$ (θ_{λ_j}, θ_{y_j} or, θ_{x_j}) are closer together than their combined errors multiplied by the error scaling term $a_\lambda \sqrt{\sigma_{\theta_{\lambda_i}}^2 + \sigma_{\theta_{\lambda_j}}^2}$, $a_y \sqrt{\sigma_{\theta_{y_i}}^2 + \sigma_{\theta_{y_j}}^2}$, and $a_x \sqrt{\sigma_{\theta_{x_i}}^2 + \sigma_{\theta_{x_j}}^2}$ respectively
3. Compare all models (1 to m-emitters) for a single sub-volume in which all θ and σ_θ values pass filtering steps 1-2. Use log likelihood ratio to compare models with user-defined p-value for the chi squared distribution with the degrees of freedom equal to the difference in the number model parameters [2].
4. Identify repetitive localizations and select localization with lowest relative error
   o Repetitive localizations are identified by the same procedure as that used in step 2.
   o Relative error is defined as $\left(\frac{a_\lambda * \sigma_{\theta_\lambda}}{\lambda_{width}}\right)^2 + \left(\frac{a_y * \sigma_{\theta_y}}{y_{width}}\right)^2 + \left(\frac{a_x * \sigma_{\theta_x}}{x_{width}}\right)^2$

References

1. Smith CS, Joseph N, Rieger B, Lidke K a (2010) Fast, single-molecule localization that achieves theoretically minimum uncertainty. Nature methods 7: 373–375. Available: http://www.pubmedcentral.nih.gov/articlerender.fcgi?artid=2862147&tool=pmcentrez&rendertype=abstract.

2. Härdle WK, Simar L (2012) Applied Multivariate Statistical Analysis. 2nd ed. Springer.

Text B.3.5 Additional details about multi-QD fitting routine.

1. Single and multi-emitter fitting performed on each sub-volume. Typically, 1-4 emitter fitting
2. Initial estimate(s)
   a. θ_I summation of all pixels divided by number of models (double check code)
   b. Position $(\theta_\lambda, \theta_y, \theta_x)$
      i. 1-emitter model: center of mass used for position estimates
      ii. m-emitter model
         1. Result from select alternating iteration for model m-1 used for deflation
         2. Maximum pixel after deflation used as initial estimate for model m
   c. Spread $(\theta_{\sigma_\lambda}, \theta_{\sigma_y}, \theta_{\sigma_x})$
      i. Standard values identified from localizations of 8 color of QDs on glass
      ii. Typical values are 10 nm $(\theta_{\sigma_\lambda})$, 1.14 pixels (θ_{σ_y}), and 0.80 pixels (θ_{σ_x})
   d. Zero used for θ_{bg}
3. Parameter optimization
   a. Newton-Raphson iterative update method used to optimize model parameters
   b. Upper limits for single steps used to aid in convergence.
   c. Alternating iteration scheme
      i. Large parameter space for simultaneous fitting of multiple parameters leads to divergence from expected results; therefore, a scheme for limiting the number of parameters estimated simultaneously has been devised.
      ii. Alternate between fixing and fitting specified model parameters. Typical, scheme depicted below:
         1. 50 iterations: optimize $\theta_\lambda, \theta_y, \theta_x$
         2. 50 iterations: optimize $\theta_I, \theta_\lambda, \theta_y, \theta_x$
         3. 100 iterations: optimize $\theta_I, \theta_\lambda, \theta_{\sigma_\lambda}, \theta_y, \theta_x$
         4. 50 iterations: optimize $\theta_\lambda, \theta_{\sigma_\lambda}, \theta_y, \theta_{\sigma_y}, \theta_x, \theta_{\sigma_x}$

Text B.3.6 Building trajectories from localizations.

Cost matrices are used to build trajectories in two steps: frame-to-frame and gap closing. Physical models are used to derive the costs for linking localizations, starting a

new trajectory (birth), and ending a trajectory (death). The cost for connecting observations 1 and 2 is

$$l_{m,n} = -\log\left(P(x_2, y_2, t_2|x_1, y_1, t_1)P(\lambda_2|\lambda_1)\right).$$

Under the assumption of Brownian motion, the probability of making observation 2 (x_2, y_2, t_2) given observation 1 (x_2, y_2, t_2) is

$$P(x_2, y_2, t_2|x_1, y_1, t_1) = e^{\frac{-(\theta_{x_1}-\theta_{x_2})^2-(\theta_{y_1}-\theta_{y_2})^2}{4D\Delta t+2\sigma_1^2+2\sigma_2^2}},$$

where

$$\sigma_1^2 = \sigma_{\theta_{x_1}}{}^2 + \sigma_{\theta_{y_1}}{}^2$$

is the spatial localization error for observation 1 and σ_2^2 is similarly defined for observation 2. Similarly, due to the spectral emission peak, the probability of making observation 2 (λ_2) given observation 1 (λ_1) is

$$P(\lambda_2|\lambda_1) = \mathrm{erf}\left(\frac{|\theta_{\lambda_1}-\theta_{\lambda_2}|}{\sqrt{2\left(\sigma_{\theta_{\lambda_1}}^2+\sigma_{\theta_{\lambda_2}}^2+\sigma_{\lambda_{\mathrm{jump}}}^2\right)}}\right),$$

where $\sigma_{\lambda_{\mathrm{jump}}}^2$ accounts for the variance in the observed spectral emission peak due to spectral jumping or bluing of individual QDs. The cost for a previously unobserved QD blinking on (birth) or a currently tracked QD blinking off (death) is determined by particle density and estimated blinking rates. Building a cost matrix from physical models is discussed in more detail in a manuscript in preparation by Relich P, Cutler PJ, Huang F, Lidke KA.

The cost matrix built from costs of linking, birth, and death is treated as a linear assignment problem to link localizations into trajectories. The spectral information of localized QDs greatly improves the accuracy of trajectories and permits SPT at higher labeling densities (**Figure S14**).

Text B.3.7 Diffusion coefficient uncertainty.

Assuming Brownian motion, the mean squared displacement for a 2D trajectory is defined as

$$\langle r^2 \rangle = 4D\Delta t,$$

where D is the diffusion coefficient, and Δt is the time lag between observations. The probability distribution of displacements given some underlying diffusion is

$$P(r|D) = \frac{r}{2D\Delta t} e^{\left(\frac{-r^2}{4D\Delta t}\right)}.$$

Given N observed displacements ($\vec{r}$) and an estimator of D that maximizes the likelihood function

$$L(\theta_D|\vec{r}) = \prod_{k=1}^{N} \frac{r_k}{2D\Delta t} e^{\left(\frac{-r_k^2}{2D\Delta t}\right)},$$

information theory uses the Fisher Information Matrix

$$I(\theta_D) = -\mathrm{E}\left[\frac{\partial^2 \log\left(L(\theta_D|\vec{r})\right)}{\partial^2 \theta_D}\right]$$

to define the minimum variance (CRB) with which θ_D can be estimated

$$\sigma_{\theta_D}^2 = I(\theta_D)^{-1} = \frac{D^2}{N}.$$

The average number of observed particles in a region of interest A at a particle density ρ over n frames is

$$\bar{\mathrm{x}} = A\rho n.$$

$\bar{\mathrm{x}}$ is directly related to the number of observed displacements (N); therefore,

$$\sigma_{\theta_D} \approx \frac{D}{\sqrt{A\rho n}}.$$

The difference between $\bar{\mathrm{x}}$ and N is dependent on the number of trajectories.

Text B.3.8 Theoretical performance of line and point scanning systems.

The number of photons that can be captured in a given frame limits the localization accuracy for each emitter in each frame for a given optical system. Fluorescent dyes and quantum dots have a finite excited state mean lifetime, τ, which ultimately bounds the emission rate to $1/\tau$ in the limit of very large excitation intensities. This maximum emission rate is commonly referred to as the saturation rate (i.e. a sample of emitters is exposed to excitation light of such high intensity that essentially none are ever in the ground state as they are immediately excited).

For emission wavelength λ_{em}, numerical aperture NA, overall optical efficiency of the emission path γ, emission rate A, and exposure time t, the theoretical best possible localization accuracy [1] is given by:

$$\delta = \frac{\lambda_{em}}{2\pi(NA)\sqrt{\gamma A t}}$$

In the limit of excited state saturation, $A = 1/\tau$ photons/sec,

$$\delta = \frac{\lambda_{em}}{2\pi(NA)\sqrt{\frac{\gamma t}{\tau}}}$$

If we desire some approximate localization accuracy δ, and wish to find the minimum exposure time required to achieve that, we can rearrange the equation, solving for t:

$$t = \left(\frac{\lambda_{em}}{2\pi(NA)\delta}\right)^2 \frac{\tau}{\gamma}$$

If we consider a single emitter species, say quantum dot 625, with a peak emission wavelength of 625 nm and mean excited state lifetime of 20 ns, a system with a numerical aperture of 1.2, and overall optical transmission efficiency of 0.04 (including detector efficiency and solid angle acceptance of the objective), then a desired localization accuracy of 10 nm would require an exposure time of ~31 μs for that emitter.

A point scanning system would use the required exposure time as the pixel dwell time (the amount of time the excitation beam must stay at each (x,y) pixel position on the sample). Since a point scanning system raster scans the point over the sample region of interest one (x,y) pixel position at a time, the maximum overall frame rate is

$$r_{point} = \frac{1}{\left(t * N_x * N_y\right)}$$

where N_x is the number of pixels in x and N_y is the number of pixels in y. A line scanning system will have the same dwell time, but this will be for an entire row (or column) of pixels, so the frame rate is

$$r_{line} = \frac{1}{\left(t * N_x\right)}$$

In the case where we have a region of interest that is composed of 128×128 spatial pixels, for the desired localization accuracy and system described above, r_{point} is ~2 fps and r_{line}

is ~250 fps. This illustrates not only a performance advantage of line scanning over point scanning systems, but also that the theoretical frame rate is much higher than currently possible with camera technology that is available at the time of this writing, and this is a key area of potential improvement as camera speeds increase.

References

1. Ober RJ, Ram S, Ward ES (2004) Localization accuracy in single-molecule microscopy. Biophysical journal 86: 1185–1200. Available: http://www.pubmedcentral.nih.gov/articlerender.fcgi?artid=1303911&tool=pmcen trez&rendertype=abstract.

B.4 Supplementary Tables

Table B.4.1 Description of Gaussian fitting variables.

Symbol	Description
	General Variables
λ	Spectral position
y	Spatial position along the line
x	Spatial position in the scan direction
λ_{width}	Width of a spectral pixel
μ_k	Counts in pixel k of single QD model
$\mu_{k_{All}}$	Counts in pixel k of N QD model with background
d_k	Counts in pixel k of experimental image
σ_θ	Theoretical error (standard deviation) for model parameter as approximated by the Cramér Rao Bound
	Model Parameters for an individual QD
θ_I	Photon counts
θ_λ	Position of spectral emission peak of QD
θ_{σ_λ}	Spectral spread (standard deviation) of QD
θ_y	Position of QD along y (line) dimension
θ_{σ_y}	Microscope point spread function in y (line) dimension
θ_x	Position of QD along x (scan) dimension
θ_{σ_x}	Microscope point spread function in the x (scan) dimension
θ_{bg}	Background offset

Table B.4.2 Single QD Characterization

Statistics for results shown in **Figure S12** are summarized in this table. Additional descriptions of the model parameters are included in **Table S1**.

Invitrogen QD specie	Number of localizations	θ_λ (nm) mean	θ_λ (nm) stdev	θ_{σ_λ} (nm) mean	θ_{σ_λ} (nm) stdev	θ_I (counts) mean
QD525	1527	525	7	8	2	208
QD565	23053	563	9	9	2	411
QD585	28777	587	10	9	2	541

QD605	36216	607	7	8	2	956
QD625	52666	622	9	10	2	800
QD655	17147	653	8	11	2	1218
QD705	25731	696	17	17	4	412
QD800	5795	733	15	15	4	209

APPENDIX C: SUPPLEMENTARY INFORMATION FOR CHAPTER 4

C.1 Supplementary Figures
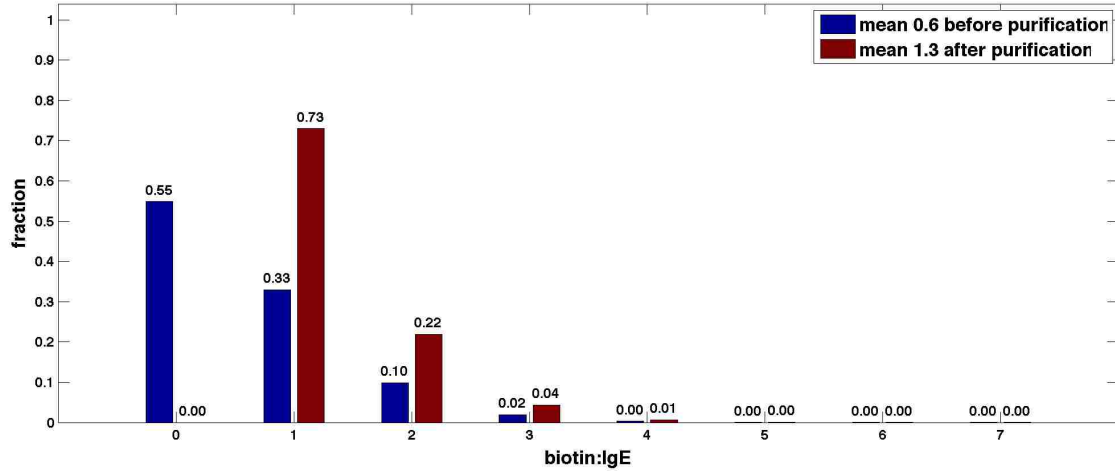
Supplementary Figure C.1.1 Theoretical distribution of biotin:IgE due to Poisson statistics before (blue) and after (red) the removal of non-biotinylated IgE.
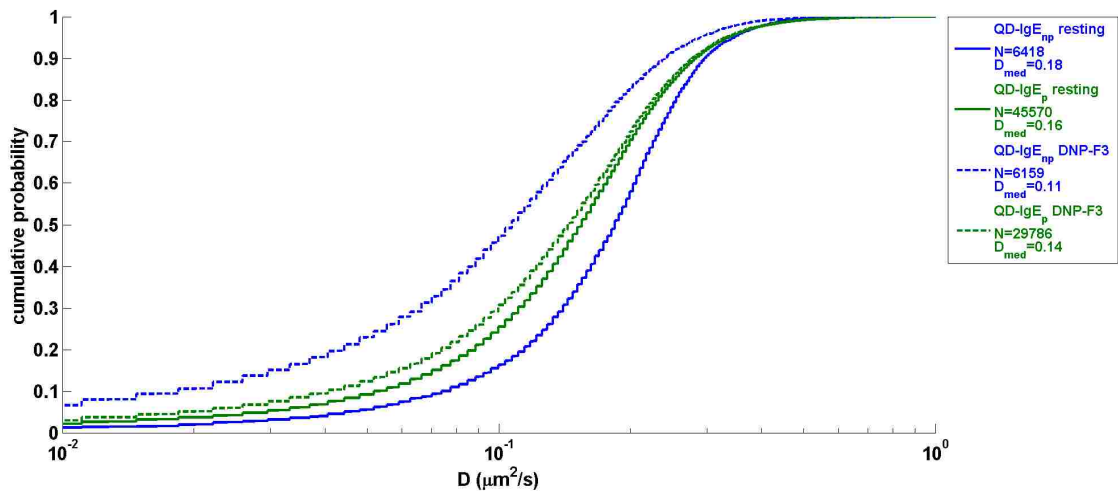
Supplementary Figure C.1.2 CPA plot of D for QD-IgE$_p$-FceRI and QD-IgE$_{np}$-FceRI. D is quantified for all trajectories an all acquisitions for each condition. N is the number of trajectories, and D$_{med}$ is the median diffusion coefficient.
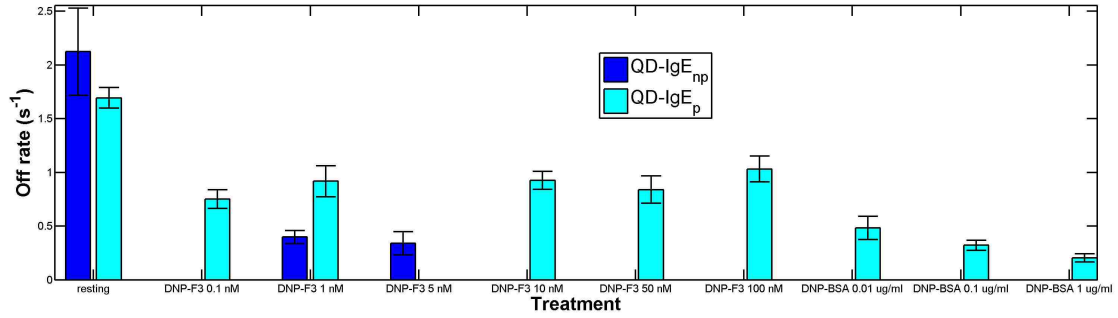
Supplementary Figure C.1.3 Off rates for QD-IgE$_p$-FceRI with variable crosslinkers and crosslinker concentrations.
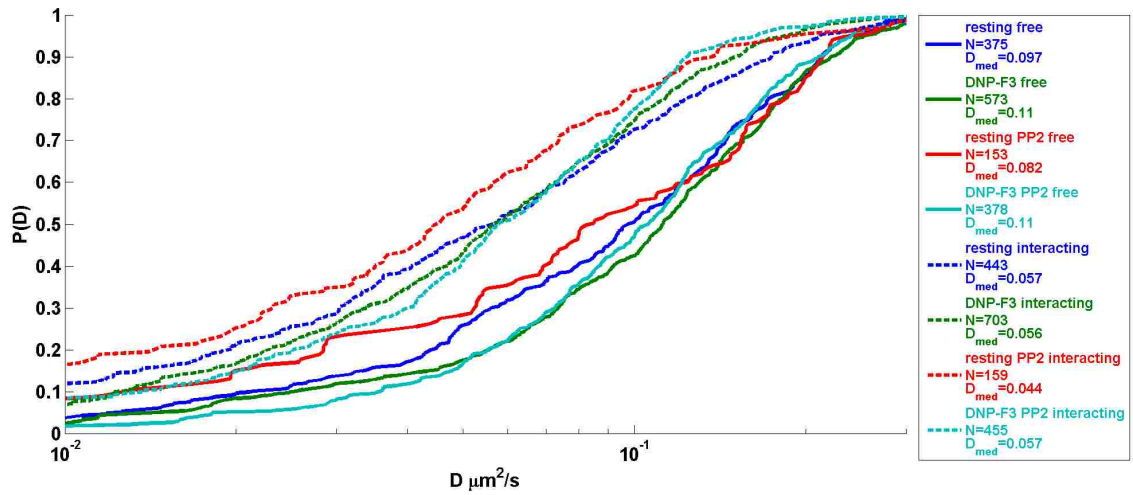
Supplementary Figure C.1.4 CPA plot of D for free and interacting trajectory segments of QD-IgE$_p$-FceRI. Free and interacting segments are determined by Viterbi analysis of HMM results.
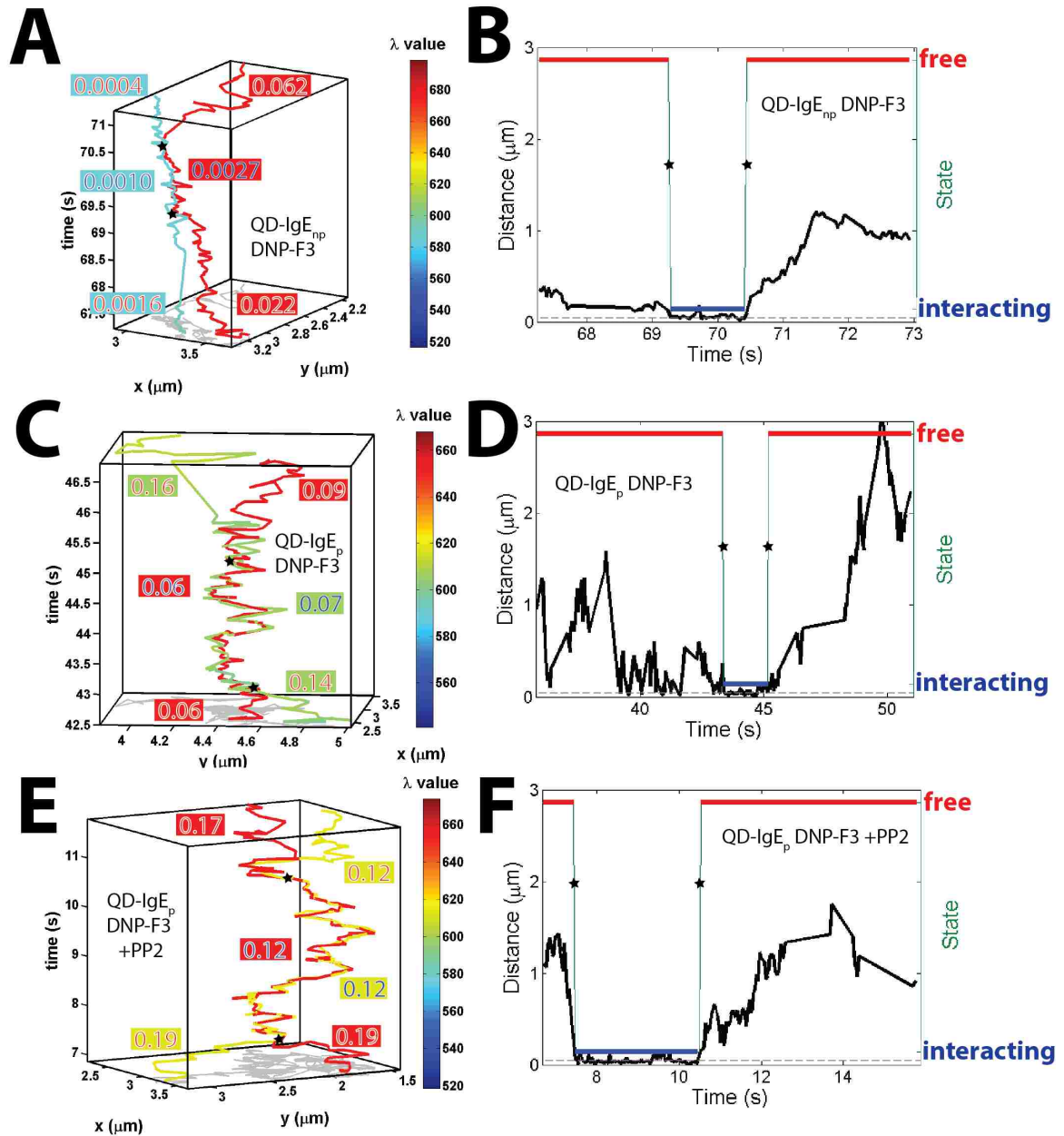
Supplementary Figure C.1.5 Examples of transient interactions for QD-IgE_np-FceRI and QD-IgE_p-FceRI. (A), (C), and (E) show examples of a transient interactions observed in mcSPT experiments, and corresponding Viterbi state distribution are included in (B), (D), and (F) respectively. The color scheme for trajectories in (A), (C), and (E) represent the estimated emission peak for the individually localized QDs. The background and foreground colors for the diffusion coefficients in (A), (C), and (E) correspond to the trajectory color and state respectively. The 68% credible interval for values of D in (B), (C), and (E) are included in **Supplementary Table C.2.2**. Stars highlight transitions between free and interacting states.
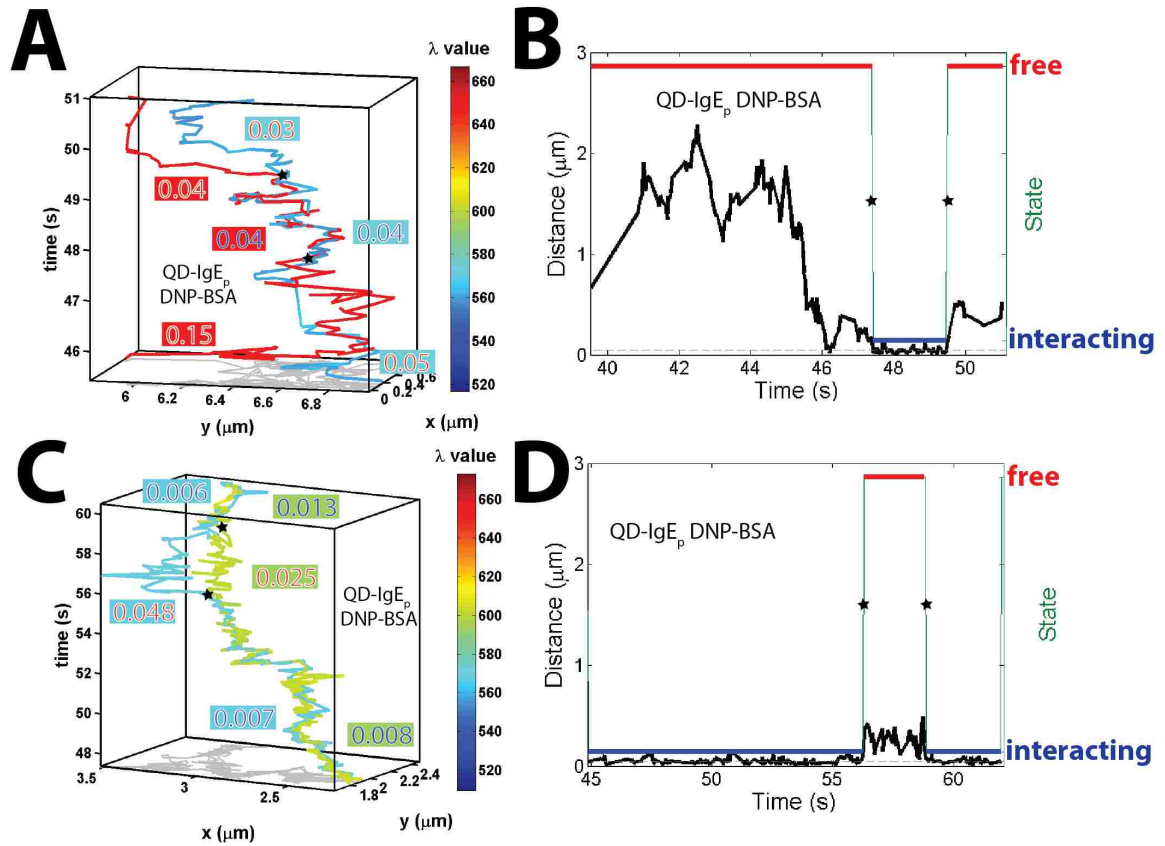
Supplementary Figure C.1.6 Examples of transient interactions for QD-IgE$_p$-FceRI. (A) and (C) show examples of a transient interactions observed in mcSPT experiments, and corresponding Viterbi state distribution are included in (B) and (D) respectively. The color scheme for trajectories in (A) and (C) represent the estimated emission peak for the individually localized QDs. The background and foreground colors for the diffusion coefficients in (A) and (C) correspond to the trajectory color and state respectively. The 68% credible interval for values of D in (B) and (D) are included in **Supplementary Table C.2.2**. Stars highlight transitions between free and interacting states.
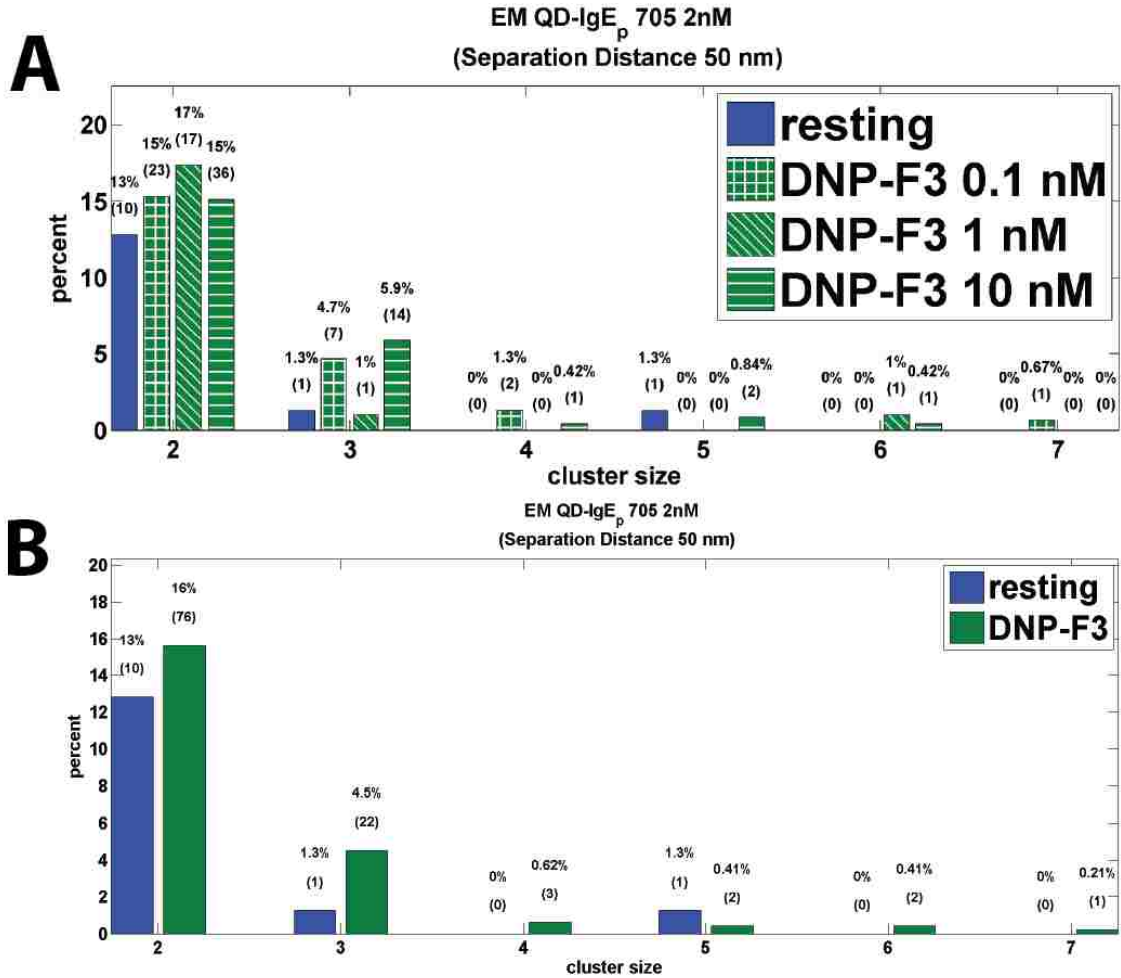
Supplementary Figure C.1.7 Distributions of cluster sizes observed for QD-IgE$_p$-FcεRI crosslinked with DNP-F3 in EM. (A) Distribution of cluster sizes for variable treatments with DNP-F3. (B) Variable treatments with DNP-F3 from (A) are pooled together. The percent and number of observations (parentheses) are shown above each bar.

C.2 Supplementary Tables

Supplementary Table C.2.1 Off rates and D from HMM analysis of mcSPT data.

Treatment	Number of acquisitions	Candidate pairs	Observed interactions	Off rate[a] s^{-1}	D_{all}[b] $\mu m^2/s$	D_{free}[c] $\mu m^2/s$	$D_{interacting}$[d] $\mu m^2/s$
QD-IgE$_{np}$ resting	11	708	24	2.1 (0.4)	0.18	0.13	0.12
QD-IgE$_{np}$ DNP-F3	24	748	56	0.42 (0.05)	0.11	0.05	0.02
QD-IgE$_p$ resting	105	7960	293	1.7 (0.1)	0.16	0.10	0.06
QD-IgE$_p$ DNP-F3	92	4656	348	0.88 (0.05)	0.14	0.11	0.06
QD-IgE$_p$ DNP-BSA	41	1674	152	0.33 (0.03)	0.12	0.09	0.06
QD-IgE$_p$ resting + PP2	32	3271	123	2.9 (0.3)	0.15	0.08	0.04
QD-IgE$_p$ DNP-F3 + PP2	33	2472	214	0.88 (0.06)	0.14	0.11	0.06
DNP-QD	13	1493	88	0.59 (0.07)	0.11	0.09	0.05

[a]Values correspond with the bar graph in **Figure 4.2A**. Error in the fit is included in parentheses.

[b]Median D for all trajectories.

[c]Median D for free trajectory segments.

[d]Median D for interacting trajectory segments.

Supplementary Table C.2.2 D and credible interval for all examples of transient interactions.

Treatment[a]	Figure	Emission peak[b]	D for free and interacting segments[c]		
			1	2	3
QD-IgE$_p$ DNP-F3	4.2C	579	0.22 (0.18,0.41)	0.07 (0.06,0.10)	0.16 (0.14,0.20)
		620	0.14 (0.12,0.19)	0.08 (0.07,0.10)	0.15 (0.13,0.17)
DNP-QD	4.2E	613	0.12 (0.10,0.16)	0.05 (0.04,0.06)	0.11 (0.09,0.14)
		693	0.13 (0.10,0.18)	0.04 (0.04,0.05)	0.12 (0.11,0.16)
QD-IgE$_{np}$ DNP-F3	C.1.5A	586	0.002 (0.001,0.003)	0.001 (0.0007,0.002)	0.0004 (0.0002,0.0013)
		677	0.02 (0.02,0.03)	0.003 (0.002,0.005)	0.06 (0.05,0.09)
QD-IgE$_p$ DNP-F3	C.1.5C	608	0.14 (0.12,0.18)	0.07 (0.06,0.09)	0.16 (0.13,0.20)
		653	0.06 (0.05,0.08)	0.06 (0.05,0.07)	0.09 (0.08,0.11)
QD-IgE$_p$ DNP-F3 + PP2	C.1.5E	612	0.19 (0.16,0.27)	0.12 (0.11,0.14)	0.12 (0.11,0.15)
		654	0.18 (0.16,0.27)	0.12 (0.11,0.14)	0.17 (0.15,0.21)
QD-IgE$_p$ DNP-BSA	C.1.6A	561	0.05 (0.04,0.06)	0.04 (0.03,0.05)	0.03 (0.03,0.04)
		650	0.15 (0.14,0.19)	0.04 (0.04,0.06)	0.04 (0.03,0.06)
QD-IgE$_p$ DNP-BSA	C.1.6C	570	0.007 (0.006,0.008)	0.05 (0.04,0.07)	0.006 (0.004,0.009)
		602	0.008 (0.007,0.009)	0.04 (0.04,0.05)	0.01 (0.01,0.02)

[a]Colored by treatment corresponding to **Figure 4.2A** and **Supplementary Table C.2.1**

[b]Colored by average emission peak (nm) for specific trajectory (i.e. color of trajectories in corresponding figure).

[c]Median D ($\mu m^2/s$) for all trajectory segments with a given state. The state is indicated by the font color corresponding to the color scheme for free (red) and interacting (blue). Credible interval (68%) as estimated by the posterior mode diffusion estimator is included in parentheses (lower credible interval,upper credible interval).

APPENDIX D: UNM SINGLE PARTICLE TRACKING

USER MANUAL

Created by Patrick Cutler
June 2013

Table of Contents

Overview

The SPT class was developed by the Lidke Lab at UNM to localize and track features in single particle tracking data. The class is based on the diagram in **Figure 1**.

Note: It is strongly recommended to follow the flow diagram (on the left of **Figure 1**) for the initial
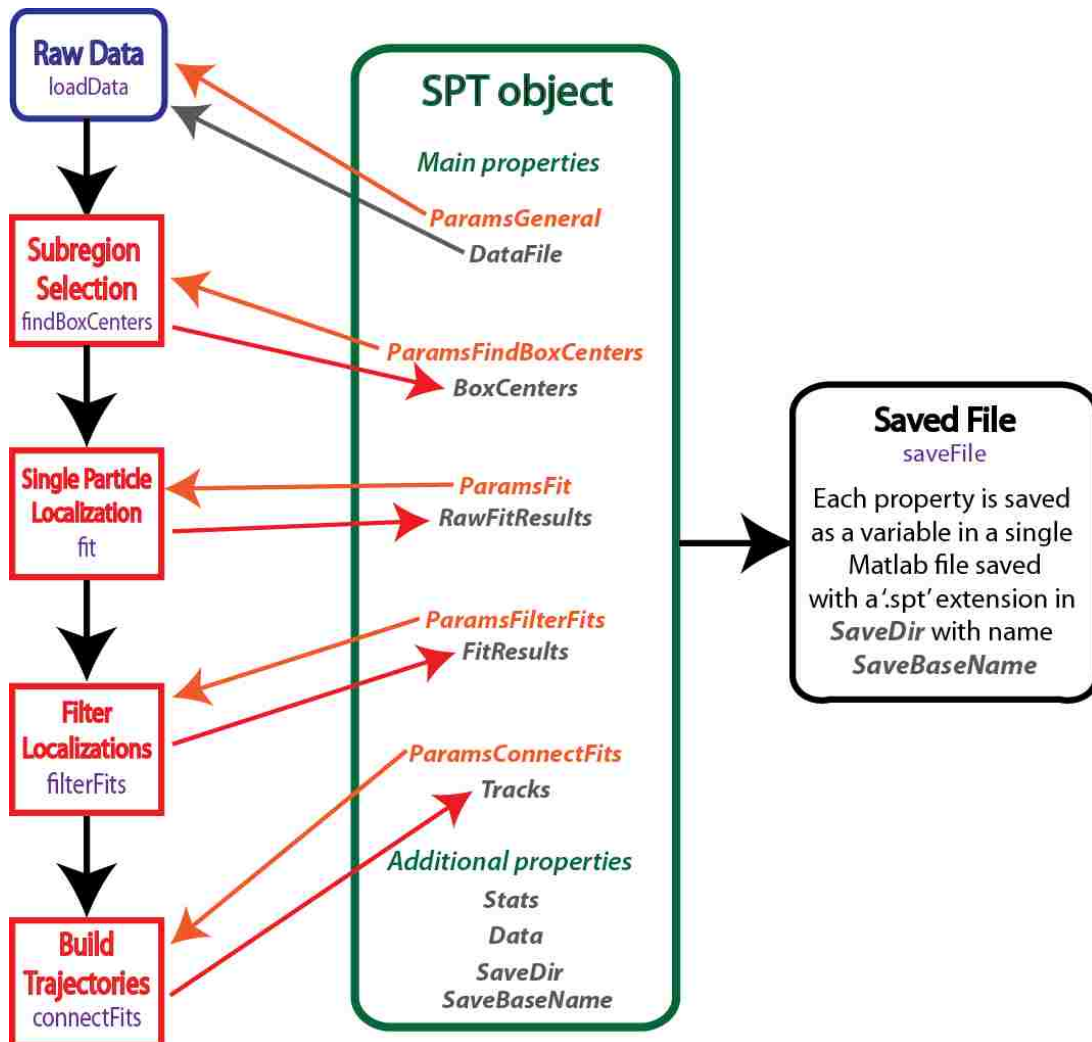

Figure 1. Organization of the SPT Class. The typical flow for populating properties of the SPT class is demonstrated with the flow diagram to the left. Steps in the SPT process are shown in red and methods are shown in purple. The properties for an SPT object are documented in the center of the diagram, and arrows are used to demonstrate the interplay between SPT object properties and tracking steps. All parameter properties begin with 'Params' and are highlighted in orange. An SPT object is saved in a '.spt' file (black box to the right).

optimization of fitting parameters.

Setup

The UNM SPT class is located in the Lidke Lab SPT repository and has dependencies on the Lidke Lab Shared and GPUgaussMLEv2 repositories. The SPT class is dependent on dipimage. Adding the following lines of code in your startup will initialize the SPT class under the assumption that all required repositories are in the default user path. After initialization run SPT.test to test the methods of the SPT class on your system.

```
%get default user path
matroot = userpath;
matroot = matroot(1:end-1);
SPTdir = fullfile(matroot,'SPT','tags','RC1'); %fullpath for directory
containing @SPT folder
addpath(SPTdir); %add directory to path
startup_SPT %use startup_SPT to initialize SPT class and all dependencies
```

Note: startup_SPT will initializes dipimage.

Note1: If you are setting up the SPTHSI subclass, then the SPT class will be setup automatically. Follow the Setup instructions for SPTHSI subclass.

Common Usage

The following lines of code in Matlab will initialize an empty object and open the GUI (**Figure 2**). See the **Graphical User Interface** section for more details.

```
sptObj = SPT;    %make empty SPT object
sptObj.gui;      % Initalize GUI (tasks performed in the GUI are performed on
sptObj variable)
```

Data can then be loaded and parameters optimized for fitting and tracking data. Parameters should be optimized for each channel. Note that multi-channel data is tracked separately using different regions of interest (ROIs) on the camera and the 'SaveAppendix' variable in the ParamsGeneralParmeters (i.e. General Parameters button) is used to identify different channels. Parameter optimization should only need to be performed once for a particular type of data. It is strongly suggested to progress through the *action buttons* (i.e. *Find Sub Regions*, *Localize Sub Regions*, *Filter Localizations*, and *Track Filtered Coordinates*) in the optimization procedure. Note that previously saved parameters files can be loaded using the *File Settings* button.

Once parameters are optimized they are saved from the GUI and batch tracking can be performed to track multiple data sets and channels. An example batch tracking script is included below.

```matlab
% batchTracking

close all
clear all


%define data directory
dataDir = 'I:\Pat Documents\Research\DATA\2013_08_06 RBL Syk-GFP QDdnp';

%define save directory
saveDir = fullfile(dataDir,'results');

%define params file
paramsFile{1} = fullfile(saveDir,'scripts','QDdnpSPTparams.mat');
paramsFile{2} = fullfile(saveDir,'scripts','SykGFPSPTparams.mat');

%find data files
dataFiles = dir(fullfile(dataDir,'rbl*.mat'));
dataFiles = cellfun(@(x)
fullfile(dataDir,x),{dataFiles.name},'UniformOutput',false);
% %only track specific files
% fileNums = 5:7;
% dataFiles = dataFiles(fileNums);

multiWaitbar('paramsFile','close');
multiWaitbar('paramsFile',0);

for ii = 2%1:numel(paramsFile)
    close all

    %perform batch tracking
    SPT.trackBatch(paramsFile{ii},dataFiles,saveDir);

    %make summary html
    SPT.summary(saveDir);

    multiWaitbar('paramsFile',ii/numel(paramsFile));
end
multiWaitbar('paramsFile','close');
```

Once data is tracked using the trackBatch method there will be a '.spt' file in the results folder for each tracked data set.

Graphical User Interface

- The top row of buttons contains *action buttons*.

- o These buttons perform the actions specified.
- o Where applicable figures are made and statistics are shown in the *display panel* (**Figure 4**).
- o *Action buttons* are red (Figure 2) if corresponding properties are not populated and green (**Figure 3** and **Figure 4**) if corresponding properties are populated.
- o If properties are not populated, then the necessary properties will be populated upon pressing the *action button*.
- The column of buttons to the right contains the *parameters buttons*.
  - o These buttons are used to set object parameters.
  - o A dialogue or the *display panel* is used to set parameters upon pressing the any of the parameter buttons.
- The panel in the center of the GUI is the *display panel*.
  - o The *display panel* is used to display statistics or to set parameters.
  - o Examples of setting parameters for File Settings are included Figure 2 and Figure 3.
  - o An example of display statistics is shown in Figure 4.
- The bottom row of buttons contains the *organizational buttons*.
  - o These buttons are used to organize files and figures.
  - o *Save* – saves a '*.spt' file
  - o *Load* – loads a '*.spt' file
  - o *Save Parameters* – saves the current parameters into an '*SPTParams.mat' file
  - o *Close Figures* – closes all current figures that are not SPT.gui figures
  - o *Tile Figures* – tiles figures for easy viewing
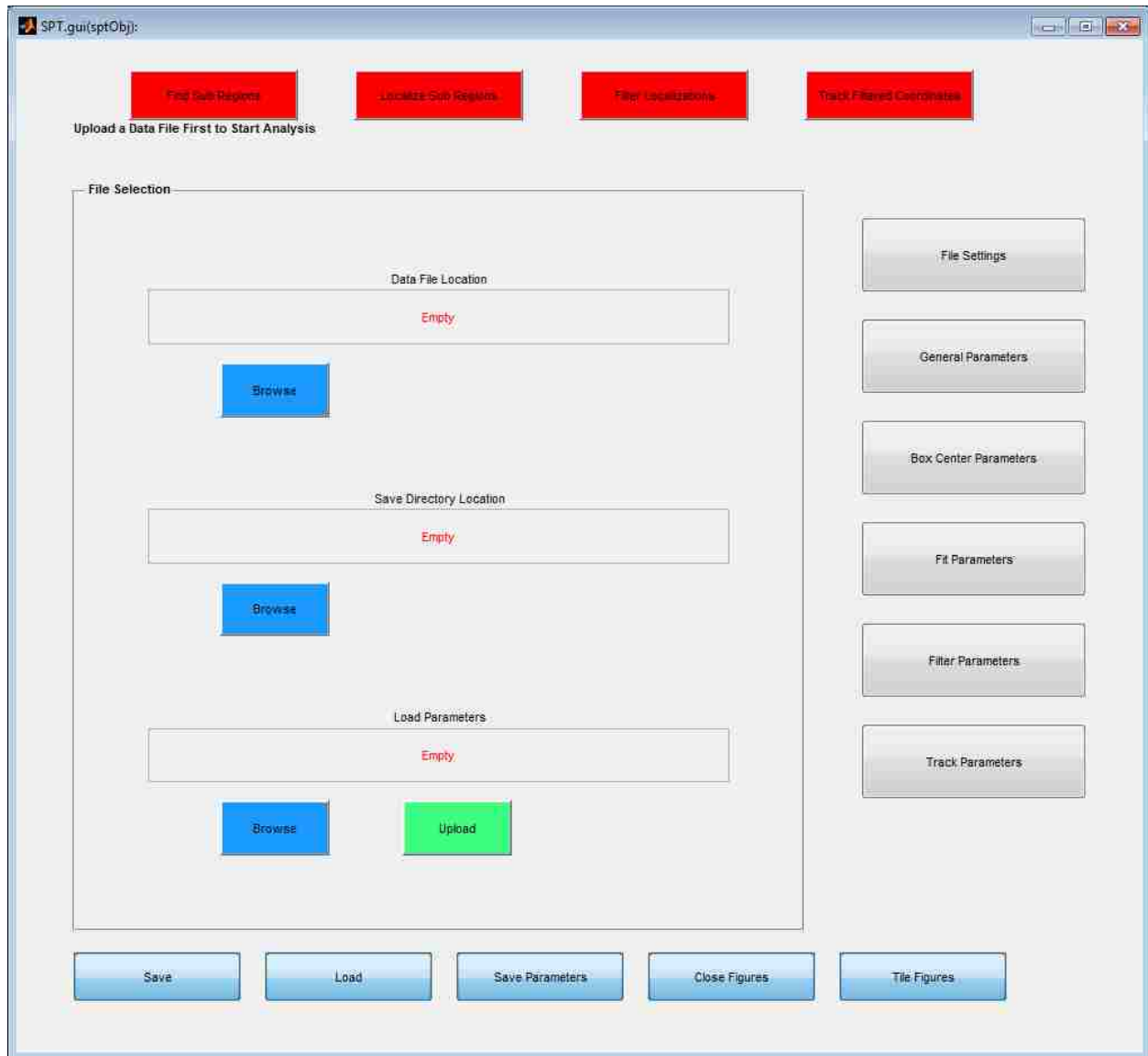
Figure 2. GUI for an empty SPT object.

Figure 3. GUI for a populated SPT object.
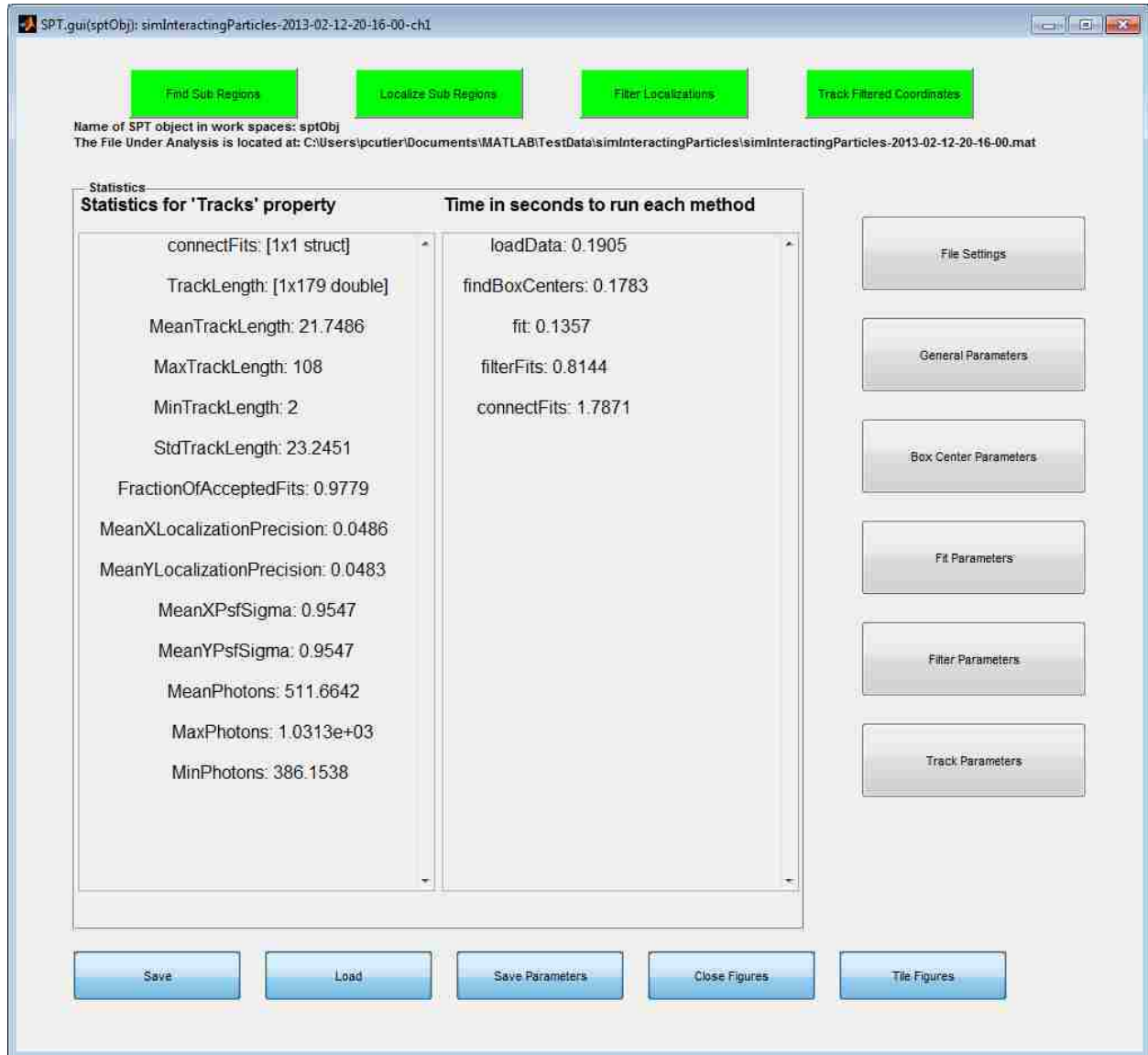
Figure 4. GUI for a population SPT object with trajectory statistics.

Summarizing Results

After tracking a batch of data using the method trackBatch, several figures are saved and an html summary of results can be easily generated using the summary method. When opened in the Matlab web browser the GUI or any figures can be opened directly from the html.

SPT class

Properties
```
DataFile - full path of file in which raw data is stored. Default []

BoxCenters - structure with centers for subregions in which to loacalize
individual features
Populated by findBoxCenters method
IF THE USER CHANGES ANY VALUE IN BoxCenters PROPERTY, THEN THE PROPERTIES
RawFitResults, FitResults, Tracks, AND Stats (spcific fields) BECOME INVALID
AND ARE CLEARED.

RawFitResults - structure with results from localizations
Populated by fit method
Property cannot be altered by user
IF RawFitResults IS ALTERED, THEN THE PROPERTIES FitResults, Tracks, AND
Stats (spcific fields) BECOME INVALID AND ARE CLEARED.

FitResults - structure array with filtered localization information with
dimensions (1 by time). Each field contains informatoin for all localizations
passing the Filtering params. Below is a list of fields:
```
- xCoord: x-coordinates of detected features. 1st column: value, 2nd column: standard deviation (zeros if not available).
- xSigma: psf sigma for x-coordinates of detected features. 1st column: value, 2nd column: standarddeviation parameter estimation (zeros if not available).
- yCoord: y-coordinates of detected features. 1st column: value, 2nd column: standard deviation (zeros if not available).
- ySigma: psf sigma for y-coordinates of detected features. 1st column: value, 2nd column: standard deviation parameter estimation (zeros if notavailable).
- Photons: "Intensities" of detected features. 1st column: values (ones if not available), 2nd column: standard deviation (zeros if not available).
- bg: "background" correspoding to each fit. 1st column: values (ones if not available), 2nd column: standard deviation (zeros if not available).
- merit: merit value indicating the quality of fit
- roiIdxAll: index for the region of interest in RawFitResults from which localization originated. Relative ROIs fit for all frames
- roiIdxFrame: index for the region of interest in RawFitResults from which localization originated. Relative to ROIs fit for the respective time frame
- model: number of emitters fit to the model selected

www.manaraa.com

- modelIdx: index for specific emitter

Populated by filterFits method. User can manually populate this property, but the format needs to be correct for tracking to work appropriately
Property is used to build trajectorie in connectFits method
IF FitResults IS ALTERED, THEN THE PROPERTIES Tracks, AND Stats (specific fields) BECOME INVALID AND ARE CLEARED.

Tracks - structure array with track information. Each element of the array contains information for a single trajectory. Each field contains an array with dimensions 1 by number of observations with details about the specified track property. Below is a list of fields:

- X: position in x dimension
- std_x: theoretical standard deviation of position estimate x dimension
- sigma_x: estimated PSF for x dimension
- std_sigma_x: theoretical standard deviation for estimated PSF for x dimension
- Y: position in y dimension
- std_y: theoretical standard deviation of position estimate y dimension
- sigma_y: estimated PSF for y dimension
- std_sigma_y: theoretical standard deviation for estimated PSF for y dimension
- Photons: estimated intensity in photons/frame
- std_Photons: theoretical standard deviation for estimated intensity
- Frame: time frame for each observation
- roiIdxAll: index for the region of interest in fit results from which localization originated. Relative ROIs fit for all frames
- roiIdxFrame: index for the region of interest in fit results from which localization originated. Relative to ROIs fit for the respective time frame
- model: number of emitters fit to the model selected
- modelIdx: index for specific emitter

Populated by connectFits method
Property cannot be altered by user

Stats - structure with statistical fitting/tracking information. Contains the following fields:

- methodTime: time needed to perform specified method
- Data: statistics about Data property
- RawFitResults: statistics about RawFitResults property
- FitResults: statistics about FitResults propterty
- Tracks: statistics about Tracks property
- Populated during the population of each propterty. If properties are invalidated by changing properties, then corresponding Stats fields are also cleared.

Property cannot be altered by user

SaveDir - full path for directory in which to save results. Default []
Note: if isempty and DataFile is defined SaveDir defaults to fullfile(obj.DataPath,'results')

Parameter Properties

ParamsGeneral - structure with general parameters for data loading and preprocessing.
IF THE USER CHANGES ANY PARAMETERS IN ParamsGeneral PROPERTY,
THEN THE PROPERTIES Data, BoxCenters, RawFitResults, FitResults, Tracks, AND Stats BECOME INVALID AND ARE CLEARED.

ParamsFindBoxCenters - structure with parameters for subregions of interest for localization.
Parameters used by findBoxCenters method
IF THE USER CHANGES ANY PARAMETERS IN ParamsFindBoxCenters PROPERTY, THEN THE PROPERTIES BoxCenters, RawFitResults, FitResults, Tracks, AND Stats BECOME INVALID AND ARE CLEARED.

ParamsFit - structure with localization parameters.
Parameters used by fit method
IF THE USER CHANGES ANY PARAMETERS IN ParamsFit PROPERTY,
THEN THE PROPERTIES RawFitResults, FitResults, Tracks, AND Stats (specific fields) BECOME INVALID AND ARE CLEARED.

ParamsFilterFits - structure with parameters for filtering localizations.
Parameters used by filterFits method
IF THE USER CHANGES ANY PARAMETERS IN ParamsFit PROPERTY, THEN THE PROPERTIES FitResults, Tracks, AND Stats (specific fields) BECOME INVALID AND ARE CLEARED.

ParamsConnectFits - structure with parameters for connecting localizations into tracks.
Parameters used by connectFits method
IF THE USER CHANGES ANY PARAMETERS IN ParamsFit PROPERTY, THEN THE PROPERTIES Tracks, AND Stats (specific fields) BECOME INVALID AND ARE CLEARED.

Transient Properties

Data - dipImage object with background subtracted and gain corrected data.
transient property that is not saved

FigInfo - information about figures
helps to keep track of current figure handles
transient property that is not saved

Dependent Properties

DataPath - folder containing DataFile

DataBaseName - base name of data file (DataFile without path or extension)

DataBaseTitleName - DataBaseName of data file (with '_' replaced with '-' underscores)

SaveBaseName - base name for saving results [DataBaseName '-' SaveAppendix]

SaveBaseTitleName - SaveBaseName of file (with '_' replaced with '-' underscores)

Methods

A brief description for each method is included below. Use the Matlab help or doc feature for more complete descriptions of each method.

Tracking Methods

`loadData` - load raw data

`findBoxCenters` - populate BoxCenters property

`filerFits` - filter RawFitResults property to populate FitResults property

`connectFits` - build trajectories and populate Tracks property

Class Manipulation Methods

`getTracks` - get reformatted trajectories and localization accuracies

`importTracks` - import trajectories tracked using another method

`trackBatch` - track batch of files

`saveFile` - save object into *.spt file

`loadFile` - load *.spt file into object

`summary` - make html summary for spt figures

`saveFig` - save figure in default format and directory

`findFigs` – find figures corresponding to all spt files

`makeRoiStack` - make stack of ROI's from BoxCenters

`copy` - make a deep copy of object

`test` - test SPT class

Plotting Methods

Note: If a property necessary for a plotting feature is not populated then it will be automatically populated.

`plotBoxCenters` - creates a plot of BoxCenters

`plotFitResults` - color overlay of Gaussian Blobs for FitResults property BoxCenters

`plotFitResultsHist` – plot histograms for raw fit results

`plotRawFitResults` - creates a color overlay from Gaussian Blobs

`plotRawFitResultsHist` - plot histograms for raw fit results

```
plotTracks - plot color coded trajectories

plotTracksDipImage - make dipTrack figure

plotTracksHist - plot histograms for Tracks
```

Parameter Methods
```
saveParams - save params file '*SPTparams.mat'

setParams - set parameter properties

getDefaultParams - get default parameters

getDefaultParamsGeneral - get default values for ParamsGeneral

getDefaultParamsFindBoxCenters - get default values for ParamsFindBoxCenters

getDefaultParamsFit - get default values for ParamsFit

getDefaultParamsFilterFits - get default values for ParamsFilterFits

getDefaultParamsConnectFits - get default values for ParamsConnectFits
```

Additional Features

Plotting Tools
Several tools used by the SPT class that are useful for investigating single particle tracking data independent of the SPT class are discussed in this section.

plotTracksV1

Interactive Features

dipTrack

Interactive Features

dipSubLoc2D

Analyzing Single Particle Trajectories
The following classes are located in the Lidke Lab SM_Analysis repository and are dependent on the appropriate setup of the SPT class. Setting up the SPT class will also setup the following classes under the assumption that all required repositories are in the default user path.

SPTANALYSIS_MOBILITY class
This class contains standard methods used to quantify the mobility of single particle trajectories in an SPT object.

Properties

```
TracksInfo - tracks in the format of track number by time by number of
spatial dimensions

SaveDir - directory under which to make analysis folder for saving results

BaseName - base name for SPT file

PixelSize - pixel size in microns

TimeStep - time step in seconds

BaseTitleName - BaseName of data file (with '_' replaced with '-'
underscores)
```

SPTANALYSIS_INTERACTIONS class

This class contains standard methods used to quantify interactions of single particle trajectories in SPT object(s).

SPTANALYSIS_GROUP class

This class contains standard methods for analyzing groups of SPT objects.

SPTHSI subclass

Setup

The UNM SPTHSI class is located in the Lidke Lab HSM repository and is dependent on the Lidke Lab SPT repository and any repositories on which the SPT class is dependent. Adding the following lines of code in your startup will initialize the SPTHSI class under the assumption that all required repositories are in the default user path. After initialization run SPTHSI.test to test the methods of the SPTHSI class on your system. Additionally run SPT.test to verify that the SPT class is properly setup.

```
%get default user path
matroot = userpath;
matroot = matroot(1:end-1);
SPTHSIdir = fullfile(matroot,'HSM','Development','SPTHSI_class'); %fullpath
for directory containing @SPTHSI folder
addpath(SPTHSIdir); %add directory to path
startup_SPTHSI %use startup_SPTHSI to initialize SPTHSI class and all
dependencies
```

Note: startup_SPTHSI will also initialize the SPT class and dipimage.

Methods

Note: SPTHSI is a subclass of SPT. Many of SPT methods are overloaded for the SPTHSI sub class. Methods unique to the SPTHSI subclass are presented here.

```
plotBoxCenters - plot BoxCenters property for a single frame in 3-D
```

hyperView - display hyperspectral image in hyperView

hyperViewROI - show current ROI in hyperView

plotFitResultsBrowser - browse FitResults figures

printFitResults - print indices for fits in current frame that passed
filtering criteria

printRawFitResults - print RawFitResults for current box

initialize_gpuGaussNDmleV1_Input - initilize input for gpuGaussNDmleV1

Example Scripts

Examples for using SPT class (SPTtesting)

```
% SPTtesting
%
% test ALL methods for SPT class
%
% Any new methods must be added to testing script

%% initialize object

% close all
% clear all
% clear classes
%
% matroot = userpath;
% matroot = matroot(1:end-1);
% TestDataDir = fullfile(matroot,'TestData');

clc

%index for data file to analyze
fileNum = 1;

%initialize SPT object
obj = SPT;

%specify data file
dataDir = fullfile(TestDataDir,'simInteractingParticles');
dataFiles = dir(fullfile(dataDir,'sim*.mat'));

if isempty(dataFiles)
    error('SPTtest:noData','SPT.test: test data files not found.')
end

%get data file
obj.DataFile = fullfile(dataDir,dataFiles(fileNum).name);
```

```matlab
%set general parameters
obj.ParamsGeneral.Roi = [0 63 0 63];
obj.ParamsGeneral.PixelSize = 0.1;
obj.ParamsGeneral.TimeStep = 0.05;
obj.ParamsGeneral.SaveAppendix = 'ch1';
obj.ParamsFindBoxCenters.MinPhotons = 10;
obj.ParamsFilterFits.MinPhotons = 10;
obj.ParamsConnectFits.costMatF2F.D = [0.5 0.5];
obj.ParamsConnectFits.costMatGC.D = [0.5 0.5];

%% reset results directory

if exist(fullfile(obj.SaveDir),'file')
    rmdir(fullfile(obj.SaveDir),'s')
end


%% load Data

obj.loadData;

%% save .spt file no tracked results (raw data should not be saved)

obj.saveFile;

%% save params file

obj.saveParams([],'ch1');


%% load .spt file (object prior to tracking)

sptFile = fullfile(obj.SaveDir,[obj.SaveBaseName '.spt']);

obj2 = SPT.loadFile(sptFile);


%% find BoxCenters

obj.findBoxCenters

%% makeROIStack (make stack of regions of interest)

[ROIStack XRoiStart YRoiStart Frame] = obj.makeRoiStack;

%% fit (user defined ROIStack)

obj.fit(ROIStack,XRoiStart,YRoiStart,Frame);

%% fit
```

176

```
obj.fit;

%% plotRawFitResultsHist (display histograms for fitting results)

obj.plotRawFitResultsHist;

%% plotRawFitResultsHist (display histograms for fitting results save
figures)

obj.plotRawFitResultsHist(1);

%% plotRawFitResults (display fitting results)

obj.plotRawFitResults;

%% plotRawFitResults (display fitting results with boxes and loclazations)

obj.plotRawFitResults(1,1);

%% plotRawFitResults (display fitting results with boxes)

obj.plotRawFitResults(1);

%% plotRawFitResults (display fitting results with loclazations)

obj.plotRawFitResults(0,1);

%% fitlerFits

obj.filterFits;

%% plotFitResultsHist (display histograms for fitting results)

obj.plotFitResultsHist;

%% plotFitResultsHist (display histograms for fitting results save figures)

obj.plotFitResultsHist(1);

%% plotFitResults (display fitting results)

obj.plotFitResults;

%% plotFitResults (display fitting results with boxes and loclazations)

obj.plotFitResults(1,1);

%% plotFitResults (display fitting results with boxes)

obj.plotFitResults(1);

%% plotRawFitResults (display fitting results with loclazations)
```

```
obj.plotFitResults(0,1);

%% connectFits

obj.connectFits;

%% getTracks in old format

[tracks tracksStd subRegionModel] = obj.getTracks;

%% plotTracks (save result)

h = obj.plotTracks(1,1);

%% plotTracks (save result)

h = obj.plotTracks;
obj.saveFig(h,'plotTracks','plotTracks');
obj.saveFile;

%% plotDipTrack (make dipTrack figure)

obj.plotTracksDipImage;

%% plotTracks (plot several sets of tracks with different colors)

numTracks = numel(obj.Tracks); %get total number of tracks
options = plotTracksV1SetOptions;%initialize plotting opitons
options.highlightTracks = 0; %don't highlight tracks in first plot instance
options.trackNum = 1:floor(numTracks/2); %specify tracks
options.colorByValue = 0; %use color specified on next line
options.color = [1 0 1]; %plot first half of tracks magenta
options.cmap = [1 0 1; 0 1 0]; %specify colormap for colorbar
h = obj.plotTracks(1,1,options);

options1 = plotTracksV1SetOptions;
options1.trackNum = ceil(numTracks/2):numTracks; %specify tracks
options1.colorByValue = 0; %use color specified on next line
options1.color = [0 1 0]; %plot second half of tracks green
options1.h = h; %set figure handle
options1.colorbar = 0; %turn off colorbar
h = obj.plotTracks(1,1,options1);

ttl{1} = sprintf('%stracks %i-%i','\color[rgb]{.75 0
.75}',options.trackNum([1 end]));
ttl{2} = sprintf('%stracks %i-%i','\color[rgb]{0 .75 0}',options1.trackNum([1
end]));
title(ttl)

%% fit channel 1

obj1 = obj.copy;
```

```matlab
obj1.ParamsGeneral.Roi = [64 127 0 63];
obj1.ParamsGeneral.SaveAppendix = 'ch2';

%% plotTracks (save result)

h = obj1.plotTracks;
obj1.saveFig(h,'plotTracks','plotTracks');
obj1.saveFile;

%%

obj1.saveParams([],'ch2');

%% plotDipTrack (make dipTrack figure)

obj1.plotTracksDipImage;

%% plotTracks (raw overlay of channel 1 with channel 2)

options = plotTracksV1SetOptions;%initialize plotting opitons
options.colorByValue = 0; %use color specified on next line
options.color = [1 0 1]; %plot ch2 tracks magenta
options.colorbar = 0; %turn off colorbar
options.displayName = obj.ParamsGeneral.SaveAppendix;
h = obj.plotTracks(1,1,options);

options1 = plotTracksV1SetOptions;
options1.colorByValue = 0; %use color specified on next line
options1.color = [0 1 0]; %plot ch1 tracks green
options1.h = h; %set figure handle
options1.colorbar = 0; %turn off colorbar
options1.displayName = obj1.ParamsGeneral.SaveAppendix;
h = obj1.plotTracks(1,1,options1);

ttl{1} = sprintf('%schannel 1','\color[rgb]{.75 0 .75}');
ttl{2} = sprintf('%schannel 2','\color[rgb]{0 .75 0}');
title(ttl(:),'fontsize',12,'fontweight','bold')

%% raw overlay of channel 1 with channel 2 (dipTrack)

options = dipTrackSetOptions;
options.im =
joinchannels('rgb',stretch(obj.Data),stretch(obj1.Data),stretch(obj.Data));

options.plotTracksOptions(1).tracks = obj.getTracks;
options.plotTracksOptions(1).colorByValue = 0;
options.plotTracksOptions(1).color = [1 0 1];
options.plotTracksOptions(2) = options.plotTracksOptions(1);
options.plotTracksOptions(2).tracks = obj1.getTracks;
options.plotTracksOptions(2).colorByValue = 0;
options.plotTracksOptions(2).color = [0 1 0];
fh = dipTrack(options);

%ensure that figure will fit on monitor at 1000%
```

179

www.manaraa.com

```matlab
monPos = get(0,'MonitorPositions');
tmpSz = obj.Stats.Data.size([1 2])*10;
if any(tmpSz([1 2]) > min(monPos(:,[3 4])))
    diptruesize(fh,min(floor(min(monPos(:,[3 4]))./min(tmpSz([1 2]))*10-
1))*100);
else
    %change size
    diptruesize(fh,1000);
end
%add scaleLine
scaleLine(findall(fh,'type','axes'),2,obj.ParamsGeneral.PixelSize);


%% test constructor with variable inputs

objEmpty = SPT(obj);

sptFile = fullfile(obj.SaveDir,[obj.SaveBaseName '.spt']);

sptStruct = obj.saveobj;

objFromStruct = SPT(sptStruct);

objFromFile = SPT(sptFile);

objEmptyFromFile = SPT(sptFile,1);

paramsFile = fullfile(obj.SaveDir,'scripts','ch1SPTparams.mat');

objFromParams = SPT(paramsFile);

%% trackBatch

close all
%    clear all

%specify data directory
matroot = userpath;
matroot = matroot(1:end-1);
dataDir = fullfile(TestDataDir,'simInteractingParticles');
%get data files
dataFiles = dir(fullfile(dataDir,'sim*.mat'));
dataFiles = cellfun(@(x)
fullfile(dataDir,x),{dataFiles.name},'uniformoutput',false);
%define parameters file for channel 1
paramsFilech1 = fullfile(dataDir,'results','scripts','ch1SPTparams.mat');
%define parameters file for channel 2
paramsFilech2 = fullfile(dataDir,'results','scripts','ch2SPTparams.mat');
%track ch2 dataFiles
sptFilesCh1 = SPT.trackBatch(paramsFilech1,dataFiles);
%track ch1 dataFiles
sptFilesCh2 = SPT.trackBatch(paramsFilech2,dataFiles);

%% find figures
```

```matlab
sptDir = fullfile(dataDir,'results');

figInfo = SPT.findFigs(sptDir)

%% make html summary

SPT.summary(sptDir)
```

Examples for using SPTHSI class (SPTHSItesting)

```matlab
% SPTHSItesting
%
% test ALL methods for SPTHSI class
%
% Any new methods must be added to testing script

%% initialize object

% close all
% clear all
% clear classes
% clc
%
% matroot = userpath;
% matroot = matroot(1:end-1);
% TestDataDir = fullfile(matroot,'TestData');


%specify data file
dataDir = fullfile(TestDataDir,'hsiInteractingParticles');

[~, hsiFiles] = hsiData.findFiles(dataDir);
fileNum = 1;

if isempty(hsiFiles)
    error('SPTHSItest:noData','SPTHSI.test: test data files not found.')
end

%initialize SPT object
obj = SPTHSI;
%specify data file
obj.DataFile = hsiFiles{fileNum};
obj.ParamsGeneral.Frames = 5:10;
obj.ParamsGeneral.Psf = [10 1 1];
obj.ParamsFilterFits.lowerBounds(1) = 20;
obj.ParamsFilterFits.upperBounds(2) = 810;
obj.ParamsConnectFits.costMatF2F.maxSearchDist = [3 3];
obj.ParamsConnectFits.costMatF2F.D = [.4 .4];
obj.ParamsConnectFits.costMatF2F.wvJump = 3;
obj.ParamsConnectFits.costMatF2F.maxWvSearchDist = 12;
```

```matlab
obj.ParamsConnectFits.costMatGC.D = [.5 .5];
obj.ParamsConnectFits.costMatGC.wvJump = 3;
obj.ParamsConnectFits.costMatGC.maxWvSearchDist = 12;

%% reset results directory

if exist(fullfile(obj.SaveDir),'file')
    rmdir(fullfile(obj.SaveDir),'s')
end

%% save parameters file for batch tracking

%change to 1-emitter fit for batch processing (reduce analysis time)
Frames = obj.ParamsGeneral.Frames;
obj.ParamsGeneral.Frames = 1:100;
obj.ParamsFit.models = 1;

obj.saveParams;

%reset values for demo
obj.ParamsGeneral.Frames = Frames;
obj.ParamsFit.models = 3;

%% load Data

obj.loadData;

%% save .spt file no tracked results (raw data should not be saved)

obj.saveFile;

%% find BoxCenters

obj.findBoxCenters

%% plotBoxCenters3D

obj.plotBoxCenters3D;

%% plotBoxCenters3D

obj.plotBoxCenters3D(6);

%% plotBoxCenters

obj.plotBoxCenters; %nneds more thorough testing!!

%% makeROIStack (make stack of regions of interest)

[ROIStack sampling] = obj.makeRoiStack;

%% initialize_gpuGaussNDmleV1_Input
```

```
obj.initialize_gpuGaussNDmleV1_Input;

%% fit (user defined ROIStack)

obj.fit(ROIStack,sampling);

%% fit

obj.fit;

%% plotRawFitResultsHist (display histograms for fitting results)

obj.plotRawFitResultsHist;

%% plotRawFitResults (display fitting results)

obj.plotRawFitResults;

%% fitlerFits

obj.filterFits;

%% plotFitResultsHist (display histograms for fitting results)

obj.plotFitResultsHist;

%% plotFitResultsHist (display histograms for fitting results save figures)

obj.plotFitResultsHist(1);

%% plotFitResults (display fitting results)

obj.plotFitResults;

%% plotFitResults (display fitting results with boxes and loclazations)

obj.plotFitResults(1);

%% connectFits

obj.connectFits;

%% getTracks in old format

[tracks tracksStd subRegionModel tracksWv tracksWvStd] = getTracks(obj);

%% plotTracks (microns and seconds)
```

183

```
h = obj.plotTracks(1,1);

%% plotTracks (save result)

h = obj.plotTracks;
obj.saveFig(h,'plotTracks','plotTracks');
obj.saveFile;

%% plotTracksDipImage (make dipTrack figure)

obj.plotTracksDipImage;

%% plotTracks (plot several sets of tracks with different colors)

numTracks = numel(obj.Tracks); %get total number of tracks
options = plotTracksV1SetOptions;%initialize plotting opitons
options.highlightTracks = 0; %don't highlight tracks in first plot instance
options.trackNum = 1:floor(numTracks/2); %specify tracks
options.colorByValue = 0; %use color specified on next line
options.color = [1 0 1]; %plot first half of tracks magenta
options.cmap = [1 0 1; 0 1 0]; %specify colormap for colorbar
options.colorbar = 0; %turn off colorbar
h = obj.plotTracks(1,1,options);

options1 = plotTracksV1SetOptions;
options1.trackNum = ceil(numTracks/2):numTracks; %specify tracks
options1.colorByValue = 0; %use color specified on next line
options1.color = [0 1 0]; %plot second half of tracks green
options1.h = h; %set figure handle
options1.colorbar = 0; %turn off colorbar
h = obj.plotTracks(1,1,options1);

ttl{1} = sprintf('%stracks %i-%i','\color[rgb]{.75 0
.75}',options.trackNum([1 end]));
ttl{2} = sprintf('%stracks %i-%i','\color[rgb]{0 .75 0}',options1.trackNum([1
end]));
title(ttl)

%% test constructor with variable inputs

objEmpty = SPTHSI(obj);

sptFile = fullfile(obj.SaveDir,[obj.SaveBaseName '.spt']);

sptStruct = obj.saveobj;

objFromStruct = SPTHSI(sptStruct);

objFromFile = SPTHSI(sptFile);

objEmptyFromFile = SPTHSI(sptFile,1);

paramsFile = fullfile(obj.SaveDir,'scripts','SPTparams.mat');
```

```matlab
objFromParams = SPTHSI(paramsFile);

%% trackBatch

close all
% clear all

%specify data file
dataDir = fullfile(TestDataDir,'hsiInteractingParticles');

%get data files
[~, hsiFiles] = hsiData.findFiles(dataDir);
%define parameters file
paramsFile = fullfile(dataDir,'results','scripts','SPTparams.mat');

%track dataFiles
sptFiles = SPT.trackBatch(paramsFile,hsiFiles);

%% find figures

sptDir = fullfile(dataDir,'results');

figInfo = SPTHSI.findFigs(sptDir)

%% make html summary

SPTHSI.summary(sptDir)

%% load .spt file (object prior to tracking)

close all
% clear all
%
% %define data directory
% dataDir =
'C:\Users\pcutler\Documents\MATLAB\TestData\hsiInteractingParticles';

sptFiles = dir(fullfile(dataDir,'results','*.spt'));
fileNum = 1;

sptFile = fullfile(dataDir,'results',sptFiles(fileNum).name);
obj = SPT.loadFile(sptFile);

%% SPTHSI_FitResultsBrowser

close all
% clear all
%
% %define data directory
% dataDir =
'C:\Users\pcutler\Documents\MATLAB\TestData\hsiInteractingParticles';
saveDir = fullfile(dataDir,'results');
```

```matlab
sptFiles = dir(fullfile(saveDir,'*.spt'));
fileNum = 1;

obj = SPTHSI(fullfile(saveDir,sptFiles(fileNum).name));

sptBrowserObj = SPTHSI_FitResultsBrowser(obj);

%% SPTHSI_FitResultsBrowser (make figure group after initialization)

sptBrowserObj = SPTHSI_FitResultsBrowser(obj,[],0);
sptBrowserObj.FrameIdx = 3;
sptBrowserObj.BrowseFlag = 1;
sptBrowserObj.BoxIdx = 4;
```

Examples for performing HMM analysis on SPTHSI data

```matlab
% HMM_analysis_2State_2013_08_28

close all
clear all

saveDir = 'I:\Pat Documents\Research\HSM_DATA\QDIgE
analyses\HMM_analysis_2State_2013_08_28';
saveName = 'HMM_analysis_2State_2013_08_28';

sptDirs = {'I:\Pat Documents\Research\HSM_DATA\2013_02_13 RBL QDIgE
Oligomers\results_2013_05_04 optimized tracking'...
    'I:\Pat Documents\Research\HSM_DATA\2013_02_14 RBL QDIgE
Oligomers\results_2013_05_04 optimized tracking'...
    'I:\Pat Documents\Research\HSM_DATA\2013_04_07a RBL QDIgE Oligomers
(fluorescent biotin)\results_2013_05_04 optimized tracking',...
    'I:\Pat Documents\Research\HSM_DATA\2013_04_07 RBL QDIgE Oligomers
(fluorescent biotin)\results_2013_05_04 optimized tracking',...
    'I:\Pat Documents\Research\HSM_DATA\2013_04_30 RBL QDIgE
Oligomers\results',...
    'I:\Pat Documents\Research\HSM_DATA\2013_04_30a RBL QDIgE
Oligomers\results',...
    'I:\Pat Documents\Research\HSM_DATA\2013_05_04 RBL QDIgE Oligomers
PP2\results',...
    'I:\Pat Documents\Research\HSM_DATA\2013_05_04a RBL QDIgE Oligomers
PP2\results',...
    'I:\Pat Documents\Research\HSM_DATA\2013_05_12 RBL QDIgE
Oligomers\results',...
    'I:\Pat Documents\Research\HSM_DATA\2013_05_12a RBL QDIgE
Oligomers\results',...
    'I:\Pat Documents\Research\HSM_DATA\2013_05_17 RBL QDIgE
Oligomers\results',...
    'I:\Pat Documents\Research\HSM_DATA\2013_05_21 RBL QDIgE Oligomers
long\results',...
    'I:\Pat Documents\Research\HSM_DATA\2013_05_22 RBL QDIgE Oligomers
long\results',...
```

186

```matlab
    'I:\Pat Documents\Research\HSM_DATA\2013_05_28 RBL QDDIgE Oligomers
DNPBSA\results',...
    'I:\Pat Documents\Research\HSM_DATA\2013_05_28a RBL QDIgE Oligomers
DNPBSA\results',...
    'I:\Pat Documents\Research\HSM_DATA\2013_05_31 QDIgE Oligomes
DNPBSA\results',...
    'I:\Pat Documents\Research\HSM_DATA\2013_05_31a QDIgE Oligomers
DNPBSA\results',...
    'I:\Pat Documents\Research\HSM_DATA\2013_08_26 RBL QDIgE\results',...
    'I:\Pat Documents\Research\HSM_DATA\2013_08_26 RBL QDIgE PP2\results',...
    'I:\Pat Documents\Research\HSM_DATA\2013_09_09 RBL QDIgE\results',...
    'I:\Pat Documents\Research\HSM_DATA\2013_09_09 RBL QDIgE PP2\results'};

multiWaitbar('finding spt files...','close');
multiWaitbar('finding spt files...',0);

sptFiles = [];
sptFilesFullPath = [];

for sptDirIdx = 1:numel(sptDirs)
    sptDir = sptDirs{sptDirIdx};
    multiWaitbar('finding spt files...',sptDirIdx/numel(sptDirs));

    sptFilesTmp = dir(fullfile(sptDir,'*.spt'));
    sptFiles = [sptFiles {sptFilesTmp.name}];
    sptFilesFullPath = [sptFilesFullPath cellfun(@(x)
fullfile(sptDir,x),{sptFilesTmp.name},'uniformoutput',false)];

    %      %reset findInteractions
    %      if exist(fullfile(sptDir,'analysis','findInteractions'),'dir')
    %          rmdir(fullfile(sptDir,'analysis','findInteractions'),'s')
    %      end

end
multiWaitbar('finding spt files...','close');


%% perform HMM on all files with DNP3

idx = ~cellfun('isempty',regexp(sptFiles,'DNP3'));
idx = idx & cellfun(@(x) isempty(x),regexp(sptFiles,'488Bio','once'));
idx = idx & cellfun(@(x) isempty(x),regexp(sptFiles,'PP2','once'));
idx = idx & cellfun(@(x) isempty(x),regexp(sptFiles,'bright_bigROI','once'));

unique(cellfun(@(x) x(1:end-23),sptFiles(idx),'uniformoutput',false))'

sptFilesChDNP = repmat(sptFilesFullPath(idx),[2 1]);

obj = SPTANALYSIS_GROUP(sptFilesChDNP);
obj.GroupName = 'DNP3';
obj.SaveDir = saveDir;
out = obj.hmmPreProcess2State([.025 .05 .075 .1]);
out1 = obj.hmmTwoState;
```

```matlab
%% make CPA plot for all DNP3 files

idx = ~cellfun('isempty',regexp(sptFiles,'DNP3'));
idx = idx & cellfun(@(x) isempty(x),regexp(sptFiles,'488Bio','once'));
idx = idx & cellfun(@(x) isempty(x),regexp(sptFiles,'PP2','once'));
idx = idx & cellfun(@(x) isempty(x),regexp(sptFiles,'bright_bigROI','once'));


unique(cellfun(@(x) x(1:end-23),sptFiles(idx),'uniformoutput',false))'

sptFilesFullPatTrim = sptFilesFullPath(idx);

multiWaitbar('CPA DNP3','close');
multiWaitbar('CPA DNP3',0);

%account for linescanning
xPsf = 0.8;
nlines = 32;
Texp = (xPsf*3+1)/nlines;

tic
clear cpaResults
for ii = 1:numel(sptFilesFullPatTrim)
    obj = SPTANALYSIS_MOBILITY(sptFilesFullPatTrim{ii});
    inputs = obj.pmDcpa('Inputs');
    inputs.Dguess = 0:0.01:5;
    inputs.dutyCycle = Texp;
    cpaResults(ii) = obj.pmDcpa(inputs);
    if ii > 1
        close(cpaResults(ii).fh)
    end
    multiWaitbar('CPA DNP3',ii/numel(sptFilesFullPatTrim));
end
toc

multiWaitbar('CPA DNP3','close');

fh = figure;
ha = axes('parent',fh);

D = cell2mat({cpaResults.D}');
Dtmp = D(~isnan(D));
Dmed = median(Dtmp);
p = 0:numel(Dtmp)-1;
p = p/max(p);
plot(sort(Dtmp),p,'parent',ha,'linewidth',2)
set(ha,'xscale','log')
axis(ha,'tight')
xlabel(ha,'D (\mum^2/s)')
ylabel(ha,'cumulative probability')
hl = legend(ha,sprintf('D_{med} = %0.2g %s\nN = %i',...
    Dmed,'\mum^2/s',numel(Dtmp)));
set(hl,'location','best','fontsize',16)
title(ha,'DNP3')
```

```matlab
saveas(gcf,fullfile(saveDir,'DNP3-Dcpa'),'fig')
saveas(gcf,fullfile(saveDir,'DNP3-Dcpa'),'png')




%% perform HMM on all files with DNPBSA

idx = ~cellfun('isempty',regexp(sptFiles,'DNPBSA'));
idx = idx & cellfun(@(x) isempty(x),regexp(sptFiles,'488Bio','once'));
idx = idx & cellfun(@(x) isempty(x),regexp(sptFiles,'PP2','once'));
idx = idx & cellfun(@(x) isempty(x),regexp(sptFiles,'bright_bigROI','once'));

unique(cellfun(@(x) x(1:end-23),sptFiles(idx),'uniformoutput',false))'

sptFilesChDNP = repmat(sptFilesFullPath(idx),[2 1]);

obj = SPTANALYSIS_GROUP(sptFilesChDNP);
obj.GroupName = 'DNPBSA';
obj.SaveDir = saveDir;
out = obj.hmmPreProcess2State([.025 .05 .075 .1]);
out1 = obj.hmmTwoState;

%% make CPA plot for all files with DNPBSA

idx = ~cellfun('isempty',regexp(sptFiles,'DNPBSA'));
idx = idx & cellfun(@(x) isempty(x),regexp(sptFiles,'488Bio','once'));
idx = idx & cellfun(@(x) isempty(x),regexp(sptFiles,'PP2','once'));
idx = idx & cellfun(@(x) isempty(x),regexp(sptFiles,'bright_bigROI','once'));

unique(cellfun(@(x) x(1:end-23),sptFiles(idx),'uniformoutput',false))'

sptFilesFullPatTrim = sptFilesFullPath(idx);

multiWaitbar('CPA DNPBSA','close');
multiWaitbar('CPA DNPBSA',0);

%account for linescanning
xPsf = 0.8;
nlines = 32;
Texp = (xPsf*3+1)/nlines;

tic
clear cpaResults
for ii = 1:numel(sptFilesFullPatTrim)
    obj = SPTANALYSIS_MOBILITY(sptFilesFullPatTrim{ii});
    inputs = obj.pmDcpa('Inputs');
    inputs.Dguess = 0:0.01:5;
    inputs.dutyCycle = Texp;
    cpaResults(ii) = obj.pmDcpa(inputs);
    if ii > 1
        close(cpaResults(ii).fh)
    end
    multiWaitbar('CPA DNPBSA',ii/numel(sptFilesFullPatTrim));
```

```matlab
    end
toc

multiWaitbar('CPA DNPBSA','close');

fh = figure;
ha = axes('parent',fh);

D = cell2mat({cpaResults.D}');
Dtmp = D(~isnan(D));
Dmed = median(Dtmp);
p = 0:numel(Dtmp)-1;
p = p/max(p);
plot(sort(Dtmp),p,'parent',ha,'linewidth',2)
set(ha,'xscale','log')
axis(ha,'tight')
xlabel(ha,'D (\mum^2/s)')
ylabel(ha,'cumulative probability')
hl = legend(ha,sprintf('D_{med} = %0.2g %s\nN = %i',...
    Dmed,'\mum^2/s',numel(Dtmp)));
set(hl,'location','best','fontsize',16)
title(ha,'DNPBSA')


saveas(gcf,fullfile(saveDir,'DNPBSA-Dcpa'),'fig')
saveas(gcf,fullfile(saveDir,'DNPBSA-Dcpa'),'png')



%% perform HMM on all files without DNP

idx = ~cellfun('isempty',regexp(sptFiles,'rbl_QDIgE-'));
idx = idx & cellfun(@(x) isempty(x),regexp(sptFilesFullPath,'PP2','once'));

unique(cellfun(@(x) x(1:end-23),sptFiles(idx),'uniformoutput',false))'


sptFilesChNoDNP = repmat(sptFilesFullPath(idx),[2 1]);

obj = SPTANALYSIS_GROUP(sptFilesChNoDNP);
obj.GroupName = 'NoDNP';
obj.SaveDir = saveDir;
out = obj.hmmPreProcess2State([.025 .05 .075 .1]);
out = obj.hmmTwoState;

%% make CPA plot for all files without DNP

idx = ~cellfun('isempty',regexp(sptFiles,'rbl_QDIgE-'));
idx = idx & cellfun(@(x) isempty(x),regexp(sptFilesFullPath,'PP2','once'));


unique(cellfun(@(x) x(1:end-23),sptFiles(idx),'uniformoutput',false))'
```

190

```matlab
sptFilesFullPatTrim = sptFilesFullPath(idx);

multiWaitbar('CPA noDNP','close');
multiWaitbar('CPA noDNP',0);

%account for linescanning
xPsf = 0.8;
nlines = 32;
Texp = (xPsf*3+1)/nlines;

tic
clear cpaResults fileInfo
for ii = 1:numel(sptFilesFullPatTrim)
    obj = SPTANALYSIS_MOBILITY(sptFilesFullPatTrim{ii});
    inputs = obj.pmDcpa('Inputs');
    inputs.Dguess = 0:0.01:5;
    inputs.dutyCycle = Texp;
    cpaResults(ii) = obj.pmDcpa(inputs);
    fileInfo(ii).BaseName = obj.BaseName;
    fileInfo(ii).BaseTitleName = obj.BaseTitleName;
    fileInfo(ii).SaveDir = obj.SaveDir;
    if ii > 1
        close(cpaResults(ii-1).fh)
    end
    multiWaitbar('CPA noDNP',ii/numel(sptFilesFullPatTrim));
end
toc

multiWaitbar('CPA noDNP','close');

fh = figure;
ha = axes('parent',fh);

D = cell2mat({cpaResults.D}');
Dtmp = D(~isnan(D));
Dmed = median(Dtmp);
p = 0:numel(Dtmp)-1;
p = p/max(p);
plot(sort(Dtmp),p,'parent',ha,'linewidth',2)
set(ha,'xscale','log')
axis(ha,'tight')
xlabel(ha,'D (\mum^2/s)')
ylabel(ha,'cumulative probability')
hl = legend(ha,sprintf('D_{med} = %0.2g %s\nN = %i',...
    Dmed,'\mum^2/s',numel(Dtmp)));
set(hl,'location','best','fontsize',16)
title(ha,'noDNP')


saveas(gcf,fullfile(saveDir,'noDNP-Dcpa'),'fig')
saveas(gcf,fullfile(saveDir,'noDNP-Dcpa'),'png')

fh1 = figure;
ha1 = axes('parent',fh1);
```

191

```matlab
fh2 = figure;
ha2 = axes('parent',fh2);

c1 = jet(numel(cpaResults));
clear Dmed N
for ii = 1:numel(cpaResults)
    D = cell2mat({cpaResults(ii).D}');
    Dtmp = D(~isnan(D));
    Dmed(ii) = median(Dtmp);
    N(ii) = numel(Dtmp);
    p = 0:numel(Dtmp)-1;
    p = p/max(p);

    line(sort(Dtmp),p,'parent',ha1,...
    'color',c1(ii,:),'linewidth',2,...
    'displayname',['{\color[rgb]{' sprintf('%g ',c1(ii,:))...
        sprintf('}(%i)%s
\nN=%i\nD_{med}=%0.02g',ii,fileInfo(ii).BaseTitleName,...
        numel(Dtmp),Dmed(ii)) '}'])

    text(double(Dmed(ii)),ii,['{\color[rgb]{' sprintf('%g ',c1(ii,:))...
        sprintf('}(%i)%s
\nN=%i\nD_{med}=%0.02g',ii,fileInfo(ii).BaseTitleName,...
        numel(Dtmp),Dmed(ii)) '}'],'parent',ha2)

    line(double(Dmed(ii)),ii,'parent',ha2,'marker','.')

end

set(ha1,'xlim',[1e-2 1],'ylim',[0
1],'xscale','log','fontweight','bold','fontsize',16)
% axis(ha,'tight')
xlabel(ha1,'D (\mum^2/s)')
ylabel(ha1,'cumulative probability')
hl = legend(ha1,'toggle');
set(hl,'location','NorthEastOutside','fontsize',12)

figure
plot(Dmed,N,'marker','x','linestyle','none')
xlabel('D (\mum^2/s)')
ylabel('# of trajectories')

figure
plot(Dmed,cellfun(@(x)
mean(x),{cpaResults.nObs}),'marker','x','linestyle','none')
xlabel('D (\mum^2/s)')
ylabel('average # obs/trajectory')

%determine variance for each independet set of acquisitions
clear DmedSet DstdSet uniqueSaveDirBase
uniqueSaveDir = unique({fileInfo.SaveDir});
for ii = 1:numel(uniqueSaveDir)
    idx1 = strcmp({fileInfo.SaveDir},uniqueSaveDir{ii});
    DmedSet(ii) = median(Dmed(idx1));
    DstdSet(ii) = std(Dmed(idx1));
```

```matlab
    [~,uniqueSaveDirBase{ii}] = fileparts(fileparts(uniqueSaveDir{ii}));
    fprintf('%55s \t %0.3g \t
%0.3g\n',uniqueSaveDirBase{ii},DmedSet(ii),DstdSet(ii))
end
% [uniqueSaveDirBase' num2cell(DmedSet)' num2cell(DstdSet)']
%make bar graph
figure;
bh = bar(DmedSet);
%get location of bars for error bars
x_loc = mean(get(allchild(bh),'xdata'));
y_height = max(get(allchild(bh),'ydata'));
%add error bar
hold on
he = errorbar(x_loc',y_height',DstdSet,DstdSet);
set(he,'linestyle','none','color',[0 0 0],'linewidth',2)
ylabel('D (\mum^2/s)')
xlabel('set of acquisitions')


%% make viterbi plots

close all
clear all

%specify save directory
saveDir = 'I:\Pat Documents\Research\HSM_DATA\QDIgE
analyses\HMM_analysis_2State_2013_08_28';

%find all groups
[figFileNames GroupNames MethodNames] = SPTANALYSIS_GROUP.findFigs(saveDir);


multiWaitbar('Viterbi Group','close');
multiWaitbar('Viterbi Group',0);

for ii = 1:numel(GroupNames)

    %load results
    figIdx = strcmp(MethodNames,'hmmTwoState') &
strcmp(GroupNames,GroupNames{ii});
    load(fullfile(saveDir,figFileNames{figIdx}),'-mat')
    udata = hgS_070000.properties.UserData;

    %find HMMPP file with best interaction distance and domain size
    [~,idx] = min(udata.sptAnalResults.lnP);
    % idx = 12;
    HMM_PreProcessFile =
fullfile(saveDir,'HMM2State',udata.sptAnalResults.HMMPPfiles{idx});

    % % fill state info
    % HMM_PreProcessData = HMM_FindStates(HMM_PreProcessFile);
    % HMM_PreProcessData = HMM_StatesDist(HMM_PreProcessFile);

    load(HMM_PreProcessFile,'-mat');
```

```matlab
    % ViterbiPlotDir =
fullfile(saveDir,sprintf('viterbi(%s)250nm',GroupNames{figIdx}));
    ViterbiPlotDir =
fullfile(saveDir,sprintf('viterbi(%s)',GroupNames{figIdx}));
    PmatrixPlotDir =
fullfile(saveDir,sprintf('pmatrix(%s)',GroupNames{figIdx}));

    if ~isfield(HMM_PreProcessData,'FilledStates')
        % fill state info
        HMM_PreProcessData = HMM_FindStates(HMM_PreProcessFile);
        HMM_PreProcessData = HMM_StatesDist(HMM_PreProcessFile);
    end

    %make figures for files with atleast 1 dimer
    nDimer = cellfun(@(x) sum(any(x == 1)),HMM_PreProcessData.FilledStates);
    [v1,idx1] = sort(nDimer,'descend');
    fileNum = idx1(logical(v1));

    %make viterbi plot
    HMM_2DviterbiPlots(HMM_PreProcessData,ViterbiPlotDir,fileNum)
    %make Pmatrix plot
    HMM_2DPmatrixPlots(HMM_PreProcessData,PmatrixPlotDir,fileNum)

    multiWaitbar('Viterbi Group',ii/numel(GroupNames));
    close all
end
multiWaitbar('Viterbi Group','close');


%% estimate D for free vs dimer

close all
clear all

%specify save directory
saveDir = 'I:\Pat Documents\Research\HSM_DATA\QDIgE
analyses\HMM_analysis_2State_2013_08_28';

IntDis = 50;

%find all groups
[figFileNames GroupNames MethodNames] = SPTANALYSIS_GROUP.findFigs(saveDir);

figMethods = cellfun(@(x) x(regexp(x,'(sptg-')+6:regexp(x,').fig')-
1),figFileNames,'uniformoutput',false);
figGroups = cellfun(@(x) x(1:regexp(x,'(sptg-')-
1),figFileNames,'uniformoutput',false);

multiWaitbar('Viterbi Group','close');
multiWaitbar('Viterbi Group',0);

for ii = 1:numel(GroupNames)
```

```matlab
    %       %load results
    %       figIdx = strcmp(MethodNames,'hmmTwoState') &
strcmp(GroupNames,GroupNames{ii});
    %       load(fullfile(saveDir,figFileNames{figIdx}),'-mat')
    %       udata = hgS_070000.properties.UserData;
    %
    %       %find HMMPP file with best interaction distance and domain size
    %       [~,idx] = min(udata.sptAnalResults.lnP);
    %       % idx = 12;
    HMM_PreProcessFile = fullfile(saveDir,'HMM2State',sprintf('%s-
IntDis(%i).HMMPP',GroupNames{ii},IntDis));

    load(HMM_PreProcessFile,'-mat');

    if ~isfield(HMM_PreProcessData,'FilledStates')
        % fill state info
        HMM_PreProcessData = HMM_FindStates(HMM_PreProcessFile);
        HMM_PreProcessData = HMM_StatesDist(HMM_PreProcessFile);
    end


    Dcount = 0;
    Fcount = 0;
    Ddimer =
struct('D',[],'Interval',struct('Ends',[],'Index',[],'Width',[]),'FileID',[],
'PairID',[]);
    Dfree =
struct('D',[],'Interval',struct('Ends',[],'Index',[],'Width',[]),'FileID',[],
'PairID',[]);
    dimerIdx = cellfun(@(x) find(sum(x ==
1)>3),HMM_PreProcessData.FilledStates,'uniformoutput',false);

    multiWaitbar('files','close');
    multiWaitbar('files',0);

    for jj = 1:numel(dimerIdx)
        if ~isempty(dimerIdx{jj})
            for kk = 1:numel(dimerIdx{jj})
                states =
HMM_PreProcessData.FilledStates{jj}(:,dimerIdx{jj}(kk));

                for mm = 1:2
                    pairId =
HMM_PreProcessData.PairID{jj}(dimerIdx{jj}(kk),mm);
                    sptObj =
SPT.loadFile(fullfile(HMM_PreProcessData.FileInfo(mm,jj).Path,HMM_PreProcessD
ata.FileInfo(mm,jj).Name));

                    %inputs for Dpm
                    Dguess = 0:.001:3;
                    Texp =
(sptObj.ParamsGeneral.Psf(3)*3+1)/sptObj.Stats.Data.size(2);
                    pValue = 0.32;
```

```matlab
                        tt = 0;
                        while tt < length(states)
                            tt = tt+1;
                            tt1 = tt+find(states(tt+1:end) ~=
states(tt),1,'first')-1;
                                if ~tt1
                                    tt1 = length(states);
                                end
                                frameIdx =
ismember(sptObj.Tracks(pairId).Frame,tt:tt1);

                                if sum(frameIdx) > 3
                                    %get inputs
                                    o = [sptObj.Tracks(pairId).X(frameIdx)'
sptObj.Tracks(pairId).Y(frameIdx)'];
                                    LA = [sptObj.Tracks(pairId).std_x(frameIdx)'
sptObj.Tracks(pairId).std_y(frameIdx)'];
                                    T = sptObj.Tracks(pairId).Frame(frameIdx);

                                    if states(tt) == 1
                                        Dcount = Dcount+1;
                                        [D, Ddimer.Interval(Dcount)] =
Dpm(o,LA,T,Dguess,Texp,pValue);
                                        Ddimer.D(Dcount) = mean(D);
                                        Ddimer.FileID(Dcount) = jj;
                                        Ddimer.PairID(Dcount,:) = [pairId tt tt1
length(T)];
                                    else
                                        Fcount = Fcount+1;
                                        [D, Dfree.Interval(Fcount)] =
Dpm(o,LA,T,Dguess,Texp,pValue);
                                        Dfree.D(Fcount) = mean(D);
                                        Dfree.FileID(Fcount) = jj;
                                        Dfree.PairID(Fcount,:) = [pairId tt tt1
length(T)];
                                    end
                                end

                                tt = tt1;
                        end
                    end

            end
        end
        multiWaitbar('files',jj/numel(dimerIdx));

    end
    multiWaitbar('files','close');


    HMM_PreProcessData.Dfree = Dfree;
    HMM_PreProcessData.Ddimer = Ddimer;

    figure
```

196

```matlab
plot(sort(Dfree.D)*sptObj.Stats.Data.PixelSize^2/sptObj.Stats.Data.TimeStep,(
0:numel(Dfree.D)-1)/numel(Dfree.D-1))
    hold all

plot(sort(Ddimer.D)*sptObj.Stats.Data.PixelSize^2/sptObj.Stats.Data.TimeStep,
(0:numel(Ddimer.D)-1)/numel(Ddimer.D-1))
    hold off
    set(gca,'xscale','log')
    medFree =
median(Dfree.D)*sptObj.Stats.Data.PixelSize^2/sptObj.Stats.Data.TimeStep;
    legendcell{1} =
sprintf('free\nN=%i\nD_{med}=%0.02g',numel(Dfree.D),medFree);
    medDimer =
median(Ddimer.D)*sptObj.Stats.Data.PixelSize^2/sptObj.Stats.Data.TimeStep;
    legendcell{2} =
sprintf('dimer\nN=%i\nD_{med}=%0.02g',numel(Ddimer.D),medDimer);
    legend(legendcell,'location','NorthWest')
    xlabel('D \mu m^2/s')
    ylabel('P(D)')
    title(GroupNames{ii})

    saveas(gcf,fullfile(saveDir,[GroupNames{ii} '-HMM-Dcpa']),'fig')
    saveas(gcf,fullfile(saveDir,[GroupNames{ii} '-HMM-Dcpa']),'png')

    save(HMM_PreProcessFile,'HMM_PreProcessData','-append')

    multiWaitbar('Viterbi Group',ii/numel(GroupNames));
end
multiWaitbar('Viterbi Group','close');

%% make CPA plots

close all
clear all

%specify save directory
saveDir = 'I:\Pat Documents\Research\HSM_DATA\QDIgE
analyses\HMM_analysis_2State_2013_08_28';

IntDis = 50;

%find all groups
[figFileNames GroupNames MethodNames] = SPTANALYSIS_GROUP.findFigs(saveDir);

multiWaitbar('Viterbi Group','close');
multiWaitbar('Viterbi Group',0);

for ii = 1:numel(GroupNames)

    %     %load results
    %     figIdx = strcmp(MethodNames,'hmmTwoState') &
strcmp(GroupNames,GroupNames{ii});
    %     load(fullfile(saveDir,figFileNames{figIdx}),'-mat')
```

197

```matlab
%      udata = hgS_070000.properties.UserData;
%
%      %find HMMPP file with best interaction distance and domain size
%      [~,idx] = min(udata.sptAnalResults.lnP);
%      % idx = 12;
    HMM_PreProcessFile = fullfile(saveDir,'HMM2State',sprintf('%s-
IntDis(%i).HMMPP',GroupNames{ii},IntDis));


    load(HMM_PreProcessFile,'-mat');

    Dfree = HMM_PreProcessData.Dfree;
    Ddimer = HMM_PreProcessData.Ddimer;

    figure
plot(sort(Dfree.D)*HMM_PreProcessData.PixelSize^2/HMM_PreProcessData.TimeStep
,(0:numel(Dfree.D)-1)/numel(Dfree.D-1),...
        'color',[1 0 0],'linewidth',3)
    hold on
plot(sort(Ddimer.D)*HMM_PreProcessData.PixelSize^2/HMM_PreProcessData.TimeSte
p,(0:numel(Ddimer.D)-1)/numel(Ddimer.D-1),...
        'color',[0 0 1],'linewidth',3)
    hold off
    set(gca,'xscale','log')
    medFree =
median(Dfree.D)*HMM_PreProcessData.PixelSize^2/HMM_PreProcessData.TimeStep;
    legendcell{1} = ['{\color[rgb]{1 0 0}'
sprintf('free\nN=%i\nD_{med}=%0.02g',numel(Dfree.D),medFree) '}'];
    medDimer =
median(Ddimer.D)*HMM_PreProcessData.PixelSize^2/HMM_PreProcessData.TimeStep;
    legendcell{2} = ['{\color[rgb]{0 0 1}'
sprintf('dimer\nN=%i\nD_{med}=%0.02g',numel(Ddimer.D),medDimer) '}'];
    legend(legendcell,'location','NorthWest')
    xlabel('D \mum^2/s')
    ylabel('P(D)')
    title(GroupNames{ii})

    saveas(gcf,fullfile(saveDir,[GroupNames{ii} '-HMM-Dcpa']),'fig')
    saveas(gcf,fullfile(saveDir,[GroupNames{ii} '-HMM-Dcpa']),'png')


    multiWaitbar('Viterbi Group',ii/numel(GroupNames));
end
multiWaitbar('Viterbi Group','close');
```

Developer Tools

SPTANALYSIS class

Class used to organize results from analysis of single particle trajectories in SPT objects. This class provides a platform from which to save standard analyses. This class is used to organize results from the SPTANALYSIS_MOBILITY and SPTANALYSIS_INTERACTIONS classes.

Making a Tag

Make the following edits to startup_SPT.m

- Line 30 change SM_Analysis repo to current tagged version
- Line 38 change HMM repo to current tagged version
- Line 42 change GPUgaussMLEv2 repo to current tagged version
- Line 45 change Shared repo to current tagged version

Edit the SPT ReadMe at line 13 to point to the new tag

Place the following lines of code in your startup

```
%get default user path
matroot = userpath;
matroot = matroot(1:end-1);
SPTdir = fullfile(matroot,'SPT','development'); %fullpath for directory
containing @SPT folder
addpath(SPTdir); %add directory to path
startup_SPT %use startup_SPT to initialize SPT class and all dependencies
```

Test the SPT class using the following lines

SPT.test

SPTANALYSIS_MOBILITY.test

SPTANALYSIS_INTERACTIONS.test

SPTANALYSIS_GROUP.test

You are now ready to make a tag of the SPT repository

In the current setup, any time a new SPT tag is made. A new tag of the HSM repo must also be made, because the SPTHSI class is a subclass dependent on the SPT class and in the HSM repo.

Edit startup_SPTHSI.m at line 11 point to the new SPT tag

Edit the SPTHSI ReadMe at line 12 to point to the new tag

Place the following lines of code in your startup file (note that setting up SPTHSI class automatically sets up SPT class)

```
%get default user path
matroot = userpath;
matroot = matroot(1:end-1);
SPTHSIdir = fullfile(matroot,'HSM','tags','RC1','SPTHSI_class'); %fullpath
for directory containing @SPTHSI folder
addpath(SPTHSIdir); %add directory to path
startup_SPTHSI %use startup_SPTHSI to initialize SPTHSI class and all
dependencies
```

Test the SPTHSI class using the following lines

SPTHSI.test

SPTANALYSIS_MOBILITY.test

SPTANALYSIS_INTERACTIONS.test

SPTANALYSIS_GROUP.test

APPENDIX E: UNM HYPERSPECTRAL LINE-SCANNING HYPERSPECTRAL MICROSCOPE USER MANUAL

UNM Hyperspectral Line Scanning Microscope User Manual

Table of Contents

UNM HSM User Manual
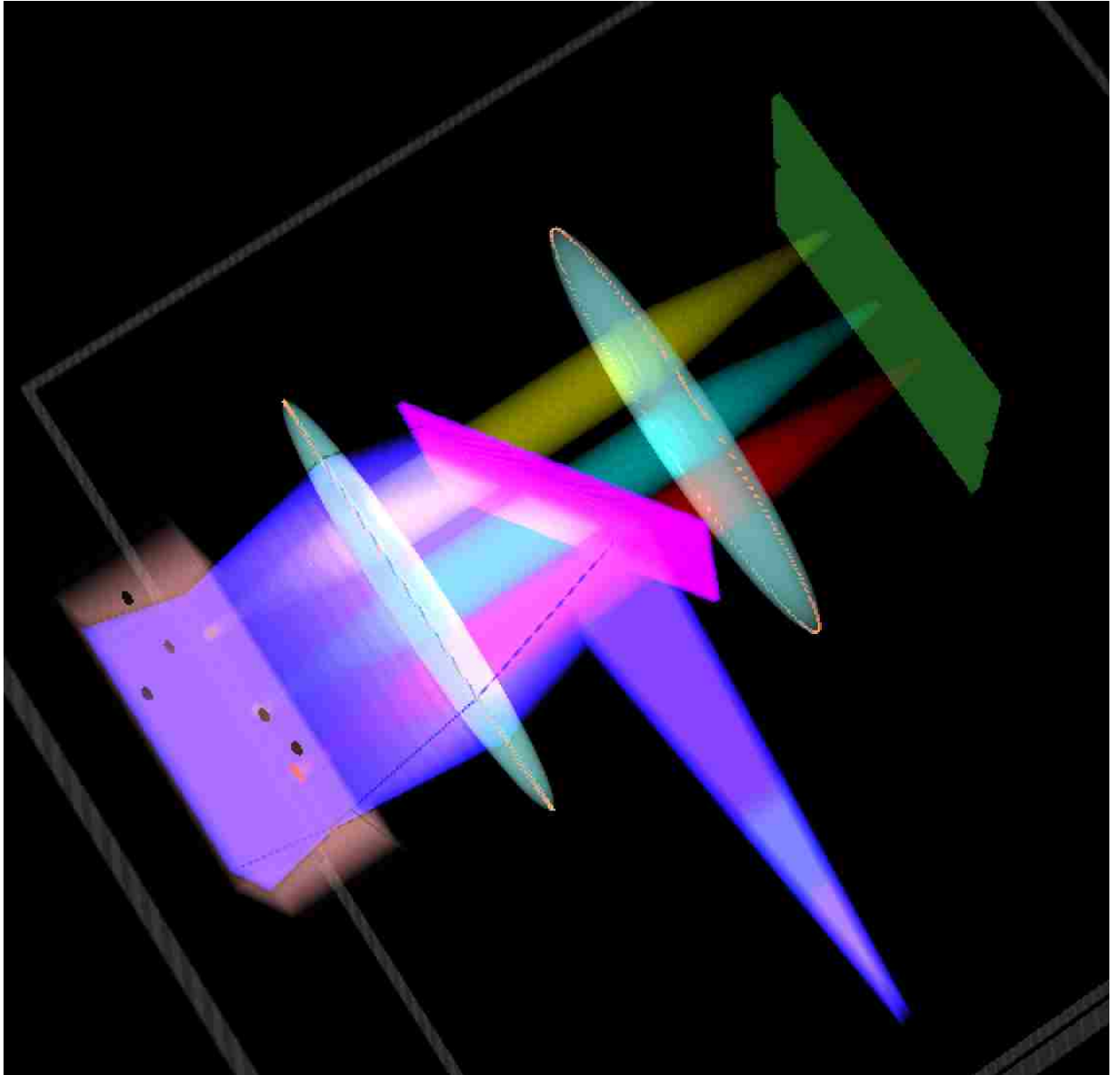
Table of Figures

I.   Instrumental Control and Settings

Instrument Initialization for Hyperspectral Image Acquisition

CheckList for Standard Operation

1) Turn on devices
2) Initialize hsmDAQ2
3) Perform gain and wavelength calibrations
4) Image Sample
5) Shutdown cameras and turn off devices

Matlab Initialization/Troubleshooting

- Add set-up section to Matlab startup file:
  ```
  %get default user path
  matroot = userpath;
  matroot = matroot(1:end-1);
  SPTHSIdir =
  fullfile(matroot,'HSM','tags','RC1','SPTHSI_class');
  %fullpath for directory containing @SPTHSI folder
  addpath(SPTHSIdir); %add directory to path
  startup_SPTHSI %use startup_SPTHSI to initialize SPTHSI
  class and all dependencies
  ```
  o Note replace RC1 with the tagged version of the software that you would like to use.
- In order to the libraries for camera control, you may need to run "mex –setup". You will know if you need to this (i.e. you will get an error when initializing the camera that tells you to).
- dipImage is used for most data manipulation.
- If matlab freezes or odd behavior is occurring, then the best practice is to restart matlab. Make sure to force quit in the task manager.
- See Instrumentation Trouble Shooting section for more details on trouble shooting

Detailed Procedure for Standard Operation

1. Turn on all devices lamp, stage, galvo, AOM, Laser, and check that flip mount mirror is plugged in. If performing experiments at 36 °C, turn on objective heater (~30 min warm up time).
2. Initialize hsmDAQ
   a. Type 'hsmDAQ2' on Matlab command line to initialize the GUI.
   b. By default, no cameras are initialized. The iXon and Luca cameras need to be initialized manually by using the checkboxes in the CCD Initialization/Shutdown panel of the GUI. Depending on the experiment you may not need to turn them both on. The iXon is for acquiring hyperspectral mages and the Luca is for collecting widefield images. The flip mount mirror switches between the two. Use the Flip Mount Toggle to switch between cameras.

UNM HSM User Manual

    c. When shutting down press the <u>Shutdown All</u> button in the <u>CCD Initialization/Shutdown</u> panel. If the iXon camera is being shutdown, then you must leave the GUI and Matlab open until the camera finishes cooling.

    d. For most experiment <u>EM Gain</u> needs to be set to 200. Do this prior to calibrations! Other camera readout parameters for the iXon can also be adjusted by using the Andor iXon Readout GUI which is displayed by checking the <u>Andor iXon Readout</u> checkbox in the <u>Other GUIs</u> panel.

    e. Initialize the MCL NanoDrive. This is recommended even if the stage is not being used to help stabilize the sample.

3. Perform gain and wavelength calibrations

    a. Best practice is to perform wavelength and gain calibrations once per day until the stability of the instrument is well characterized.

    b. Note that by default the most recent spectral calibration is loaded.

    c. All equipment needed for calibrations are included in the <u>HSM Calibration box</u> which should be located on the shelf in PANDA 118.

    d. Perform gain calibration. See the <u>Gain Calibration</u> section.

    e. Perform wavelength calibration. See the <u>Wavelength Calibration</u> section.

4. Image Sample

    a. Add DI water to 60x objective.

    b. Position sample and focus with oculars. FOV for the camera is approximately in the center of the ocular FOV.

    c. Note that in turret position 1 the lamp is used for exciting the sample. With the turret in any other position and the emission path directed to the camera the laser line is used to excite the sample. The laser line will only excite the sample when the emission path is directed to the camera.

    d. Focus on sample with the camera

        i. Depending on the experiment, cells may be easier to focus on using the transmission light.

        ii. Increasing the Number of Steps Per Scan or the Number of Scans may aid in focusing. It is suggested to start with 128 steps per scan and 1000 scans. This should provide ample time to investigate the sample.

        iii. Press the <u>iXon Scan (HyperView)</u> button.

        iv. <u>HyperView</u> will immediately open and provide real-time feedback for focusing.

        v. For the fastest scan rate use 32 steps per scan. If initially focusing with 128 steps, align the ROI on the left edge of the FOV.

        vi. Once sample is in focus close hyperView. If acquisition finishes while still focusing, click 'don't save' in the pop up. Then Focusing may be repeated.

        vii. Number of Scans may be set arbitrarily long for focusing.

        viii. Note that anytime the <u>iXon Scan (HyperView)</u> button is pressed data is being asynchronously saved during the acquisition. By closing

UNM HSM User Manual

> hyperView during an acquisition or clicking 'don't save' in the pop up, the data is automatically deleted. Best practice is to close hyperView between acquisitions.

- e. Acquire data
    - i. Once the sample is in focus begin acquiring data by pressing the iXon Scan (HyperView) button.
    - ii. After the acquisition you will be asked if you would like to save the data. The data is actually already saved due to asynchronous saving, but if you do not want to keep the data then press no and it will delete the folder/file.
- f. Repeat a-e until your cells die or you are tired of being alone in a dark room!!

5. Shutdown cameras and turn off devices
    - a. Press the Shutdown All button in the CCD Initialization/Shutdown panel. If the iXon camera is being shutdown, then you must leave the GUI and Matlab open until the camera finishes cooling.
    - b. Disable the MCL NanoDrive
    - c. Turn off all devices lamp, stage, galvo, AOM, Laser, and objective heater. Unplugging the flip mount mirror is optional.

Warning: if the exposure time is set for both the Luca and iXon using the Scanning Parameters panel. It is important to alter your settings when acquiring with the different cameras.

II.   HSM Calibration

HSM Calibration box contains all components necessary for calibration.

Wavelength calibration lamp positioning

Green Chroma slide for gain calibration

**Figure 1. Calibration Equipment**

www.manaraa.com

Gain Calibration

Details for performing a new gain calibration. A gain image needs to be collect at least once every 24 hours. The main factors that affect the gain are the EM gain and preAmp gain along with the temperature of the EMCCD. The EM gain is set using the EM Gain textbox. The preAmp gain is set using the Andor iXon Readout GUI.

1. Load Green Chroma slide (Figure 1. Calibration Equipment) onto microscope (water not required).
2. Make sure that turret is in position 1 and the shutter is open for lamp excitation.
3. Use the iXon focus (Raw) button to focus on the slide.
    o Adjusting the focus up and down will allow the user to optimize the range of the intensities on the camera. In the LiveView the max intensity in the image is displayed in the figure title (Figure 2. Gain Calibration). A max intensity of ~1500 will adequate intensity sampling for typical SPT experiments.
    o After exiting the focus, a dipimge window will pop up. Use pixel testing to verify that a range of at least 100-1000 counts is sampled. If range of intensities is not appropriate then redo focus. (Figure 2. Gain Calibration)
    o Verify the spectral alignment by typing 'sum(focus,[],1)' into the command line. A sharp drop off should be observed in the first several spectral pixels indicating the alignment of the spectrometer (Figure 2. Gain Calibration). Drop off of intensity is due to the 500 LP filter in the emission path.
    o Note that several dark pixels are necessary for baseline correction.
4. Set the number of EM gain calibration frames using the Number of EM Gain Calibration Frames textbox. The default value of 20 is typically sufficient.
5. Press the iXon EM Gain Calibration button to perform the calibration.
    o Several figures will be displayed to help the user verigy the quality of the gain calibration and the alignment of the spectrometer
    o Verify the quality of the line fit to the data (Figure 2. Gain Calibration).
    o Verify the spectral alignment. A sharp drop off should be observed in the last several spectral pixels indicating the alignment of the spectrometer (Figure 2. Gain Calibration). Drop off of intensity is due to the 495 LP filter in the emission path. Verify the position set in text box in the Wavelength Calibration panel. This step is important for a proper wavelength calibration.

UNM HSM User Manual

~100 counts

~1000-2000 counts

~100 counts
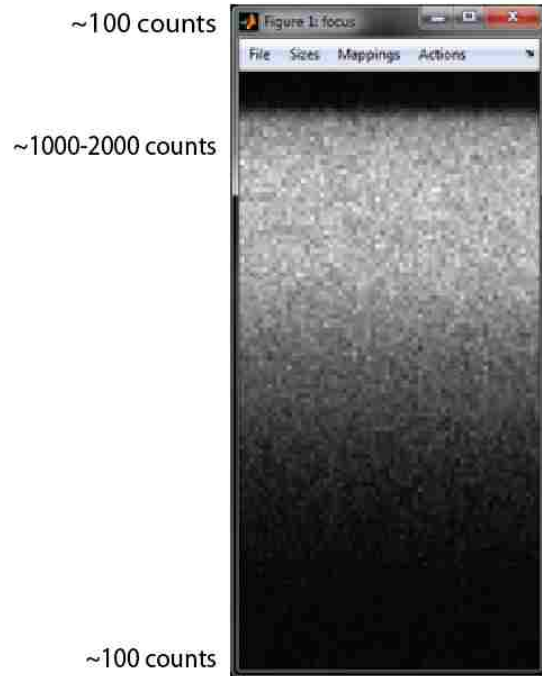
Example intensity distribution for gain calibration after focusing on Green Chroma slide. Note that this will be inverted about the horizontal axis from what is shown during live focusing.
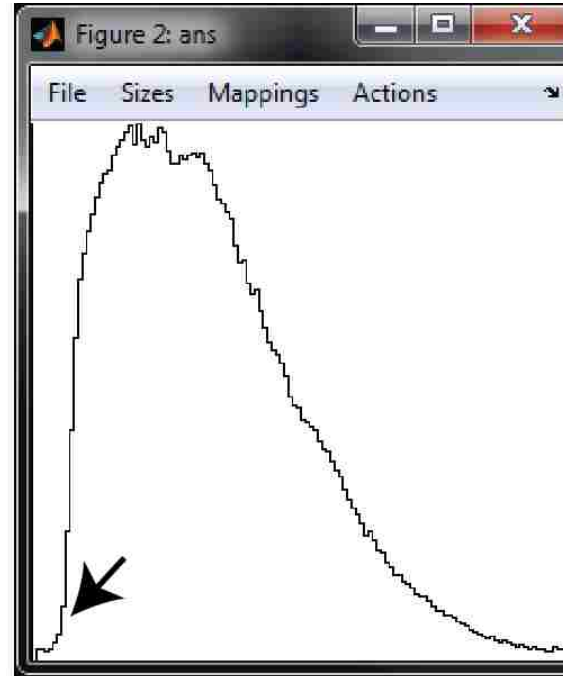
Example intensity distribution from sum(focus,[], command. Drop off of intensity due to the 500 L identified by the arrow indicates proper spectrometer alignment.

Verify the Quality of the line (red) fit to the data (blue x) using this automatically generated plot. Gain factor for typical settings should be around 0.07.
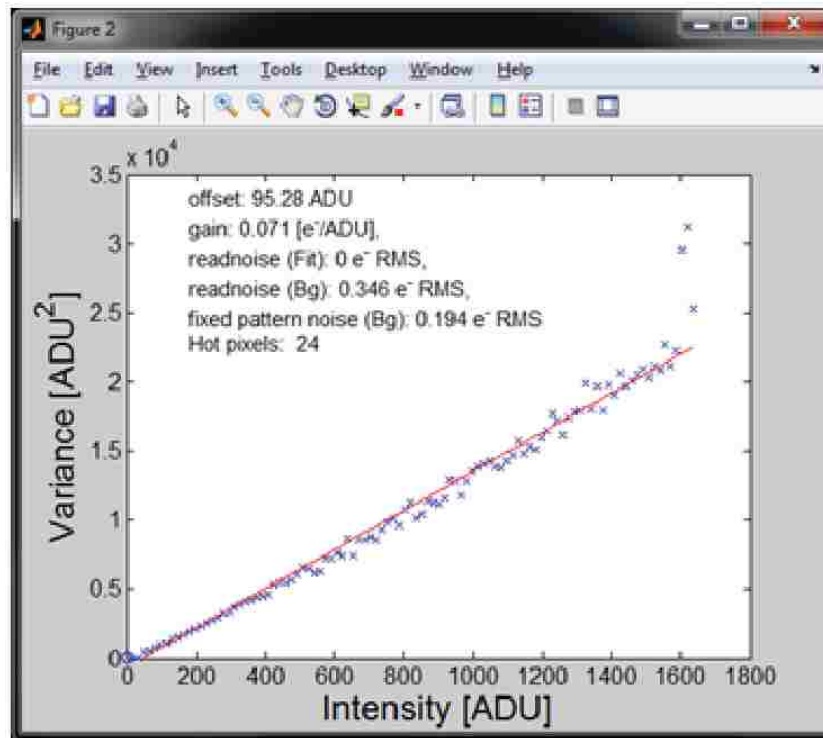
offset: 95.28 ADU
gain: 0.071 [e⁻/ADU],
readnoise (Fit): 0 e⁻ RMS,
readnoise (Bg): 0.346 e⁻ RMS,
fixed pattern noise (Bg): 0.194 e⁻ RMS
Hot pixels: 24

**Figure 2. Gain Calibration**

Wavelength Calibration

Details for performing a new wavelength calibration.

1. Make sure that iXon camera is turned on.
2. Place the LIGHTFORM wavelength calibration lamp (**Error! Reference source not found.**) over the objective and turn off all room lights.
3. Turn on the lamp.
4. Adjust the lamp position to get good signal to noise.
   a. Using the iXon focus (Raw) button, start a focus acquisition.
   b. Make sure that the flip mount is in the correct position. Press the Flip Mount Toggle button to toggle the flip mount between states.
   c. Adjust the lamp position to obtain good signal (you should be able to see several spectral lines).
   d. Stop the focus acquisition by closing the focus window or hitting the Abort Acquisition button in the middle of the GUI.
   e. The exposure time can also be adjusted in order obtain better signal to noise. Typical values of 0.01 can be used.
   f. Once finished be sure to stop the focus acquisition.
5. Press the Calibrate button in the Wavelength Calibration panel.
6. Remember to reset exposure time to 0 after calibration!

Note: The two main peaks from calibration lamp are used to shift the spectrum on a pixel wise basis in relation to an initial calibration.

Additional Calibration Procedures

See Michael Malik's dissertation for a detailed description of additional calibration procedures.
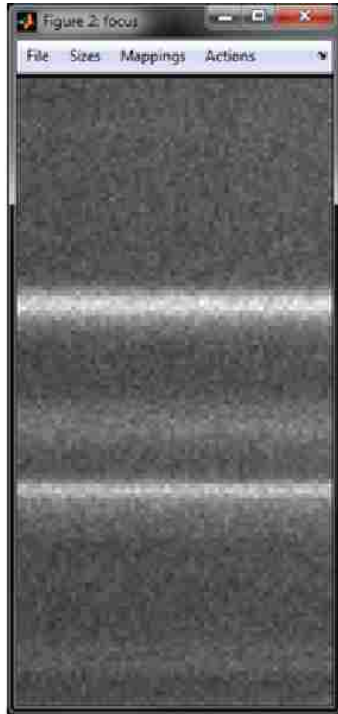
Example intensity distribution for wavelength calibration after focusing with calibration lamp. Note that this will be inverted about the horizontal axis from what is shown during live focusing.

Figure 3. Wavelength Calibration
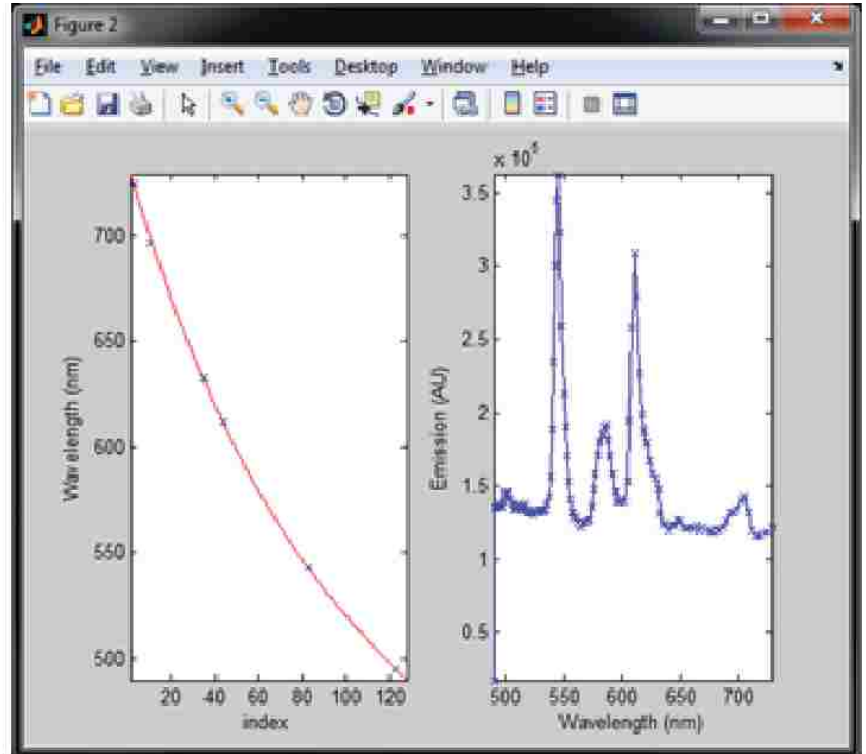
Verify the quality of the spectral calibration. (left) Red line is the polynomial fit fit to the data (blue x) using this automatically generated plot. (right) Shows spectral features of the calibration lamp.
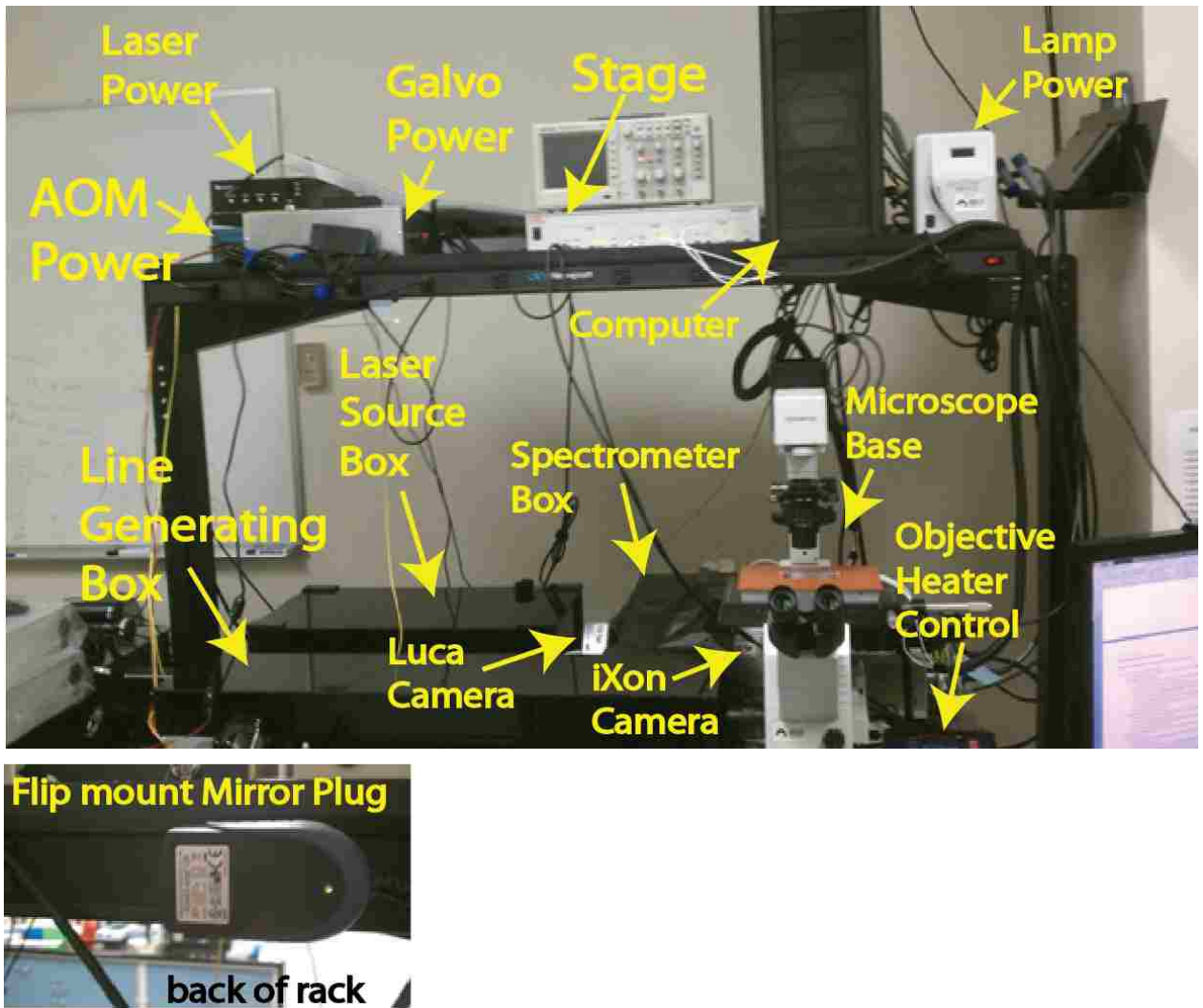
III. Instrumentation

Figure 4. Picture of Instrument

IV.   File Structure

Data Saving and Documentation

- Data is asynchronously saved during acquisition when the 'iXon Scan (HyperView)' button is pressed in the 'iXon CCD Settings' panel.
- The 'hyperView' GUI is used to manipulate data visualization in real-time. See HyperView GUI Usage section for more details.
- All data for a single acquisition is saved in a single folder. The folder is saved in the Save Directory listed in the 'Save Info' panel. See 'Data
- The folder base name is 'hsmImage' and can be altered in the 'Filename Base' section of the 'Save Info' panel. The date is also augmented onto the base name for the folder/filename. The default folder/filename would be in the format 'hsmImage-yyyy-mm-dd-HH-MM-SS'
- It is important to add comments to the acquisition for later reference. This is performed by editing the 'Comments' text box in the 'Save Info' panel. Note that comments are easily edited/added in the hyperView GUI or using the hsiData class after data acquisition.
- In order to easily document experiments, all experiments from a single acquisition period should be saved in a separate acquisition folder. The method 'hsiData.htmlSummary' should be used to summarize acquisitions.

Data Structure

- All data is saved in a single folder with a base name and date information as discussed in the Data Saving and Documentation section. The folder contains the following files:
  - A '.hsi' file in which the base name is the same as the folder name. This is a mat file saved with the '.hsi' extension. This file contains a params structure which contains information about the data acquisitions. The fields of the structure are as follows:
    - sz – column vector containing the size of each frame. sz(1) is the number of spectral bins. sz(2) is the number of pixels along the line. sz(3) is the number of steps per scan.
    - wv – column vector containing wavelength sampling information. Length is sz(1).
    - t – scalar with acquisition time for each scan.
    - pixelSize – scalar with estimated size of each spatial pixel on sample.
    - nt – scalar with number of time frames.
    - iXon – structure with details about camera acquisition parameters.
    - acqInfo – string describing the acquisition.
    - comments – cell array with dimensions number of comments by 2. The first column contains date information and the second column contains a string with the actual comment.

- o Series of image cytometry standard (.ics) files. There is a file that corresponds to each frame. They are saved with the same base name and date format as the folder and hsi file with '_#####' augmented on the end. The augmented numbers refer to the frame number, which is zero based.
  - Include details of '.ics' file format here?
- o Additionally background and gain read noise information are saved in mat files.
  - The background file is saved with the name 'HSM_Background' augmented with the date and time. A background is always acquired prior to acquisition when using the iXon Scan (HyperView) pushbutton. The following variables are saved in the background file:
    - CameraStruct – structure with details about camera acquisition parameters
    - bg – raw background image
    - bgMean – precomputed mean of the background image
    - temperature – the temperature of the camera at the time of background acquisition
    - time – date and time of background acquisition. Use datestr(time) to get a print out of the date and time. Corresponds to time augmented with HSM_Background for the file name.
  - The gain read noise file is save with the name 'HSM_Calibration' augmented with the date and time. The gain read noise information is only saved if a current gain calibration has been loaded/acquired. A gain calibration is performed/loaded using the iXon EM Gain Calibration pushbutton.
    - CameraStruct – structure with details about camera acquisition parameters
    - bd – calibration image
    - bg – background image
    - temperature – the temperature of the camera at the time of calibration acquisition
    - gain – vector of outputs from function 'cal_readnoise'. gain(1) is n(e-) variance in the background. gain(2) is the 1/slope of the fit in [photons per ADU]. gain(3) is n(e-) readnoise fit. gain(4) is mean background. Reference for gain calibration L.J. van Vliet, D. Sudar and I.T. Young in Cell Biology volume III, J.E. Celis (eds.) Digital Fluorescence Imaging Using Cooled CCD Array Cameras, pp.109-120, 1998.
    - time – date and time of calibration acquisition. Use datestr(time) to get a print out of the date and time.

Corresponds to time augmented with HSM_Calibration for the file name.

- o Additional figures may also be saved in the folder using the hsiData class.
- Changes to data structure
    - o Version 1.01
        - Added 'LaserPower' field to params structure. This variable contains the laser power at time of acquisition.

## Data Loading, Manipulation, and Visualization (hsiData)

- hsiData is a class developed for loading, manipulating, and visualizing hyperspectral image data. This class is the core code used for loading data for the 'SPTHSI' class (more detail included in the Single Particle Tracking section) and the 'hyperView' GUI.
- Dragging and dropping a '*.hsi' file into the Matlab workspace will initialize an hsiData object.
    - o The hsiData object will be named hsiObj. If a variable called hsiObj already exists in the workspace, then the object will be called hsiObj# where # corresponds to a number.
    - o The command 'hsiObj.hyperView' will open the hyperView GUI
- The help for hsiData (help hsiData) provides more details about class capabilities
- The script 'hsiData_examples.m' contains example usage of the class.
- RGB representations of hyperspectral images are compiled using the hsiData (makeRGB method) class or the hyperView GUI. Both approaches save RGBs in the folder with the raw data for quick viewing and summarizing (hsiData.htmlSummary).
- See the sample scripts in Sample Scripts section

Single Particle Tracking (SPTHSI)

- The SPTHSI class is used for single particle tracking in hyperspectral images
- Note that a CUDA compatible GPU is necessary to pro single molecule localizations, but is not required to view results.
- See the SPT user manual for more details

UNM HSM User Manual

V.   hsmDAQ GUI Details

The hsmDAQ is the main data acquisition GUI for the hyperspectral line scanning microscope. This section includes details for panels, pushbuttons, textboxes, etc. in the hsmDAQ GUI. An image of the hsmDAQ GUI is shown below.
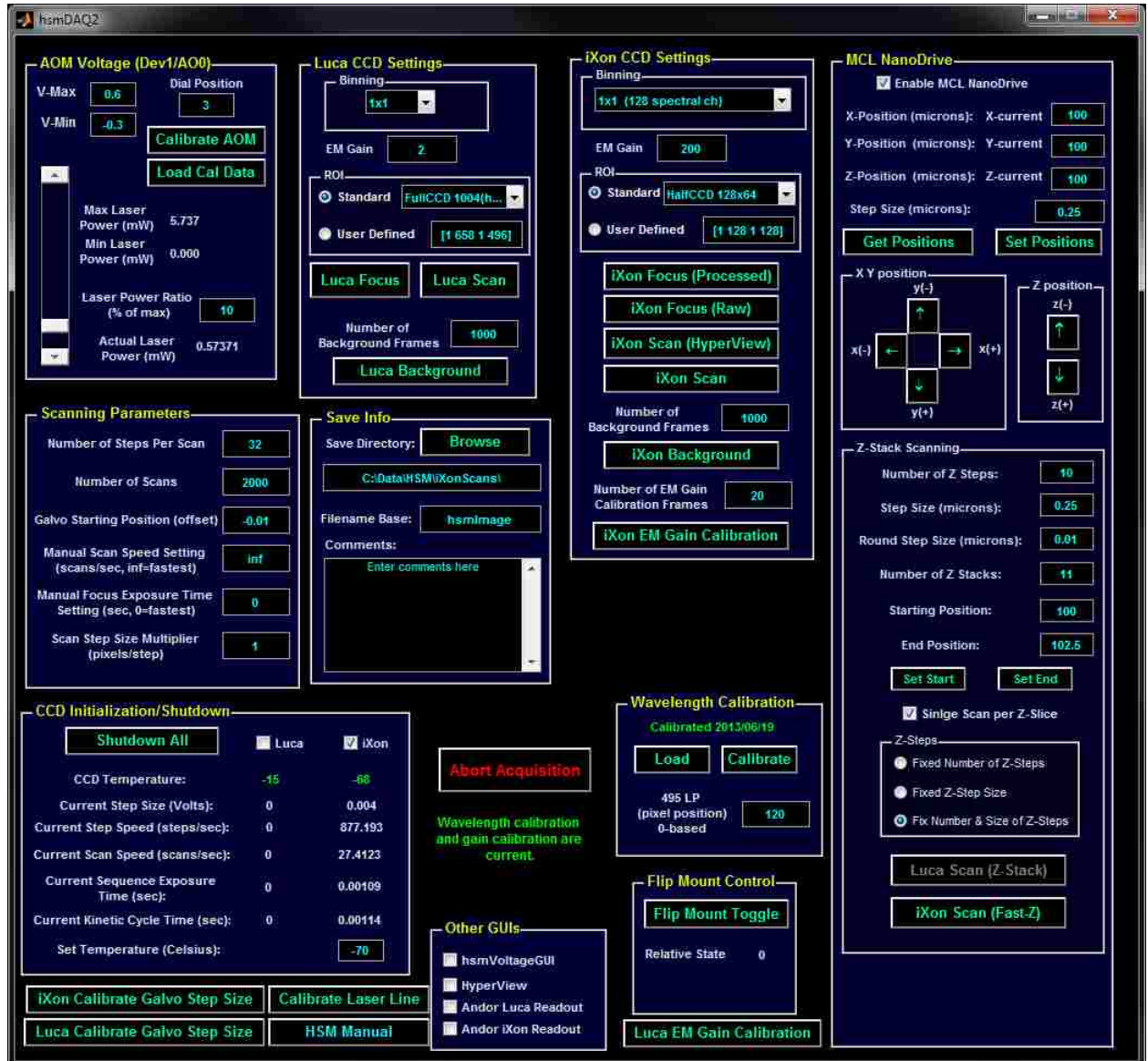
AOM Voltage (Dev1/AO0) panel

Panel with GUI controls for AOM (acusto optic modulator) which controls laser power.

V-Max textbox

UNM HSM User Manual

V-Min textbox

Dial Position Textbox

Calibrate AOM pushbutton

Load Cal Data pushbutton

Load the most recent AOM calibration data set. AOM calibration data is saved in 'Y:\HSM\Calibrations\AOM'.

Laser Power Ratio scrollbar

Laser Power Ratio textbox

Luca CCD Settings panel

iXon CCD Settings panel

Panel with GUI controls for iXon camera.

Binning list

EM Gain textbox

ROI panel

iXon Focus (Processed) pushbutton

Nonfunctioning button. A method for continual movement of the Galvo needs to be implemented prior to usage of this feature. This button should initiate a continuous collection of line scanning for focusing on the sample.

iXon Focus (Raw) pushbutton

Continuously collect frames from the camera. Live gray scale representation is shown. The last gray scale representation is returned to the workspace as the variable 'focus' and automatically displayed upon closing the window (aborting the acquisition). The dimensions of 'focus' are position along the laser line and the wavelength respectively. The wavelength dimension is low spectral channel (~500 nm) to high spectral channel (~800 nm).

UNM HSM User Manual

iXon Scan (HyperView) pushbutton

Collect a line scanning hyperspectral image with asynchronous saving and live viewing with HyperView GUI. A background is automatically acquired prior to image acquisition. If there is not a current calibration for the acquisition parameters, then the user is prompted to proceed. After the acquisition, the user is prompted to save the image. The image is asynchronously saved during acquisition; therefore, if the user selects not to save the data the saved file is deleted.

iXon Scan pushbutton

Collect a line scanning hyperspectral image. Live viewing RGB images are reconstructed using pseudo channels splitting the spectral bins into 3 approximately equal channels in which red, green, and blue channels correspond to high (~800 nm) to low (~500 nm).

Three variables are returned to the workspace two of which are automatically displayed. They are 'scan' (dipimage object), 'sequence' (dipimage object), and 'wv' (matlab array, not shown automatically).

- The 'scan' variable is the RGB representation for each frame obtained during live viewing and shows the field of view on the sample to the user. The dimensions 'scan' are the position along the laser line, scanning position of the laser line, and time respectively. Some frames in 'scan' may be empty because the data may not be obtained for every frame during the live viewing.
- The 'sequence' variable is the 4 dimensional raw data (as seen by the CCD, not reconstructed). The dimensions are the position along the laser line, the wavelength, the scanning position of the laser line, and time respectively.
- The wavelength dimension is oriented according to the 'wv' variable returned to the workspace. The variable 'wv' indicates the approximated center of each spectral bin in accordance to the spectral calibration. If no spectral calibration is loaded, then this consists of a vector of integers beginning at one.

Number of Background Frames textbox

Number of frames to collect for background image.

iXon Background pushbutton

Collect a background image with number of frames specified in Number of Background Frames textbox. Important acquisition parameters for background correlating to an acquired image are camera ROI, binning, horizontal shift speed, vertical shift speed, vertical shift voltage, preamp gain, frame transfer mode, baseline clamp, exposure time, and EM gain. Background is retained as a field in the handles structure named 'iXonBackground' which is a structure containing two variables 'bg', 'CameraStruct', and 'temperature'. The variable bg is the background image in a dipimage object. The variable CameraStruct is a structure with all of the camera settings at the time of background acquisition. The variable temperature is the camera temperature at the time of background acquisition. If the current background has the same acquisition parameters

as the current settings then the Background and Calibration Indicator Static Text will be updated.

Number of EM Gain Calibration Frames textbox
Number of frames to collect for EM gain calibration.

iXon EM Gain Calibration pushbutton
Perform EM Gain calibration. Important acquisition parameters for a gain calibration correlating to an acquired image are temperature, EM gain, and preamp gain. If there is a calibration file in the calibration folder less than 24 hours old that has the same important acquisition parameters as the current settings, then that calibration file will be selected and the Background and Calibration Indicator Static Text will be updated. Old calibration files are deleted after 1 week. Follow the instructions in Gain Calibration section prior to pressing button. Gain calibration procedure is as follows:

- Collect a background with number of frames specified in Number of EM Gain Calibration Frames textbox. Shutter is kept closed for background collection. Saved in variable 'bg'.
- Collect a calibration image with number of frames specified in Number of EM Gain Calibration Frames textbox. Saved in variable 'bd'.
- Calculate the readnoise using 'cal_readnoise.m' which is based on L.J. van Vliet, D. Sudar and I.T. Young in Cell Biology volume III, J.E. Celis (eds.)   Digital Fluorescence Imaging Using Cooled CCD Array Cameras, pp.109-120, 1998. The gain is obtained by fitting a line to the variance vs intensity plot. Output is saved as 'gain' and gain(2) is the inverse of the slope of the fit line which is interpreted as the gain. Multiplying gain(2) by an acquired image will convert the raw image to photoelectrons (inferred from the gain calibration). Gain calibration figures will be shown.
- The variables bg, bd, gain, temperature, and CameraStruct are saved in the folder 'Y:\HSM\Calibrations\EM Gain' in a file with the base name 'EMgainCalibraiton' augmented with the date. The variable temperature is a scalar with the camera temperature at the time of the calibration. The variable 'CameraStruct' is a structure with all of the camera's acquisition parameters at time of calibration.

Scanning Parameters panel

Save Info panel

Save Directory
Save hyperspectral image files in specified directory. Use the Browse button or text box to alter the save directory.

Filename Base
Base file name for saving hyperspectral image files. Base name is always augmented with date information for the actual file name.

Comments

Insert text for comments to be saved in hyperspectral image structure. Describe the sample and other parameters.

Luca Line Scanning Analysis panel

This panel is no longer used and should probably be removed??

CCD Initialization/Shutdown panel

Panel with GUI control for initialization and shutdown of the Luca and iXon cameras.

Shutdown All

Shutdown Luca and iXon cameras. Using this button is the proper way to shutdown the cameras because it unloads the Andor library from the matlab environment.

Luca checkbox

Initialize the Luca camera. This is defined by the serial number in the GUI code. If the camera is changed then this serial number needs to be changed.

iXon checkbox

Initialize the iXon camera. This is defined by the serial number in the GUI code. If the camera is changed then this serial number needs to be changed.

Set Temperature textbox

Define a set temperature for the iXon camera. This only affects the camera settings/temperature if it is defined prior to initialization of the camera. This is useful for not having to cool/warm the camera completely when trouble shooting.

Wavelength Calibration panel

Panel with GUI control to load/perform spectral wavelength calibration. Text in red (no calibration loaded) or green (date details of current calibration) give details about current calibration status. Spectral calibration data are saved in 'Y:\HSM\Calibrations\Wavelength\'. Loading or performing a calibration will result in calibration plots which can be inspected for quality assurance.

Load

Load a previously acquired spectral calibration.

Calibrate

Perform wavelength calibration. See Wavelength Calibration section for more details on setting up the calibration. The spectral calibration is performed by using 6 estimated peak positions (547, 588, 616, 708, 736, & 768) for the calibration lamp. The peaks were estimated using emission characteristics of the lamp measured on a ? (get details of prosnitz fluorimeter) fluorimeter in September 2010. See data file 'Y:\HSM\Calibrations\Wavelength\ PatLampCalibration1009.mat'. Longer wavelength peaks are not very well defined. The calibration method can be improved in longer wavelength region by calibrating with the

UNM HSM User Manual

LIGHTFORM lamp and the Krypton calibration lamp. The built in matlab function 'interp1' is used to fit a cubic to the calibration peaks to perform the calibration.

Flip Mount Control panel

Panel with GUI controls for flip mount mirror for using either the Luca or iXon cameras. The relative state is always initially set to zero and can be noted in order to keep track of the current state.

Flip Mount Toggle

Toggle the flip mount between states.

Other GUIs panel

Panel with checkboxes for view other related GUIs.

hsmVoltageGUI checkbox

HyperView checkbox

Andor Luca Readout checkbox

If checked then view the Andor Luca Readout GUI which allows for the adjustment of readout parameters. These parameters include: Horizontal Shift Speed, Vertical Shift Speed, Vertical Shift Voltage, PreAmp Gain, Frame Transfer Mode, and Baseline Clamp. Note that the Andor Luca Readout GUI and the Andor iXon ReadoutGUI can't be open simultaneously.

Andor iXon Readout checkbox

If checked then view the Andor iXon Readout GUI which allows for the adjustment of readout parameters. These parameters include: Horizontal Shift Speed, Vertical Shift Speed, Vertical Shift Voltage, PreAmp Gain, Frame Transfer Mode, and Baseline Clamp. Note that the Andor Luca Readout GUI and the Andor iXon ReadoutGUI can't be open simultaneously.

Abort Acquisition pushbutton

Background and Calibration Indicator Static Text

iXon Calibration Galvo Step Size pushbutton

Luca Calibration Galvo Step Size pushbutton

UNM HSM User Manual

Calibrate Laser Line pushbutton

Luca EM Gain Calibration pushbutton

www.manaraa.com

VI.   HyperView GUI Usage

The hyperView GUI is the user interface for live viewing and post-viewing hyperspectral data sets. Examples of the GUI are provided in Figure 5 and Figure 7. Note that there is an additional 'Z-stack' panel in the 5D case. The user can view details on the functionality of the GUI components by using the 'Tool Tips' checkbox. Two additional GUIs are also used to manipulate the representation(s) of data and edit comments (Figure 6).
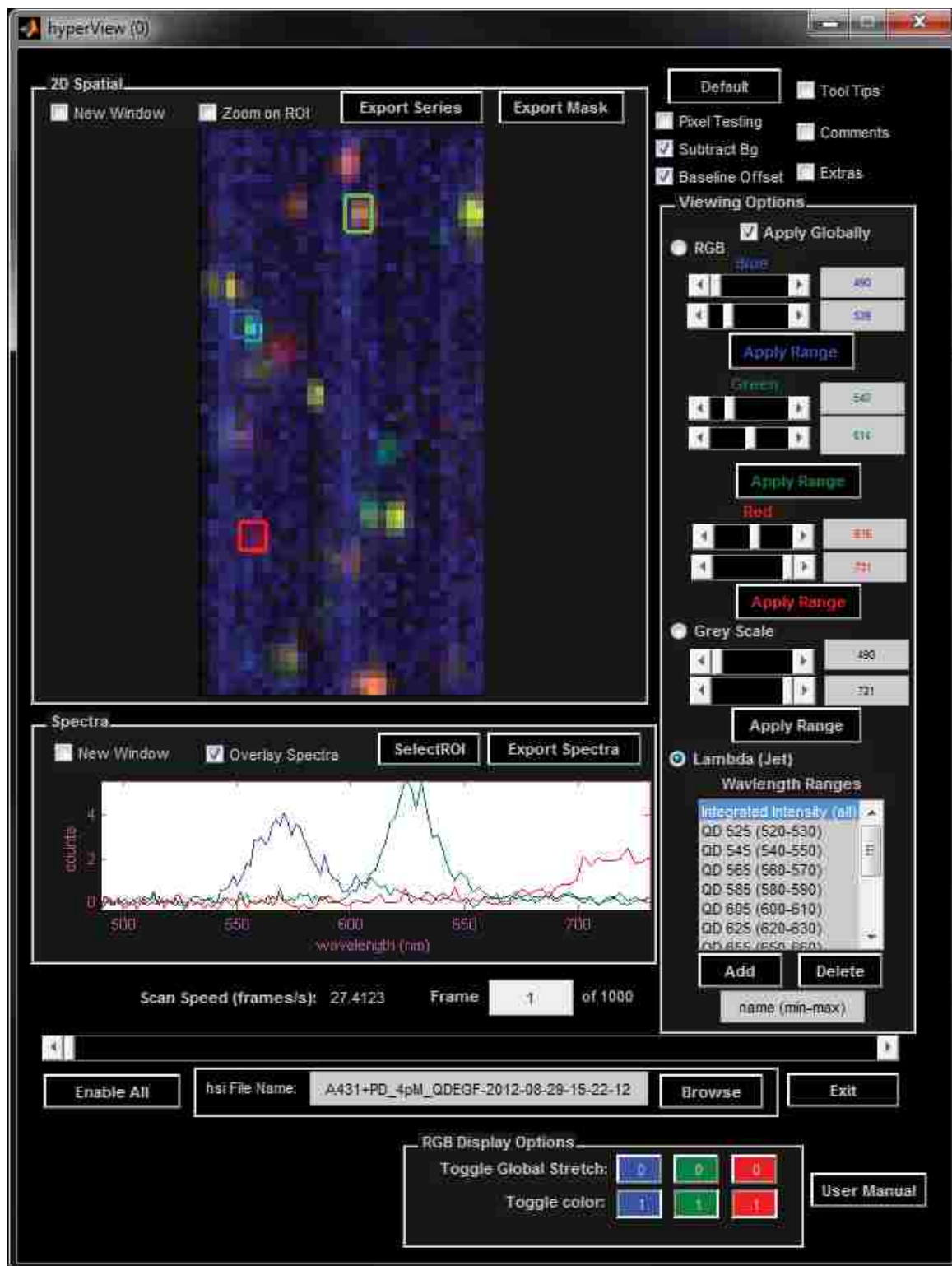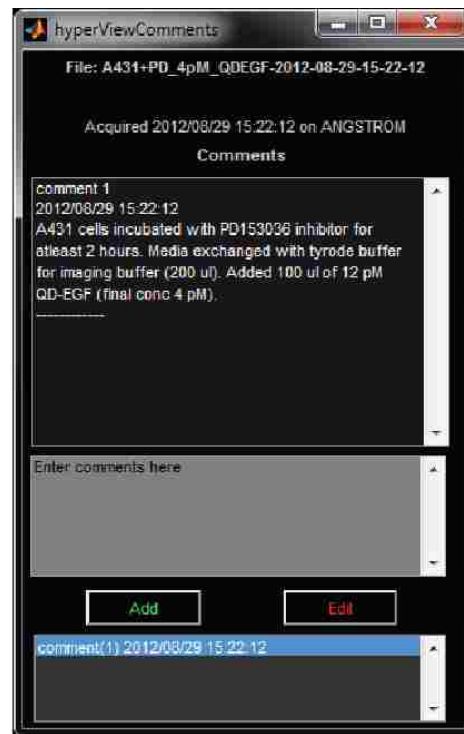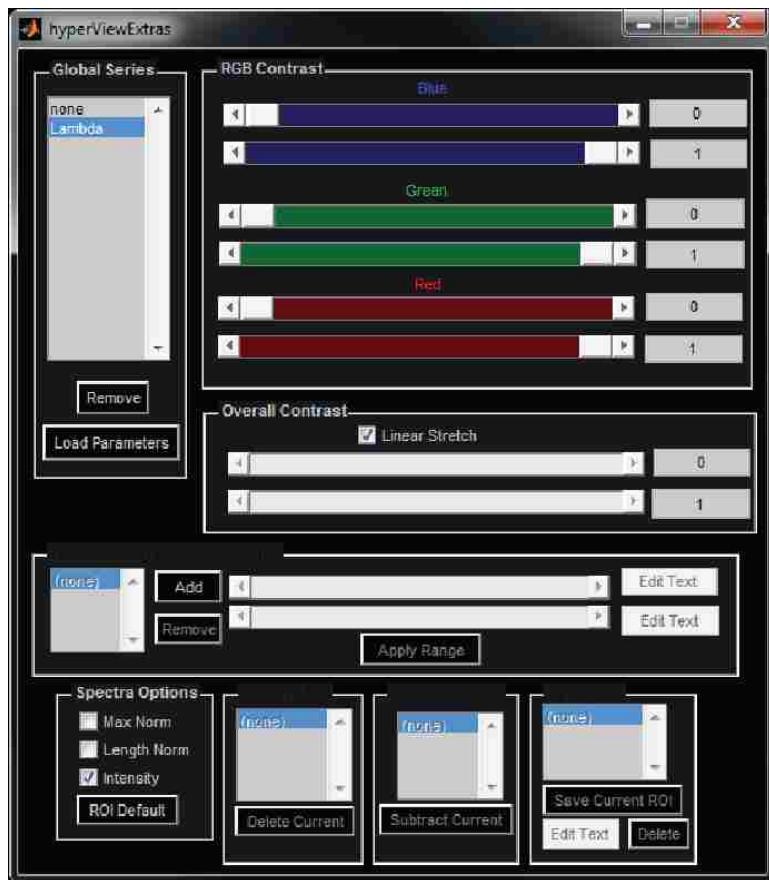
Figure 5. Main hyperView GUI 4D data (x,y,λ,t)

left, hyperView Extras GUI.
right, hyperView Comments GUI.
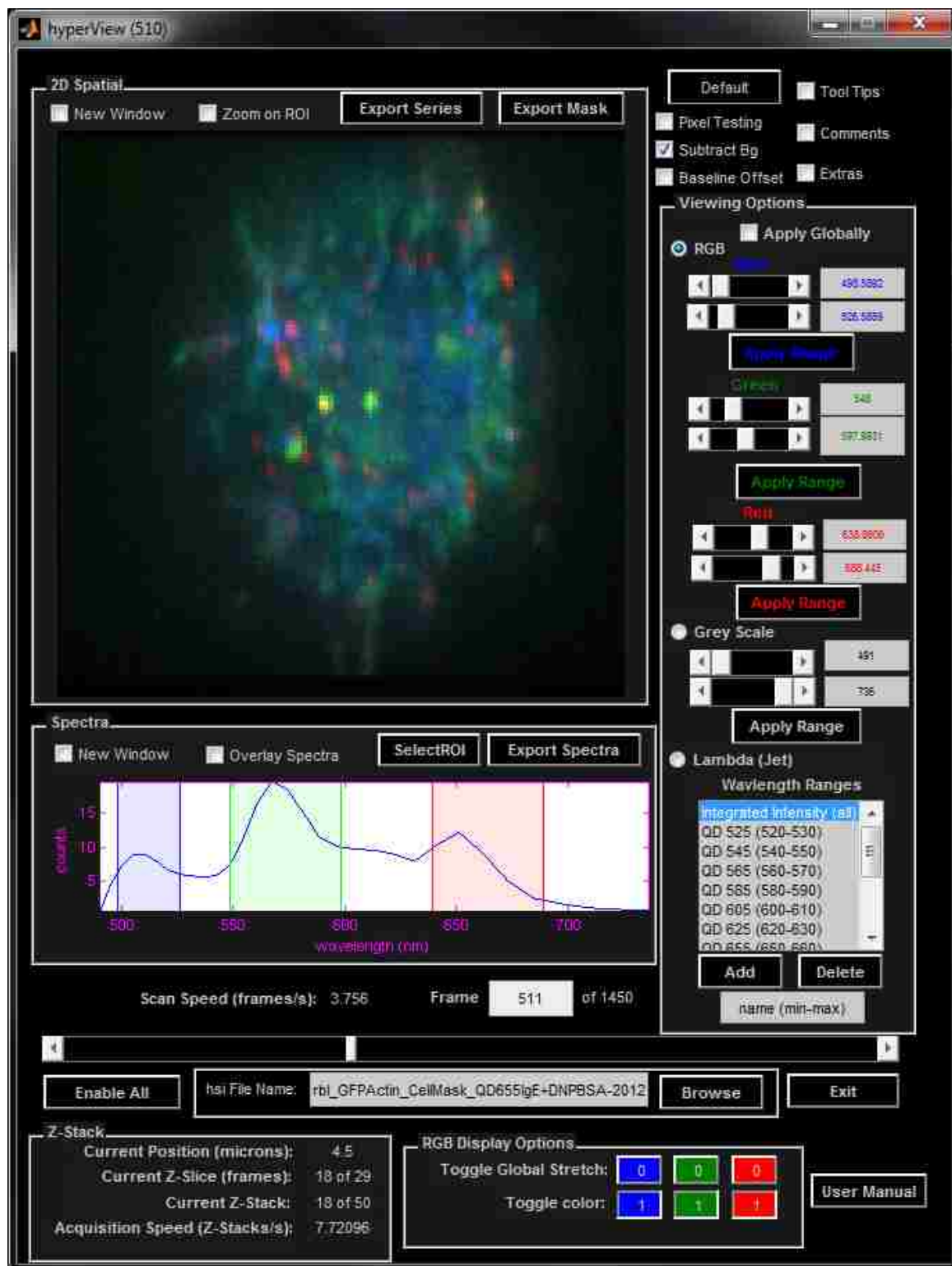
Figure 6. Additional hyperView GUIs

Figure 7. Main hyperView GUI 5D data (x,y,λ,z,t)

VII.   Instrumentation Trouble Shooting

Slit alignment

If the PSF of individual QDs appears to have a significant aberration in the line scanning dimension (see figure to the right; highlighted by red x), then the slit alignment may need to be adjusted. If the slit alignment appears to be off, then you can use tetraspek beads to test its alignment. See bullets below. After realigning the slit it is good to check whether or not the slit is in focus. To check the focus on the slit simply set the camera ROI to 128x128. Acquire using "iXon Focus (Raw)", you should be able to see a sharp edge in the line dimension.

Figure 8. QD PSF with misaligned slit.

- Rotating the micrometer for the stage translation back towards the wall
  - moves the slit towards the camera
  - PSF skews to the right (as viewed in hyperview; right along the line scanning dimension)
  - Left figure below
- Rotating the micrometer towards the microscope
  - moves the slit away from the camera
  - PSF skews to the left (as viewed in hyperview; left along the line scanning dimension)
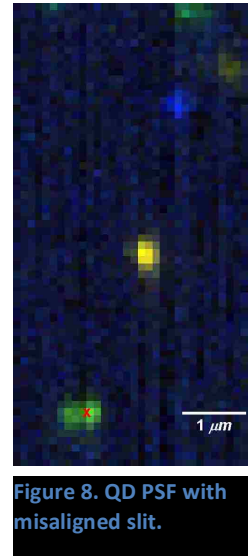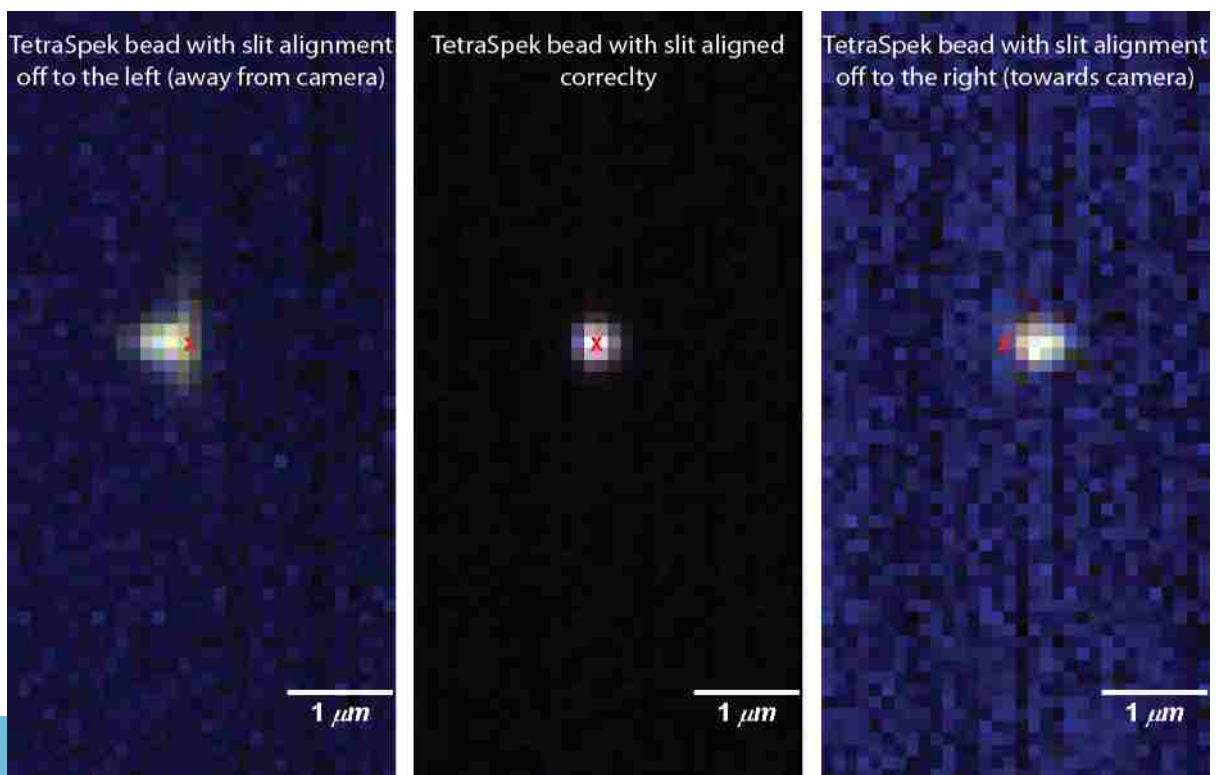 - Right figure below

Figure 9. Slit alignment with tetraspek beads

Light leakage into spectrometer box

Verify that all panels are on the spectrometer box and blackout cloth is in place around spectrometer to limit light leakage. It is recommended to have all room lights turned off while acquiring data on the HSM he help limit effects of stray light.

Objective Correction Collar

Poor Signal to Noise

Alignment of laser to fiber

The laser power entering/exiting the fiber with no ND filters should be ~16 mW.

EM Gain Setting

The EM Gain is set to 2 by default but should be adjusted to 200 for most low signal to noise experiments (i.e. SPT experiments).

VIII.   Sample Scripts

Example scripts for manipulating hyperspectral data.

makeSummary

Example script for making a summary for a set of data acquisitions.

```
%makeSummary

%% make spectral and intesity figures

close all
clear all

%data directory
dataDir = pwd;

%spectral frames to plot
spFrames = 1:2000; %sum all spectra
spFrames1 = 1:5:50; %specific frame to show spectra for
%spectral range to sum over
spCutoff = [400 800];

% find hsi files
[hsiFileNames hsiFullFileNames] = hsiData.findFiles(dataDir);

for ii = 1:length(hsiFullFileNames)
    fprintf('file %i of %i\n',ii,length(hsiFullFileNames));
```

```matlab
    %make object
    hsiObj = hsiData(hsiFullFileNames{ii});

    %find spectral range
    [~, minWvIdx] = min(abs(hsiObj.AcqParams.wv - spCutoff(1)));
    [~, maxWvIdx] = min(abs(hsiObj.AcqParams.wv - spCutoff(2)));
    wvRange = false(size(hsiObj.AcqParams.wv));
    wvRange(maxWvIdx:minWvIdx) = true;

    %      hsiObj.BaseName
    %      hsiObj.AcqParams.LaserPower

    if exist(fullfile(hsiObj.Path,'figures'),'dir')
        rmdir(fullfile(hsiObj.Path,'figures'),'s')
    end

    %load data
    data = hsiObj.loadFrames;
    %spectrum for each frame
    sp = squeeze(sum(sum(data(:,:,:,:),3),2));
    %time course of fluoresence intensities
    I = squeeze(sum(sp(wvRange,:),1));

    %plot sum image
    h = dipshow(squeeze(sum(sum(data,4),1)));
    monPos = get(0,'MonitorPositions');
    tmpSz = [size(data,2) size(data,3)]*10;
    if any(tmpSz([1 2]) > min(monPos(:,[3 4])))
        diptruesize(h,min(floor(min(monPos(:,[3 4]))./min(tmpSz([1
2]))*10-1))*100);
    else
        %change size
        diptruesize(h,1000);
    end
    hsiObj.saveFig(h,'sumImage')

    %plot spectra
    h = figure;
    spFramesTmp = spFrames;
    spFramesTmp(spFramesTmp>size(sp,2)) = [];
    %      spLegendName = cellfun(@(x) sprintf('frame %i',x),
num2cell(spFramesTmp),'uniformoutput',false);
    plot(hsiObj.AcqParams.wv,sum(sp(:,spFramesTmp),2),'linewidth',2)
    title(gca,hsiObj.BaseTitleName)
    axis tight
    xlabel('wavelength (nm)')
    ylabel('counts (photons)')
    %      legend(spLegendName)
    %
hsiObj.saveFig(h,sprintf('spectraFrames(%s%s)',sprintf('%i',spFrames(1)
),sprintf(',%i',spFrames(2:end))))
    hsiObj.saveFig(h,'spectra')

    %plot spectra
```

```matlab
    h = figure;
    spFramesTmp = spFrames1;
    spFramesTmp(spFramesTmp>size(sp,2)) = [];
    spLegendName = cellfun(@(x) sprintf('frame %i',x),
num2cell(spFramesTmp),'uniformoutput',false);
    plot(hsiObj.AcqParams.wv,sp(:,spFramesTmp),'linewidth',2)
    %
plot(hsiObj.AcqParams.wv,sum(sp(:,spFramesTmp),2),'linewidth',2)
    title(gca,hsiObj.BaseTitleName)
    axis tight
    xlabel('wavelength (nm)')
    ylabel('counts (photons)')
    legend(spLegendName)

hsiObj.saveFig(h,sprintf('spectraFrames(%s%s)',sprintf('%i',spFrames1(1
)),sprintf(',%i',spFrames1(2:end))))
    %     hsiObj.saveFig(h,'spectra')



    %plot time course of integrated intensities
    h = figure;
    plot((1:length(I))/hsiObj.FrameRate,I,'linewidth',2)
    title(gca,hsiObj.BaseTitleName)
    axis tight
    xlabel('time (s)')
    ylabel('counts (photons)')
    hsiObj.saveFig(h,sprintf('IntensityVsTime(%i-%i)',spCutoff))

    close all
end

%% put all intensity plots in a single figure

close all

[name fullname] = hsiData.findFiles;

%sort names by time in name
[~, idx] = sort(cellfun(@(x) x(end-
18:end),name,'uniformoutput',false));
name = name(idx);
fullname = fullname(idx);



clear xval yval
xval = nan(numel(name),2000);
yval = nan(numel(name),2000);
for ii = 1:numel(name)
    figName = fullfile(fileparts(fullname{ii}),'figures',sprintf('%s-
IntensityVsTime(%i-%i).fig',name{ii},spCutoff));
    if exist(figName,'file')
        open(figName);
        xvalTmp = get(findall(gca,'type','line'),'xdata');
        if iscell(xvalTmp)
```

```matlab
            xvalTmp = xvalTmp{1};
        end
        xval(ii,1:numel(xvalTmp)) = xvalTmp;
        yval(ii,1:numel(xvalTmp)) =
get(findall(gca,'type','line'),'ydata');
    end
end


[path folderName] = fileparts(pwd);


h = figure;
set(gca,'ColorOrder',hsv(numel(name)))
line(xval',yval','linewidth',2)
legend(regexprep(name,'_','-'),'location','SouthOutside')
axis tight
title({regexprep(folderName,'_','-');'all acquisitions'})
xlabel('time (s)')
ylabel('counts (photons)')
saveas(h,sprintf('AllFilesIntensityVsTime(%i-%i)',spCutoff),'png')
saveas(h,sprintf('AllFilesIntensityVsTime(%i-%i)',spCutoff),'fig')

%% put all spectral plots in a single figure

close all

[name fullname] = hsiData.findFiles;

%sort names by time in name
[~, idx] = sort(cellfun(@(x) x(end-
18:end),name,'uniformoutput',false));
name = name(idx);
fullname = fullname(idx);



clear xval yval
xval = nan(numel(name),128);
yval = nan(numel(name),128);
for ii = 1:numel(name)
    figName = fullfile(fileparts(fullname{ii}),'figures',sprintf('%s-
spectra.fig',name{ii}));
    if exist(figName,'file')
        open(figName);
        xvalTmp = get(findall(gca,'type','line'),'xdata');
        if iscell(xvalTmp)
            xvalTmp = xvalTmp{1};
        end
        xval(ii,1:numel(xvalTmp)) = xvalTmp;
        yvalTmp = get(findall(gca,'type','line'),'ydata');
        if iscell(yvalTmp)
            yvalTmp = yvalTmp{1};
        end
        yvalTmp = yvalTmp-min(yvalTmp);
        yval(ii,1:numel(xvalTmp)) = yvalTmp/sum(yvalTmp);
    end
end
```

```matlab
[path folderName] = fileparts(pwd);

h = figure;
set(gca,'ColorOrder',hsv(numel(name)))
line(xval',yval','linewidth',2)
legend(regexprep(name,'_','-'),'location','SouthOutside')
axis tight
title({regexprep(folderName,'_','-');'all acquisitions'})
xlabel('time (s)')
ylabel('counts (photons)')
saveas(h,sprintf('AllFilesSpectra'),'png')
saveas(h,sprintf('AllFilesSpectra'),'fig')


%% make hsiData html summary

close all
clear all

%data directory
dataDir = pwd;

hsiData.htmlSummary(dataDir);
```

hsiData_examples

Examples usage of hsiData objects.

```matlab
% hsiData_examples
%
% Example usage of hsiData. File names used here are only examples you
% will need to change names of files. For easy reference, it is
suggested
% that you copy/save a renamed copy (i.e. hsiData_examples_pat) of this
% file in your matlab search path.
%
%   <a href="matlab:edit('SPThsiTutorial.m');">run tutorial</a>
%
% Created by Pat Cutler October 2012


%% user interactive initialization

close all
clear all

obj = hsiData;
obj.loadAcqParams;
```

```matlab
%% scripted initialization

close all
clear all

% DataFile =
'C:\Data\HSM\iXonScans\Pat\2012_01_19\rbl_GFPActin_CellMask_QDIgE_DNPBS
A-2012-01-19-14-10-36\rbl_GFPActin_CellMask_QDIgE_DNPBSA-2012-01-19-14-
10-36.hsi';
% DataFile = 'Y:\HSM\iXonScans\Pat\2012_01_17\rbl_2_QDIgE+DNPBSA-2012-
01-17-18-06-16\rbl_2_QDIgE+DNPBSA-2012-01-17-18-06-16.hsi';
DataFile =
'T:\HSM\iXonScans\Pat\2012_01_20\rbl_GFPActin_CellMask_QDIgE705_DNPBSA-
2012-01-20-18-26-52\rbl_GFPActin_CellMask_QDIgE705_DNPBSA-2012-01-20-
18-26-52.hsi';
obj = hsiData(DataFile);

%% show image in HyperView2

obj.hyperView;

%% load frames from file

% frames = []; %load all frames
frames = [1 5]; %load first frame
% frames = [1 obj.Tframes]; %load first and last frame

data = obj.loadFrames(frames);
obj.Stats.time


%% preload raw data and then load frames

frames = []; %load all frames
% frames = 1; %load first frame
% frames = [1 obj.Tframes]; %load first and last frame

obj.loadRawData;
data = obj.loadFrames;
obj.Stats.time %show time necessary for

%% find all rgbSeries for a specified

hsiDataObj.findFigs

%% make/save additional figures

close all
clear all

%data directory
dataDir = 'I:\Pat Documents\Research\HSM_DATA\2012_09_20';
```

236

```matlab
%spectral frames to plot
spFrames = [1 200 300 400 1000];
spLegendName = cellfun(@(x) sprintf('frame %i',x),
num2cell(spFrames),'uniformoutput',false);

% find hsi files
[hsiFileNames hsiFullFileNames] = hsiData.findFiles(dataDir);

for ii = 1:length(hsiFullFileNames)
    %make object
    hsiObj = hsiData(hsiFullFileNames{ii});

    %       hsiObj.BaseName
    %       hsiObj.AcqParams.LaserPower

    %load data
    data = hsiObj.loadFrames;
    %spectrum for each frame
    sp = squeeze(sum(sum(data(:,:,:,:),3),2));
    %time course of fluoresence intensities
    I = squeeze(sum(sp,1));

    %plot spectra
    h = figure;
    plot(hsiObj.AcqParams.wv,sp(:,spFrames),'linewidth',2)
    title(gca,hsiObj.BaseTitleName)
    axis tight
    xlabel('wavelength (nm)')
    ylabel('counts (photons)')
    legend(spLegendName)

hsiObj.saveFig(h,sprintf('spectraFrames(%s%s)',sprintf('%i',spFrames(1)
),sprintf(',%i',spFrames(2:end))))

    %plot time course of integrated intensities
    h = figure;
    plot((1:length(I))/hsiObj.FrameRate,I,'linewidth',2)
    title(gca,hsiObj.BaseTitleName)
    axis tight
    xlabel('time (s)')
    ylabel('counts (photons)')
    hsiObj.saveFig(h,'IntensityVsTime')

end

%% make isosurface for multiple channels in 3D image

close all
clear all

% DataFile =
'C:\Data\HSM\iXonScans\Pat\2012_01_19\rbl_GFPActin_CellMask_QDIgE_DNPBS
A-2012-01-19-14-10-36\rbl_GFPActin_CellMask_QDIgE_DNPBSA-2012-01-19-14-
10-36.hsi';
```

UNM HSM User Manual

```matlab
% DataFile =
'T:\HSM\iXonScans\Pat\2012_01_20\rbl_GFPActin_CellMask_QDIgE705_DNPBSA-
2012-01-20-18-26-52\rbl_GFPActin_CellMask_QDIgE705_DNPBSA-2012-01-20-
18-26-52.hsi';
% DataFile =
'T:\HSM\iXonScans\Pat\2012_01_20\rbl_GFPActin_CellMask_QD655IgE_DNPBSA-
2012-01-20-18-48-47\rbl_GFPActin_CellMask_QD655IgE_DNPBSA-2012-01-20-
18-48-47.hsi';
DataFile =
'Y:\HSM\iXonScans\Pat\2012_01_20\rbl_GFPActin_CellMask_QD655IgE_DNPBSA-
2012-01-20-18-48-47\rbl_GFPActin_CellMask_QD655IgE_DNPBSA-2012-01-20-
18-48-47.hsi';
obj = hsiData(DataFile);
% frames = 1;
frames = obj.Tframes;
obj.LoadParams.zSlice.idx(1:3) = 0;
channels = [640 680; 500 531; 560 612];
% channels = [ 670 740; 560 612; 500 531];
c = [1 0 0; 0 0 1; 0 1 0];
isoValue = [.2 .4 .3];
alpha = [.5 .5 .5];
%preload raw data
obj.loadRawData;

close all
clear data
hdip = figure; %figure handle for dipimage figure
hiso = figure; %figure handle for isosurface figure
ahiso = gca; %axes handle for isosurface
xlabel(ahiso,'x (nm)')
ylabel(ahiso,'y (nm)')
zlabel(ahiso,'z (nm)')
view(ahiso,-45,45)
%set lighting for isosurface
camlight;
lighting(ahiso,'gouraud')
for ii = 1:size(channels,1)
    %identify closest wavelength indices
    [v idx(1)] = min(abs(obj.AcqParams.wv-channels(ii,1)));
    [v idx(2)] = min(abs(obj.AcqParams.wv-channels(ii,2)));
    idx = sort(idx);
    %set spectral mask
    obj.LoadParams.masks.spectral =
zeros(size(obj.LoadParams.masks.spectral));
    obj.LoadParams.masks.spectral(idx(1):idx(2)) = 1;
    %sum spectral data over spectral dimension
    data{ii} = squeeze(sum(obj.loadFrames(frames)));
    %normalize data and reverse zdirection
    data{ii} = data{ii}(:,:,end:-1:1)/max(max(max(data{ii})));
    %make isosurface
    fv(ii) = isosurface(data{ii},isoValue(ii));
    %adjust vertices to be in microns
    fv(ii).vertices = fv(ii).vertices.*...
        repmat([obj.AcqParams.pixelSize*1e-3
obj.AcqParams.pixelSize*1e-3 obj.AcqParams.ZstepSize],...
        [size(fv(ii).vertices,1) 1]);
    %make iso suface
```

238

```
        ph(ii) = patch(fv(ii),'parent',ahiso,'facecolor',c(ii,:),...
            'EdgeColor','none','facealpha',alpha(ii));
end
%make dipimage RGB
dipshow(hdip,colorspace(dip_image(data([1 3 2])),'RGB'));
dipmapping(hdip,'global')
```

Perform Spectral Unmixing

Import calibration spectra

```
% importSpectra

close all
clear all

%specify data directory
superResDir = 'I:\Pat Documents\Research\HSM_DATA\2013_08_27 RBL fIgE
QDdnp Fixed\SRresultsSum';

%get wavelength information
[hsiFileNames, hsiFilesFullName] =
hsiData.findFiles(fileparts(superResDir));
hsiDataObj = hsiData(hsiFilesFullName{1});
wv = hsiDataObj.AcqParams.wv;

%specify calibration directory with raw invitrogen spectra
calDataDir = 'I:\Pat Documents\Research\HSM_DATA\2013_06_13 RBL Alexa
IgE';
% calDataDir = 'E:\Data\HSM\iXonScans\Pat\2013_06_13 RBL Alexa IgE';

AFnames = [488 514 532];

afspInvitrogen = zeros(numel(AFnames),numel(wv));
for ii = 1:numel(AFnames)

    afname{ii} = sprintf('%s %i','Alexa Fluor',AFnames(ii));

    afnameInvitrogen{ii} = sprintf('%s %i Invitrogen','Alexa
Fluor',AFnames(ii));
    AFfileName = sprintf('%s.csv',afname{ii});
    [spData columnTitle] =
xlsread(fullfile(calDataDir,'SPTresults','scripts',AFfileName));
    afspInvitrogen(ii,:) = interp1(spData(:,1),spData(:,3),wv);
    afspInvitrogen(ii,:) =
afspInvitrogen(ii,:)/sum(afspInvitrogen(ii,:));
    afspInvitrogenMaxNorm(ii,:) =
afspInvitrogen(ii,:)/max(afspInvitrogen(ii,:));
end
```

```matlab
%specify calibration directory with collected spectra
calDataDir1 = 'I:\Pat Documents\Research\HSM_DATA\2013_06_20 RBL Alexa
IgE';
% calDataDir1 = 'E:\Data\HSM\iXonScans\Pat\2013_06_20 RBL Alexa IgE';

[hsiFileNames, hsiFilesFullName] = hsiData.findFiles(calDataDir1);

calSpNames = {'A488_Laser5-2013-06-20-14-13-21';
    'A514_Laser5-2013-06-20-14-06-59';
    'A532_Laser10-2013-06-20-13-57-07';
    'H2O_Laser100-2013-06-20-11-48-42'};
names1 = {'Alexa Fluor 488' 'Alexa Fluor 514' 'Alexa Fluor 532' 'Raman
585'};
spNames1 = {'A488' 'A514' 'A532' 'Raman585'};

sp1 = zeros(numel(names1),numel(wv));
for ii = 1:numel(names1)

    hsiObj =
hsiData(hsiFilesFullName{strcmp(calSpNames{ii},hsiFileNames)});

    figureFiles = dir(fullfile(hsiObj.Path,'figures','*.fig'));
    figureFiles(cellfun('isempty',regexp({figureFiles.name},'-
spectra.fig'))) = [];

    h = open(fullfile(hsiObj.Path,'figures',figureFiles.name));

    sp1(ii,:) =
get(findall(findall(h,'type','axes','tag',''),'type','line'),'ydata');
    sp1(ii,:) = sp1(ii,:)-mean(sp1(ii,end-3:end-2));
    sp1(ii,:) = sp1(ii,:)/sum(sp1(ii,:));
    spMaxNorm1(ii,:) = sp1(ii,:)/max(sp1(ii,:));

end


%augment together spectra
sp = [sp1];
spMaxNorm = [spMaxNorm1];
%augement names
names = [names1];
spNames = [spNames1];

%switch position of Raman and Chromeo calibration spectra
% idx1 = [5 6];
% idx2 = [6 5];
% sp(idx1,:) = sp(idx2,:);
% spMaxNorm(idx1,:) = spMaxNorm(idx2,:);
% names(idx1) = names(idx2);
% spNames(idx1) = spNames(idx2);

%plot spectra
h1 = figure;
plot(wv,spMaxNorm,'linewidth',2)
```

UNM HSM User Manual

```matlab
hold on
plot(wv,afspInvitrogenMaxNorm,'--','linewidth',2)
hold off
axis tight
xlabel('wavelength (nm)')
ylabel('normalized counts')
legend([names afnameInvitrogen])

saveas(h1,fullfile(superResDir,'CalSpectra'),'png')
saveas(h1,fullfile(superResDir,'CalSpectra'),'fig')

save(fullfile(superResDir,'CalSpectra'),'sp','afspInvitrogen','names','spNames','wv')
```

Make data file with variables containing concentration maps for each specie.

```matlab
% makeDataFiles

%% get concentration maps for individual dyes

close all
clear all

dataDir = 'I:\Pat Documents\Research\HSM_DATA\2013_08_27 RBL fIgE QDdnp Fixed';

superResDir = fullfile(dataDir,'SRresultsSum');

if ~exist(superResDir,'dir')
    mkdir(superResDir)
end

% fileStr = {'rbl_3colors(100pM)'};
fileStr = {'rbl_'};
spName = {{'A488' 'A514' 'A532'}};
spIdx = {[1 2 3]}; %index for SP in

[hsiFileNames, hsiFilesFullName] = hsiData.findFiles(dataDir);

spInfo = load(fullfile(superResDir,'CalSpectra'));

channel = [400 600];

% sp(:,[2 3]) = 0;

multiWaitbar('sets of data','close');
multiWaitbar('sets of data',0);

for kk = 1:numel(fileStr)
```

241

```matlab
    fileId =
find(~cellfun('isempty',strfind(hsiFileNames,fileStr{kk}))));


    sp1 = zeros(numel(spIdx{kk})+1,numel(spInfo.wv));
    sp1(1:numel(spIdx{kk}),:) = spInfo.sp(spIdx{kk},:);
    sp1(numel(spIdx{kk})+1,:) = 1/(numel(spInfo.wv)-2);


    %baseline clamp
    sp1(:,end-1:-1:end-2) = 0;


    nonNegConstraints = ones(1,numel(spIdx{kk})+1);
    nonNegConstraints(end) = 0;



    multiWaitbar('making data files for SR','close');
    multiWaitbar('making data files for SR',0);

    count = 0;
    for ii =  fileId(:)'

        count = count+1;

        hsiDataObj = hsiData(hsiFilesFullName{ii});
        data = hsiDataObj.loadFrames;

        %find spectral range
        [~, minWvIdx] = min(abs(hsiDataObj.AcqParams.wv - channel(1)));
        [~, maxWvIdx] = min(abs(hsiDataObj.AcqParams.wv - channel(2)));
        wvRange = false(size(hsiDataObj.AcqParams.wv));
        wvRange(maxWvIdx:minWvIdx) = true;

        data = data(wvRange,:,:,:);

        sz = size(data);
        data1 = reshape(data,[sz(1) prod(sz(2:end))]);
        sp = sp1(:,wvRange);

        [c, resid] = cls(data1',sp',nonNegConstraints);

        resid = reshape(resid,sz);

        paraCCD.PixelSize = hsiDataObj.AcqParams.pixelSize*1e-3;
        paraCCD.FrameTime =
hsiDataObj.AcqParams.t*hsiDataObj.AcqParams.sz(3);

        assignin('caller','spNames',spName{kk})
        assignin('caller','wv',spInfo.wv)

save(fullfile(superResDir,hsiFileNames{ii}),'paraCCD','sp','wv','spName
s')

        dataModel = zeros(sz);
        for jj = 1:numel(spIdx{kk})
```

UNM HSM User Manual

```matlab
assignin('caller',spName{kk}{jj},sum(reshape(c(:,jj),sz(2:end)),3))

save(fullfile(superResDir,hsiFileNames{ii}),spName{kk}{jj},'-append')
        end
        multiWaitbar('making data files for SR',count/numel(fileId));
    end
    multiWaitbar('making data files for SR','close');
    multiWaitbar('sets of data',kk/numel(fileStr));

end

multiWaitbar('sets of data','close');
```